Assessment and Development of Novel Transition Metal Oxide Radiation Detectors

Ahmad M. Subahi

Submitted for the Degree of
Doctor of Philosophy
from the
University College London

Radiation Physics Group
Department of Medical Physics and Bioengineering
University College London
Gower Street, London, WC1E 6BT, UK

July 2011

بسم الله الرحمن الرحيم

IN THE NAME OF ALLAH THE MERCIFUL, THE BENEFICENT

This thesis has been written for the sake of Allah

Declaration

I, Ahmad Subahi, confirm that the work presented in this thesis is my own. Where information has been derived from other sources, I confirm that this has been indicated in the thesis.

Signature

.....

Abstract

New radiation detector materials based on transition metal oxides [TMOs] are being developed for applications in radiation protection. The TMOs are cheap, simple to manufacture and have semiconducting properties, indicating either p-type or n-type characteristics. Thus, p-n hetrojunction diodes may be formed by combining p-type and n-type specific TMOs to produce radiation sensitive detectors. This is done by layering the materials in a flame-spraying process.

Work by Mott on amorphous semiconductors has inspired this work to addressing the theoretical analysis of the disordered TMOs. It is found that charge carriers are polarons due to the presence of localised states in the TMOs. Moreover, the charge transport mechanism is "Mott Hopping", whereby conductivity obeys the relationship of $\log \sigma \sim -[1/T]^{1/4}$. Practically, early studies have shown that TMO detectors perform successfully at room temperature as ionising radiation detectors. However, limitations existed in their very early design, which used Cu tape electrodes and, though demonstrated acceptable levels of response. This response did not meet the full expectation of the TMO detectors. New electrode deposition and materials, therefore, are sought to form ohmic and well-deposited electrodes. In this work, electrodes of Ag and Al were physically vapour deposited on either side of the detector.

The electron microscope was used to fully evaluate the structure of the TMO materials. It is found that the flame-spray deposition is uniform with 3.56% of surface variation. Bulk and surface were scanned and were found to vary by 3.18% with variation in oxygen level of 0.55%. Mechanical polishing has shown a high level of validity to improve the surface by 94%. TMOs have demonstrated superior absorption efficiency of 19%, compared to Si [5%] of 200 μm thickness with 33 keV of incident photon energy. In contrast, CZT showed a superior intrinsic efficiency of 0.47%, compared to TMOs [0.02%] at 33 keV.

In terms of x-ray and UV radiation tests, excellent correlations between TMO detectors, and IC and Si photodiode were observed. Also, detection was found to be uniform as expected across the p-n hetrojunction with a variation of 6% as an average. Finally, the TMO detectors were claimed to be feasible for detection of photons in the energy range of UV up to diagnostic x-ray.

Acknowledgments

First of all, I would like to express my thanks to Allah, then to my great parents, siblings, wife and family for their encouragement and support.

Additionally, it is essential to list those who assisted me in order to fulfil this task in an accepted manner, also, helped me to widen my knowledge and improve my skills in research. My first supervisor Dr. G. Royle is the first on my list as I would like to thank him so much for his great support, concern and patience. Moreover, I would like to thank Dr. J. Griffiths for her consistent advice as a second supervisor.

Additionally, I am most grateful to the Radiation Physics group as a whole, including Prof. R. Speller and Dr. Caroline Reid together with my close colleagues and friends in the Radiation Physics group, especially, Mr. Mashari Alnaaimi, Mr. Walid Ghoggali and Mr. Esam Banoqitah. It was really great to have the opportunity to work closely in such a group at such a university, located in the heart of London, UK.

In addition, my thanks would go jointly to Mr. J. Boardman and Mr. P. Moir-Riches as they are running the manufacturing of the TMO detectors. Also, my thanks would go to Mr. K. Reeves for his endless help in the electron microscopy, based at the Archaeology department, Mr. S. Etienne for his appreciated support in the physical vapour deposition process, based at the London Centre for Nanotechnology and Dr. L. Petaccia for his unlimited supply of information and advice for the synchrotron experiments, based at Elettra, Italy.

It would be unfair if I did not thank the Saudi government, namely the Ministry of Higher Education for being my sponsor and giving me the opportunity to pursue my studies at the University College London to finally, obtain a PhD degree in Medical Physics.

Publications

Subahi A, Griffiths J, Petaccia L, Moir-Riches P, Boardman J, Royle G. UV Response of a Transition Metal Oxide Diode. In: NSS. USA: 2010. p. 1502-1504.

Subahi AM, Griffiths JA, Mannan S, Boardman J, Moir-Riches P, Royle GJ. Assessment and development of novel transition metal oxide materials as a photovoltaic sensor [Internet]. In: Berghmans F, Mignani AG, van Hoof CA, editors. Optical Sensing and Detection. Brussels, Belgium: SPIE; 2010 [cited 2010 Jun 27]. p. 77262E-9.Available from: http://link.aip.org/link/?PSI/7726/77262E/1

Subahi AM, Royle GJ, Griffiths JA, Speller RD, Moir-Riches P, Boardman J. Assessment of novel Transition Metal Oxide radiation detectors [Internet]. In: Nuclear Science Symposium Conference Record, 2008. NSS '08. IEEE. 2008 [cited 2010 Jun 27]. p. 2418-2423.Available from: 10.1109/NSSMIC.2008.4774843

Table of Contents

List of Figures

List of Abbreviations

Symbol	Stands for	Symbol	Stands for	Symbol	Stands for
( )	Referencing except equations and figures	**I_0**	Incident photons	**SSR**	System spatial resolution
[ ]	Highlight	**IC**	Ion chamber	**TM**	Transition metal
A^0	Angstrom	**IQ**	Inter-quartile range	**TMO**	Transition metal oxide
BG	Band gap	**K_α**	Absorption edge	**UOF**	Upper outer fence
BSE	Backscattered electron microscopy	**kV**	X-ray tube voltage	**VB**	Valence band
CB	Conduction band	**LCN**	London centre for nanotechnology	**W**	Hopping energy
CCE	Charge collection efficiency	**LOF**	Lower outer fence	**X**	Exposure
CFT	Crystal field theory	**LSF**	Line spread function	**XPS**	X-ray photoemission spectroscopy
CTM	Charge transport mechanism	**LTEC**	Linear thermal expansion coefficient	**XRD**	X-ray diffraction
E	Energy	**min**	minute	**Z_{effe}**	Effective atomic number
EA	Electron Affinity	**nA**	Nano-ampere	**α**	Localisation length
EDXS	Energy dispersive x-ray spectroscopy	**O**	Oxygen	**Δ**	d-d splitting energy
e-h	electron-hole pair	**pA**	Pico-ampere	**ε_{abs}**	Absorption efficiency
E_k	Kinetic energy	**PSF**	Point spread function	**ε_i**	Intrinsic efficiency
EM	Electron microscopy	**PVD**	Physical vapour deposition	**ρ**	Density
ESF	Edge spread function	**R**	Hopping range	**μ**	Linear attenuation coefficient
E_f	Fermi level	**R^2**	Linear regression	**μ/ ρ**	Mass attenuation coefficient
FWHM	Full width at half maximum	**ROI**	Region of interest	**σ**	Conductivity
h	Hour	**SD**	Standard deviation	**φ**	Work function
I	Transmitted photons	**SEM**	Scanning EM	**χ^2**	Chi square fitting

Chapter 1

1 Introduction

1.1 Overview

Radiation detection has reached an advanced technological level and has applications in medicine, industry and many other fields. However, there remain many factors which continue to reduce the ultimate performance of radiation detectors. For example, the high cost of production of large area Si detectors, the cooling systems necessary for Ge detectors and the fragility presented in the IC [ion chamber]. Thus, research continues to find new detector solutions that can offer high performance combined with economy and robustness (1,2).

The operation of thin film photovoltaics are based on the generation of photo-voltage at X [exposure] to sunlight, discovered by Becquerel in 1839. Semiconductors are found to be convenient for this purpose due to the possibility of p-n junction formation. Solanki listed the most important factors of a semiconductor material for suitability in thin film photovoltaic applications. These factors can be summarised into suitable BG [band gap] E [energy], high absorption coefficient, diffusion length of charge carriers [long-range order], availability, reproducibility and non-toxicity. All these factors will be addressed for TMO materials in this project (3).

Several materials [e.g. CdTe, CZT and GaAs] possess the factors listed above, however, Si is the most common semiconductor amongst them. Different techniques are available in depositing thin film semiconductors, such as PVD [physical vapour deposition], sputtering and chemical vapour deposition (3). Therefore, Luque et al questioned; why are different semiconductors are being sought if Si is so well established? The simple answer is to achieve superior manufacturability at low cost for large scale [up to few m^2] detectors (4). Photovoltaic thin film semiconductors have wide range of applications. The two main applications of concern in this project are x-ray/gamma-ray detection (5,6) and solar cells (3,4).

In consequence, new radiation detectors based on semiconducting TMOs are being produced, using a flame-spraying technique in which pre-oxidised TMO powder is injected into a flame by a controlled process and deposited in layers onto a standard ceramic tile substrate. Both the materials and the production process are being developed jointly with Atmos technologies, the industrial partner to this project. The heat of the flame causes the pre-oxidised TMs powders to oxidise. Layers of varying p-type and n-type TMOs are sprayed onto the substrate, building up a p-n hetrojunction based radiation detector. Thus, when TMOs are sandwiched between two electrodes, they are able to switch reversibly from a high conductivity, σ [ON] to a low σ [OFF], meaning that diode type structure can be created (1,2,7).

For this project, TMO detectors were manufactured and supplied by Atmos Technologies Ltd. Atmos suffered from shortage in funding during this project, therefore, there was a significant shortage in samples. However, after a certain period of time, the project started to perform independently from Atmos. Therefore, the priority of this project was to maintain low cost throughout the assessment and development of the TMO materials and detectors. In other words, Atmos was involved only at the beginning of the project by supplying a set of full detectors and single-layered samples. After that, the author took the responsibility of all the measurements performed, including EM, synchrotron, PVD, mechanical polishing and radiation tests.

TMO detectors operate at room temperature in the photovoltaic mode, where no bias is applied across the TMO detectors. Preliminary tests performed at diagnostic x-ray and UV E's. Results showed acceptable response to radiation in comparison with IC and Si photodiode, respectively.

This chapter will explain the desirable detector specifications for different applications, TMs and TMOs. This is followed by a summary of the TMO applications. This summary will address the applications of the TMOs in recent time. After that, aims and motivations of the project will be clarified. Finally, scope of the thesis will be detailed to understand the flow of the thesis in regard to the project as a whole.

1.2 Desirable Detector Specifications

This section will list the desirable detectors specifications then at the final conclusions of the thesis, TMO detectors will be assessed according to these desirable specifications, which are as follows.

- Cost and Robustness

One of the main requirements of any radiation detector material either for radiation monitoring or solar cell applications is reasonable cost. Thus, it is important to note the cost of survey meter for radiation monitoring applications and solar cells, such as Si, in the market to be compared with Atmos TMOs. Gas filled survey meters, which detects from 7 keV of γ-ray can be more than a thousand of GBP (8). The accuracy of the survey meter will be linked to linearity shortly. Also, photovoltaic Si solar panels are found to cost £700 per m^2 (9).

Another desirable feature in radiation detectors is robustness. Robustness will provide the ease of use while surveying, so sudden hits and vibrations do not affect the physical status of the detector. IC [ionisation chamber] is known to be fragile due to air equivalent material surrounding the chamber, which contains air. Hence, care must be taken while dealing with IC (10).

In terms of Si, Si is relatively robust with 6.5 Mohs hardness, however, Si surface need passivation to avoid oxidation by SiO_2, which will turn the semiconducting Si [1.12 eV] to an insulating SiO_2 [10 eV] (11).

- Design

In terms of detector design, large active area detectors are preferable for solar cells, compared to radiation monitor. Also, the active area should be uncovered by electrodes or otherwise to avoid scattering the UV radiation, which is not the case with diagnostic x-ray. This is because thin layer [few μm] of metallic electrode will contribute insignificantly to the output signal as it will be discussed in 7.2.1.6 Detailed Line Profile (3).

- Range

In terms of energy range, TMOs should cover the range of 25 kV to 150 kV for diagnostic x-ray (8,10) and 3 eV to 120 eV for solar cells, which is the range of the UV primarily (3).

- Linearity

Linearity is the net signal produced by a detector, plotted as a function of photon fluence rate. X-ray detectors should ideally have a linear response to x-ray photon fluence rate at a constant kV (1,2,12-17). This is because linearity allows a direct conversion to dose rate in dose meters. However, linearity is tolerable with a variation up to 10%. This is because the American Association of Physicist in Medicine sat this baseline with x-ray photon fluence rate, provided that a correction factor is applied, which is not the case in dose meters (18).

However, this feature [linearity] is not required in solar cells as solar cells are preferable to be non-linear detectors to generate a signal in the highest possible magnitude with small photon fluence rate (17).

- Photon Energy Dependence

Radiation detectors are not expected to be linear with energy. However, some shows linear response at certain energies, which increases their liability to be used at this energy. This is because calibration is needed to correct for this non-linearity for direct dose measurements. One of the calibration methods is to compare the response of any detector to that of a well-known detector as suggested by Theocharous for CdTe calibration by Ge detectors (19). Fluke biomedical IC shows linear response [R^2=0.999] with x-ray energy in the range of 30 kV – 80 kV. On the other hand, Si photodiode shows non-linear response to Elettra synchrotron radiation in the UV range as it will be discussed in the bulk of the thesis.

- Reproducibility and Signal Stability

Reproducibility presents repeat x-ray irradiation tests made on the same detector under identical conditions. Furthermore, signal stability is a measurement performed to find the degree of variation of a single net signal over time scale of graduated intervals. These two tests would show how reliable is a detector to be used on the field (1).

The American Association of Physicist in Medicine specified the precision of the signal, which is represented by the reproducibility and stability, to be 3% of the average signal value as a maximum (18). Hence, typical diagnostic x-ray IC and photovoltaic Si photodiode reproducibility can be in the order of 0.3% and 0.8%, respectively.

- Atomic Number [Z]

In terms of material specifications, high Z material are desired for high photoelectric interaction probability for low [UV] and medium [diagnostic x-ray] energies. This is because the probability of the photoelectric interaction varies directly with Z^4 of the material. Si showed poor photoelectric absorption in high energies due to its relatively low Z [14], which requires a thickness of 100 cm that is unrealistic (20).

- Efficiency

Efficiency is the ability of the material to convert radiation to electrons (ε_{abs}) in the bulk of the active area then allow charge carriers to reach electrodes (CCE) without recombination or trapping (21).

The highest efficiency of Si solar cells is 24.7%, however, commercial solar cells efficiencies are in the range of 17% to 18%. Also, for more realistic comparison with amorphous TMOs, amorphous Si has a typical efficiency within the range of 6% to 8% (3). Moreover, typical efficiency of CZT at 33 keV can be 47% as it will be seen in the bulk of the thesis.

- Noise Level

In terms of signal to noise ratio, authors suggested that the signal should be 4 to 5 orders of magnitude compared to the noise level. This is applied on all radiation monitoring and solar cells, such as Si and $GaSe_2$ (22,23).

1.3 Transition Metals and Transition Metal Oxides

TMs occupy groups 3 to 12 of the central part of the periodic table and can be defined as elements possessing, either completely or partially filled d orbitals in one or more oxidation states. In fact, the oddity of the position of the d orbitals is the main feature for the TMs, where this oddity accounts for the variety of the TMs electronic properties. The term transition arises from the transitional position of the TMs between the metallic elements in groups 1 and 2 and the non-metallic elements in groups 13 to 18 (1,24).

TMs range from the wide spread elements such as Iron in the earth crust to the extremely rare elements such as Tc, which does not occur naturally and was first prepared in 1937. TMs groups are subdivided into first row [filling of 3d orbitals], second row

[filling of 4d orbitals] and so on (24). This project will focus on first-row TMs, owing to their low cost, abundance and non-toxicity (25).

TM compounds have variable oxidation states, which mean that they can form a substantial number of compounds. TM compounds have long-term stability even with the unpaired electrons in the d shells, whereas, out of the d-block, atoms with unpaired valence electrons [outer electrons] are called radicals. Radicals are short-lived and highly reactive. TMs in complexes, including TMOs, with open shells, and unpaired electrons are stable and common because the open d shells are contracted and core-like. This will be explained in chapter 2 Theory (24). On the other hand, TMOs have O [oxygen] as ligands, which have the predominant oxidation state of -2 [O^{2-}]. TMOs, also, have a wide range of BG's, however, our interest is in semiconducting TMOs, which have the BG range of 3 – 5 eV (1).

Ambiguities in oxidation states may arise when charge is partitioned between elements, which show variability in oxidation state. This led to the proposal of mixed valency, which allows the presence of more than one oxidation state in a TMO, for example, Fe_3O_4 have both Fe^{3+} and Fe^{2+} TM centres. This fact is important as it will contribute to the explanation of CTM [charge transport mechanism] in chapter 2 Theory (1,24,26).

Finally, it is important to mention that Atmos used TMOs in the structure of spinel, corundum and rock salt. Spinel has octahedral and tetrahedral coordination, whereas, corundum and rock salt have only octahedral coordination. TMO structure and coordination will be addressed in chapter 2 Theory, meanwhile, summary of Atmos TMOs will be given in chapter 3 Materials and Methods (24,27).

1.4 Summary of Transition Metal Oxides Applications

TMOs have long been known and have wide variety of applications due to their transitional character. This is because TMOs can undergo metal-insulator transition as a function of temperature or pressure (27). For example, TMOs are widely used as solid state gas sensors for environmental safety purposes (28-30). On specific TMO, Cr_2O_3, is used for soft material mechanical polishing due to its relatively high Mohs hardness (31), they are used to dope organic wide band gap materials for p-type applications (32) and,

last but not least, TMOs can be used as oxidising catalyst in methane-methanol interaction (33).

In considering TMOs as radiation detectors, Duffy stated that TM ions give rise to absorption bands in the UV region (34). Some investigation into the use of TMOs as UV detectors has been undertaken. ZnO is found in literature to be a promising common n-type TMO, used for UV detection only, however, ZnO is usually used with Si to form a p-n hetrojunction and difficult and expensive methods of material deposition are required as ZnO has to be in a very high quality status. These deposition methods can be pulsed laser deposition or molecular beam epitaxy. Other, more complicated TMOs have been investigated, such as $La_{0.29}Pr_{0.38}Ca_{0.33}MnO_3$ – Nb:$SrTiO_3$, however, this material only responded to photon E ranges of 1.4 to 2.1 eV before undergoing saturation. In addition, other aspects were applied, such as doping [Li:NiO] and biasing [up to – 6 V]. Additionally, some authors did not test their TMOs with UV radiation. They just tested the I-V curves characteristics, which showed diode-like behaviour. Finally, Kuznetsov suggested coating Si photovoltaic solar cell with TMO to increase its output due to TMO high ε_{abs} [absorption efficiency] to UV, where an improvement in the output of 5% was observed (35-43).

In terms of diagnostic x-ray detection, little literature exists in the use of TMOs as x-ray detectors. Alternatively, Atmos oxide [will be discussed later in chapter 3 Materials and Methods], in particular, can be found in literature for some physical properties only as it will be seen in the bulk of the thesis. In (2003) and (2004), Arshak conducted a series of measurements, using Gamma radiation [Cs-137] on a selection of few rock salt first-row TMOs, such as MnO and CuO. Arshak used TMO-Si hetrojunctions in the bulk of his analysis and similar aspects to UV measurements, including biasing and doping, were applied to the measurements. Crucially, Arshak radiation response curves were characterised by saturation to a certain extent and non-linearity, although the hetrojunctions he used were tested by I-V curve and showed diode-like behaviour (44-49).

As it was mentioned above, Atmos uses a variety of TMOs, including spinel, corundum and rock salt structures. However, most of the TMO used by Atmos are not common in literature for radiation detection applications. On top of that, the deposition mechanism used by Atmos is the flame-spray deposition process, which involves

injecting pre-oxidised power into the flame to be oxidised and deposited onto a substrate. The flame-spray process will be explained in details in chapter 3 Materials and Methods.

The production of oxides from powders is common in literature. Rao et al. mentioned the preparation of oxides by using pelletized starting powders then heating them up near the melting point. Also, Okutan et al. used TMO staring powders to prepare TiO_2 samples. However, that was for chemical preparation, unlike Atmos flame-spray technique since Okutan was after crystalline TMO. Moreover, none of the authors pre-oxidised the powders before deposition, which makes Atmos process unique. The pre-oxidation phase is found to improve the stability of the oxide material (50,51).

1.5 Aims and Motivations

The ultimate aim of this project is to develop a technology for use as ionising radiation detectors for medical applications. One significant goal is to develop a technology for real-time radiation monitoring for radiation protection purposes. Clearly, this application will require robust, large area materials and in the fraction of the cost, compared to the currently used semiconductors in the market. This is because the TMO detector manufacturing process offers the prospect of being able to coat controlled and supervised areas with large area detectors [active wall tile]. This means, TMO detectors have the potential to overcome the issues of high cost and fragility often associated with other radiation detectors (1,2,7).

In addition, these novel TMOs perform successfully as intrinsic semiconductors at room temperature in the photovoltaic mode, meaning there is no requirement to bias or dope the material. Initial testing, even at this very early stage of detector development, has elicited very promising results, when compared with literature, IC and Si photodiode.

Finally, as it was explained in section 1.4 Summary of Transition Metal Oxides Applications, Atmos TMOs have never been used as ionising radiation detectors in the diagnostic x-ray range. Even in terms of UV, ZnO is the only common TMO detector in use, which will free the way for Atmos TMO to enter the UV field as well for solar cell applications. This means, a great deal of work is awaiting to be carried out on Atmos TMO detectors in order for them to meet their true potential.

1.6 Scope of the Thesis

After giving the introduction, a comprehensive theoretical study will be fulfilled with a view to understanding Atmos TMOs charge carrier type and CTM. By this mean, it will be possible to link the theoretical modelling to the experimental results afterwards. Then materials and methods will be discussed, including background, corresponding equations and system setup for every single assessment or development attained in this project.

After that, the thesis will be divided in four main sections. The first section will assess the prototype TMO detectors and will compare their performance to that of the IC. To avoid interrupting the sequence of the thesis, some aspect will be left vague deliberately in the text. This is because any rush of results will make no sense at that stage.

The second section will be achieved by the aid of the EM [electron microscopy], where several tests will be performed together with justifications to the limitations presented in the first section during x-ray radiation assessment. Also, following the analysis of the EM, recommendation will be made in which the priority will go to the most effective limitations.

Section three involves the prioritised developments in term of electrodes, and surface preparation. Due to the importance of the surface preparation, two solutions will be investigated, which are mechanical polishing and sputtering.

The final section assesses the performed solutions and determines their effectiveness through the use of experiments, such as CCE [charge collection efficiency]. Broadly, the final section will be speaking of radiation tests in terms of x-ray and UV, attenuation coefficient, efficiency, and noise behaviour.

Finally, conclusions will be drawn with referring to the rest of the solution as a form of future work. This is followed by references list then appendices. In fact, appendices play a big role in the thesis as many repetitive analyses are available. So, by the aid of the appendices, it is possible to include the main results and discussion, leaving any repeated measurement or images at the appendices for referencing.

Chapter 2

2 Theory

2.1 Introduction and Definitions

Serious attempts to characterise and understand the electronic structure of TMOs began in 1930s. This is because TMOs exhibit such a wide variety of properties and phenomena, where attentions should be drawn to the correlations among structural and operational properties. This is owing to their potential use in the development as novel electronic radiation detector devices (27,34,50,52).

Some definitions would prove useful at this stage. An orbital is the region in space occupied by a single electron or a pair of electrons. According to Pauli Exclusion Principle, the maximum number of electrons per orbital is two and where this achieved, the electrons must have opposite spin (50).

Orbital overlapping is the key factor in turning a localised orbital into an itinerant orbital via a convenient bonding in the case of perfect crystals. Orbital overlapping means multiple orbitals can occupy the same space and where orbitals overlap, a bond is formed immediately (50).

The basic way of representing the crystal geometry of a TMO is by arranging the O ions around the TM ion in a method called Coordination, which arises from arrays formed from cations and their nearest anion neighbours. Octahedral and tetrahedral coordinations are the most common coordinations in TMOs (24,27,34,53). The oddity of the position of the 3d orbitals is the main feature for the TMOs. 3d orbitals are contracted, core-like and contribute much less than 4s orbital, and it is the 3d orbitals, which assign the TMOs electrical properties. This is depicted in Figure 1 for first-row TMOs (1,2,24,50,54). The orbitals responsible, therefore, for bonding and valance shell formation are 4s. In other words, the bonds holding the complex together are very largely built from the 4s TM orbitals together with O 2p orbitals, as 3d orbitals overlap insignificantly with the O 2p. On top of that, 4s orbital is of the more penetrating type as

it has subsidiary maxima fairly close to the metal nucleus and they are [subsidiary maxima] represented by the number of nodes. These nodes are equal to the actual orbital presence in each orbital principal quantum number [4s = 4 and 3d = 1] obtained from electron configuration. Consequently, the 3d electrons are more shielded from the nuclear charge in complexes compared to 4s. This greater shielding result in their being less well bound, and their radial distribution thus grows [see Figure 1] (1,24,50).

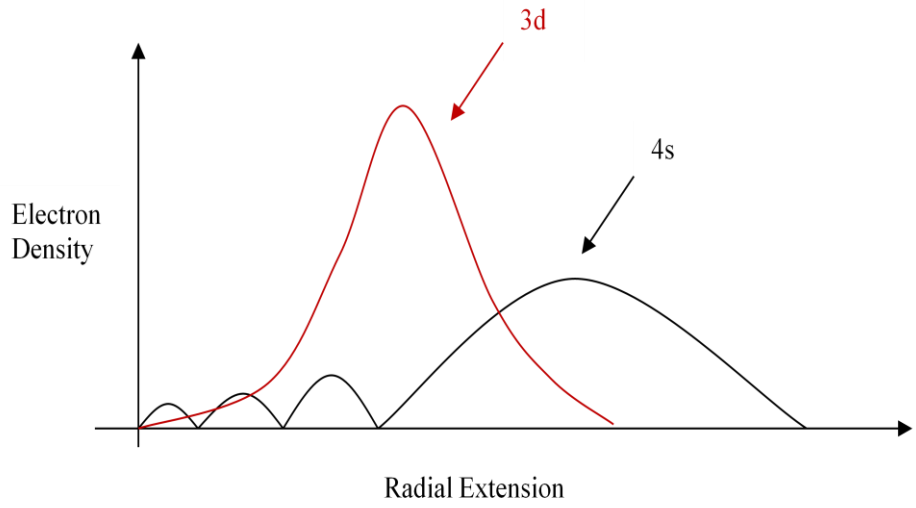

Figure 1: 3d and 4s wave-form functions [not to scale] **(24)**

Mott defined amorphous materials as a solid in which one or more of the three-dimensional periodicity is absent. He suggested that amorphous solid prepared by physical heating can be insulators or wide BG [> 2 eV] semiconductors. The terms disordered, non-crystalline, amorphous, glassy or vitreous are synonyms but the last two terms are restricted to non-crystalline materials prepared by cooling from melt only. The TMOs used in this project are amorphous consist of a central TM ion surrounded by O ions. In terms of coordination, for instance, Mn^{2+} in MnO can be considered as the central ion in an octahedral MnO_6 unit. In this unit, the six O ions create an electrostatic field surrounding the TM ion, where CF [crystal field] arises (1,2,12,24,27,34,53).

Mott (active from 1968 to 1990), Cox (1992), Gerloch (1994) and Rao (1998) have paid valuable efforts to build the models, which account for the structure and electrical properties of TMOs, and form the foundation of much of the work being carried out on TMOs today. The CFT [crystal field theory] describes how TM ions are perturbed by their environment. Here, the five 3d orbitals are split into two sets. The top two orbitals set is called e_g and the lower three orbitals set is called t_{2g}. This splitting gives rise

to a crystal field splitting E between the higher E e_g and the lower E t_{2g}. Therefore, d-d transitions are must be taken into account and not to be confused with the BG (2,27,34,53).

This is because the transition from the VB [valence band] to the CB [conduction band] through the BG [in other words, CTM] is the key factor in the theoretical section of this project. Friedrich and Stefan did some XPS [x-ray photoemission spectroscopy] work on NiO and they emphasised that confusion might occur between p-d transition [VB to CB] and d-d transition. This is because the BG is sandwiched between a filled VB and an empty/partially filled CB. The VB is predicted to be made up of O 2p orbitals, whereas, the CB is made up of TM 3d orbitals (2,24,27,50,54).

The importance of the CFT arises because the molecular environment will have an effect on the CT, since the TMs 3d orbitals are highly affected by the molecular environment. According to CFT, this is because each environment, such as Octahedral or Tetrahedral, has its own orbital splitting and ions arrangements (1,24).

Defects are defined as sites, where the periodic potential of a perfect lattice is disturbed and they can simply be random. Also, defects change the net charge of the network, while keeping the same crystal structure. They act as scattering/absorbing centres and, so, lower the μ and σ of electronic carriers by introducing localised states within the BG (27,50,55,56).

Due to the presence of defects and consequently, localised orbitals, certain charge carriers show up. Polarons are the agreed charge carriers by all authors in literature and these are defined as carriers trapped at one site by the local lattice polarisation they cause. Polarons characterise by having a specified CT mechanism called Hopping as it will be discussed shortly (2,54,57).

2.2 p-type and n-type TMOs

It is essential to explain why some semiconducting TMOs show p-type characteristics, whereas, others show n-type characteristics. In terms of p-type TMOs, electrons are removed by extra oxidation, which will have an effect on the stoichiometry [O to TM ratio] of the TMOs. For instance, NiO shows p-type characteristics. This is because the average oxidation state of Ni is lower than Ni^{2+}, which fits perfectly with O predominant oxidation state [O^{2-}] and so, there must be some holes in the levels of NiO (2,27,58).

On the other hand, n-type semiconducting TMOs are obtained when higher oxidation states [higher than TM^{2+}] are predominant i.e. opposite to the p-type process. Conduction then arises from transfer of the extra electrons provided by the TM. Therefore, modifying the stoichiometry will affect the type of the TMO, where an excess of O [oxidation] gives more holes in the VB (2,27,50).

In consequence, when p-type TMO is put in contact with n-type TMO, a junction will be formed. This junction is a hetrojunction as p-type TMO is totally different material from n-type TMO. The hetrojunction differs from homojunction [e.g. Si photodiode] by having different E bands for CB, VB, EA [electron affinity is the difference between CB and vacuum level] and φ [work function is the difference between E_f and vacuum level], where E_f is the Fermi level. The only similar level in hetrojunction is the E_f and is defined as the top filled level in the ground state out of the CF. The equality of the E_f's indicates reaching the equilibrium (59).

2.3 Crystal Field Theory

The CFT was the first theoretical model to differentiate between free ions and ions in crystal patterns. The main idea of the CFT is that in the free ions, all electrons are subject to three central factors; E_k [kinetic energy], attraction to nucleus and repulsion between each other. On the other hand, in the environment of other ions [crystal pattern], electrons are expected to be subject to one more factor besides the factors listed above. This factor is the effect of the electric field established by the surrounding ions. This electric field is called CF (24).

The BG of a TMO is predicted to be sandwiched between a filled VB and an empty/partially filled CB, furthermore, the VB is predicted to be made up of O 2p orbitals [as the O^{2-} ion has the filled shell electron configuration $2p^6$], meanwhile, the CB is made up of TM 3d orbitals. The basic view of how TM ions are perturbed by their environment is shown in Figure 2 (24,27,34,50).

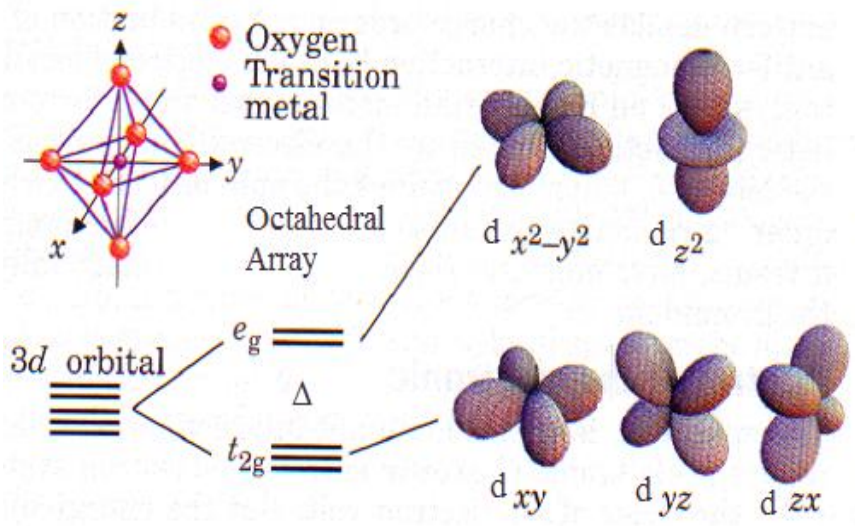

Figure 2: 3d Orbitals of a TM ion in an octahedral coordination [NB: 3d orbitals are in the same E level before splitting, and for e_g and t_{2g} sets individually], reproduced from reference **(55)**

In Figure 2, a TM ion in octahedral coordination is depicted. The five 3d orbitals are split into two sets. The first top set is called e_g, where two orbitals have lobes of maximum probability directly pointing at the near neighbouring O ions. The lower set is called t_{2g}, where the remaining three orbitals have nodal planes in the e_g orbitals directions. The labelling e_g and t_{2g} come from their orbital symmetry behaviour of an ideal octahedron. Figure 2 shows how the octahedral environment gives rise to a CF splitting E [Δ] between the higher E e_g and the lower E t_{2g}. Indeed, e_g orbitals have higher E than t_{2g} orbitals because electrons in the e_g orbitals [orbitals directed along coordinate axes] experience a greater repulsion from the negative ligands [O] than those in the t_{2g} [concentrated between the axes] (24,27,53).

In a tetrahedral coordination, the 3d orbitals splitting is preserved just like in the octahedral coordination. However, the splitting is reversed to become lower E e and higher E t_2. Note that the g subscript is not used any longer as there is no centre of symmetry in the tetrahedral coordination. This is because four pyramidal O ions are surrounding the TM ion, unlike the octahedral coordination (24,27).

The differentiation between the subsets [e_g and t_{2g}] in the octahedron was based on orbitals being oriented directly at or between the point charges [O ions]. However, in the tetrahedron, all 3d orbitals point between the O ions, though some are closer to the point charges than other. Accordingly, the magnitude of the tetrahedral orbitals splitting is less

than that in the octahedral. Gerloch showed that for the same TM [same 3d orbitals radial functions], these splittings are related by the following expression. Where, the negative sign emphasizes the inversion of t and e orbital subsets (24).

$$\Delta_{tet} \approx -\mathbf{0.5}\,\Delta_{oct} \qquad \text{Equation 1}$$

The Δ arises from electrostatic perturbation of the TM 3d orbitals by surrounding O ions together with orbital overlapping. The electron configuration for ions in octahedral sites or otherwise are obtained by placing electrons in the t_{2g} and e_g orbitals according to Pauli Exclusion Principle. Moreover, the ground states of the free ions obey Hund's First Rule. This means that the electrostatic repulsion between electrons is minimised by arranging them as far as possible with parallel spins in different orbitals of the same E level. If these orbitals are then filled, anti-parallel spins are possible. After that, moving to higher E levels is required after filling all of the current orbitals. For instance, in an Octahedral coordination, t_{2g} will be filled by spin up electrons, then after filling the three orbitals, spin down is possible. After filling all the three orbitals of t_{2g} with both, spin up and spin down electrons, moving to e_g orbitals is allowed.

It is important to clarify the difference between d-d transition and the BG. For instance, Cr_2O_3 is a p-type TMO and is very common in Atmos TMOs. The d-d transition in the Cr_2O_3 is 2.1 eV. However, the BG, which represents the CT E, is 3.7 eV (24,27,50,60).

It is worth mentioning that the effect of the CF on s orbitals will be only to shift its E. The three p orbitals are directed along the three axes [x, y and z] and so, electrons in these orbitals [for octahedral and tetrahedral] will suffer equal repulsion from point charges sited on those axes. Thus, the E's of the three p orbitals remain equal (24).

The Atmos TMOs studied in this project [which will be introduced in chapter 3 Materials and Methods] are based mainly on spinel structure. TMO spinels are compounds containing TMs in the general formulae AB_2O_4. O ions are arranged in the tetrahedral coordination with cation A and in the octahedral coordination with cation B. The spinel has the oxidation states of $A^{2+}[B^{3+}]_2O^{2-}{}_4$. Also, corundum structure [U_2O_3] and rock salt structure [DO] are obtained in some cases, where both structures are in the octahedral coordination. NB: U and D represent TM ions. Corundum has the oxidation states of $[U^{3+}]_2O^{2-}{}_3$, whereas, rock salt has the oxidation states of $D^{2+}O^{2-}$ (24).

In addition, the band structure with a well-defined BG is a feature of a crystalline solid without defects. Yet, for amorphous TMOs, which are deposited by spraying mechanism, this is not true. Defects result in a lack of long-range order that expands the band [CB and VB] edges exponentially. So, instead of the well-defined BG, there is a gradual exponential transition from the CB with freely moving electrons to localised states of traps, where electrons are immobilised. Similar behaviour is shown with the VB and holes as well and thus, hopping conduction is the only possible CTM (58,61,62).

The next models will be explaining type of charge carriers and CTM specified only for amorphous TMOs. This is because Atmos TMOs characterised by having localised states owing to the presence of defects.

2.4 Type of Charge Carriers

Despite the wide insulating nature of all oxides, TMOs show some degree of intrinsic semi-conductivity. The transport properties of most of these oxides are dominated, in practice, by defects and non-stoichiometry (27).

Any carrier moving in a semiconducting oxide will polarise the surrounding lattice. Polarons are defined as trapped carriers at one site by the local lattice polarisation they cause. The lattice polarisation accompanies the carrier in its motion. Thus, an electron moves as a heavy particle in a band because it carries its polarisation well with it. Hopping of polarons therefore becomes the predominant CT process. Charge carrier hopping occurs when carriers move from site to site by overcoming the potential barrier [see Figure 3 below] (2,24,27,50,52,56,57,63).

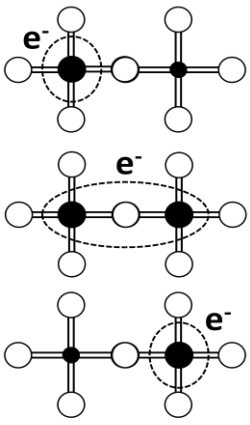

Figure 3: Hopping of electron as a polaron within a portion of a TMO lattice between nearest-neighbour TM ion [TM: black circles, meanwhile, O: white circles] **(2,52)**

Polaron theory has been applied to semiconducting TMOs. In 1933, Landau was the first to propose the creation of polarons. In essence, d-band electrons are thought to move between TM ions via the 2p orbitals of O ions as seen in Figure 3 (2,12,63).

Mott described the hopping of polarons in terms of polarisation wells in glassy TMOs. For instance, in the n-type Fe_3O_4, hopping of an extra localised electron from site to site would change Fe^{3+} to Fe^{2+}. Thus, the ionic radius of the Fe sites increases for Fe^{2+}. This is accompanied by polarisation of the surrounding lattice, which is the origin of the distortion that traps the charge carriers. This distortion moves with the carrier during its migration to an adjacent Fe ion. NB: hole transfer should be viewed as Fe^{3+} to Fe^{4+} (27,50,52,56,57,64).

An electron in a solid system interacts with both, other electrons and lattice. At high temperature [room temperature], the former interaction is ignored since the electron will have a sufficient E to overcome the coulomb gap between the two electrons. Hence, Mott stated that $\log \sigma \sim - [T_o/T]^{1/4}$, where T is the absolute temperature and T_o is a constant [T_o will be explained in section 2.5.2 Mott Hopping Modelling]. On the contrary, this is not the case in electron interaction with the lattice, where the formation of, and Mott Hopping of, polarons take place. This means that TMOs behave as typical semiconductors, where the resistivity decreases with increasing temperature exponentially (12,27,63,65-70).

The increase in σ with temperature is due to the interaction of electrons with the lattice. As the phonons [lattice vibrations] increase with temperature, they can interact with electrons in which the phonons are absorbed and lead the electrons to move between states. In other words, electrons can exchange E with phonons, moving them from one localised state to another. This is responsible of shortening the life time of electrons in localised CB states and, thus, leads to delocalisation. Hence, this interaction with the lattice is the reason in forming polarons, and can be represented by the mean free path (59,63).

The mean Free Path is a measure of the average distance travelled by a particle during a certain period before it interacts with other particles, including the lattice nuclei. A carrier's mean free path falls as temperature rises due to phonons, however, the mean free path cannot fall below the inter atomic spacing (13,56). Moreover, the potential well extends due to the polarisation of a lattice around a trapped electron [electron in a

localised state] as seen in Figure 4. This expansion is owing to the fact that the polarisation will cause a displacement of the surrounding ions due to the movement of the charge carrier. This ion displacement will cause it to release E. Figure 4 also shows the hopping mechanism of polarons, where level 2 is called the activation level in which the polaron is ready to hop as soon as it receives any extra E. The lattice view of Figure 4 was shown in Figure 3 (12).

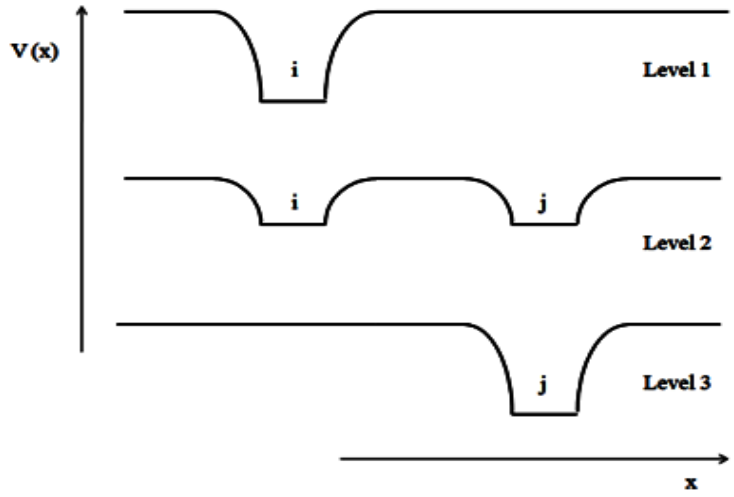

Figure 4: Hopping of polarons from site i to site j in terms of potential wells due to polarisation of lattice around a trapped electron; level 1: before hopping; level 2: activated state when electrons can move; level 3: after hopping **(12,57)**

Broadly, the difference between ordered and disordered materials is that E bands may be smeared out in disordered materials, so some localised states may appear in the forbidden gap. These localised states are traps and, hence, activation E [1/2 polarisation E as seen in Figure 4] is needed to excite a polaron to a state, where it will be mobile. This E [activation E], applied for doped crystalline solids, was proposed by Mott, during his work on glasses containing TMs, where the polarisation well is formed around the charge carrier. According to Anderson, disordered TMOs suffer from having localised states in which electrons are thought of as localised on a TM by the random field caused by defects. As hopping is the only possible conduction in these localised states, the next section will focus on Mott hopping process and its application to Atmos TMOs (12,54,57,63,67,71).

2.5 Charge Transport Mechanism

2.5.1 Historical Introduction and Definitions

In 1956, Conwell and Mott first suggested the hopping process from occupied to unoccupied localised impurity states. Coincidently and independently, Pines, Abrahams and Anderson proposed the same hopping mechanism at that time (70,72).

The localisation state was first expressed in detail by Anderson in 1958, expressing the absence of diffusion in some random lattices. This is because when an electron of an energy E is placed in a random volume, the electron will not diffuse away due to the localised states, which are owing to the static intrinsic disorder. Mott based his model on the Anderson model, and this model was named the Mott Hopping Model. Mott's work on amorphous semiconductors resulted in his winning the Nobel Prize in 1977 (12,63,70-73).

In 1968, Mott stated that the conduction in glasses containing TMs is similar to impurity conduction in doped semiconductors [e.g. Ge], which is hopping. In fact, hopping process occurs in a wide range of materials, such as doped semiconductors, glasses and amorphous semiconductors. This is because, whether the material which hosts the impurities is crystalline or non-crystalline, the impurity atoms are distributed randomly. In this sense, the difference between crystalline materials and non-crystalline materials is that the distances between sites i and j in Figure 4 are not constant in non-crystalline materials, unlike crystalline materials (12,57,73,74). In addition, due to the random presence of defects, conducting electrons experience a potential, which varies randomly along the TMO material, which will interrupt the conduction process (27,73).

2.5.2 Mott Hopping Modelling

A key relation in the behaviour of CTM in disordered semiconducting TMOs materials is the prediction by Mott. This prediction suggests that the σ is temperature-dependant as $\log \sigma \sim - [T_o/T]^{1/4}$ for hopping among localised states in a three-dimensional system. This prediction is represented mathematically in the following equation (12,51,67,68,70,73-80).

$$\sigma = \sigma_o e^{-(\frac{T_o}{T})^{1/(1+d)}} \qquad \text{Equation 2}$$

α is the exponential decay of the localised states wave-functions. In other words, α is the length of the distorted lattice around a polaron and is in the order of few A^0's [Angstroms] in TMOs e.g. $\alpha = 3.5/A^0$ in Vanadium oxides (63,70,73,74,77). d represents the space dimension for hopping as three-dimensional hopping, which means d = 3. Additionally, the σ parameter [σ_o] is estimated from Diffuson [not to be confused with diffusion] theory. Briefly, Diffuson theory is a differential mathematical object based on the random motion of electrons within a disordered lattice in the physics of condensed matter. This parameter [σ_o] is dependent on the overlapping of orbital wave-function and phonon frequency (27,73-76).

N[E] is the density of states, which is defined as the number of states per unit volume for an electron in the system. Thus, Mott stated that (12,51,67,70,74-79).

$$T_o = \frac{16\alpha^3}{kN(E)} \qquad \text{Equation 3}$$

Where, k is Boltzmann constant. Finally, Mott expressed the hoping range [R] and the hopping E [W] as (2,12,51,70,73,75-77).

$$R = \left[\frac{3}{2\pi\alpha N(E)kT}\right]^{1/4} \qquad \text{Equation 4}$$

$$W = \frac{3}{4\pi R^3 N(E)} \qquad \text{Equation 5}$$

From Equation 4 and Equation 5, the average W should be minimum, when N[E] is maximum. This is because the electron will have the greatest chance to find another site with nearly the same E. In addition, the longer the α, the smaller the R, which will require more E to activate the hopping process. This leads to the conclusion that any lack of long-range order will negatively affect the response of the TMO detector. Therefore, we are aiming to improve the manufacturing process to avoid any limitation mentioned above (2,27,57).

2.6 Summary

3d orbitals determine the electronic properties of the TMOs as they are core-like and contribute much less than the other 4s orbital. When p-type TMO is brought in contact with n-type TMO, a p-n hetrojunction will be formed (2,24,54).

Theories of the electronic structure of TMOs were explained, starting by the CFT. The CFT puts the free ions in a lattice then it explains how these ions will arrange themselves according to the electrostatic force produced between them. Also, the CFT accounts for the production of the d-d band with Δ in Octahedral and Tetrahedral coordinations and they are the most common coordination in Atmos TMOs. This would eliminate the confusion, which might occur between the d-d transition and the actual BG (24).

Mott's work on amorphous materials inspired the theory of the charge carriers type [polarons] and CTM [hopping]. Due to the presence of defects in Atmos amorphous TMOs, polarons are formed. Polarons move from site to site by a CTM called Mott hopping. Mott predicted that the σ is temperature-dependant and related by $\log \sigma \sim -[T_o/T]^{1/4}$ for hopping in localised states in a three-dimensional system (63,80).

So far, it is possible to clarify the purpose of addressing the theory. As explained earlier, 3d orbitals determine the electronic properties of the TMOs. Consequently, the d-d transition arises from CFT and this must not be confused with the actual BG [p-d transition]. This is because the actual BG is needed to be used in many aspects across the thesis, such as CCE and p-n hetrojunction BG estimation. In addition, polarons would cause the presence of extended potential wells. This indicates the need for extra E [> BG] to allow a charge carrier to hop from site to another [localisation E]. The localisation E will be quantified in section 7.4.2 Charge Collection Efficiency. Then, finally, modelling the only CTM possible for polarons [Mott hopping] would make it possible to correlate the response of the TMO detector with the EM images interpretation as it will be seen in chapter 5 Identification of Materials and Limitations. In the light of the EM analysis, we are able to improve the TMO detectors from initial status to current status as it will be demonstrated in this thesis.

After addressing the theory of the TMOs, the experimental materials and methods are presented. The next chapter will discuss the manufacturer, TMOs used as part of this project and all the techniques applied to assess or develop the TMO detectors.

Chapter 3

3 Materials and Methods

3.1 Atmos Technologies Ltd.

Atmos Technologies Ltd. was founded at Daresbury Laboratories, Warrington, UK by Mr. Jeffery Boardman in the mid 1990s, who is still director manager of the company. Recently, Atmos has moved from Daresbury Laboratories to another company called 2D Heat Ltd, also based in Warrington, UK (1,81,82).

Atmos Technologies have designed a robotic flame-spray manufacturing method to produce the large-sized, low cost and robust TMOs, for application in radiation detectors and heating elements. The production process has won an award for low C technology in producing heating elements. The only waste product of the process is CO_2 and the production process does not require full clean room conditions, thereby reducing running costs. The heating elements are 50% more efficient in heat transfer, when compared to ordinary coiled wires heating methods for domestic oven and hob use (7,81,82).

3.2 Detectors Manufacturing and Design

TMOs are deposited onto the substrate via the flame spray process developed by Atmos. TM pre-oxidised powders are injected into the flame by a controlled process and deposited in layers onto the substrate, using a depositing robot nozzle [see Figure 5]. The heat of the flame is produced from the combustion of a fuel gas with O and causes the TM pre-oxidised powders to melt, oxidise then to be blasted on the substrate surface (2,7,83). Table 1 summarises the characteristics of the flame-spray process.

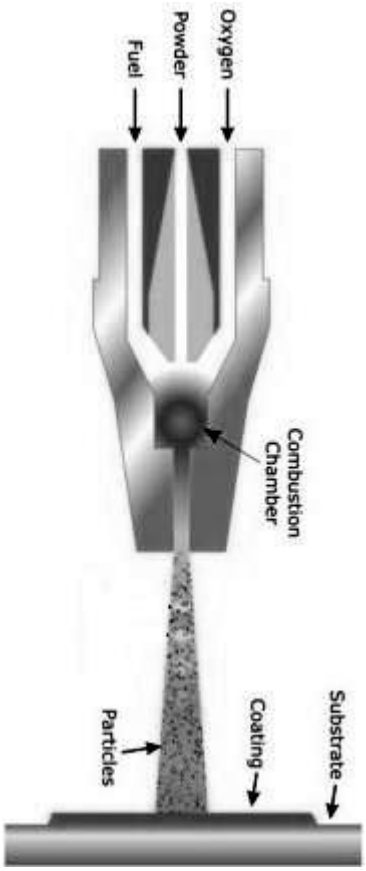

Figure 5: Flame-spray process, reproduced from reference **(84)**

Flame-spray process characteristics	Value
Flame temperature	1500 ^{o}C
Fuel gas type	Acetylene [C_2H_2] and O
Fuel gas flow	16 l/min for C_2H_2 and 40 l/min for O
Deposition rate	20-25 g/min
Particles velocity	200-600 mm/sec

Table 1: Flame-spray process characteristics **(83)**

This depositing mechanism [flame-spray] produces amorphous semiconducting TMOs with wide BG as demonstrated by Mott. Mott said any physical heating technique [cooling from melt] is used mainly for preparing amorphous materials, which can be wide BG semiconductors or insulators (12).

Although the flame-spray technique is the only deposition technique Atmos has access to, other possible techniques are present. Roa et al. listed chemical methods of oxide deposition. This includes the CVD, which is used in Diamond. Chemical methods are capable of depositing amorphous and crystalline TMOs. However, chemical deposition requires knowledge of the TMO crystals thermodynamics and reaction kinetics, which make chemical methods not straight forward. The advantage of the chemical methods is that the stoichiometry is controllable and pure oxides are possible to be produced (50). This can overcome many limitations in the flame spray technique, such as contamination, splash and defects as will be explained in chapter 5 Identification of Materials and Limitations.

Other physical deposition methods are available for radiation detectors fabrication. This includes sputtering and PVD [physical vapour deposition]. However, physical methods require the row material to be already oxidised as oxidation process is not involved neither in vacuum PVD nor sputtering (45,46). PVD and sputtering can deposit uniform material, however, it is always recommended to follow each deposition by one of the evaluation techniques, such as EM, XPS, XRD or electron diffraction (85). Also, TMOs melting points are relatively high [> 1000 ^{o}C], hence, the PVD might require high temperature levels capabilities to be suitable for TMOs deposition.

The first prototype generation of TMO detectors used for radiation measurements consists of a p-type TMO flame-sprayed over an n-type TMO slightly offset from the centre on a glazed-ceramic tile substrate with two Cu tape strips on the sides, acting as electrodes. This is depicted in Figure 6. NB: electrodes and contacts can be used interchangeably. Atmos produced a range of TMO prototype detectors in the size of 2.5 x 5 cm^2 and 7.5 x 7.5 cm^2 (1,2).

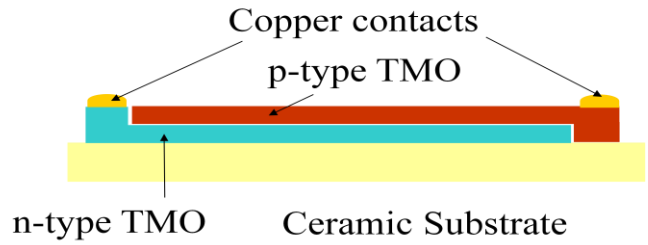

Figure 6: Schematic side-view diagram of the prototype TMO detectors **(1,2)**

After that, a second detector design was suggested and produced. This design has more conventional radiation detector geometry, with the two TMO layers being sandwiched [stacked] between the electrodes. A Cu electrode is flame-sprayed onto the substrate followed by n-type TMO then p-type TMO and finally, the second Cu electrode is sprayed onto the top surface. This is shown in Figure 7 (1).

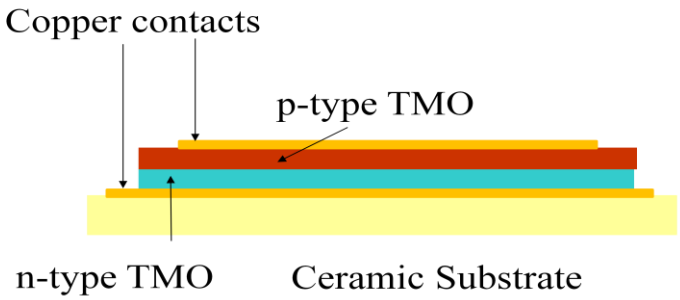

Figure 7: Schematic side-view diagram of the stacked TMO detectors

The second stacked detector design was suggested due to the obvious limitations in the initial prototype design. These limitations can be summarised as the prototype design is not common in literature unlike the stacked design (3). Charge loss is expected in the initial prototype design as a generated charge carrier, for example, in the middle of the detector has to travel long distance across the width of the detector [several cm's] to reach the electrodes. Meanwhile, a charge carrier generated needs to travel only the thickness [hundreds of μm's] of the TMOs layers in the second design. In addition, the Cu tape electrodes of the initial prototype design are loose and do not act efficiently to collect all generated charge carriers.

However, the stacked design failed to show any response to radiation, unlike the prototype design. This is due to poor boundary between different layers in contact, which is supported by our EM studies of those materials. Thus, all radiation tests and developments will be focused on the prototype design. Based on our EM results, development to the current manufacturing process was suggested together with an

alternative detector design. This will be stated in chapter 5 Identification of Materials and Limitations.

The initial design is suitable for solar cells, where the second standard design is suitable for radiation monitoring. This is because the active are in the initial design is not covered by any electrodes to avoid insensitivity of the detector as expressed in 1.2 Desirable Detector Specifications.

3.3 Atmos Transition Metal Oxides

As it was explained in section 2.3 Crystal Field Theory, the Atmos production method is capable of producing spinel TMOs. These materials are listed in Table 2 in the form of pre-oxidised powders and flame-sprayed TMOs.

Pre-oxidised powder materials	Pre-oxidised powder composition	Flame-sprayed compounds	Flame-sprayed compounds chemical states	Type
FeCrAl	Fe (75%), Cr (15%) and Al (10%)	$FeCrAlO_4$	$Fe^{2+}Cr^{3+}Al^{3+}O_4$	n
FeCoV	Fe (49%), Co (49%) and V (2%)	Mixture of $CoFeVO_4$ and $CoFe_2O_4$	$Co^{2+}Fe^{3+}V^{3+}O_4$ and $Co^{2+}(Fe^{3+})_2O^{2-}{}_4$	n
NiAl	Ni (85%) and Al (15%)	$NiAl_2O_4$	$Ni^{2+}(Al^{3+})_2O^{2-}{}_4$	n
MnNi	Mn (66%) and Ni (34%)	$NiMn_2O_4$	$Ni^{2+}(Mn^{3+})_2O^{2-}{}_4$	n
FeNiCo	Fe (54%), Ni (29%) and Co (17%)	Mixture of $CoFe_2O_4$ and $NiFe_2O_4$	$Co^{2+}(Fe^{3+})_2O^{2-}{}_4$ and $Ni^{2+}(Fe^{3+})_2O^{2-}{}_4$	p
Ni	Ni (100%)	NiO	$Ni^{2+}O^{2-}$	p
FeCr	Fe (50%) and Cr (50%)	$FeCr_2O_4$	$Fe^{2+}(Cr^{3+})_2O^{2-}{}_4$	p
Fe	Fe (100%)	Mixture of FeO and Fe_3O_4	$Fe^{2+}O^{2-}$ and $Fe^{2+}(Fe^{3+})_2O^{2-}{}_4$	p
Cr	Cr (100%)	Cr_2O_3	$(Cr^{3+})_2O^{2-}{}_3$	p

Table 2: Atmos TMOs

Notably, Table 2 contains the exceptions of the corundum structure [Cr_2O_3] and the rock salt structure [NiO and FeO]. These materials in particular did not show spinel structure because their powders were not pre-oxidised, and so pure Ni, Fe and Cr powders were used instead. Moreover, Atmos quoted the exact composition with the oxidation states, based on their XRD [x-ray diffraction] results.

The TMOs listed in Table 2, will be used in this project for materials identifications and developments. However, radiation tests will be focusing on only fixed p-type and n-type TMOs combination, for consistency in development at assessment. This combination involves Cr_2O_3 as a p-type TMO and $NiMn_2O_4$ as an n-type TMO. Table 3 gives a list of the TMO detectors label together with their size.

Detector Label	Size [cm^2]	**Detector Label**	Size [cm^2]
TMOD1	7.5 x 7.5	**TMOD3**	2.5 x 5
TMOD2	2.5 x 5	**TMOD4**	2.5 x 5

Table 3: Cr_2O_3-$NiMn_2O_4$ TMO detectors used for radiation tests

3.4 Tube X-ray

3.4.1 Introduction

An MXR-160 metal-ceramic x-ray tube with Tungsten anode, supplied by COMET, was used to fully illuminate the TMO detectors with x-ray photons in the diagnostic x-ray range. The x-ray tube was integrated with a control panel [HS-MP1], high voltage and water cooling systems, provided and installed by AGO Installations Ltd (1,2,86).

This x-ray tube has a maximum kilo-voltage [kV] output of 160 kV and a maximum x-ray tube current of 30 mA. According to the instructions accompanied with the x-ray tube, precautions were taken to be under the maximum limit to avoid damaging the tube, and so experimental conditions were kept below 80 kV with 6 mA and 10 mA with 50 kV for all experiments (2,86,87).

X-ray kV range of 30 kV to 80 kV corresponds to a range of mean output photon E of 20.1±0.6 keV to 37.1±1.1 keV. This equivalent keV range is obtained by simulating the x-ray tube with 1.4 mm of Al as inherent filtration, using xcomp5r software. The SD [standard deviation] quoted with each E value is obtained from reference (88). This software was used as Meyer evaluated six computer codes and concluded that xcomp5r is one of the most reliable software with high accuracy [3%] (88).

3.4.2 System Setup and Measurements Protocols

Tube x-ray radiation tests were carried out with the setup shown in Figure 8. The source to detector distance was set after ensuring that the largest surface area detector [TMOD1] is fully illuminated, using Gadox paper. The output of the x-ray source was observed to stabilise within 10 sec of starting each exposure. Consequently, each measurement was started after 15 sec into the exposure. Also, warming up the x-ray tube together with cooling it down at the end of each experiment was followed according to reference (87) and (86) (1,2).

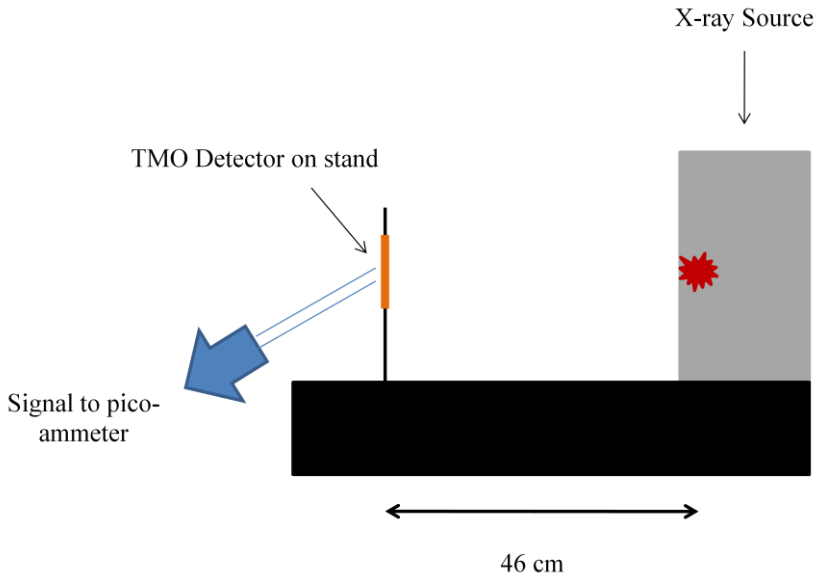

Figure 8: Tube x-ray system setup

TMO detectors were connected in series to a Keithley 6487 pico-ammeter, which monitored the current produced by the detector throughout the radiation measurements [current mode]. The pico-ammeter has a current range from 20 fA to 20 mA, a maximum resolution of 10 fA and an accuracy of less than 0.3% (1,2,7).

The pico-ammeter was turned on one hour before any current measurements were made in order for it to reach its operating temperature and so, achieve optimum accuracy [0.3%]. The temperature in the laboratory was also monitored regularly and was found to vary by not more than 1 ^{o}C. The current measurements recorded are the mean of 200 individual data points, sampled over 60 sec. This number of data points was chosen as being the optimal compromise between precision and time, based on analysis of a range of data point values from 1 to 1500, which found that reproducibility within one SD could be achieved with 200 points in 60 sec (1,7).

Care was taken to neither touch nor move the detector prior to or during the measurements. If the detector needed to be moved, it was allowed to stabilise for 15 minutes prior to starting the measurement (1).

All measurements were made in complete darkness, although initial testing observed a negligible difference in the detector signal with changes in the laboratory's ambient light level. This is because the BG E's of the TMOs vary from 3 – 5 eV, which makes them insensitive to visible light [3 eV for violet], especially, with the potential well expansion explained in section 2.4 Type of Charge Carriers. This makes TMOs insensitive even to the borderline of 3 eV (1,2).

3.4.3 Ion Chamber [IC]

The IC is a gas-filled detector in which incident x-ray photons are absorbed in the internal air volume. When absorption takes place, x-ray photons will interact with air atoms. This will result in ion pairs formation (10,13).

The role of the bias voltage [300 V] is to separate the resultant electron-ion before recombination occurs. This will allow the ions to reach the cathode, where electrons reach the anode then to be directed to the electrometer. In other words, collection of all charges created by the direct ionisation in the air though the application of bias voltage. Thus, radiation is converted into electric charge (10,13).

The IC used is the calibrated 15 cm^3 96035B, supplied by Fluke Biomedical. The IC is connected in series with a Keithley 35050A dosimeter for exposure measurements. This IC is feasible in the range of 25 kV – 150 kV (8,10).

The IC was used in this project for two main reasons. The first reason is to compare the current produced in the IC with the current produced in Atmos TMO detectors. This can be achieved by placing the IC in the same setup shown in Figure 8 and for the same kV and mA steps. The resultant exposure rate can be converted into current according to the following equation (13,89).

$$X = \frac{Q}{m.sec} \qquad \text{Equation 6}$$

Where, X is exposure rate [C/kg.sec]

Q is the total charge

m is the mass of air inside the chamber

The second reason is to calculate the photon fluence rate of the used x-ray tube at different tube currents. So, the photon fluence rate can represent the degree of linearity of the detector response as well as it will be involved in CCE calculations. This can be obtained from the relation of exposure rate to E fluence rate as follows (13,89).

$$X = \psi \left(\frac{\mu_{en}}{\rho}\right)\left(\frac{e}{w_{air}}\right) \qquad \text{Equation 7}$$

Where, Ψ is the E fluence rate [J/m^2.sec]

μ_{en}/ρ is the mass E absorption coefficient [tabulated in reference (90)]

e electron charge

w_{air} is the E required to produce one ion-electron pair in air

After that,

$$Photon\ Fluence\ Rate = \frac{\Psi}{E} \qquad \text{Equation 8}$$

Where, Photon fluence rate is in photons [p]/m^2.sec and E is the photon energy

3.5 Electron Microscopy [EM]

3.5.1 Introduction

In order to develop any device from its prototype condition up to the final presentation, where it can be applied clinically for instance, it is essential to understand clearly how

this device works and precisely which materials it contains. This is fully applied to the TMO radiation detectors and can be achieved using the powerful EM technique (2,27).

The EM is a type of microscope, which implements electrons in rastered fashion to illuminate a sample to produce a magnified image [10000 times]. This large magnification is due to the very small wavelength of the electron [~ 10^{-10} m], which is basically de Broglie wavelength [Wave-Particle Duality], compared to the light photon [~ 10^{-6} m for red light] (91,92).

The EM used in this project is SEM [scanning EM] supported by BSE [backscattered EM]. In the SEM mode, images produced show mainly topographic information about the sample surface. This is because SEM produces images by detecting low E secondary electrons [~ 5-10 eV] emitted from the surface of the sample as a result of the interaction between the primary electrons and the sample. In BSE mode, images indicate both topographic and compositional information as the flux of backscattered electrons produced by a sample varies directly with the sample's Z. Thus, in the BSE images, the brighter the area, the greater the Z of the elements present in that area. Additionally, SEM is usually equipped with EDXS [energy dispersive x-ray spectroscopy] for surface mapping. EDXS analysis is based on the characteristic x-ray produced by the surface of the sample. NB: SEM will be used to indicate SEM, BSE and EDXS techniques, unless otherwise is stated (1,91,93-95).

In order for the SEM to produce accurate images, the object under investigation must be electrically conductive to prevent charge pile-up. Although the TMO samples analysed in this work are semi-conducting, the ceramic tile substrate on which they are sprayed is not and thus, the samples were coated in C for the scanning procedure to be successful (1,91,94,96).

3.5.2 System Specifications

The SEM system used is based in the Archaeology department, UCL. The components of the EM system are the SEM with built-in BSE detector, x-ray detector and finally, the dedicated software for analysis. These components are shown in Figure 9.

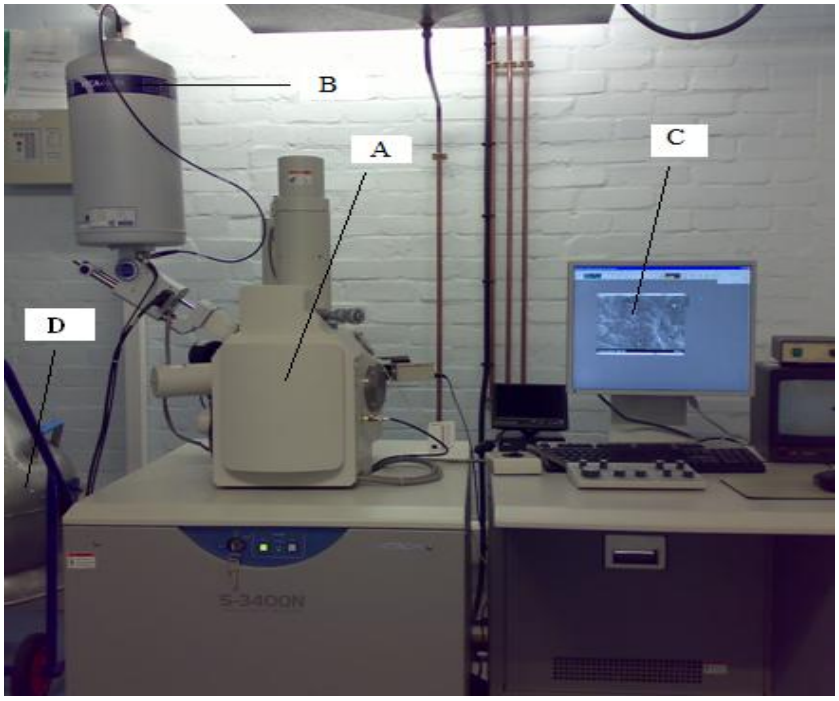

Figure 9: EM components: [A] Vacuumed chamber with sample mount inside [B] X-ray detector [C] Computer hardware and software [D] Liquid nitrogen container

The SEM used is the Japanese manufactured Hitachi S-3400 in the high vacuum [10^{-8} mbar] SEM and BSE mode imaging. The accelerating voltage was set at 20 kV, resulting of a primary electron beam of 20 keV. This is to ensure that it exceeded the K_{α} [absorption edge] x-ray line excitation E's of the first-row TMs. Those two systems [SEM and BSE] are connected to a PC with software called Hitachi S-3400N (1,2,94-96).

The x-ray detector attached to the SEM in order to detect the characteristic x-rays for EDXS is the HPGe INCA X-Sight x-ray detector, supplied by Oxford Instruments. This detector is connected to another PC [not shown in Figure 9] with software known as INCA used for further analysis (1,2,97).

3.5.3 Spatial Resolution

Calculating the SR [spatial resolution] of the system would help to increase the degree of certainty in interpreting EM image. This is because the key factor in image quality assessment is the SR, which describes the dimensions of the smallest detectable structure. If pixel intensity [y-axis] is plotted against the pixel location [x-axis], the FWHM [full width at half maximum] of the resulting curve [Gaussian curve] represents the SR, where the narrower the FWHM, the better the SR (98).

When a point source is projected through an imaging system, the resulting image will not be exactly the same as the source because there is no perfect imaging system. This imaging system will introduce some artefacts, such as blurring into the resulting image. This will result in a Gaussian distribution [point spread function, PSF] of the points over x-axis [pixel location] as a function of pixel intensity. Ideally, this Gaussian distribution should be a straight line at a single pixel (98).

Since it is difficult to produce point sources in practice, line sources may be used instead, which provide a measure called the LSF [line spread function]. Alternatively, a test object with a knife edge can be used, which provides a measure called the ESF [edge spread function]. The first derivation of the ESF will produce the LSF. Gaussian fitting of this function will accurately specify the FWHM (98).

χ^2 shows the quality of the fitted Gaussian curve on the derived data points. One is the optimum χ^2 fitting. Mathematically, χ^2 can be obtained by the following equation (98-100).

$$\chi^2 = 1 - \left[\sum_{i=1}^{n} \frac{(y_i - x_i)^2}{SD_i^2} / DOF\right] \qquad \text{Equation 9}$$

Where,

χ^2: Chi square fitting

y_i: The derived data point on the derivation curve

x_i: The corresponding point on the fitted Gaussian curve

n: Number of data points

SD: Standard deviation

DOF: Degree of freedom, which is the difference between number of data points and number of parameters in the fitting Gaussian function

3.5.4 Sample Preparation

Atmos has supplied a series of detectors in the form of single flame-sprayed layer samples, where each sample consists of either n-type or p-type TMO flame-sprayed over a glazed-ceramic tile substrate. In addition, the second stacked design will be used to assess different layers interfaces and to further understand why the second stacked design did not show any response to radiation.

UCL together with KCL [King's College] worked jointly to prepare samples for the SEM tests. Diamond saws were used to cut the samples in small pieces [few mm^2] without causing significant damage to the cut edges. This is because Diamond has the highest degree of hardness [10] on Mohs scale. The Mohs scale is a hardness scale based on specimen scratch resistance, linked to reference materials sat by Mohs from 1 for Talc to 10 for Diamond (101).

This indicates that the Mohs hardness of a polisher should be higher than the polished material in order to be able to scratch the surface of the polished material. Automated water-lubricated SiC [from 200 grits down to 1200 grits] desks were used to prepare samples surfaces, as SiC has a high Mohs hardness value, which is in the order of 9.2. NB: some samples are embedded in resin to obtain clearer SEM images, especially, in vacuum and top TMO surface interface (102).

After that, an automated alumina cloth [9 on Mohs scale] polisher with a water-based diamond sprayed surface was used to finish the polished surfaces/edges and minimise the scratches caused by SiC papers. This was to remove any deformation caused by the invasive SiC polishing (103). Finally, whenever the insulating substrate was required for scanning, the sample was covered in C. Thus, a vacuum deposition C coater called Edwards Auto 306 was used to coat samples for some selected tests (94).

3.5.5 Scanning Methodology

This section describes the steps followed in the experiments to scan the TMO samples. After ensuring that the sample is conducting/semi-conducting, either by nature or by C coating, the sample was placed on the holder tray. The surface of the sample [TMO layer] was connected to the tray, using C tape. This is because after placing the tray in the vacuum chamber, the sample will be automatically earthed. The height of the sample was measured, to avoid hitting the top of the sample with the bottom of the electron probe, which might cause severe damage to the system. To ensure the maximum possible resolution of the SEM, it is necessary to place the tray as close as possible to the electron probe and, therefore, it was important to measure the height of the sample. The size of the tray together with the height of the sample were typed in the computer software before starting the acquisition.

Air was processed then outside the chamber [vacuum] to start shooting electrons. The first images to be acquired in real time were SEM images in the TV mode. After lifting the sample as close as possible to the electron probe, the best possible resolution images were obtained together with switching from TV mode to mode 3. These modes [TV, 1, 2 and 3] will control the speed of the raster fashion, where the slower [mode 3], the highest resolution. Of course, modifying all the possible system settings, such as x-plane, y-plane, brightness, contrast and probe current was useful. Images were also made in mode 3 BSE where the best possible resolution was achieved by modifying system settings. In terms of EDXS, another PC was implemented in this stage with the INCA software. This software has certain steps to be followed, starting with the sample's label and finishing with the final report. This second PC will speak to the first PC to transfer the same viewed image and do the analysis on it. In this position, a compositional table will be given as well as a surface map.

3.5.6 Electron Microscopy Images Thresholding

EM image thresholding is required to distinguish between defects and pure material. Therefore, in order to quantify EM images, image processing software should be used. The freewares ImageJ and GIMP were used for analysing EM images. ImageJ is provided by the US National Institute of Health [NIH], 1997 (104). GIMP was written by S. Kimball and P. Mattis from university of California, Berkeley in 1996 (105).

Image thresholding can be set by a statistical method called Outliers. This method is suggested by Bohndiek for thresholding breast tissue samples images in order to quantify the degree of fats in these samples (106). Outliers would predict a range [inter-quartile range, IQ], where values which fall out of this range are considered inconsistent with the rest of the values (107). This method divides an image histogram into four portions and takes the mean value at 75% and 25% [see Figure 10]. The difference between the upper [75%] and lower [25%] is the IQ value. This value is multiplied by 1.5 and is then subtracted from the lower [25%] mean to form the lower outer fence [LOF]. The IQ value is multiplied by 1.5 then added to the upper [75%] mean to form the upper outer fence [UOF]. Mathematically, (108,109).

$$LOF = 25\% - (1.5\ X\ IQ) \qquad \text{Equation 10}$$

$$UOF = 75\% + (1.5\ X\ IQ) \qquad \text{Equation 11}$$

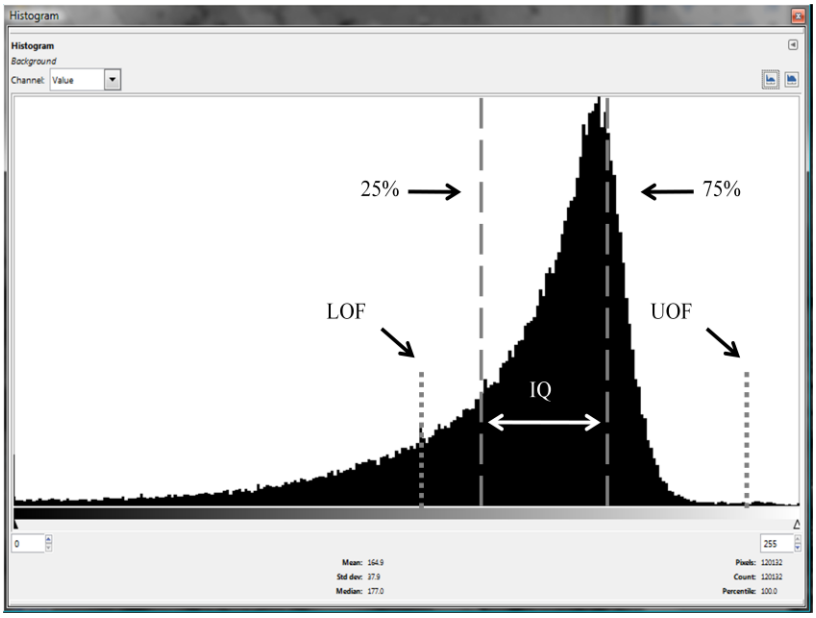

Figure 10: Outliers statistics on a histogram; IQ: interquartile, LOF: lower outer fence and UOF: upper outer fence

According to the Outlier statistics, any value out of the range from the LOF to the UOF is considered a defect. By this method, it is possible to set a threshold on the image, where any value fall within the LOF to UOF is considered as genuine value (107).

3.6 Physical Vapour Deposition [PVD]

The PVD process includes transforming a deposited material's particles into the gaseous state by physical thermal evaporation. The deposition of the materials occurs in a high vacuum chamber [10^{-7} mbar], which allows the evaporated particles to travel directly to the substrate [target], where they condense back to the solid state (110).

The PVD process was used as a form of electrode development in order to deposite ohmic electrodes. The deposition of the ohmic electrodes took place at the London Centre for Nanotechnology [LCN] (2).

The Metal Box BOC EDWARDS FL 400 with its Auto 306 Intellemetrics IL 820 control panel was used to deposit the metal wafers on the TMOs. The detectors were prepared by means of the areas of interest being left exposed, while, the rest of the detector area was covered by foil. The detectors were mounted on a tray to be placed upside down inside the vacuum chamber. Metal rods were placed in two floating pots at the bottom of the chamber. A vacuum was formed in the chamber until the pressure inside

the chamber became 10^{-7} mbar as a minimum. After that, the tray was circulated simultaneously with the temperature increment of the floating pots. Once the metals in the pot started to evaporate, the pot temperature remained constant until all the metals were evaporated and delivered onto the tray. The deposition rate was 3.5 nm/sec and the total film thickness was about 1.5 μm (2).

Besides improving the conventional electrode structure [Cu tape] by using the PVD process, electrode materials selection is essential to optimise the ohmic electrodes. Selection of electrode materials is based on many factors, including φ, EA and BG (2,59,111).

An ohmic electrode is a non-rectifying electrode used for the collection of charge created by incident radiation. Non-rectifying means the I-V curve at the TMO-electrode metal interface is linear and symmetric. In other words, ohmic electrodes must create negligible interface resistance compared to the semiconductor in contact (17,93,112).

Once two materials are placed in contact, electrons will flow from the one with the lower φ until the equilibrium is reached i.e. E_f's are equalised. Thus, the material with the lower φ will show positive charge, while, the material with the higher φ will become negative. This means that an electrostatic potential will be formed and is known as Contact Potential $|\varphi_{metal} - \varphi_{TMO}|$ (59,112).

In theory, metals with φ close to the semiconductor's EA form an ohmic electrode for n-type semiconductors, while, metals with higher φ, equal to the sum of the p-type semiconductor's BG and EA, form ohmic electrodes for p-type semiconductors. This is because at equilibrium, no band bending is expected in the CB and VB when the E_f's are aligned i.e. no contact potential. In a simpler sense, the TMO and the metal in contact should have the same φ's. This can be inspected in Figure 11 (59,111).

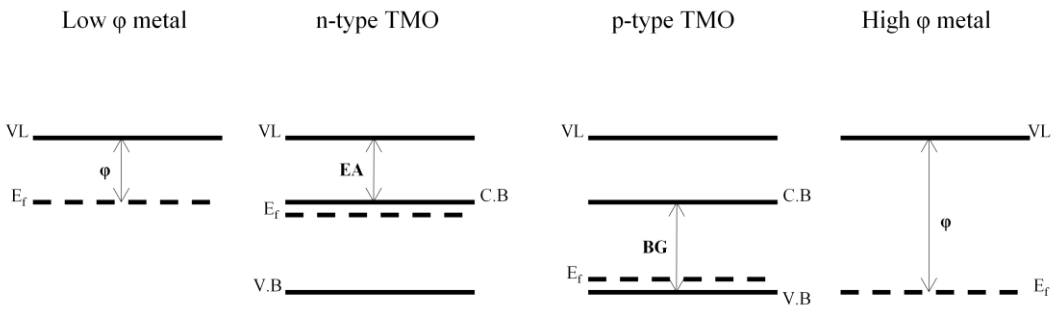

Figure 11: E band diagram for p-type and n-type TMOs; VL: vacuum level

According to Brennan, it is not easy to find true ohmic contacts. This is because a little bending is expected at equilibrium due to the small E_f difference between the metal and semiconductor in contact. This bending will lead to the formation of the contact potential $|\varphi_{metal} - \varphi_{TMO}|$. However, Yang indicated that electrodes are still considered ohmic or very low contact potential as long as the contact potential is in the order 0.51 eV. This value [0.51 eV] is an average barrier height calculated from Yang's lowest theoretical and experimental results (59,113).

3.7 Elettra Synchrotron

A Synchrotron is a particle accelerator, where electric field [acceleration] and magnetic field [bending] are synchronised with the particle beam. The deflection of particles emits photons due to loss of E. Linear accelerators are used to eject particles with intermediate E's [MeV] into the synchrotron rings which are then accelerated to high E's [GeV]. The produced radiation is a unique form of radiation because of the high intensity and tuneable monoenergetic feature of the source (13,114).

The Elettra synchrotron based in Trieste, Italy was used in this project. Elettra features a third generation synchrotron radiation source with beam E of 2.4 GeV inside the storage ring. The storage ring circumference is 259.2 m and supplies 24 beamlines (115).

Beamtime in a beamline called BaD ElPh was allocated for experiments on the Atmos TMOs. In this beamline, two sources were used. The first source was an external tube x-ray source for XPS measurements. The second source was the synchrotron source for TMO response to UV radiation measurements. Specification and methodology of each source will be explained as follows (115).

3.7.1 X-ray Photoemission Spectroscopy

3.7.1.1 Introduction

XPS is the E measurement of emitted electrons from solids generated by the photoelectric effect. This emission is due to the absorption of x-rays relative to the binding E of a material's electrons. As a result, the emitted electrons are characteristic for each core level they were emitted from. Hence, the material can be characterised in accordance to the E of the emitted electrons (26,54,116-118).

XPS spectra were obtained by illuminating the sample then measuring the E_k and the number of electrons which escape from the material's surface [tens of nm's]. Thus, XPS requires a high vacuum environment [10^{-9} mbar]. It is possible to change from binding E to the E_k and vice versa using the following equation, providing the incident x-ray E [hw] is known (26,54,116-120).

$$E_k = hw - BE \qquad \text{Equation 12}$$

h represents Planck's constant, w is the frequency, and BE is the binding E. It is worth mentioning that Reinert et al. published a long report-like journal in 2005. This publication is a comprehensive study of the XPS from early days (1887) up to the date of writing the journal (2005). Hence, it is strongly recommended for any further information (54). Wagner et al. wrote a comprehensive book, which is considered to be the reference for all XPS spectra as it includes all possible XPS spectra of the periodic table elements, besides their complexes, such as oxides and fluorides (116). For simplicity, NIST provides an online service for determining corresponding materials of the XPS spectra (121).

The XPS system was calibrated using pure Cu $2p_{3/2}$ at the BE of 932.62 eV as it was suggested by many authors (116,118,119,122-124). The subscript 3/2 is one of the total momenta [angular + spin] of orbital p in accordance to its spectral splitting. Hence, Table 4 shows angular momentum [l], spin [s], and total momenta [l±s] of s, p and d orbitals. NB: $2p_{1/2\ \&\ 3/2}$ is called spin doublet (34,116).

Orbital	l	s	l±s splitting
s	0	±1/2	±1/2
p	1	±1/2	3/2 and 1/2
d	2	±1/2	5/2 and 3/2

Table 4: Angular, spin and total momenta of s, p and d orbitals

3.7.1.2 System Specifications

The XPS system is located in one of the four vacuum chambers of the BaD ElPh beamline end station. The experimental end station has three independent ultra high vacuum [UHV] chambers [down to 10^{-11} mbar] as seen in Figure 12. The first chamber is divided into two dependant chambers, which are noted as A and B in Figure 12. Chamber A is called lock-chamber due to the possibility to open it then insert the sample then lock

it then vacuum it. Chamber B is used to transfer the sample from chamber A to chamber C i.e. from a vertical transfer to a horizontal transfer. Chamber C is the synchrotron line and is called the preparation chamber. This is because it includes the Ar ion sputtering gun together with sample mounting tools [e.g. screw driver]. Finally, chamber D contains the XPS system, including the external x-ray source [see Figure 12E] and electron analyser. The sample holder [starts in chamber A and ends up in chamber D in Figure 12] can move in x, y and z directions together with rotational and angular motions (115,125).

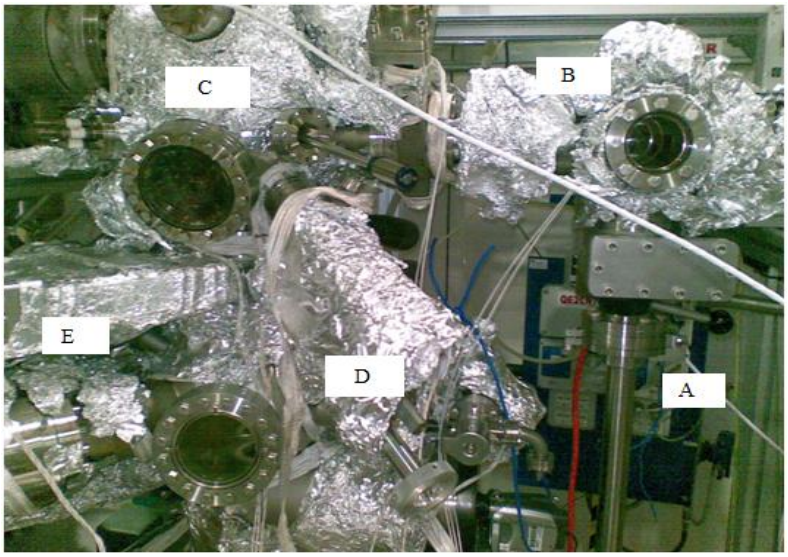

Figure 12: BaD ElPh UHV chambers: [A] lock-chamber [B] Transfer chamber [C] Synchrotron and preparation chamber [D] XPS chamber [E] External x-ray source

The TX400 Al [K_α of 1486.6 eV] external x-ray source was used for XPS experiments. This source was supplied by a company called PSP Vacuum Technology, based in the UK (54,115,125,126). The photoelectron hemispherical analyser is the SPECS Phoibos of 150 mm radius with a 2D-CCD detector system. The CCD detector is a large area [40 x 20 mm^2] detector, which offers a live acquisition of the spectra onsite (115,125,127). Finally, this XPS system will be used only to evaluate Ar sputtering effect on Atmos TMOs at the stage of surface preparation.

In terms of sputtering, the high voltage [500 kV] generates ions in the inert gas [Ar]. These ions are directed towards a target, which is the surface of the TMO. Once the bombardment takes place, surface atom removal occurs. This process will remove hundreds of A^0's from the surface (85).

Single-layered flame sprayed TMO samples in the size of 1 x 1 cm^2 were in use. These samples are similar to the samples used in the EM measurements. After mounting the sample on the sample holder in chamber A in Figure 12, the sample was moved manually until it reached chamber C. In chamber C, the sample holder was fixed using the screw driver attached to the chamber. This is followed by moving the sample to its final stage in chamber D. Recall that the problem of sample charging was overcome by earthing the sample using C tape.

3.7.2 BaD ElPh Beamline

3.7.2.1 System Specifications

The BaD ElPh undulator-based beamline is one of the 24 beamlines of the Elettra synchrotron. This undulator is made of six periodic magnetic arrays. The BaD ElPh is operated in the low photon E of 4.6 – 40.0 eV (7,115,125).

The BaD ElPh consists of a Si switching mirror to transfer the photon beam from the main ring toward the BaD ElPh beamline, a spherical pre-focusing mirror, which focuses the beam into an entrance slit, a monochromator and an Au-coated mirror, which refocuses the beam [300 x 300 μm] on the sample at the end station [chamber C in Figure 12] (115,125).

The pre-focusing mirror has two sections, which are a Si section used for photon E's up to 13 eV and a Pt-coated section used for photon E's above 13 eV. The monochromator has three [Al/MgF_2, SiC and Pt] spherical gratings to cover the photon E of 4.6 - 40 eV (115,125).

The BaD ElPh is equipped by a removable AXUV-100 photodiode, located between the Au-coated refocusing mirror and the end station. The AXUV-100 was supplied by a Canadian company called International Radiation Detector Incorporation and is a Si-based [BG = 1.12 eV] photodiode. The AXUV-100 operates at room temperature and in photovoltaic current mode. This detector covers the photon E range of 1.12 eV – 31 keV (115,125,128).

3.7.2.2 Methodology

The TMO detector was mounted centrally in the beam at the BaD ElPh beamline and connected to the Keithley 6487 pico-ammeter. The AXUV-100 Si photodiode could be

moved in and out of the beam directly in front of the TMO detector for comparison purposes (7). Similarly, the AXUV-100 Si photodiode was connected in series to Keithley 6487 pico-ammeter, which monitored the current produced by the photodiode throughout the measurements (7,125).

Only two gratings were used in this project, which are Al/MgF_2 for the E range 4.6 – 14 eV and Pt for the E range 15 – 40 eV. This is because Al/MgF_2 and Pt produce higher photon flux, compared to SiC. A Pre-focusing mirror was used according to the grating due to E range. This means, Pt pre-focusing mirror is used with Pt grating, whereas, Si pre-focusing mirror was used with $AlMgF_2$ grating (125).

Several tests were performed as it will be seen in section 7.2.2 Synchrotron UV Analysis. The same measurement protocols, presented for the x-ray tube, were followed in Elettra. This is in terms of sampling time [60 sec], number of readings [200 readings] and prior/during experiment precautions (7).

3.8 Attenuation Coefficient and Efficiency

3.8.1 Theoretical Calculation

XMuDat is a freeware software, supplied by the Institute of Biomedical Science, University of Wien, Austria and was written by R. Nowotny (129). XMuDat is capable of plotting the μ/ρ as a function of E for elements and compounds by weight percentage. The calculation of μ/ρ is based on the tabulated μ/ρ, provided by Hubbell et al. (130).

μ is a quantity used to characterize the probability of interaction of photons in a material. μ is represented by Equation 13. The inverse of μ is the mean free path. The dependency of μ on the type of the material and photon E makes it problematic for tabulation. Alternatively, μ/ρ is used widely as it is independent of the physical state of the material (17).

$$I = I_0 e^{-\mu d} \qquad \text{Equation 13}$$

Where,

I_0 is the intensity of the primary photon beam

I is its intensity at a depth d

μ decreases with increasing E [this will be explained in section 7.3 Attenuation Coefficient], however, there are abrupt jumps in μ at certain E's. These jumps occur when the E of the photon matches one of the binding E's of the atom. This is because the absorption of the photons increases drastically and the μ jumps to a higher value. The advantage of these abrupt changes in μ is used in radiation imaging to enhance image contrast (17).

The μ of a compound at certain E can be obtained by taking the fraction of its individual components [mixture rule] according to (17).

$$\mu(total) = \sum_{i=1} w_i \mu_i \qquad \text{Equation 14}$$

w_i is the fraction of i^{th} element in the compound. Ahmed demonstrated that the total μ of a stacked sample with different compounds is the sum of their μ's in accordance to their thickness in Equation 13. On this basis, the ε_{abs} of a sample with layers of different compounds and thicknesses can be written as (17).

$$\varepsilon_{abs} = 100 - (\frac{I}{I_0} x100) = e^{-\sum_{i=1}^{n} \mu_i d_i} \qquad \text{Equation 15}$$

3.8.2 Experimental Measurement

The ε_{abs} measurement can be achieved by placing a CZT [$Cd_{0.9}Zn_{0.1}Te$] detector behind the TMO detector in order to record I [transmitted photons] from a point source through the TMO detector. The CZT detector is a 9 cm SPEAR [single point extended area radiation] sensor, supplied by eV Microelectronics. The detector consists of a CZT crystal [5 x 5 x 5 mm^3] in low attenuating Al housing together with a preamplifier followed by a filter board then finally, the 4-pin Lemo connector (131,132).

This system is dedicated to the URSA II spectrometer and its software, provided by the American company SE International Incorporation. The whole system operates at room temperature. The point source used in this experiment was Cs-137, as Cs-137 has a photopeak around 33 keV, which was the E required for some of these experiments, such as μ [linear attenuation coefficient] (133).

Figure 13 shows the system setup, where the wide beam geometry (17,134) was followed in this experiment. x and d represent the thickness of the TMO and the substrate, respectively.

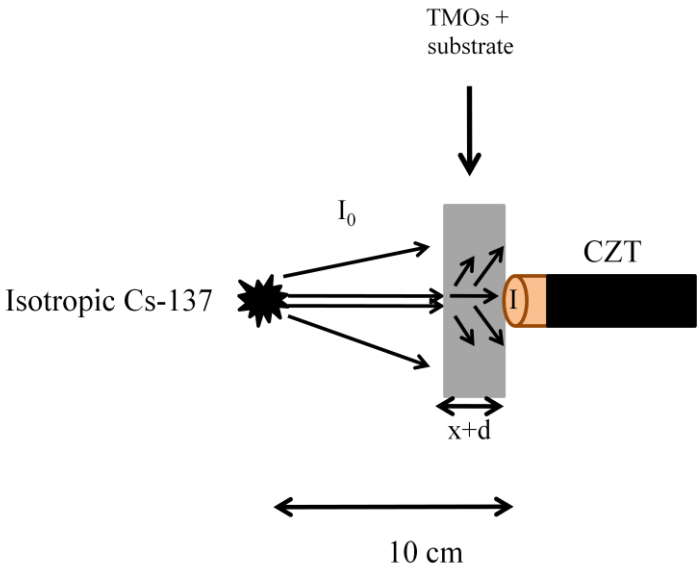

Figure 13: ε_{abs} experiment setup

The setup shown in Figure 13 with no x+d thickness was used to calculate the ε_i [intrinsic efficiency] of the CZT according to the following equation (13).

$$\varepsilon_i = \frac{number\ of\ pulses\ recorded}{number\ of\ photons\ incident\ on\ the\ detector} = \frac{number\ of\ pulses\ recorded}{source\ activityxsolid\ angle} \quad \text{Equation 16}$$

The solid angle is the detector surface area [5x5 mm^2] divided by the square of the source-to-detector distance [10 cm] (13,131,132). After that, the net ε_{abs} of the TMO was deduced by subtracting the ε_{abs} of the substrate from the ε_{abs} of the total TMO detector [TMO + substrate]. Also, corrections were applied to correct for CZT ε_i and thickness in order to be able to compare it with TMO.

Chapter 4

4 Initial Status of TMO Detectors

4.1 Introduction

This chapter will assess the very first prototype TMO detectors in terms of linearity, photon E dependence, reproducibility and signal stability. These tests will evaluate the behaviour and reliability of these prototype TMO detectors, therefore, it is important to have reference points to be compared with the TMO detectors results. This reference will be the ion chamber [IC]. The IC will be compared with the prototype TMO detectors in every aspect mentioned above.

The 15 cm^3 96035B IC was placed in the setup shown in Figure 8. This is the same setup, where the TMO detector will be placed. Recalling Equation 6, Equation 7 and Equation 8, it is possible to calculate the current and photon fluence rate from the exposure. Beam E in Equation 8 is the simulated mean E of 50 kV, using the xcomp5r. 50 kV in the UCL x-ray source is found to be equivalent to 30.0±0.9 keV. Moreover, all of the measurement protocols and setups were explained in 3.4.2 System Setup and Measurements Protocols.

The TMO detector sample tested in this section is the TMOD1 mentioned in Table 3. It is worth mentioning that the design of this detector [TMOD1] is the design sketched in Figure 6. In particular, it is the design with the two Cu tape stripes on both sides [n-type and p-type TMOs], acting as electrodes.

It is very important to express that most of the work in the remainder of this thesis was made according to the initial results obtained from this chapter. Therefore, some questions are left unanswered deliberately in the text until the answer arises at the relevant point in the thesis. For example, the presence of defects in the manufacturing process will be suspected but not confirmed until the EM experiments are performed. By this approach, the sequence of the project will not be interrupted by the rush of presenting results. Hence, motivations from the initial tests will be stated in order to be sensible to move to the following chapter.

4.2 Linearity

Linearity is the net signal [signal - noise] produced by a detector, plotted as a function of the x-ray tube current [mA] for a constant x-ray tube voltage [kV]. mA is represented by the photon fluence rate. X-ray detectors should ideally have a linear response to x-ray photon fluence rate at a constant kV (1,2,12-16). Accordingly, Figure 14 shows the net signal from the IC plotted as a function of the x-ray photon fluence rate at a constant kV of 50 kV.

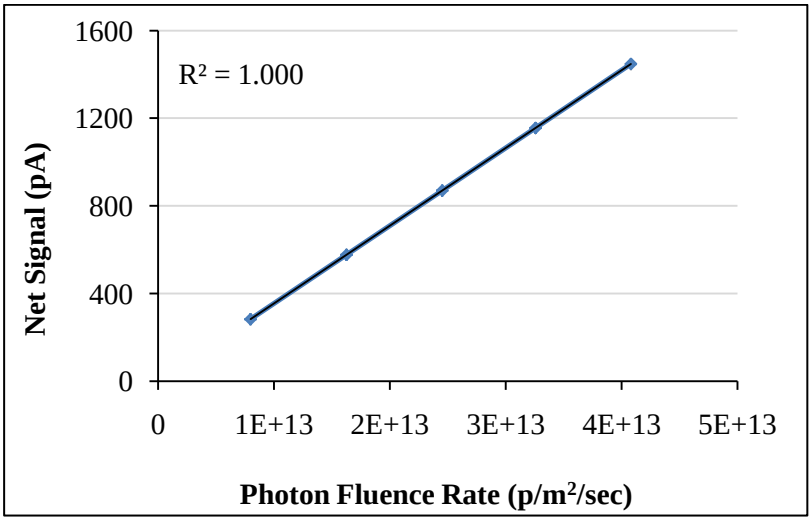

Figure 14: Linearity of IC at 50 kV

From Figure 14, the IC has a linear response [R^2 = 1.000] to x-ray photon fluence rate. Note that the net signal was converted from exposure to current [pA], using Equation 6 in order to be compared directly with the TMO detector as will be seen later. Also, the SD is plotted but not apparent as it is in the order of the fraction of a pA in the net signal. The fluctuation in the x-ray tube was estimated, using the IC and is found to be in the order of 10^{10} p/m^2/sec. Therefore, both SD's [net signal and photon fluence rate] are not apparent in Figure 14. NB: this is applied to all figures with photon fluence rate and current net signal, unless something different is stated.

A linearity test was performed on the TMOD1 at constant kV of 50 kV [see Figure 15]. A near-linear [R^2 = 0.980] relationship between the TMOD1 signal and the x-ray photon fluence rate is observed.

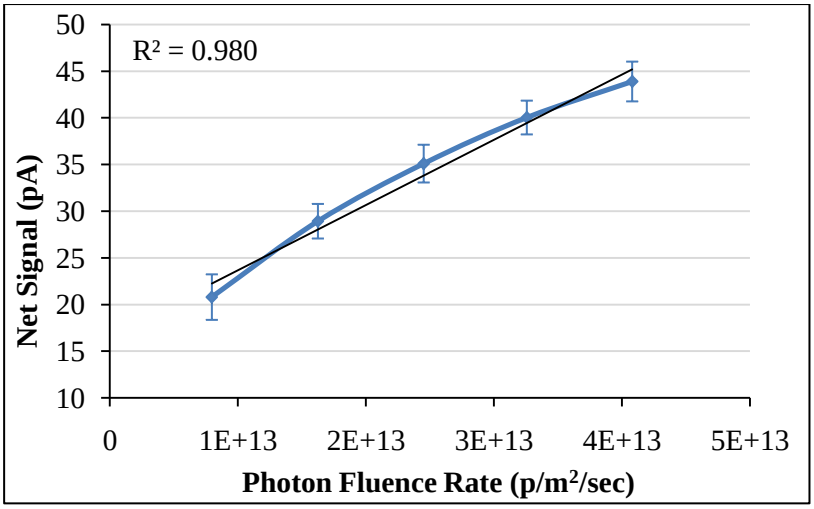

Figure 15: Linearity of TMOD1 at 50 kV

The cause of this near-linearity is suspected to be due to poor manufacturing of the detector, namely the flame-spray material deposition method. This is because any presence of defects would cause charge immobilisation in the detector due to lack of long-range order. This is beside the suspected structure of the p-n hetrojunction. It is doubted that a well-defined p-n hetrojunction can be formed, using the flame-spray technique as the manufacturing process involves blasting the p-type pre-oxidised powder on the pre-deposited n-type TMO layer together with rapid cooling process. Therefore, p-type TMO-contaminated n-type TMO layer is expected at the hetrojunction. Also, the granular nature of the surface would contribute to form the undefined p-n hetrojunction (1,2).

Due to those imperfections, a build-up effect of charge will follow each irradiation, leading to successive filling and empting of the defects. Therefore, the TMOD1 is expected to have some memory, yet the net signal is considered to be memory-free as the signal will increase in accordance to the increased noise, which is subtracted from the net signal. Also, the rate of charge carriers crossing the p-n hetrojunction along the detector is not constant due to granularity and contamination, as stated by Cox who indicated that the presence of defects causes non-linearity as structure symmetry disappears (1,2,27).

It is noticeable that the TMOD1 did not show any saturation in the photon fluence rate range showed in Figure 15. The photon fluence rate is in the range of $8x10^{12}$ – $4x10^{13}$ $p/m^2/sec$ with a mean E of 30 ± 0.9 keV, which falls within the acceptable range [25 kV – 150 kV] for radiation monitor as explained in 1.2 Desirable Detector Specifications.

Thus far, the linearity test was performed on both the IC and TMOD1. So, the next step would be comparing Atmos TMO detector with the reference point specified, which is the IC. By this method, it will be possible to find out the most suitable step after knowing that the TMO detector behaves feasibly according to the IC.

In order to compare the IC response to TMOD1 response in terms of linearity at 50 kV, Figure 14 and Figure 15 are combined in Figure 16. This is done to obtain both linearity curves [TMOD1 and IC] in one figure. Additionally, as the net signal coming from the IC is much greater than the TMOD1 net signal, the net signal axis [y-axis] was converted into log scale.

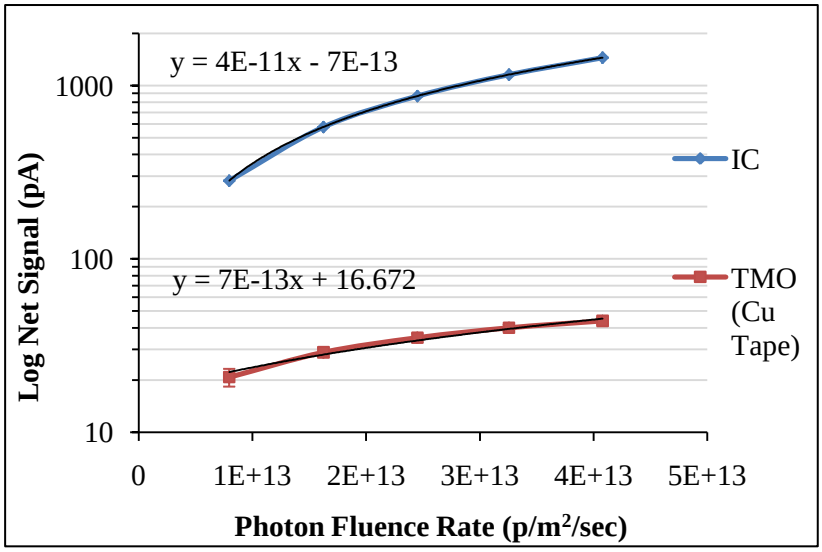

Figure 16: Cu tape TMOD1 vs. IC linearity comparison at 50 kV

From Figure 16, the TMOD1 net signal forms 4.6% as an average of the IC net signal. This degree of relatively low net signal can be referred to several aspects. Cu tape electrodes are always the first suspected reason as it is the most apparent non-optimised factor. This is because Cu tape increases the capacitance as it stores signals underneath it. Also, using Cu on both sides might cause some rectification to the signal owing to incompatibility φ‘s. Therefore, CCE is the value which needs to be improved in TMOD1. This will be performed later in section 7.4 Efficiency.

The two extra factors that affect the magnitude of the net signals are material deposition and detector design. In terms of materials deposition, any defects, including contamination will either immobilise or scatter the charge away, while moving across the detector. Also, the detector design has an effect as a generated charge in the middle of the detector will suffer from transferring a long distance [e.g. 3.25 cm in TMOD1] to reach

any of the electrodes. This will increase the possibility of charge scatter, trapping and e-h [electron-hole] recombination. Therefore, loss of charge is expected in such design. This was the reason for manufacturing the second stacked detector shown in Figure 7, however, this design did not respond to radiation due to reasons will be stated in section 5.13 Failure of the Stacked Design.

Furthermore, surface preparation would contribute significantly to the production of relatively low net signals. This is because of the formation of undefined p-n hetrojunctions, which will lead to the requirement of more E to overcome the depletion layer. Also, the undefined p-n hetrojunction would cause e-h recombination in some defected locations at contact point.

The sensitivity of the detector can be represented by the slope of the linear curve. This is because the greater the slope, the better the sensitivity. In Figure 16, the equations of the linear curves are shown for the IC and TMOD1. The sensitivity of the TMOD1 is found to be in the order of 2% compared to the sensitivity of the IC. This relatively low degree of sensitivity of the TMOD1 is owing to the poor CCE, provided by Cu tape electrodes, which will be quantified in section 7.4 Efficiency.

As the SD represents the fluctuation of the net signal, the TMOD1 was found to fluctuate 76% more than the IC. This is in terms of linearity at 50 kV. Although static noise, which will be introduced in section 7.5 Noise, might have an effect, care was taken to keep movement near the detector and pico-ammeter to minimum. Cu tape contribution to fluctuation cannot be ignored. This is because successive charging and discharging is expected together with the trapping and de-trapping as a result of material defects.

4.3 Photon Energy Dependence

Photon E dependence is the detector's response plotted against kV at a constant mA. An x-ray detector's response should ideally be related to the kV^2 for a constant mA. However, a linear response is expected in this case. This is because there are two competing effects that contribute to the shape of the E dependence curve. One is the fact that x-ray photon fluence rate increases with kV^2 and the other is that the x-ray beam becomes increasingly more penetrating as the x-ray tube kV increases in the form of exponential decay. In other words, the mean photon E increases, which means less absorption in the IC is expected at higher photon E's (1,2,13,14).

On this basis, Figure 17 approximates a linear response [R^2 = 0.999] as a function of kV at a constant mA of 6 mA.

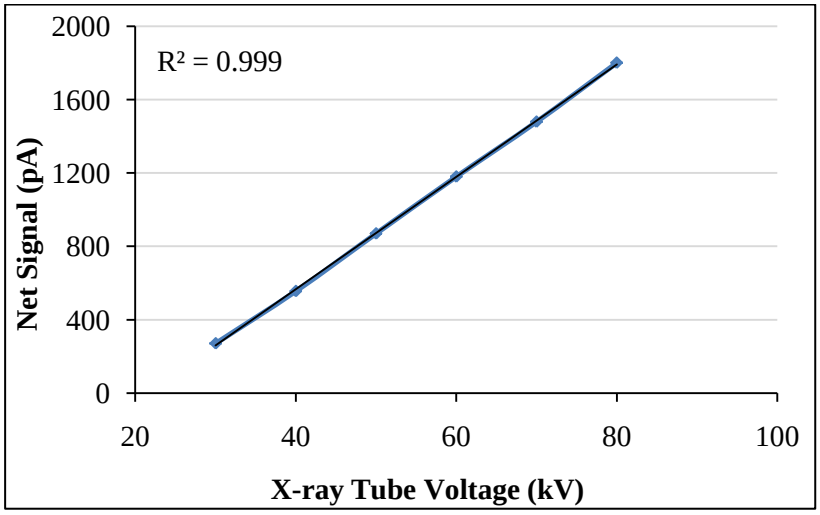

Figure 17: Photon E dependence of IC at 6 mA

Analogously to linearity, the net signal was converted from exposure to current, using Equation 6 above, in order to be compared directly with the TMO detector as it will be seen later. Also, the SD is plotted but not apparent as it is in the order of the fraction of a pA in the net signal. Furthermore, the fluctuation in the kV was estimated, based on the x-ray unit control panel and found to be in the order of 1 kV. Therefore, both SD's [net signal and kV] are not apparent in Figure 17. NB: this is applied to all figures with kV and current net signal, unless something different is stated. Additionally, as it was mentioned earlier, the kV range [30 – 80 kV] is equivalent to a mean output E range of 20.1±0.6 – 37.1±1.1 keV. This is obtained by simulating the UCL x-ray tube, using xcomp5r.

Figure 18 shows the photon E dependence test on the TMOD1. A near-linear [R^2 = 0.986] response of the TMO detector signal as a function of kV at a constant mA of 6 mA is observed. Likewise, the reason for the near-linearity is the mal-manufacturing deposition process provided by the flame spray technique. This is together with the unprepared TMO surfaces.

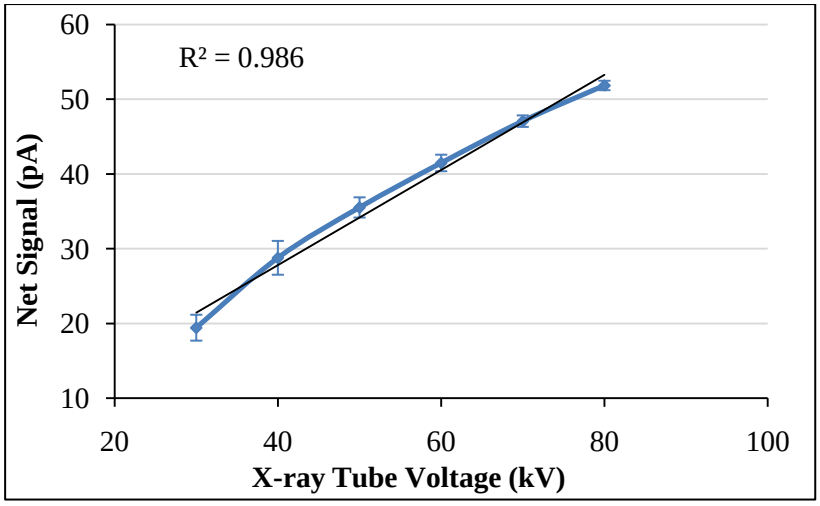

Figure 18: Photon E dependence of TMOD1 at 6 mA

Also, note that the x-ray mean photon E range [20.1±0.6 – 37.1±1.1 keV] in this experiment is in the typical diagnostic range and no detector saturation is observed. This indicates that the detector has a range suitable for beam monitoring in a diagnostic x-ray setting as explained in 1.2 Desirable Detector Specifications (1).

Analogously, Figure 17 and Figure 18 were combined in Figure 19 to be depicted in the same figure for IC and TMOD1. This is in terms of photon E dependence at constant mA of 6 mA.

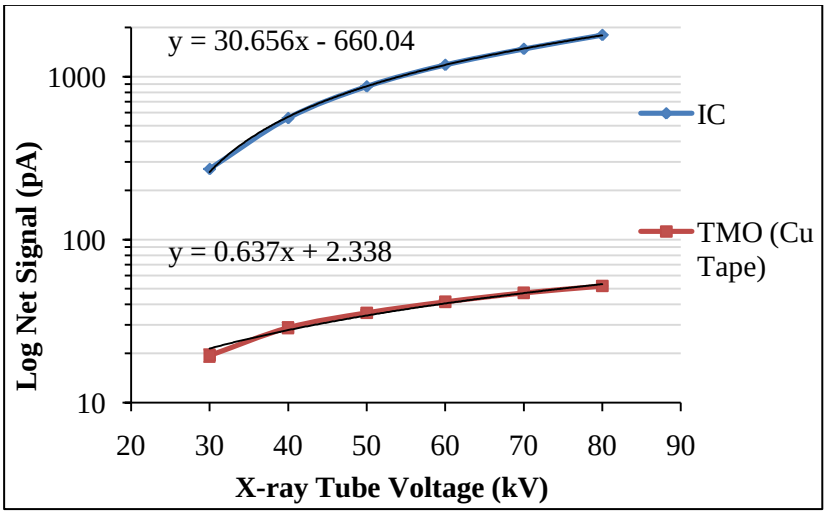

Figure 19: Cu tape TMOD1 vs. IC photon E dependence comparison at 6 mA

In Figure 19, the TMOD1 net signal forms 4.3% as an average of the IC net signal. The same reasons of Cu tape, detector design, defects and surface preparation mentioned in the previous linearity section are applied to the photon E dependence.

In addition, the sensitivity of the TMOD1, compared to the sensitivity of the IC, represented by the slopes is in the order of 2% as well. Similar factor would affect the sensitivity, which is the CCE. Also, the TMOD1 fluctuates 62% more than the IC mainly due to defects and Cu tape.

4.4 Reproducibility

This section presents three repeat x-ray irradiation tests made on the same detector under identical conditions 0 h [zero hour], 1 h and 24 h apart. It is ideal to have the reproducibility with no noticeable difference [within the SD] between anytime measurements (1).

4.4.1 In Terms of Linearity

Figure 20 shows the reproducibility of the IC in terms of linearity at constant kV [50 kV]. The three curves are of 0 h, 1 h and 24 h of time intervals between each measurement. The setup used was kept perfectly still to achieve identical conditions between measurements.

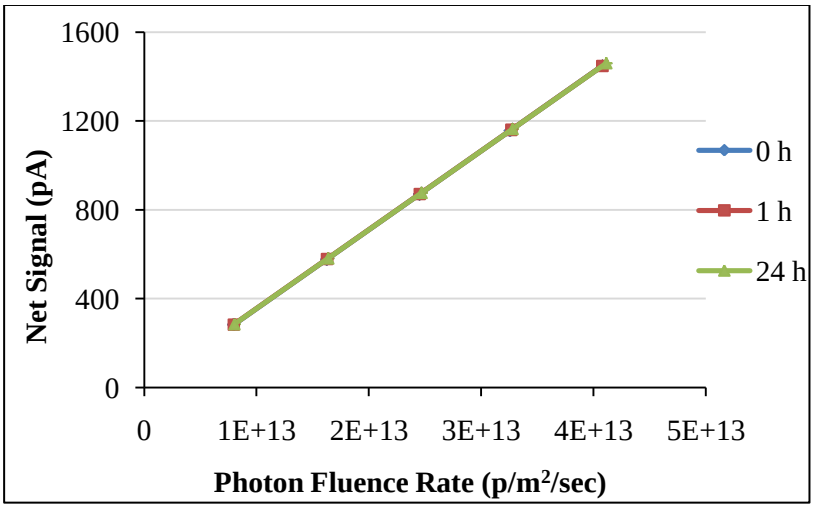

Figure 20: Linearity reproducibility of IC at 50 kV

In Figure 20, the IC showed a reproducible behaviour with a difference of 0.3% only. This degree of reproducibility can be used as an empirical value to be compared with the TMO reproducibility results. By this method, it will be possible to know how far Atmos TMO detectors from such a reliable detector [IC].

On this basis, Figure 21 shows three repeat linearity measurements on the TMOD1 at the times 0 h, 1 h and 24 h. It is depicted that the TMOD1 detector has the effect in which the magnitude of the signal depends on the degree of prior irradiation. This is quantified and found to be 8.5% decrement in each irradiation as an average. In other words, the net signal decreased from 0 h irradiation to 24 h irradiation by an average of 17%. NB: the detector does not recover even after resting for 24 h, compared to 1 h. The explanation for this fact will be presented shortly.

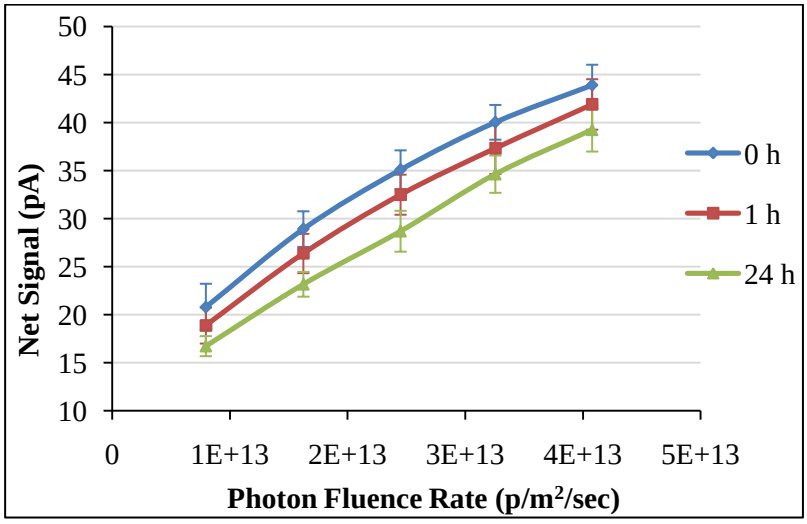

Figure 21: Linearity reproducibility of TMOD1 at 50 kV

There might be two reasons for this effect, presented in the TMO detectors. The first reason is the defects. Charge will be trapped then stored in these defects, which will lead to decreasing the net signal accordingly. The second reason is considered to be major, and that is the use of Cu tape electrodes.

The presence of the Cu tape would highly increase the capacitance of the detector. So, when the charge reaches the electrodes, Cu tape attached on top of the TMO together with the insulating medium [air or glue] at the Cu tape – TMO interface would act as a capacitor and store the charge in it. This will prevent the charge from fully reaching the electrode and pico-ammeter. This means that the rate of the output is less [8.5% signal reduction in each irradiation as an average] than the actual output from the detector itself. Therefore, the detector needs time to recover and goes to 0 h behaviour after flushing out the stored charge in the electrodes. This fact will be supported in section 5.11 Cu Tape Insufficiency. Also, Cu is doubted to be compatible with both, n-type and p-type TMOs. There might be a rectification in the n-type TMO as low φ electrode material is required as mentioned in section 3.6 Physical Vapour Deposition.

Finally, Figure 22 is the combination of Figure 20 and Figure 21. The reproducibility in terms of linearity of the TMOD1 is of the total average of 17% [0 – 24 h]. This degree of reproducibility makes the initial structure of the TMO detectors not acceptable as indicated in 1.2 Desirable Detector Specifications. This is to be compared to the IC value, which is in the order of 0.3%. As it was mentioned above, the main factor believed to be influencing the reproducibility is the electrode structure of Cu tape due to capacitance and rectification.

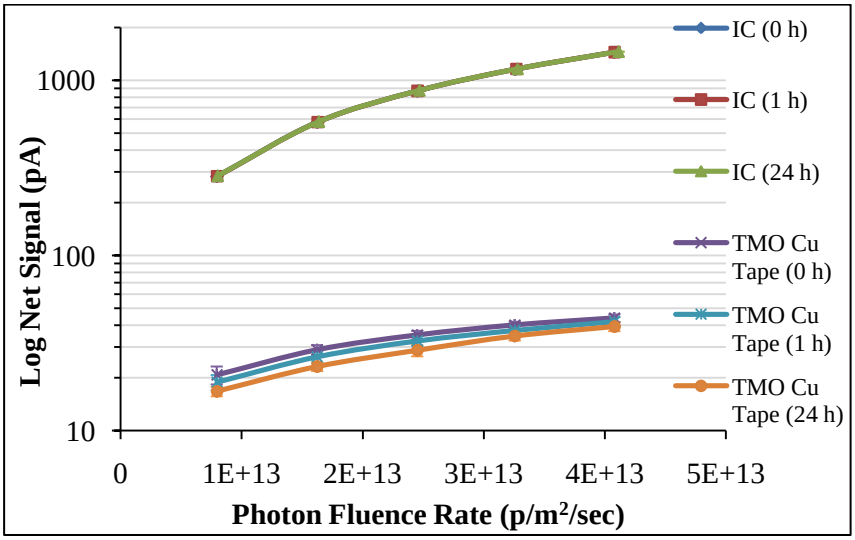

Figure 22: Cu tape TMOD1 vs. IC reproducibility comparison at 50 kV

4.4.2 In terms of Photon Energy Dependence

The same procedure as in the previous section was followed to plot the reproducibility of the IC in terms of photon E dependence. However, this time by keeping the mA constant at 6 mA and varying the kV. This is depicted in Figure 23.

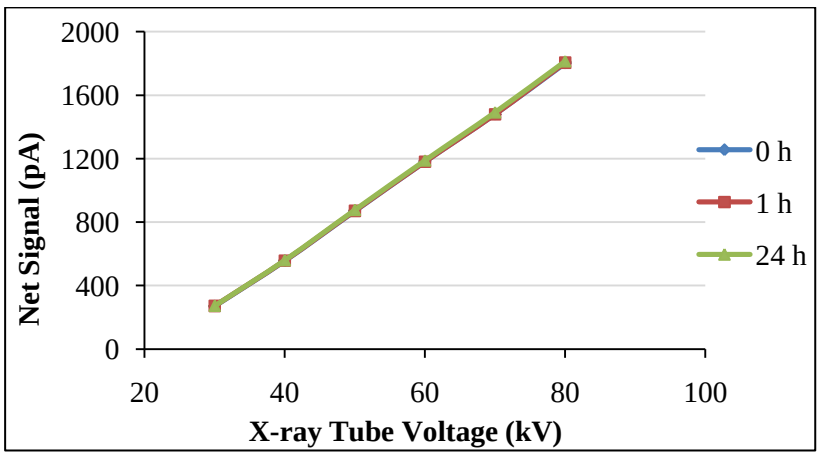

Figure 23: Photon E dependence reproducibility of IC at 6 mA

From Figure 23, photon E dependence reproducibility showed a similar variation percentage to linearity reproducibility, which is in the order of 0.3%. On the other hand, Figure 24 shows three repeat measurements at 0 h, 1 h and 24 h of the TMOD1 in terms of photon E dependence. On the same basis, net signal reduction arises majorly due to Cu tape and minorly due to defects. It is found that the same level of decrement in linearity is presented in photon E dependence, which is in the order of 8.5% as an average in each irradiation. This gradual decrement [8.5%] leads to a total decrement in net signal from 0 h to 24 h of 17% as an average.

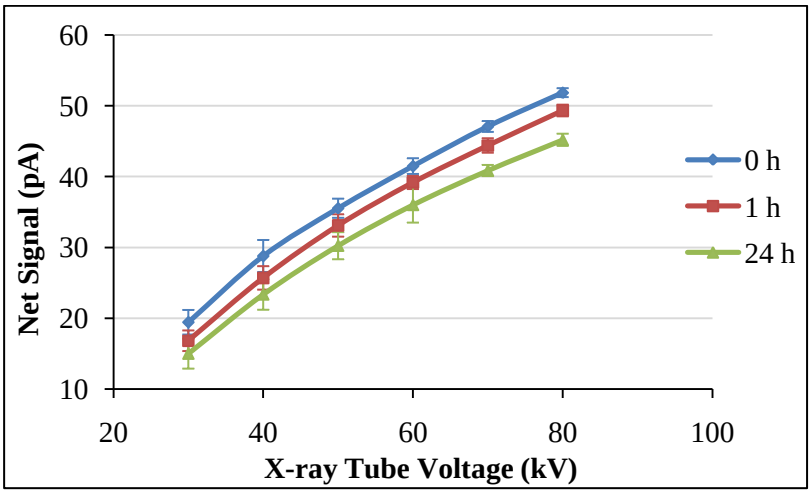

Figure 24: Photon E dependence reproducibility of TMOD1 at 6 mA

Likewise, Figure 25 is the combination of Figure 23 and Figure 24. Similar values of 0.3% and total average of 17% for IC and TMOD1, respectively are observed. This degree of reproducibility makes the initial structure of the TMO detectors not acceptable as indicated in 1.2 Desirable Detector Specifications.

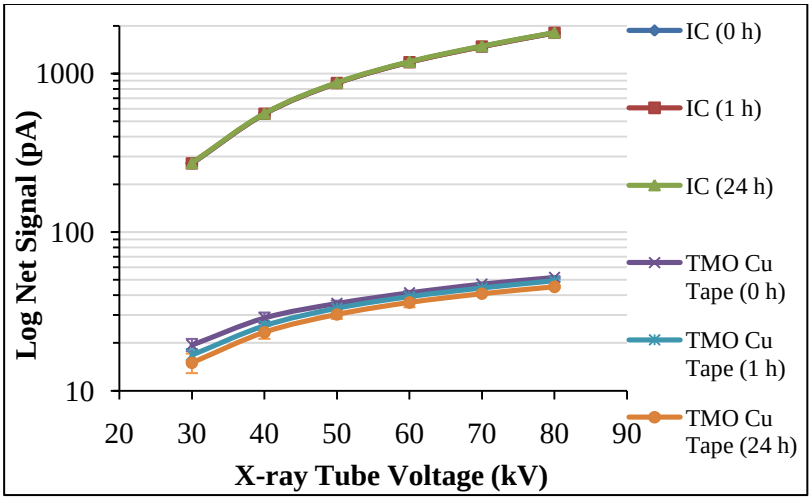

Figure 25: Cu tape TMOD1 vs. IC reproducibility comparison at 6 mA

4.5 Signal Stability

Signal stability is a measurement performed to find the degree of variation of a single net signal over time scale of graduated intervals. This was performed at constant 50 kV and 6 mA, and without moving the setup [see 3.4.2 System Setup and Measurements Protocols]. The time intervals were at 1 min, 15 min, 30 min, 45 min, 60 min and 1440 min [24 h]. Table 5 shows the behaviour of both, IC and TMOD1 at similar time intervals. Note that, each time interval presented in Table 5, and in every coming signal stability test, is the sum of the previous time together with the current time e.g. signal at 60 min will be written as 150 min [i.e. 90 min + 60 min].

Time (min)	IC net signal (pA)	TMOD1 net signal (pA)
1	870.0±0.5	35±2
15	870.0±0.5	34±1
45	--	33±1
90	--	32±2
150	870.5±0.5	31±2
1590	871.0±0.5	30±2

Table 5: Cu tape TMOD1 vs. IC signal stability comparison at 50 kV and 6 mA

It is found that the signal variation of the IC over the time scales presented in Table 5 is 0.3% on average. This proves the reliability of the IC together with its feasibility to be used as a reference point to be compared with Atmos TMO detectors. In terms of TMOD1, the net signal keeps decreasing with time during the time intervals; the net signal at 24 h was decreased by 14% compared to the original signal at 1 min.

As previously mentioned, this reduction in net signal is believed to be mainly due to the use of Cu tape. This is owing to the capacitance caused by the Cu tape pasted on top of the TMO layer. This is together with the effect of charge stored in the defects.

As this test is the last test used to compare between IC and TMOD1, it is essential to mention that comparison between the IC and semiconductor has been well performed in literature. e.g. Alkhazov et al. and Martin performed a comparison between Si semiconductor and IC. Martin found that the response of Si photodiode is comparable to the IC, where the difference quoted was within 3%. This is for wide beam geometry and

for x-ray tube kV of 60 – 120 kV, which highlights experimental setup comparable to our setup [section 3.4.2 System Setup and Measurements Protocols]. This indicates that the TMO detector should, ideally, have comparable net signal magnitude to the IC, yet, this is not the case in Atmos prototype TMO detectors (135,136). In consequence, obtaining comparable response and sensitivity to Si, one of the well-known radiation detector materials currently used in the market, would increase the potential of the TMO detectors and widen their future applications to imitate Si applications.

4.6 Summary and Conclusions

In conclusion of this section, the TMOD1 was compared to the IC. Quantifications [%] of the TMOD1 results in comparison to the IC results are listed in Table 6.

Radiation test	Field of comparison	Cu tape TMOD1 – IC [%]
Linearity		
	Net signal magnitude	4.6
	Sensitivity	2
	SD	76
Photon E dependence		
	Net signal magnitude	4.3
	Sensitivity	2
	SD	62
Reproducibility		
	In terms of linearity and photon E dependence from 0 h to 24 h	17 [Cu tape signal decrement] and 0.3 [IC signal variation]
Signal stability		
	Signal stability from 0 h to 24 h	14 [Cu tape signal decrement] and 0.3 [IC signal variation]

Table 6: Summary of Cu tape TMOD1 vs. IC comparison

The novel TMO radiation detectors are at the very first prototype level, with many iterations of detector optimisation still to be carried out [see 1.2 Desirable Detector Specifications for comparison]. Crucially, initial testing, even at this early stage of detector development, has exhibited very promising results regarding the response of simple detectors to ionising radiation. Nevertheless, the detectors are still some way from achieving their full potential and more developments are needed to optimise the manufacturing process in particular (1,2).

Recalling all the reasons, which might widen the gap between the TMO detector and IC behaviour, it is important to confirm each one of these reasons scientifically. Therefore, the thesis will be built with the aim of assessing then developing the TMO detectors, based on the findings of this chapter.

All the limitations presented in Table 6 need to be optimised in order for them to be comparable to the IC. Therefore, solid reasons for these limitations are required. The production process should be assessed as a first step before assessing any other issue presented in the prototype TMO detectors. Therefore, techniques of the micro-scale analysis are needed to assess the production mechanism in all aspects.

This leads to the use of the EM system. The EM system is capable of giving images and compositional analysis, which can be used to evaluate Atmos deposition process and materials. This can be in terms of surface analysis, uniformity, composition, contamination and defects. Also, certain aspects, such as p-n hetrojunction and electrode application can be assessed in details. This would make it possible to priorities then suggest the possible development, which can be followed to optimise the prototype TMO detectors. This will be depicted in the next chapter.

Chapter 5

5 Identification of Materials and Limitations

5.1 Introduction

Following on from the work presented in chapter 4 Initial Status of TMO Detectors, we now assess the manufacturing process in the micro-scale level. This is because surface preparation, degree of uniformity, defects, contamination, hetrojunction and interfaces are all of utmost importance to be addressed. This is owing to their direct effect on the CTM of the TMO detectors in which improving these aspects would result in increasing the signal magnitude, stability and sensitivity of the prototype TMO detectors as listed in chapter 4 Initial Status of TMO Detectors. This can be achieved successfully by using the EM techniques. By this method, it is possible to confirm all the hypothesis suggested in chapter 4 Initial Status of TMO Detectors. Also, the EM would clarify polarons Mott hopping process indicated in chapter 2 Theory above.

A series of experiments with different goals can be carried out to obtain the most beneficial information from the EM, which has perfectly enlightened the path toward assessing the prototype TMO detectors.

As it was explained in section 3.5 Electron Microscopy, single flame-sprayed layer samples were supplied by Atmos. This means that each sample consisted of either n-type or p-type TMO flame-sprayed over a glazed-ceramic tile substrate. On top of that, the second stacked design was used to evaluate different layers interfaces and to understand why the second stacked design did not show any response to radiation. Consequently, the following properties were assessed (1,2).

5.2 Electron Microscopy Spatial Resolution

In order to avoid any future misinterpretation of the EM images or the elemental compositions, it is worth addressing the associated errors clearly. The average SR of the EM system in different magnifications was calculated, using the ESF technique, and

found it equals 5 µm, meaning that the SD of any interpreted EM image produced by this system should not be less than 5 µm. In fact, it would be more convenient to call the calculated resolution as System Spatial Resolution [SSR], as the calculated resolution is dependent upon factors, such as sample preparation. So, as the samples used were not prepared primarily for the EM SR calculation, it is fair to describe it as the *whole system* SR. Thus, the term SSR will be used rather than SR.

The SD given by the EM system associated with each corresponding compositional analysis is ±0.50%. The final global errors associated with each quoted quantity in any image or table in the EM section, therefore, should be ±5 µm and ±0.50%, respectively (1,2).

The patch used to calculate the SSR is basically, a radiation collimator made up of a graphite base covered with apertured pure Au. These apertures are L-shaped and placed side by side along the whole collimator. Figure 26 shows a sketch of a single patch together with its dimensions.

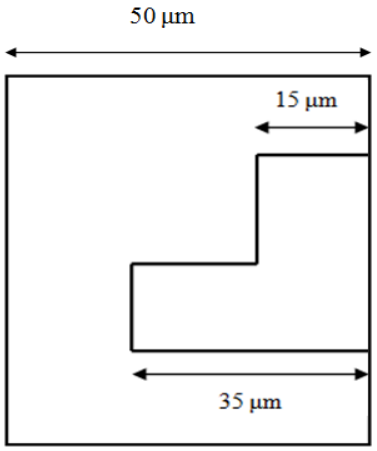

Figure 26: Sketch of a single patch dimensions used to calculate the SSR of the EM

EM images were acquired in three different magnifications, which are x200, x500 and x2000 [x2k] then the SSR were calculated for each image. Ideally, the SSR should be identical for all levels of magnifications.

In order to calculate the SSR, two software packages were used: ImageJ and the scientific graphing and analysis software, OriginPro 2008 [developed by the OriginLab company] (98,100).

Figure 27 shows a BSE image of x500 magnification. Here, the edge of one of the L-shaped apertures will be used to provide the ESF, where the rectangle has been drawn.

The bottom of the image provides information [from left to right] about the accelerating voltage, electron probe to sample distance, level of magnification, imaging mode and finally, the scale.

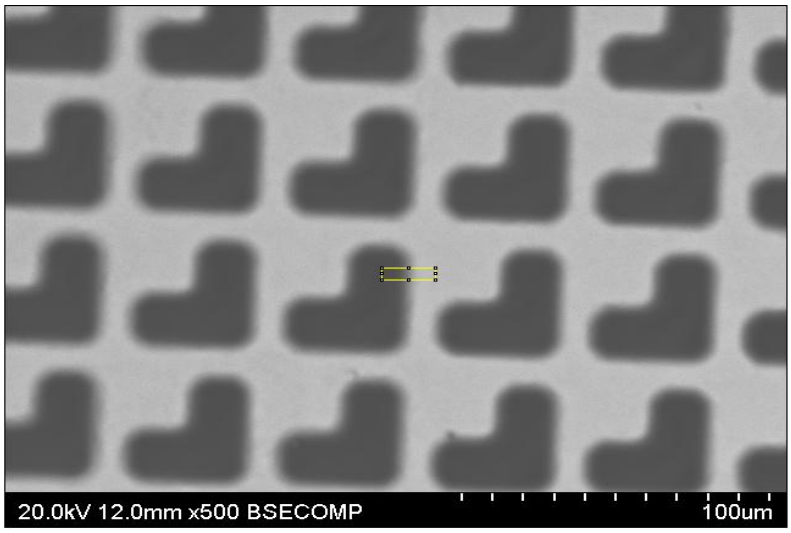

Figure 27: Profile taken to provide the ESF

Firstly, the profile [pixel intensity, which is the gray scale, against pixel location] taken in Figure 27 was plotted, in order to represent the ESF [this is shown in Figure 28]. NB: the rectangle in Figure 27 encloses 11 line profiles for better statistics.

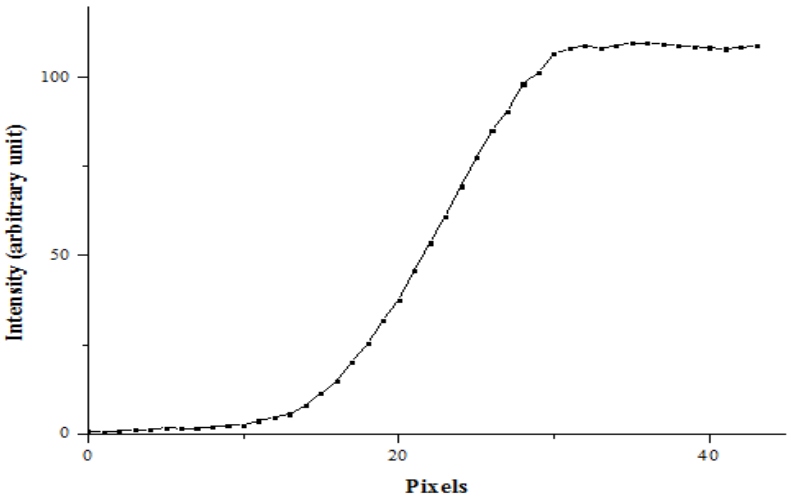

Figure 28: Plot of ESF [average of 11 profiles]

Since the first derivative of the ESF gives the LSF, the ESF in Figure 28 is derived, using Origin. A Gaussian PSF model was fitted to the data, from which the FWHM is measured. The derivative data points and the fitted Gaussian model [continuous line] are demonstrated in Figure 29. As the FWHM represents the SSR, it is found that the FWHM equals 12±1 pixels.

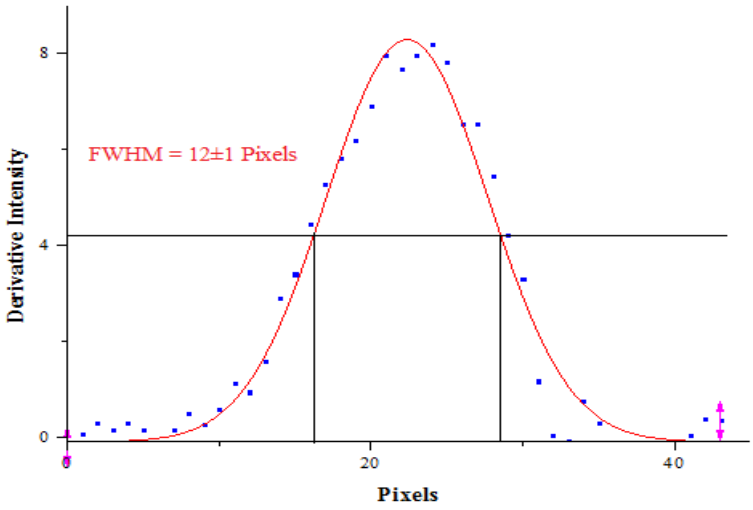

Figure 29: Differentiated data points with fitted Gaussian model [continuous line] and its corresponding FWHM of x500 magnification

Figure 29 offers the SSR in pixels [12±1 pixels], yet, the required resolution should be in µm in order to make sense on the EM images. Therefore, the total number of pixels per patch should be known which can be obtained by plotting full profile across the whole patch.

As some variations were observed in the L-shaped apertures across the sample [this was confirmed by the manufacturer], it is advisable to use more than one patch to calculate the whole number of pixels across the whole patch. Therefore, four full profiles of four patches were plotted and the average number of pixels across each patch was calculated. Figure 30 depicts the inverted image with the full 11 profiles on four patches. For simplicity, the image is inverted in order to obtain a profile up-side down. This is followed by Figure 31, which is a plot of the average full profiles shown in Figure 30.

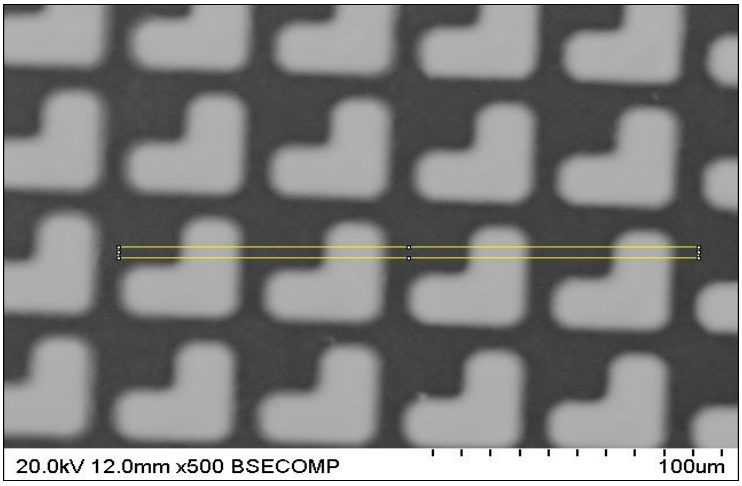

Figure 30: Inverted image with four full 11 profiles

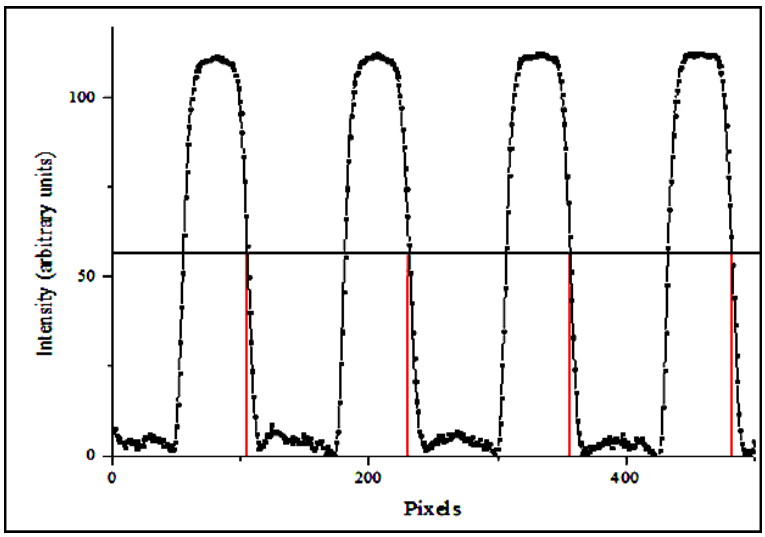

Figure 31: Plot of the four full profiles

Figure 31 shows that the average total number of pixels across the whole patches T = 126±1 pixels. By reference to Figure 26, the width of the whole patch is 50 µm. From this, it is possible to calculate the actual pixel dimensions and the SSR at x500 magnifications in µm as follows.

Consider the width of the entire patch = 50±1 µm then the actual pixel dimension [D] is

$$D(\mu m) = \frac{Width\ of\ the\ entire\ patch\ (\mu m)}{T\ (pixels)} = \frac{50\ \mu m}{126\ pixels} = 0.40\ \mu m \qquad \text{Equation 17}$$

So,

$$SSR(\mu m) = D(\mu m) x\ FWHM(pixels) = 0.40 * 12 = 4.80 \pm 0.40\ \mu m \qquad \text{Equation 18}$$

From Figure 30, it can be seen that the profiles [both full and ESF] were not perfectly parallel to the patches borders, which will cause underestimation of the SSR. ImageJ cannot plot a profile for tilted profiles parallel to the patch. Also, rotating or tilting the image may cause deterioration in the SSR due to image interpolation. For simplicity, the tilting angle was measured as 1.96^{o}, so each SSR value should be multiplied by the Cosine [COS] of that 1.96^{o}. However, the difference that COS 1.96^{o} can make is smaller than the estimated SD [0.40 µm], thus, including this correction is meaningless and should be ignored.

Following the same steps, the SSR was calculated for x200 and x2k magnifications. Table 7 gives a summary of the actual pixel dimension as well as the SSR for each magnification level. EM images and profiles analysis of x200 and x2k magnifications can be found in Appendix 9.1.1.

Magnification	SSR [FWHM] ± 1 [pixel]	Actual pixel dimension in µm [D]	SSR [µm]	χ^2 fitting
x200	5	1.02	5.10±1.02	0.98
x500	12	0.40	4.80±0.40	0.95
x2k	51	0.10	5.10±0.10	0.89

Table 7: SSR of each magnification level

5.3 Grain Size and Nature

The EM allows measuring pre-oxidised powder grains size and observing the shape of the pre-oxidised powders as well as the flame-sprayed surface. Analysis of the EM images shows that powder grains are approximately spherical. Figure 32 [left] shows the pre-oxidised powder grains [FeCrAl] with a graded grain size up to 40 µm. Figure 32 [right] shows the molten granular top surface after the flame-spray [n-type $FeCrAlO_4$] of the same staring pre-oxidised powder [FeCrAl] (1,2). NB: the flame-spray process was explained in section 3.2 Detectors Manufacturing and Design.

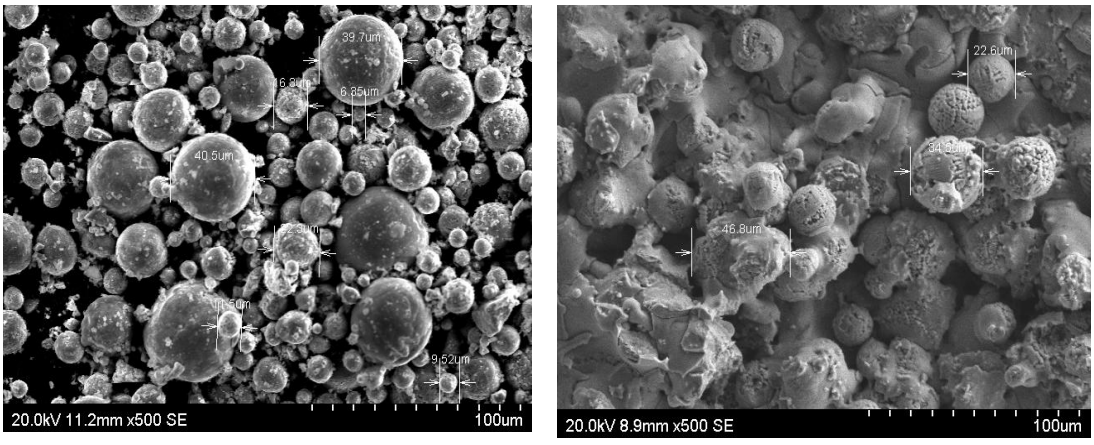

Figure 32: n-type FeCrAl pre-oxidised powder grains before [left] and after [right] flame-spray [$FeCrAlO_4$] **(1,2)**

Table 8 gives a summary of the pre-oxidised starting powders maximum grain size. NB: EM images of the pre-oxidised powders in Table 8 can be found in Appendix 9.1.2.

Powder composition	Maximum grain size	Type
FeCrAl	40	n
MnNi	50	n
NiAl	50	n
Ni	60	p
FeCr	85	p
FeNiCo	128	p

Table 8: Pre-oxidised powders maximum grain size **(2)**

It is believed that the rapid cooling phase associated with the manufacturing and each deposition process leads to the formation of the granular powder particles and surface as seen in Figure 32. For a clearer EM image of the granular pre-oxidised powder, Figure 94 in Appendix 9.1.2.1 demonstrates this for FeNiCo particles as this material possesses the largest grain size [128 μm]. This granular semi-spherical shape is because powder particles are pelletized by shooting the starting pre-oxidised powder in a tank of water to give it its spherical structure.

As the flame-spray deposition process takes place in the open air, once the flame of the nozzle deposits then moves away from an area, the TMO material will immediately cool down rapidly. As it was mentioned in section 3.2 Detectors Manufacturing and Design, Mott indicated that cooling from melt will produce only amorphous materials, as the fast cooling phase does not allow time for reorientation of the TMOs particles before the TMO material turns into solid completely (12,50).

In order to quantify the degree of surface granularity shown in Figure 32 [right], GIMP software was used with the Edge Detection function [Find Edges in ImageJ] to outline the edges of the grains presented on the surface. The Edge Detection tool will highlight sharp changes in image pixel values, where the highest intensity indicates the presence of edge (104). By this method, it is possible to plot a histogram of the surface then apply the Outliers statistics explained in section 3.5.6 Electron Microscopy Images Thresholding in order to set a threshold on the image to distinguish between granular and smooth surfaces.

Unfortunately, the image presented in Figure 32 [right] cannot be used as a ruler measure interferes with the image. BSE images are preferred and so all the comparisons presented in this section will be based on BSE images for consistency. This is because BSE images have relative contrast, where the brighter the image, the more Z of the material. This will be clarified shortly, when the quantification of surface granularity is performed. Hence, Figure 33 shows another image of the same n-type $FeCrAlO_4$ sample but at a different location at x500 magnification.

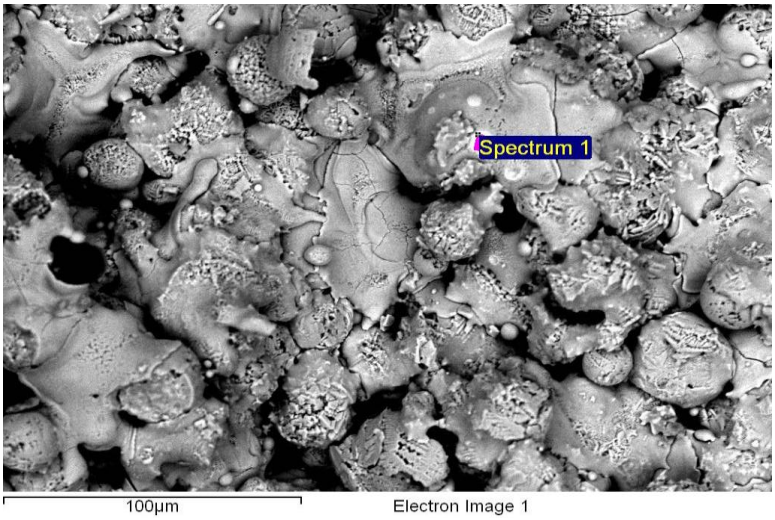

Figure 33: x500 BSE Flame-sprayed n-type $FeCrAlO_4$ surface

An ROI [region of interest] was taken from Figure 33 then the Edge Detection function was applied on the ROI. A histogram was plotted for the produced Edge Detection ROI, and the Outliers statistics was applied to the histogram.

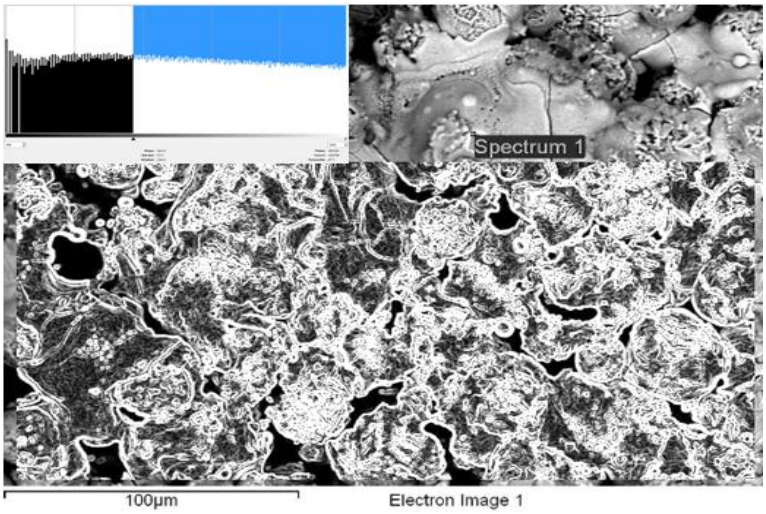

Figure 34: ROI on Figure 33 above with histogram inset

From Figure 34, the Outliers are taken on the histogram for the LOF only. This is because the highest intensity [bright areas] indicates the borders of the grains, and so, the dark areas represent the smooth surface. By this method, it is possible to quantify the bright areas in the image as a percentage. This is beneficial in quantifying the granularity of the surface as the bright areas are related to the grains on the surface. NB: the importance of quantifying the granular nature of the surface will be addressed shortly.

This method was applied on different BSE images with different magnifications [see Appendix 9.1.2.2]. Consequently, 67% granularity is calculated as an average for the Atmos flame-sprayed sample surfaces.

For further investigation, the surface of the image was plotted in 3D. Thus, the ROI selected in Figure 34 was plotted as seen in Figure 35. This demonstrates the severe granularity of the surface [67%].

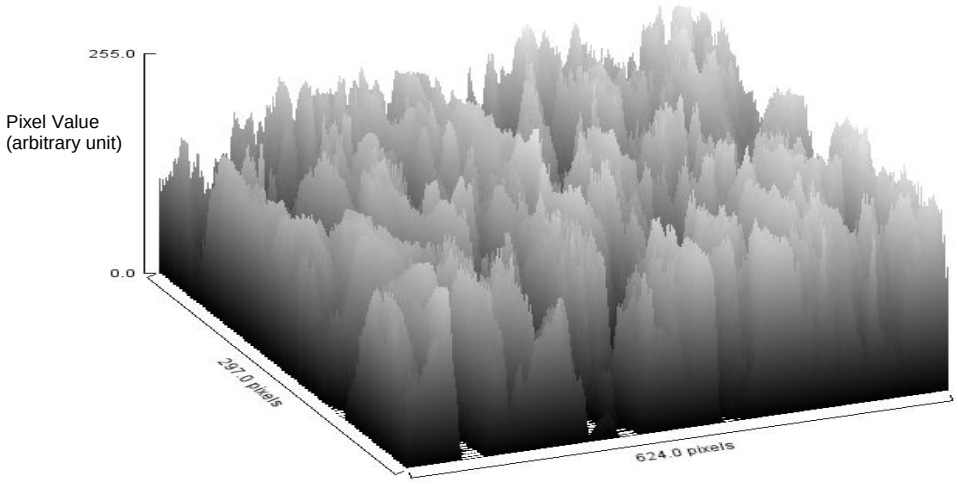

Figure 35: Surface plot of the ROI sat in Figure 34

From Figure 35, the high level of granularity [67%] of the surface can be seen. This surface plot explains how p-type TMO is deposited onto n-type TMOs. The gaps between the grains of the n-type TMO are filled by the p-type TMO during the deposition, which leads to contamination of both layers [p and n types]. This contamination would lead to e-h recombination as a defined border at the hetrojunction is not set. Therefore, relatively low signal is expected at this stage. Although the mobility of charge carriers at the surface is half the mobility of the charge carriers in the bulk (137), it is possible to observe the level of traps presented in the surface. These traps are able to localise charge carriers and prevent them from hopping from site to another.

According to the study performed above, a gradual cooling process is strongly recommended to eliminate the granular nature of the surface together with allowing enough time for the material to be arranged. Non-granular surface is sought in order to be able to build a defined p-n hetrojunction. This is to improve the near-linearity found in chapter 4 Initial Status of TMO Detectors, besides, the relatively low net signals obtained. Also, a non-granular surface will help in minimising the possible contamination between different deposited layers. This is because when the p-type TMO layer deposited on top of the previously deposited granular n-type TMO surface, the p-type TMO will fill the gaps caused by the granular nature of the n-type TMO. This will lead to obtain a p-type contaminated n-type TMO layer. In other words, undefined p-n hetrojunction will be produced. So, the surface after each deposition ought to be prepared carefully.

5.4 Compositional Analysis

In this test, the same samples analysed in the previous section are used. This is because Atmos supplied the pre-oxidised powders together with the single layered TMO samples at the same time. So, as powders used to manufacture the single layered TMO samples were consumed, there was only one sample overlapping. Overlapping means pre-oxidised powder and single layer TMO of the same material are available. This is therefore applied to FeCrAl sample only.

The n-type TMO $FeCrAlO_4$ sample is tested under the EM for compositional analysis. This serves to compare the composition before and after the flame-spray. Table 9 shows a comparison between the pre-oxidised powder [FeCrAl] and the flame-sprayed sample [$FeCrAlO_4$], where values in Table 9 are the average of three different positions on the same sample.

Pre-oxidised powder	Flame-sprayed TMO
Fe [60.76%]	Fe [45.00%]
O [18.02%]	O [30.73%]
Cr [16.88%]	Cr [12.02%]
Al [4.34%]	Al [3.52%]
None	C [8.73%]

Table 9: Effect of the flame-spray technique on the starting pre-oxidised powder **(2)**

By analysing Table 9, the pre-oxidised powder and flame-sprayed TMO have the same compositions with a rise only of C in the flame-sprayed TMO. In fact, the presence of C is expected due to the use of the flame-spraying technique, which involves the process of burning. As the amount [8.73%] is relatively high, C contamination from the nozzle is suspected. This will be discussed in more detail in section 5.8 Surface and Bulk Comparison.

A close reduction, by an average of 24.54±0.50%, was shown in the elements presented in the samples in Table 9, excluding C and O. This indicates the uniformity of the oxidation process during the flame-spraying. Note that, the 0.50% error is the SD of the mean. According to the calculation provided by Taylor, if the SD is constant for each single measurement, then the mean SD will be the same. This is applied to all subsequent averaged values (1,2,99).

Interestingly, a lack of H content is seen in the EM compositional results, implying that the TMOs are not hygroscopic as the samples had been exposed to the ambient environment for few weeks prior to this analysis. This is observed in all tested TMO samples (1,2).

Also, an increase in the overall O concentration of the order of 58.64% is observed due to the flame spray process. It should be noted that the starting powders used are pre-oxidised and Table 9 confirms the degree of pre-oxidation of 18.02%. A similar level of pre-oxidation is claimed by Atmos and is not constant across all the provided pre-oxidised powders. In general, it is possible to claim that the flame-spray mechanism increases the oxidation of the pre-oxidised powder by two third [2/3] (1,2).

5.5 Surface Uniformity

Scanning and analysing different positions on the same flame-sprayed sample gives information about surface uniformity. Table 10 shows a comparison between two different positions on an n-type TMO [mixture of $CoFeVO_4$ and $CoFe_2O_4$] sample. It is found that any variation in concentration observed is within an average of 4.86%. Moreover, a reproducible degree of oxidation is observed with a variation of 3.80% across the sample (1,7).

Element	Weight %	Element	Weight %	Comparison %
Fe	39.73	**Fe**	38.15	-3.98
Co	29.84	**Co**	31.46	5.15
O	23.92	**O**	23.01	-3.80
C	2.44	**C**	4.54	46.26
Mn	1.95	**Mn**	0.58	-29.74
V	1.69	**V**	1.58	-6.51
Total	99.57	**Total**	99.32	Ave. = 4.86

Table 10: Comparison between two different positions on the same n-type TMO [mixture of $CoFeVO_4$ and $CoFe_2O_4$] sample. NB: Ave. indicates average

From Table 10, comparisons are calculated from {large value – small value/large value} x 100 and are applied in all subsequent EM comparisons. The negative sign indicates a reduction in values from position 2, compared to values from position 1, whereas, the average is calculated regardless of the sign. It is essential to mention that the totals in Table 10 are not 100% accurate, due to the presence of trace elements [e.g. Zr, K and Mg]. These are present in amounts less than the SD [0.50%], and so were not quoted in the table. Table 10 does, however, show the presence of Mn, which was not quoted in the pre-oxidised powder. Therefore, Mn in this sample is considered as contamination due to residual in the nozzle, where Mn is expected to be deposited prior to the manufacturing of this sample. On this basis, this will give an indication that the first position with Mn [1.95%] was deposited prior to the second position with Mn [0.58%]. This is because, as the nozzle is used, the previous residual is considered to be cleaned. In essence, C showed the highest variation of 46.26%. This amount [46.26%] is believed to be mostly from contamination from the nozzle. Hence, Mn [29.74%] and C [46.26%] variations are not included in the average [4.86%] calculated in Table 10. Excluding contamination [Mn and C] is done deliberately because quoting Mn and C would be a misleading value as it will increase the average variation of the other elements significantly.

It is very important to understand that the large values of contamination are for their variations only. In other words, the variation of Mn contamination is 29.74% due to the change in value from 1.95% to 0.58%. However, the Mn contamination itself is

relatively low as it shows the value of 1.27% as an average. This is applied on all the subsequent contamination analysis, including C contamination.

Thus far, all surface uniformity analyses were about the sample analysed in Table 10 in particular. In order to increase the accuracy of this analysis, the same process in Table 10 is followed on three different samples. Table 11 shows a summary of the analysis of three TMO samples.

TMO sample	Ave. variation, excluding C [%]	Variation in O [%]	Variation in C [%]
Mixture of FeO and Fe_3O_4	2.80	4.20	14.49
$FeCrAlO_4$	3.25	1.77	3.15
Cr_2O_3	3.31	4.19	34.78

Table 11: Summary of the comparison between two different positions on the same TMO sample for three different samples

Based on Table 11 together with Table 10, it is possible to quote that the average variation of Atmos flame-spray deposition is 3.56%. Also, the average variation in reproducibility of oxidation can be quoted as 3.49%. The average variation of Atmos flame-spray technique quoted [3.56%] is calculated with excluding the variation in Mn [Table 10 only] and C [Table 10 and Table 11]. This is because there is no contamination found in the samples analysed in Table 11 above except the presence of C. Also, as C is considered as contamination arising mainly from the nozzle of the deposition robot, Table 11 shows the variation of C in each sample. Apparently, C varies significantly across the samples, where the maximum variation between two sites on the same sample could be as large as 46.26%. As a result, surface preparation is strongly recommended to omit this contamination of C.

A question may arise at this point, which is what is the acceptable limit in variation? This is really dependant on the samples and the application. Therefore, it is not possible to find similar work in literature to quote their variation. For instance, Tan used the SEM for surface analysis, where a variation of 23.64% in Ti was acceptable. This variation is considerably large in the TMO samples (138).

Alternatively, as the current method of manufacturing produces radiation detectors in working order [see chapter 4 Initial Status of TMO Detectors], the maximum variation found in the current batch of TMO samples, can be set as the acceptable limit of variation in all TMO samples. The maximum variation is 6.51%. This maximum variation can be found in Table 10 in V.

5.6 Effect of Continued Exposure to Radiation

Exposure to radiation may cause internal changing owing to charge migration. Therefore, a test was conducted to investigate whether the compositional analysis suffers from noticeable change after irradiation. The protocol was to scan a never-irradiated TMO detector then after constant exposure [50 kV, 5 mA, 5 cm away from x-ray source and for 3 h], another scan was performed in the same position. C tape was used to mark a reference point to make sure comparison was performed on the same position. Table 12 shows no difference in material composition in the n-type sample $NiMn_2O_4$ outside an average of 4.46% (1).

Element	Weight %	**Element**	Weight %	Comparison %
Mn	39.27	**Mn**	40.62	3.32
O	28.30	**O**	27.13	-4.13
Ni	22.39	**Ni**	23.80	5.92
Cr	4.01	**Cr**	3.99	< SD
C	6.03	**C**	4.46	-26.04
Total	100.00	**Total**	100.00	Ave. = 4.46

Table 12: Comparison between before [left] and after [right] heavy irradiation on the same n-type sample [$NiMn_2O_4$]

This discrepancy [4.46%] is to be compared with the average discrepancy in Table 10. This is because Table 12 showed the average results of three different positions on the same sample. Thus and for identical statistics, one sample is compared with one sample, where the discrepancy in Table 12 [4.46%] falls within the surface variation of 4.86% in Table 10. This might indicate that no noticeable changes can be spotted by the EM in the material after heavy irradiation.

C is excluded from the average in Table 12 owing to the reasons presented in section 5.5 Surface Uniformity. Furthermore, Cr should not show up in this sample as it was not quoted in the staring pre-oxidised powder. This indicates that Cr is a contaminant and thus, excluded from the average in Table 12. This sample confirms that the nozzle was used to deposit the p-type Cr_2O_3 TMO prior to the deposition of $NiMn_2O_4$ TMO. This is because a TMO detector of the combination of Cr_2O_3-$NiMn_2O_4$ is very common in Atmos detectors. In fact, these are the TMOs used in the detector sample TMOD1 in chapter 4 Initial Status of TMO Detectors. Finally, the variation in O [4.13%] falls within the SD of O variation [3.80±0.50%] in Table 10.

5.7 Contamination and Splash

As it was mentioned earlier, the current production process uses the same flame-spray nozzle for different materials deposition. This leads to the observed contamination between the sprayed TMO surfaces. Figure 36 shows an example of this type of contamination, where the image of the TMO is interspersed with bright metallic areas, namely pure Cu. This is because during the manufacturing of the single layered samples, a new idea of flame-spraying Cu electrode was applied to take over the Cu tape. Thus, contamination of pure Cu is expected. NB: analysis of the flame-sprayed Cu electrodes will be shown later. Appendix 9.1.3 shows more EM images of Cu-contaminated TMO surfaces (1).

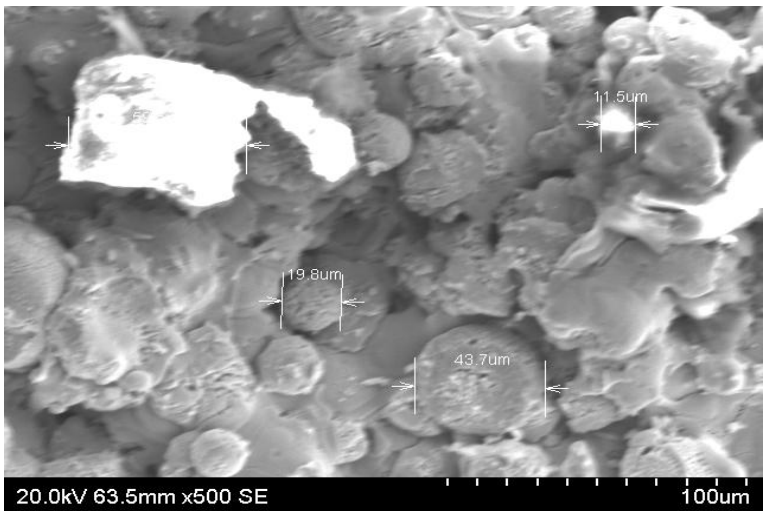

Figure 36: Surface contamination of n-type TMO [$FeCrAlO_4$] **(1)**

Moreover, the EM images showed splash of the deposited materials. This is because the deposited material [TMO or Cu] particles escape the flame of the nozzle due to the strength of the gas flow. This is depicted in Figure 37.

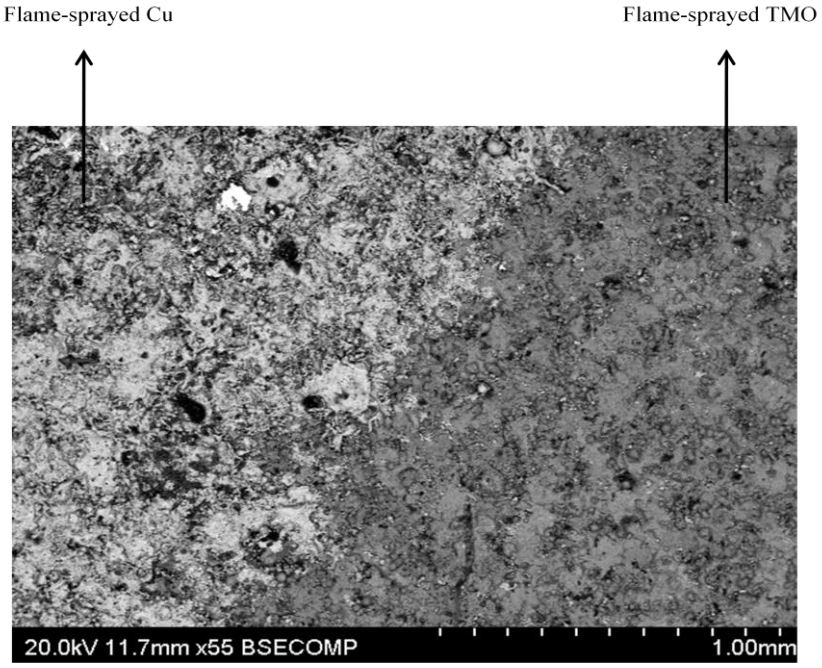

Figure 37: Cu-TMO [Cr_2O_3] interface [top view]

Figure 37 shows the surface interface of the flame-sprayed Cu and a p-type TMO [Cr_2O_3] material. It is clear that excess of Cu metal rich sites are spread all over the TMO surface [bright dots on the right diagonal side of Figure 37]. On this basis, n-type TMO is expected to be contaminated by p-type TMO. This is owing to the manufacturing process, which deposits p-type on n-type TMO [recall 3.2 Detectors Manufacturing and Design]. To prove this, Figure 38 shows the surface of the p-n TMOs hetrojunction. The p-n interface, together with the contamination, is not possible to be observed due to the similarity in effective atomic number, Z_{effe} [this will be explained in section 7.3 Attenuation Coefficient] of p-type and n-type TMO compositions, compositional analysis is performed on this sample.

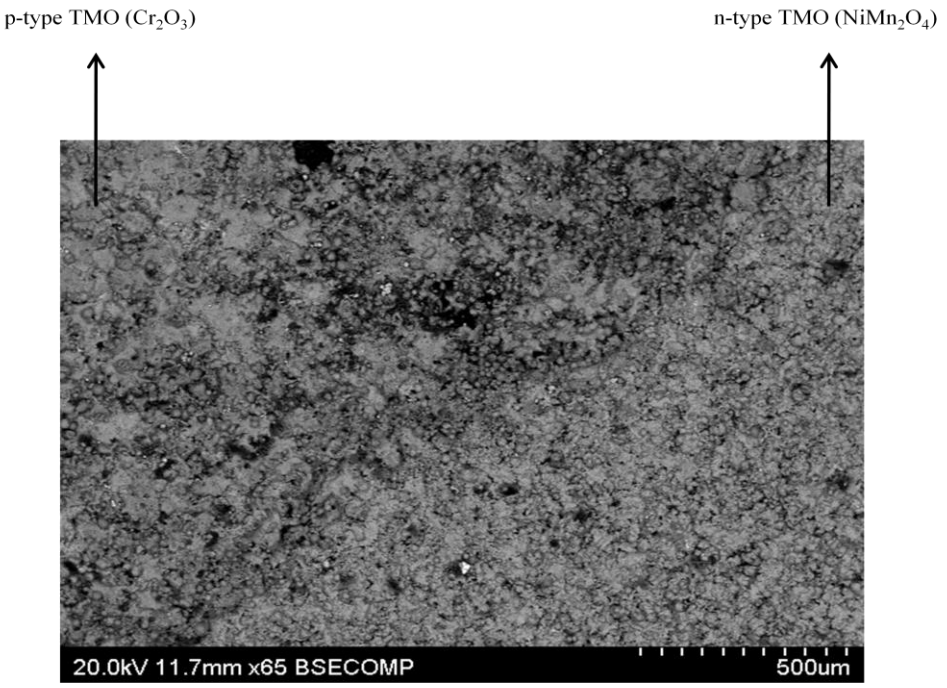

Figure 38: p [Cr_2O_3]-n [$NiMn_2O_4$] hetrojunction [top view]

It is found that Cr_2O_3 acts as p-type TMO, whereas, $NiMn_2O_4$ acts as n-type TMO in this sample. However, there is an excess of Cr [8.52%] on the n-type surface. This is expected as Atmos deposits n-type prior to p-type TMOs. More top view interface images can be seen in Appendix 9.1.3.

Surface contamination and splash can be avoided by cleaning the nozzle in each deposition. This is together with applying a mask to the flame to avoid particles escaping the flame. This is because contamination by Cu on the surface will scatter incident radiation and radiation scattering will reduce the sensitivity of the TMO detector as a whole. More importantly, any presence of metallic centres will act as charge scattering or absorbing medium. In terms of electrons moving across the TMO material, electron rich metallic centres will scatter these moving electrons and prevent them from hopping in the right direction towards the electrodes. In terms of holes moving across the TMO material, electron rich metallic centres will cause e-h recombination and hence, reduces the number of holes, reaching the electrode. This is because these electron rich metallic centres are introduced to the TMO media by the residual splashing of the previously deposited material and hence, this will contribute to the relatively low signal observed in chapter 4 Initial Status of TMO Detectors (13,27,59).

An increase in the noise level will also occur due to deposition of free electrons by the metallic centres. Mathematically, the factor R in Equation 4 will be minimised due to maximising the factor α.

Therefore, in conjunction with the recommendations mentioned above [nozzle masking and cleaning], surface preparation can prove useful to eliminate the contamination of the surface. Finally, it is worth mentioning that charge do transport across the surface, however, the mobility of charge in the bulk of the material is twice the mobility of charge on the surface. This leads us to examine the bulk of the TMO samples as it will be seen in the following section (137).

5.8 Surface and Bulk Comparison

The surface of the n-type TMO [$FeCrAlO_4$] shown in Figure 32 [right] and analysed in Table 9 [right] is the surface condition prior to mechanically polishing a few μm's from the surface. The average TMO layer thickness of this sample is 100±5 μm. After mechanically polishing the surface, the bulk is scanned in order to compare the newly exposed core with the previous surface. The polishing procedure was explained in section 3.5.4 Sample Preparation (1).

Figure 39 shows the EM image of the polished bulk of the same TMO sample [$FeCrAlO_4$]. Mechanical polishing appears to be effective as no grains can be spotted on Figure 39, compared to Figure 33.

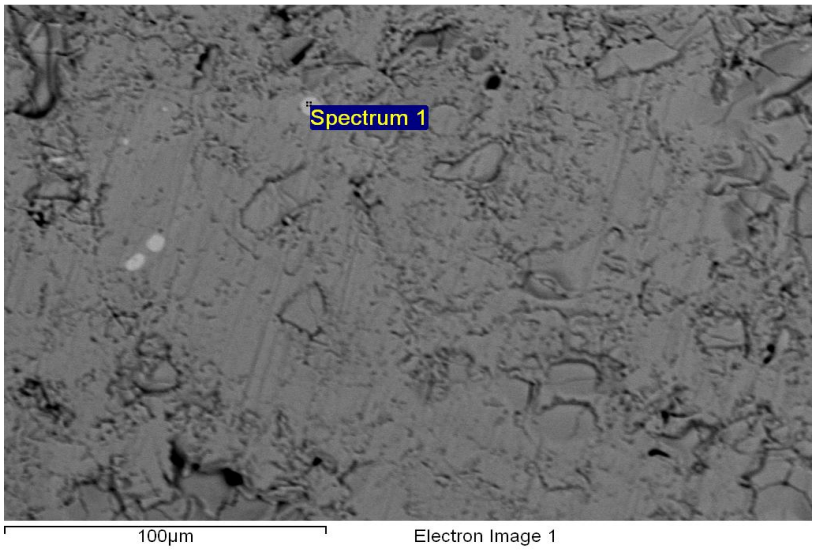

Figure 39: Bulk [polished surface] of the n-type TMO [$FeCrAlO_4$] **(2)**

In order to compare Figure 39 to Figure 33 quantitatively, the same ROI taken from Figure 33 is taken from Figure 39. This is followed by the same Edge Detection analysis explained in section 5.3 Grain Size and Nature [see Figure 40].

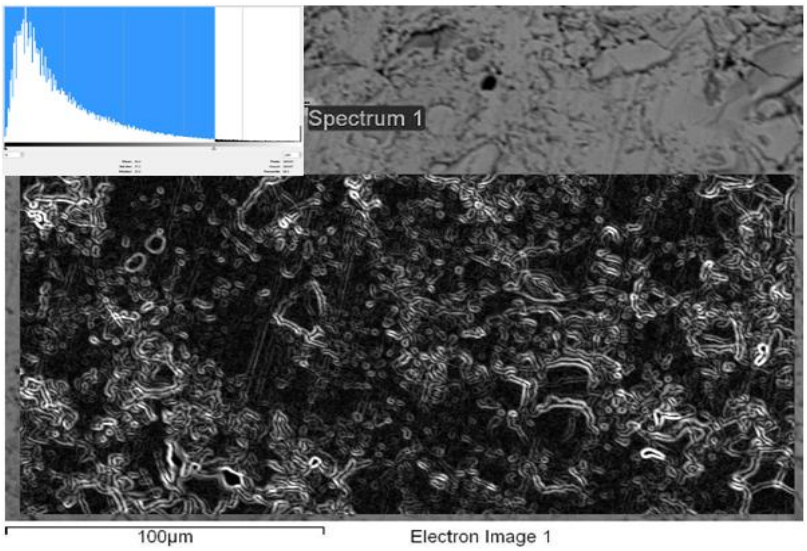

Figure 40: ROI from Figure 39 with histogram inset

From Figure 40, the Outliers are taken from the histogram for the UOF only, unlike Figure 34. This is because the majority of pixels intensities fall within the dark areas as depicted in the histogram in Figure 40. This method was applied to different BSE images with different magnification [see Appendix 9.1.4]. As a result, an average of 4% of granularity is found on the mechanically polished surfaces. This is to be compared with the unpolished surface in Figure 34, which has an average surface granularity of 67%. In other words, the mechanical polishing improves the surface by 94%.

In order to fully compare the polished surface with the unpolished surface, the polished surface in Figure 39 was plotted. This is to be compared with Figure 35. From Figure 41, it is found that the core of the TMO is more compact than the surface. This is a desired feature in σ since any defects or granular media act to diminish the CTM across the TMO.

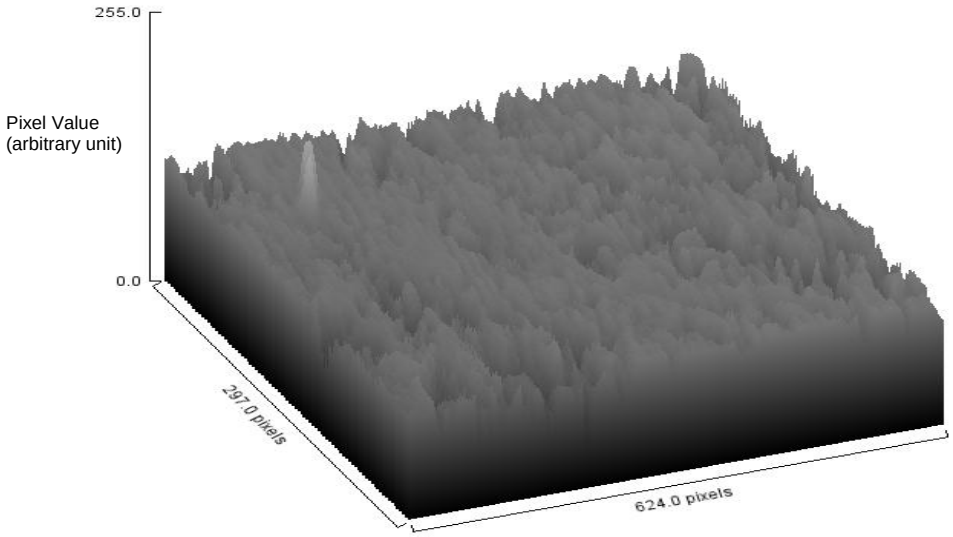

Figure 41: Surface plot of the ROI sat in Figure 40 above

From Figure 41, it can be seen that valleys are still presented in the polished surface, which represents the bulk of the material, which indicates the presence of defects in the bulk of the TMO material. Ideally, the bulk should be solid without any defects. Also, bright dots can be noticed in Figure 39. This confirms the contamination of the bulk similarly to the surface [see section 5.7 Contamination and Splash]. Therefore, it is essential to estimate the defects available in the bulk of the TMO material i.e. mechanically polished surface.

The Outliers method is used to estimate the number of defects presented in the image. However, this time the histogram was plotted on the image itself, unlike the granularity estimation, which involves histogram plotting of the Edge Detection function image. In this way, it is possible to set a threshold on the image in which any value which falls out of the LOF – UOF is considered a defect. Hence, Figure 42 shows a thresholded ROI, where black areas highlight the defects in the ROI.

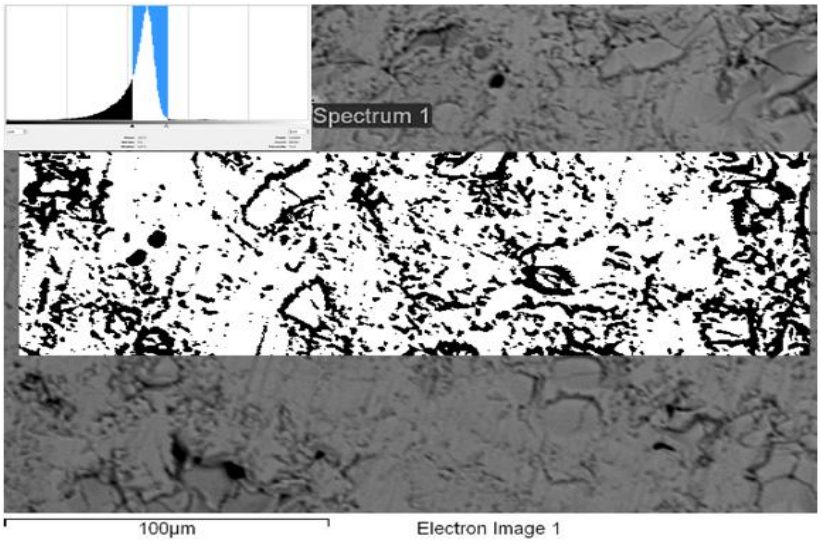

Figure 42: Defects estimation of the ROI with the histogram inset; black areas represent defects

The above method is applied on different ROI [see Appendix 9.1.4] and the average proportion of defects in Atmos samples is concluded to be 30%, where the defects include voids, cracks and pure metal contamination. Mechanical polishing is not capable of omitting this bulk contamination. This is because this type of contamination [core contamination] is provided by the deposition process during the growth of the TMO layer. Thus, nozzle cleaning and flame masking is recommended to reduce this contamination. A full mechanical polishing evaluation will be addressed in section 6.3.1 Mechanical Polishing as a form of surface improvement.

Table 13 gives a compositional analysis in order to compare the bulk with the surface of the TMO sample [$FeCrAlO_4$]. Notably, Table 13 [left] possesses the same values presented in Table 9 [right] as it is the average of three different positions on the same sample [$FeCrAlO_4$]. Similarly, values in Table 13 [right] are the average of three different positions on the same sample after polishing. So, from Table 13, it is shown that the compositions of the surface and the bulk vary by 3.18% as an average, excluding contamination [Fe, Ni and C].

Element	Weight %	Element	Weight %	Comparison %
Fe	45.00	**Fe**	49.25	8.63
O	30.73	**O**	30.56	-0.55
Cr	12.02	**Cr**	12.64	4.91
Al	3.52	**Al**	3.67	4.09
C	8.73	**C**	2.53	-71.02
--	--	**Ni**	1.35	100
Total	100.00	**Total**	100.00	Ave. = 3.18

Table 13: Compositional analysis of the surface area [left] and bulk [right] of the n-type TMO [$FeCrAlO_4$]

Although Fe is one of the elements of the starting pre-oxidised powder [FeCrAl], part of the Fe is considered contamination in the bulk in this comparison. Due to the relatively high level of variation found [8.63%]. This is expected as the core of the sample is contaminated by pure Fe sites, as shown in Figure 39 and Figure 101 in Appendix 9.1.4, where the bright areas are apparent.

Ni appears in the core but not in the surface of the sample [see Table 13], and so, Ni is considered to be contamination from the nozzle as the core is formed prior to the surface in Atmos manufacturing process. Also, comparing the amount of O in the surface and core shows that O varies by 0.55% only. This implies that the surface is not affected by the O present in the ambient environment.

Finally, it is important to introduce the significant difference in C contamination between the surface and the core of the sample. The core of the sample shows a reduction in C contamination by 71.02%. This finding would imply that mechanical polishing is highly capable of the elimination of C contamination provided by the nozzle.

Thus far, it is not yet proven experimentally in which form C is presented on the TMO surface. However, it is believed that, as CO_2 is an expected waste product due to the flame-spray process, the C contamination might be due to the formation of CO_2 during the manufacturing process. CO_2 waste is confirmed by Atmos [see section 3.1 Atmos Technologies Ltd.]. Furthermore, in terms of literature, surface C contamination is common in semiconductors grown by thermal process. Surface C contamination is

demonstrated in three forms [CO, CO_2 and CO_3] by Schulz on GaN semiconductor samples due to the involvement of thermal process. Again, due to the production of CO_2 the form accepted in Atmos TMOs would be CO_2 at this stage (139). In fact, this will be confirmed experimentally in section 6.3.2 Argon Ions Sputtering.

5.9 Mapping Elemental Distribution

The EM software is capable of building a compositional map distribution of the surface, using the EDXS technique. By this method, it is possible to find out any inhomogeneity or defect in the sample in terms of spreading uniformity. This is because ideal sample compositions should be evenly distributed across the whole sample, however, with different concentrations depending on the stoichiometric ratios of the used compounds. Figure 43 shows the conventional EM image [top-left corner] of an area of the surface of an n-type TMO [Mixture of $CoFeVO_4$ and $CoFe_2O_4$], along with maps of elemental compositions of the same area. Counts of these images were collected over 45 min.

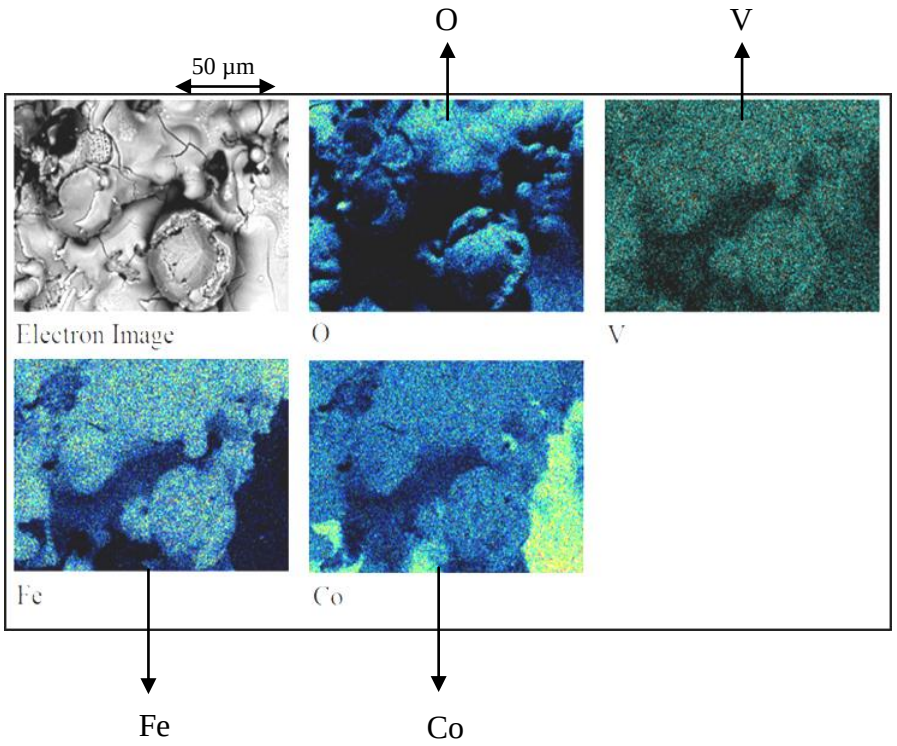

Figure 43: A conventional EM image of an n-type TMO [Mixture of $CoFeVO_4$ and $CoFe_2O_4$], followed by compositional maps for four elements present in the sample **(1)**

The maps in Figure 43 demonstrate the various constituent elements distributed across the sample, where the brighter the area, the more corresponding element concentration in that area. The compositional analysis of this sample can be referenced to Table 10 above. However, the position shown in Figure 43 does not include any contamination, neither C nor Mn, unlike Table 10. This allows observation of the actual elemental distribution without any disturbance from contamination. Therefore, Table 14 gives the compositional analysis of the position shown in Figure 43 in particular. Notably, values in Table 14 do not conflict with values in Table 10. It is all about the disappearance of contamination.

Element	Weight %
Fe	39.64
Co	33.40
O	25.20
V	1.76
Total	100.00

Table 14: Compositional analysis of the position depicted in Figure 43 above of the n-type TMO [Mixture of $CoFeVO_4$ and $CoFe_2O_4$]

From Figure 43, O and V are distributed but with the presence of some dark areas. This darkness is due to shadowing artefacts in the EDXS acquisition since the artefacts are always around the same position on the EM image. Also, O suffers from more shadowing than V due to the difference in Z between O [8] and V [23]. This is because V would interact with more electrons than O. Mainly, this is owing to the granular nature of the surface, where peak-scattered electrons will suffer fewer interactions than the ones which fall in the valleys (1).

Furthermore, in regard to the shadowing artefacts, Co and Fe are evenly distributed in 80% of the image area. In terms of Co, the remaining 20% shows excess of Co in the right side of the Co map together with some bright areas at the bottom of the same map. On the other hand, Fe shows severe deficiency in the same areas, where Co shows excess of concentration.

A possible explanation of this situation is that Fe ions are swapped by Co ions in $CoFeVO_4$. This is because V can be found evenly distributed in the debated area, which has excess of Co and deficiency of Fe. This indicates that V is contributing to the new compound formed in the debated area, which based on $CoFeVO_4$, as $CoFe_2O_4$ has no V. Fundamentally, the compound $Co^{2+}Co^{3+}V^{3+}O_4$ [Table 2] is expected to be formed. This is because, in literature, Co and Fe can be used interchangeably as Co can dope Fe compounds and vice versa. For instance, in 1978, Diepen et al. published a paper about Fe-doped CoV_2O_4 at tetrahedral sites i.e. Co in CoV_2O_4 [recall spinel] by annealing at 910 ^oC. This indicates that heat can act as a catalyst to cause this exchange [Fe-Co], which can be produced by the flame-spray process [see Table 1]. Co doping in Iron oxides is also confirmed by Cornell (53,140).

As the EM is not chemical state sensitive. It is not possible to give the exact new compound formed in the debated areas. However, as the flame-spray technique is capable of producing spinels, VCo_2O_4 is suspected.

5.10 Cross-Sectional Analysis

All images studied thus far have shown the top view of the samples. In order to examine the cross-sectional structure of the TMO detectors, a double sprayed layer sample edge is scanned. The sample was embedded in resin for clearer vacuum-surface interface then coated with C prior to imaging as the resin and ceramic tile substrate are electrical insulators [section 3.5.4 Sample Preparation] (1).

Figure 44 shows the cross-section of the detector in the descending order of resin, p-type TMO, n-type TMO then ceramic substrate. The average TMOs thickness can be determined as 233±5 μm [ideally, 100 μm each]. Note that, the surface of this sample is not prepared.

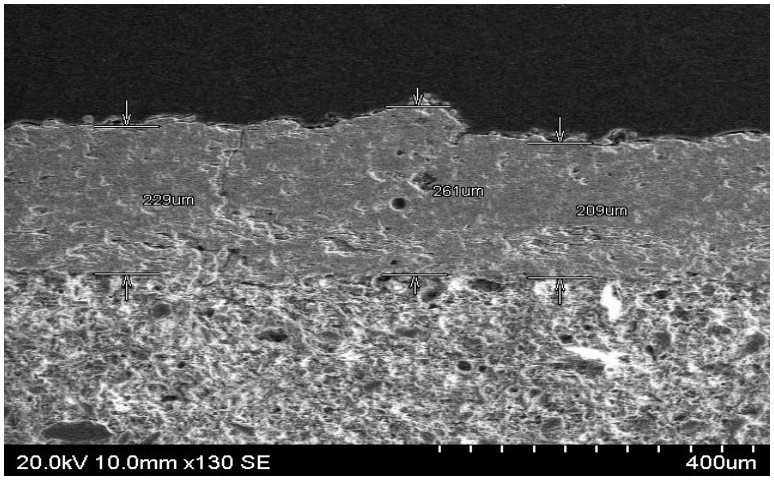

Figure 44: Cross-sectional EM image; in descending order, resin, p-type TMO, n-type TMO then ceramic tile substrate

From Figure 44, there is no definite line between the p-n hetrojunction as expected in earlier sections. Also, the substrate is porous, which cause the TMO to diffuse into it. Layers diffusion is a key factor in the flame-spray process, as depositing the n-type TMO on the ceramic tile substrate causes the TMO to fill the gaps in the substrate. This will affect the p-n hetreojunction as filling a hole in the substrate causes the formation of a hole in the surface of the n-type TMO. Consequently, this hole [formed on n-type TMO surface] will be filled by the p-type TMO, which will lead to the formation of a hole on the p-type TMO surface in return. This is in addition to the rapid cooling phase, which causes the formation of the granular nature of n-type and p-type TMO surfaces.

Also, blasting the melt of the p-type TMO on top of the n-type TMO will result in the p-type TMOs diffusing into the n-type TMOs. This is because the various TMOs have similar physical properties, including melting points, as will be seen later. On top of that, Figure 44 shows severe defects in the form of voids and cracks in the bulk of the sample. These defects will also contribute to the diffusion. Therefore, more compact TMO layers are preferable in this case.

Zoomed in EM images emphasises the presences of voids and cracks in the sample. Thus, Figure 45 shows an example of a crack, where the top arrow is pointing. The bottom arrow indicates the stacking spaces and voids caused by the porous substrate. In consequence it is apparent from Figure 44 and Figure 45 that the n-type defects are twice the p-type defects due to the porous substrate. Note that, cracks are caused due to the mismatching between the substrate and TMO thermal properties as it will be seen in section 5.12 Substrate Analysis.

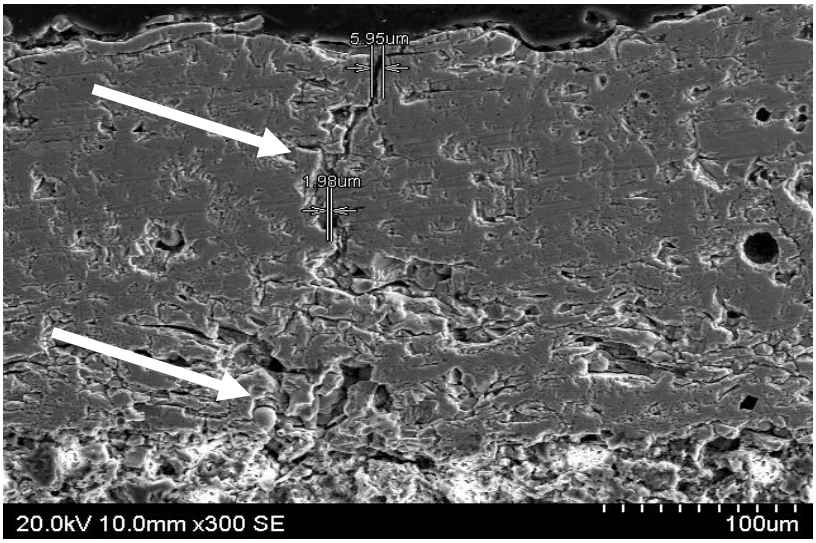

Figure 45: Cross-sectional EM image; a zoom in a crack [top arrow] and void [bottom arrow]

In terms of CTM, such defects will act as a trap or charge store [capacitor]. In this case, charge will be stuck and cannot move along the sample unless they receive E which allows them to overcome the potential barrier of the crack. Technically, this will increase the expansion of the potential well presented in Figure 4 (50,61).

According to the conclusion drawn in section 5.8 Surface and Bulk Comparison, it is highly expected that pure metal contamination is present in the inner core of the sample. This is due to splash and uncleanness of the nozzle. Thus, the BSE images would prove useful as the BSE is Z dependant. This is clarified in Figure 46 in which the bright areas indicate metal-rich sites. As it was explained in section 5.7 Contamination and Splash, these metal centres will act as either scattering centres or recombination centres for charge carriers (13,27,59). In addition, the effect of defects in the bulk of the material is twice the effect of the defects on the surface. This is because the mobility of charge in the bulk of the material is twice the mobility of charge on the surface (137).

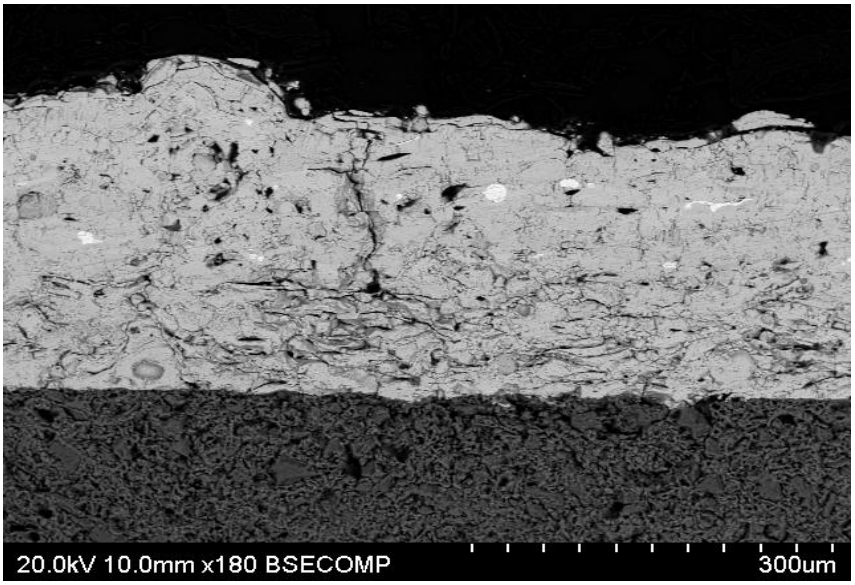

Figure 46: BSE cross-sectional image

In terms of defects quantification, Figure 46 is used for this purpose. This can be achieved by the aid of the Outliers technique. The same process used for defects estimation in Figure 42 is applied on Figure 46. This, together with other cross-sectional images, can be found in Appendix 9.1.5. This is to estimate the average defect percentage of several cross-sectional images [see Figure 47].

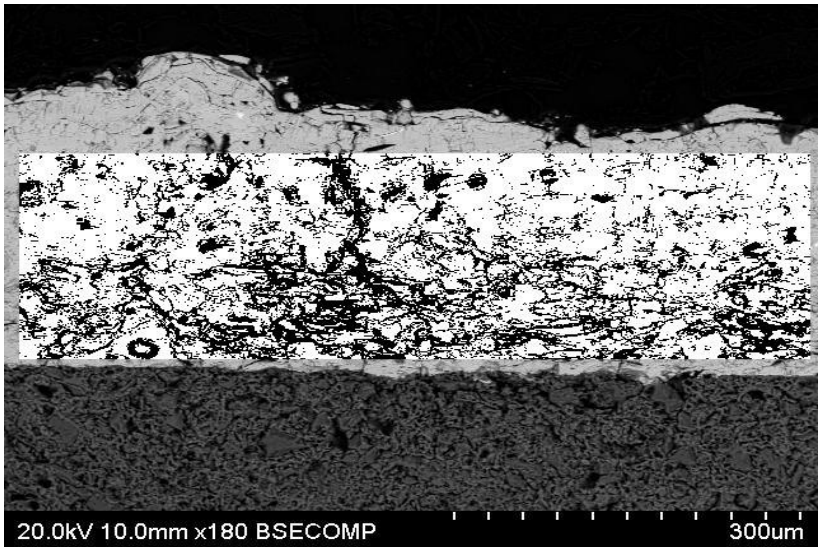

Figure 47: Threshold ROI on Figure 46 above; black areas are defects

From Figure 47 together with Appendix 9.1.5, the average defects are calculated to be in the order of 30%. This would highlight the average defects presented in the bulk of the material, which is also in the order of 30% [see Figure 42]. This is expected as vertical average defects should be identical to horizontal average defects. In other words,

defects are uniform on Atmos flame-sprayed samples for the same manufacturing criteria. Furthermore, surface plotting would prove useful at this stage. This is because, plotting the cross-section of the p-n hetrojunction as a surface would allow observing the environment in which charge carriers transport through. This is illustrated in Figure 48 for the same ROI in Figure 47. The rest of the cross-sectional surface plot can be found in Appendix 9.1.5.

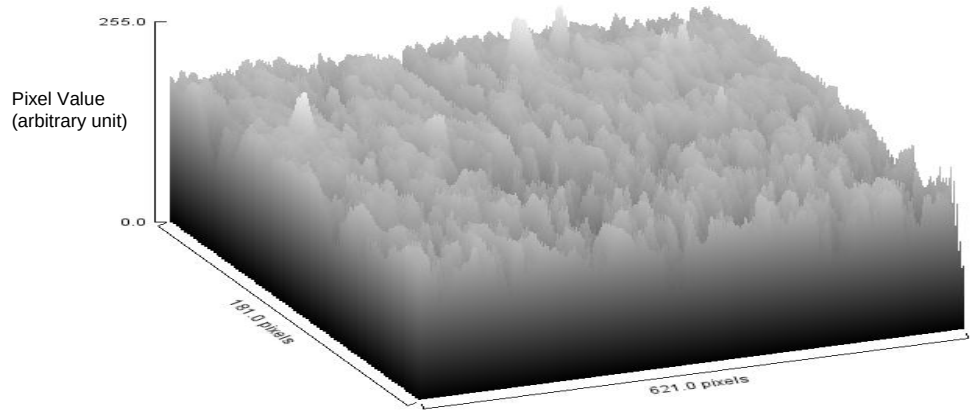

Figure 48: Surface plotting of the cross-sectional image ROI in Figure 47 above

The layout of the surface plot in Figure 48 looks similar to the layout of the surface plot in Figure 41 as both have the same degree of defects [30%]. However, the effect of the defects in Figure 48 is twice the effect of the defects in Figure 41 as indicated earlier (137). The non-uniformity in Figure 48 is represented by peaks and valleys. Valleys forms the defects as the peaks should be in identical level due to sample polishing apart from some spikes owing to the presence of pure Fe contamination. As a result, it is possible to imagine how a charge carrier would be localised easily in any of the valleys and remain until the extended potential barrier is overcome as explained in Figure 4.

In terms of comparison, Figure 48 shows the undesired defected bulk of the TMOs, where the desired level of compactness of the bulk will be shown in section 5.12 Substrate Analysis. This is because part of the substrate showed non-defected compact bulk [glazed layer] and, hence, the comparison will be postponed until the substrate part is reached.

So far, all the cross-sectional analyses were performed in terms of EM images. However, it is always useful to make some compositional analysis. Figure 49 shows a

cross-sectional image with two boxes on the image. The top box refers to the position of the compositional analysis of the p-type TMO [Mixture of FeO and Fe_3O_4], meanwhile, the bottom box refers to the position of the compositional analysis of the n-type TMO [$NiMn_2O_4$]. This is followed by Table 15, which shows the compositional analysis of each position. The compositional analysis in Table 15 is the average of two different positions on the same sample.

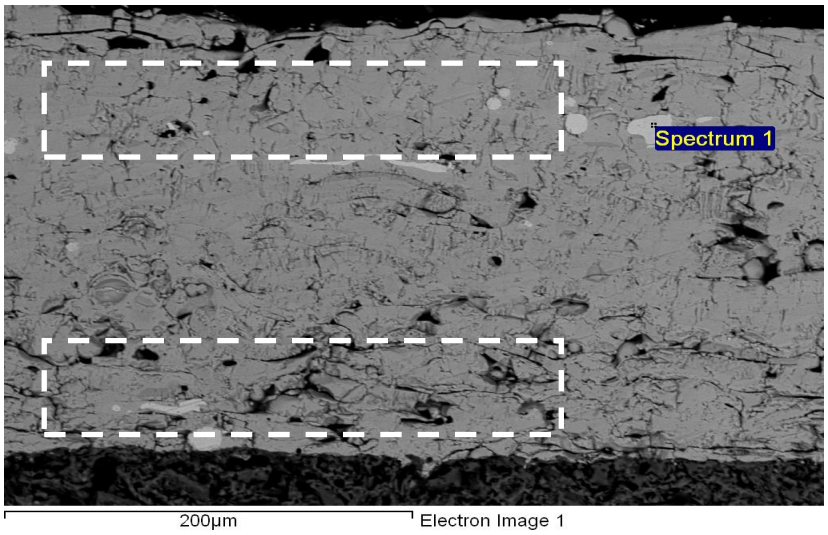

Figure 49: Compositional analysis of the cross-sectional view; the boxes show the p-type analysis position [top] and n-type analysis position [bottom]

n-type TMO [weight %]	p-type TMO [weight %]
Fe [35.17%]	Fe [51.93%]
C [23.71%]	C [23.67%]
O [23.05%]	O [24.40%]
Mn [11.77%]	--
Ni [6.30%]	--
Total [100.00%]	Total [100.00%]

Table 15: Compositional analysis of the cross-sectional image in Figure 49; top box corresponds to right column and bottom box corresponds to left column

From Figure 49 and Table 15, p-type TMO shows Fe of 51.93%. This amount includes the Fe metal contamination represented by the bright areas from Figure 46 to Figure 49. More importantly, n-type TMO should be made up of $NiMn_2O_4$ only. However, this is not the case in Table 15 [left]. Instead, there is an excess of Fe, which forms 35.17% of the sample. This confirms the idea of diffusion between layers. During the deposition of the p-type TMO, the flame melts the surface of the n-type TMO and makes it viscous, so, blasting the p-type particles on top of the n-type viscous surface then causes the p-type layer to migrate into the n-type layer. This severely eliminate the formation of the p-n hetrojunction, however, this will not stop the detector from operating, as the detector turns from a p-n hetojunction to a p-i-n hetojunction. By this means the depletion layer will widen, so more E is needed to overcome the hetrojunction with less detection sensitivity. This accounts for the relatively low signals observed in chapter 4 Initial Status of TMO Detectors. Additionally, this amount of Fe [35.17%] includes the Fe contamination (141).

Furthermore, the ratio of Ni-Mn in Table 15 [46.47%] is comparable to the ratio of Ni-Mn in Table 12 [42.18% as an average]. This is because the same n-type TMO was analysed in section 5.6 Effect of Continued Exposure to Radiation but on a different sample. Also, C cannot be evaluated in this section. As the sample is coated in C to be scanned under the EM, therefore, C shows a relatively high percentage [23.69% as an average] compared to all compositional analyses shown in the EM section so far.

Finally, it is worth mentioning that the cross-sectional analysis accounts for most of the limitations presented in chapter 4 Initial Status of TMO Detectors. The presence of defects [in all forms] contributes to the near-linearity, irreproducibility due to charge pile-up and memory effect. It is understood that the defects store charge in them, which need time to flush out. This has an effect on the noise level as well as the fluctuation represented by the SD. Also, low signal and low sensitivity due to defects are explained as the charge carriers are not free to reach the electrodes safely without scattering or recombination.

Cornell et al. demonstrated that there is an inverse relation between surface area and particle size. Consequently, Atmos is advised to deposit medium [60 µm - 50 µm] grain sizes. This will improve the packing density of the TMO layers as smaller grain sizes will splash away. On the contrary, larger grain sizes will increase the porosity of the TMO layer [see Table 8] (53).

Annealing is a very common process to eliminate defects from materials. Therefore annealing is recommended and used by many authors in literature. For Fe and Ni oxides samples, Grosvenor et al. recommended annealing the samples in vacuum at 600 ^{o}C for 30 min. Also, Y. Gong et al. strongly recommended annealing any TMO sample as it helps to avoid trapping the flow of charge carriers (12,142-144).

5.11 Cu Tape Insufficiency

The first limitation in Atmos detector design noted by the author is the electrodes. Figure 32 [right] shows clearly how the Cu tape is being applied onto an unprepared TMO surface. In addition, Figure 50 shows two cross-sectional EM images of snapped sample. This sample was not prepared following the methods explained in section 3.5.4 Sample Preparation but snapped instead. This was done to observe the features of the surface without using any destructive method of preparation [e.g. polishing].

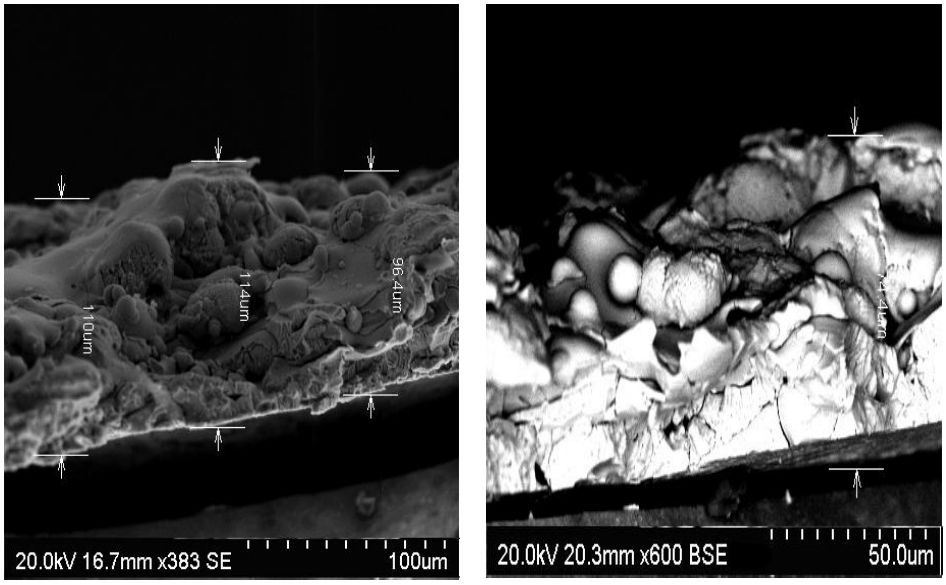

Figure 50: Cross-sectional EM images of snapped TMO samples

In applying the Cu tape onto the unprepared TMO surface, the tape will attach only to the peaks of the surface grains, leaving the rest of the surface bare without any electrodes in contact. It is possible to quantify the bare surface percentage by referring back to section 5.3 Grain Size and Nature. As the granular nature would form 67% of the surface, the valleys [bare areas] are assumed to be the rest of the surface, which is in the order of 33%.

Moreover, the adhesive glue, existing on the side, facing the TMO layer would increase the capacitance of the detector effectively. This is because the resistance is low [1 Ω] if it is measured [using an Ohmmeter] on the top Cu tape surface [glue-free]. However, the resistance increases by a factor of three if it is measured across the Cu tape i.e. one of the Ohmmeter's probe on the surface of the Cu tape and the other probe on the bottom of the Cu tape, where the glue exist.

Furthermore, Cu tape adhesive glue loses its quality by time. This is shown in Figure 51, where a gap of 342±5 μm exists between the TMO surface and the bottom of the Cu tape. This results in the storing of charge between the Cu tape and the TMO layer. Hence, reduction in reproducibility is observed in section 4.4 Reproducibility. Also, low signal is expected due to charge loss or in other words, poor CCE. On this basis, looking for another electrode deposition method is central at this point. This is because any radiation evaluation would be a misleading value as the electrodes are not optimised. New electrode deposition processes will be explained in detail later in section 6.2 Electrodes Physical Vapour Deposition and assessed in section 7.2 Radiation Tests for PVD.

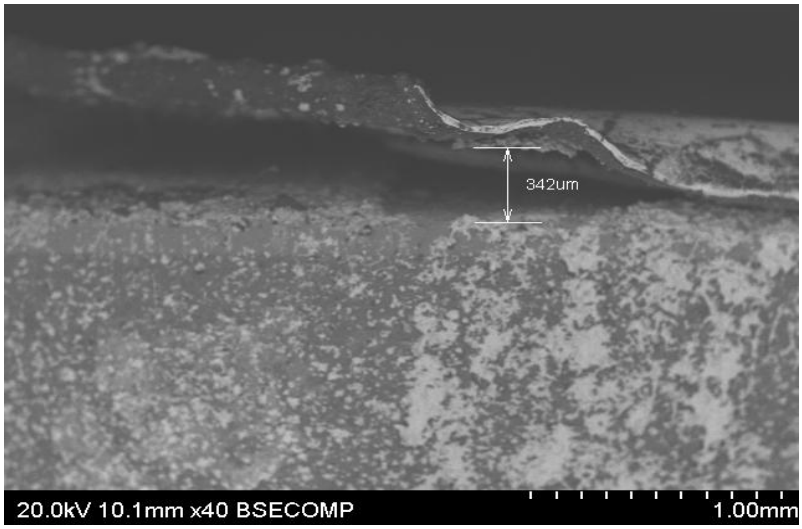

Figure 51: Loss of adhesion quality of the Cu tape

5.12 Substrate Analysis

As it was mentioned in section 1.5 Aims and Motivations, the ultimate goal of this project is to be able to accurately and reproducibly coat supervised and controlled areas with TMOs. Hence, ceramic wall tiles are used as substrates for the TMO detectors. In fact, Atmos used two types of substrates, which are ceramic tile and glazed-ceramic tile. The

glazed-ceramic tile is the ceramic tile with a thin layer of glaze on top of it. So, in order to use the most of the EM, glazed-ceramic tile is analysed in this section. NB: ceramic tile substrates are shown in section 5.10 Cross-Sectional Analysis.

Figure 52 shows a cross-sectional image of the single layered TMO sample. This sample was snapped and the TMO layer is not of concern at this stage. NB: the gap between the TMO layer and the substrate is due to snapping, which pulled the two layers [TMO and substrate] apart.

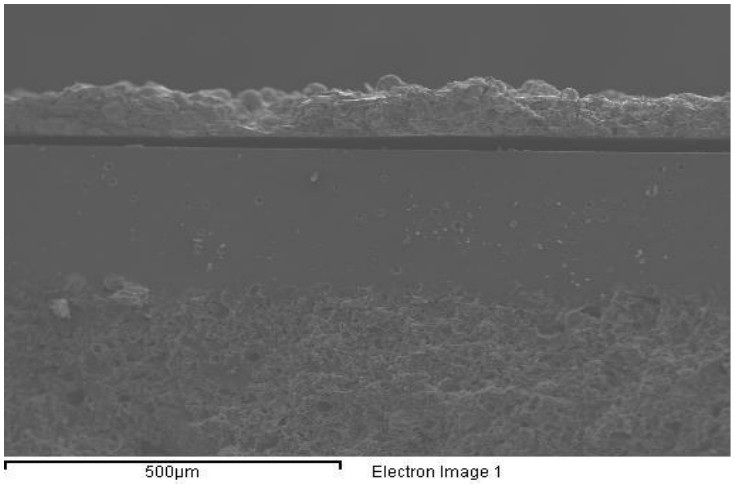

Figure 52: Cross-sectional image of a snapped single layered TMO with the substrate

From Figure 52, two different layers can be seen in the same substrate. The top layer is the glaze, while, the bottom layer is the ceramic tile. The glaze layer has the thickness of 300±5 µm and is compact compared to the ceramic tile underneath.

Now it is possible to refer back to section 5.10 Cross-Sectional Analysis. As it was promised that a desired compact layer will be analysed to be compared with the bulk of the TMO materials. The Outliers statistics are applied on the glazed layer in Figure 52 in order to estimate the defects. Figure 53 shows the threshold image, where the black dots show the defects and the white area shows the uniform bulk of the glaze layer.

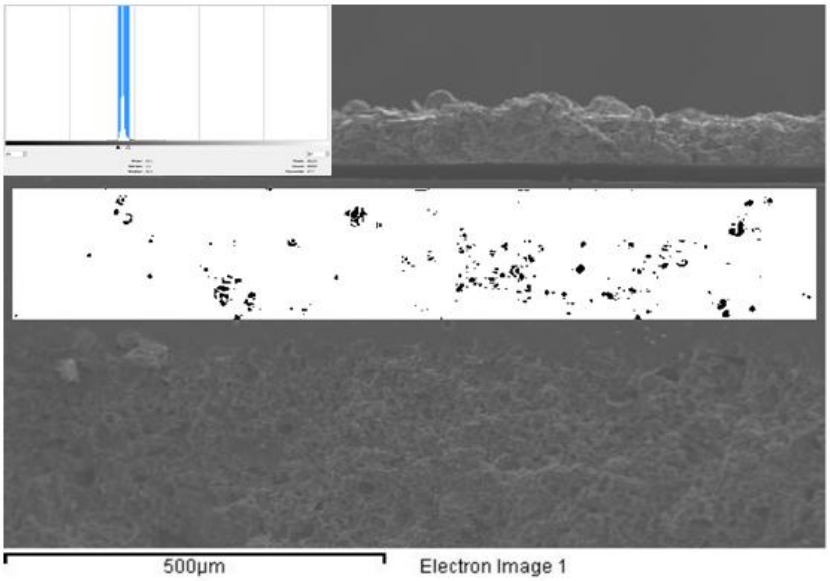

Figure 53: Threshold glaze layer; black dots are defects and histogram inset

From Figure 53, the glaze substrate showed a much lower proportion of defects when compared to Figure 47. Quantitatively, the average calculated amount of defects was found to be 2% of the ROI seen in Figure 53. This value [2%] is to be compared with the average calculated amount of defects [30%] in the ROI seen in Figure 47. In fact, the glaze layer has improved purity by 93% compared to the bulk of the flame-sprayed TMOs. Figure 54 shows the surface plot of the ROI in Figure 53.

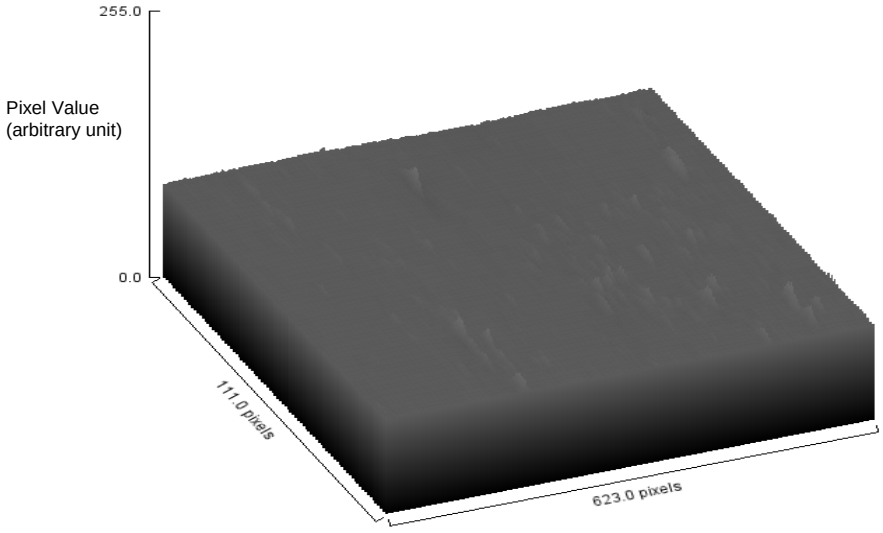

Figure 54: Surface plot of the ROI in Figure 53

Clearly, the bulk of the glaze is uniform when compared to the bulk of the TMO materials surface plot shown in Figure 48, regardless of the few peaks found in the surface plot of the glaze. These peaks are believed to be formed due to air bubbles during

the firing of the ceramic tile underneath. As the glaze layer is placed on top of the ceramic layer during firing, the glaze layer melts down on top of the ceramic layer followed by a gradual cooling process (145).

The compactness and uniformity of the glaze layer raises the need for annealing of Atmos TMOs. Annealing would allow the TMO materials to melt on top of the substrate and then all the stacking spaces, voids and cracks will be eliminated. In order to avoid the presence of any air bubbles, annealing should be performed in vacuum. In addition to placing the TMO sample on a vibrating plate to speed up the removal of any gaseous bubbles residual in the bulk of the TMO materials. The vibrator plates are used in sample preparations, when samples are embedded in resin to remove of any air bubbles presented in the resin.

Compositional analysis was performed to find out the materials making up the substrate. By this method, it is possible to look for the thermal properties of the substrate, where the need for substrate thermal properties will be explained shortly. Figure 55 highlights two positions on the substrate, where the compositional analysis took place. This is followed by Table 16, which shows average compositional analysis of the two different sites shown in Figure 55.

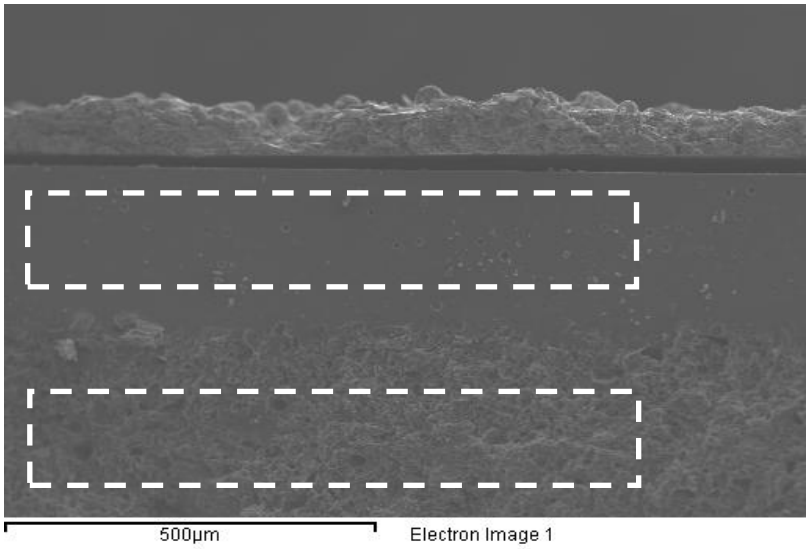

Figure 55: Cross-sectional image of a snapped single layered TMO sample; the boxes show the glaze analysis position [top] and ceramic tile analysis position [bottom]

Element	Glaze [weight %]	Ceramic tile [weight %]	Comparison [%]
O	60.77	62.57	2.88
C	16.16	16.05	-0.68
Si	11.17	11.28	0.98
Zn	4.06	--	-100
Ca	2.30	0.65	-71.74
Al	2.01	6.63	69.68
Zr	1.75	1.18	-32.57
K	1.04	0.64	-38.46
Mg	0.71	--	-100
Total	99.97	99.00	--

Table 16: Substrate different layers compositional analysis

From Table 16, and with the aid of literature as the EM is insensitive to chemical states, the glaze layer is composed principally of silica [SiO_2]. Zn, Ca, K and Mg are all metals present in the form of oxides and are called flux. Small amounts [2.30% – 0.71%] of flux are added to the SiO_2, while manufacturing [firing] to lower its high melting point [1830 ^oC] by half for ease of use. Zr oxide is also an additive [1.75%] to silica to give it its opaque character and thus, is called opacifier. Small amounts [2.01%] of Al in the glaze layer are presented in the form of alumina [Al_2O_3] for stiffness purposes. NB: C value is a misleading value as the sample was coated with C to be able to scan it under the EM (145).

The ceramic tile is made up mainly of Al_2SiO_5 [Al silicate]. Similarly, flux [Ca and K oxides] and opacifier [Zr oxide] are in use. Also, Al_2O_3 is added to stiffen the mixture. In terms of comparison, Si and O are identical in both layers [glaze and ceramic tile]. The amount of Al increased by 70% due to the presence of Al silicate and alumina, unlike the glaze, which has only small amounts [2.01%] of alumina. Flux [Ca and K only] are used in the ceramic tile in a lesser extent than the glaze layer due to the relatively lower melting point [1545 ^oC] of Al silicate compared to silica [1830 ^oC] (145).

It is therefore possible to observe the distribution of the compositions of the substrate, listed in Table 16. This is shown in Figure 56, where counts were collected over 45 min. Materials concentrated in the TMO layer only are omitted.

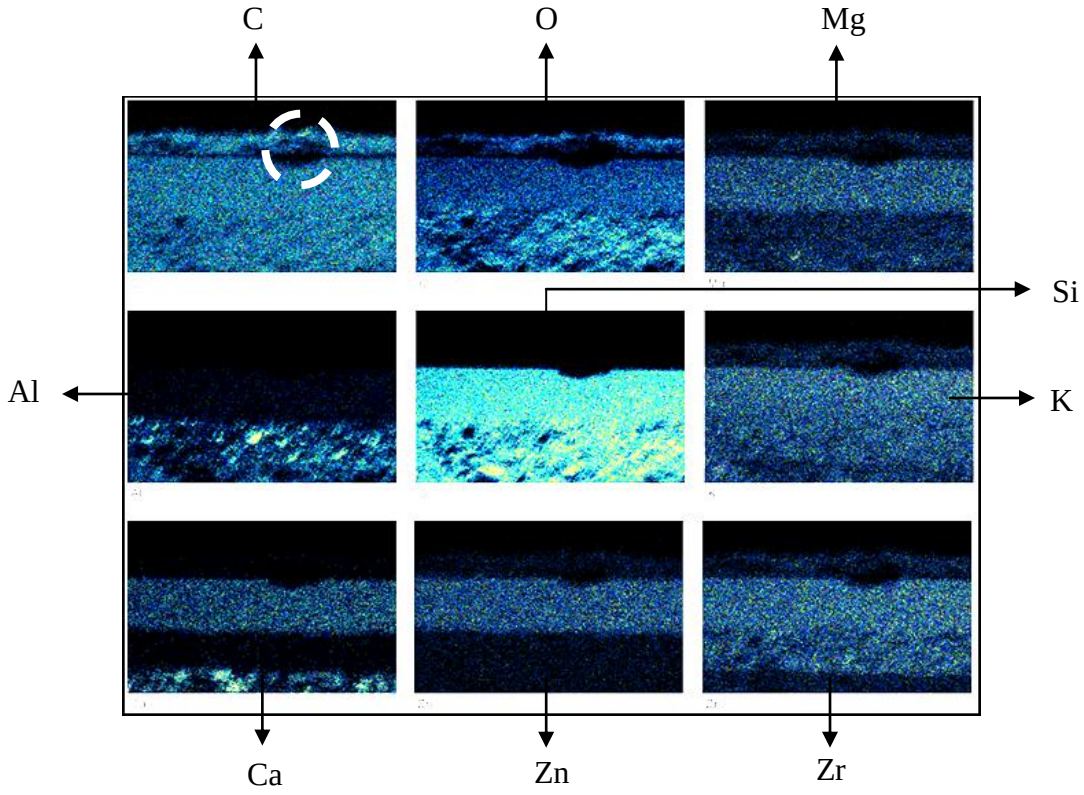

Figure 56: Elemental map distribution of the substrate; the dashed circle shows a hidden fracture in the sample

From Figure 56, Si shows the highest concentration in both, ceramic and tile. In fact, Table 16 indicates that the highest concentrations should be O then C but this is not the case as shown in Figure 56. This is expected as O and C are shared in the TMO layer as well, unlike Si, which is concentrated on the substrate only. Also, Si contributes significantly in the main composition of both, glaze [silica] and ceramic tile [Al silicate]. C is a misleading value as the amount [16.11% as an average] in Table 16 is disturbed by the C used to coat the sample. Interestingly, small concentrations of C are distributed all over the substrate in Figure 56. This is because small amounts of SiC are expected. Although TMO is not of our concern at this stage, it is important to mention the contamination of C found in Figure 56.

Apart from few dots [2.01%] of Al in the glaze layer, Al is highly concentrated in the ceramic tile owing to the Al silicate. In terms of flux materials, K, Zr, Zn and Ca are evenly distributed in the glaze layer. Moreover, the ceramic tile has no Zn [as shown in Table 16] and has evenly distributed K. Ca and Zr show unique distribution in the ceramic tile. It is found that Ca concentrates at the bottom of the ceramic tile only, whereas, Zr concentrates at the top of the ceramic tile only.

The dashed circle in Figure 56 shows a hidden fracture in the glaze layer. Fractures cause inter-layer movements, which result in cracks and the removal of the TMO layers as the TMO section on top of the fracture is highly affected by the fracture beneath it. This is clearly depicted in the C and O maps. It is essential to mention that, ideally, Mg, K, Ca, Zn and Zr should not appear on the TMO layer yet some dots can be seen on the TMOs. These are the trace elements mentioned in section 5.5 Surface Uniformity above, which prevented some of the totals in the compositional tables to be 100%.

Although the TMO detector responds correctly to radiation [see chapter 4 Initial Status of TMO Detectors], glazed-ceramic tile and ceramic tile substrates limit this response. This is owing to the incompatibility of the thermal properties of the TMO and substrate. The term TEC [thermal expansion coefficient] is simply defined as the material dimensional response to temperature change due to phonons. Our concern is basically focused on LTEC [linear thermal expansion coefficient] i.e. material expansion in two dimensions only. The LTEC increases exponentially with temperature (146).

The LTEC is raised at this point because it is believed that thermal mismatching between the substrate and the TMO is the main cause of the presence of cracks. In fact, the term thermal mismatching is a general term, which includes the LTEC. It is important to select a substrate with similar LTEC to the TMO deposited on top of it. This is because as the flame is depositing the TMO on the substrate, both of them [substrate and TMO] will expand according to their LTEC and the temperature difference between room temperature and flame temperature. More importantly, is the cooling phase process. When both materials [TMO and substrate] are exposed suddenly to room temperature, they will shrink according to their LTEC as well. Any difference in shrinking process between the TMO and the substrate would cause the formation of cracks immediately. Figure 57 [top] shows surface crack in a TMO sample. NB: this type of crack is the surface crack of the cross-sectional crack presented in Figure 45 and Figure 46. Also,

Figure 57 [bottom] shows a polished surface, where polishing unveils the cracks in the bulk of the sample. This indicates that the cracks are deep and hence, cause severe reduction in CTM as explained in section 5.10 Cross-Sectional Analysis. More EM images of cracks can be found in Appendix 9.1.6.

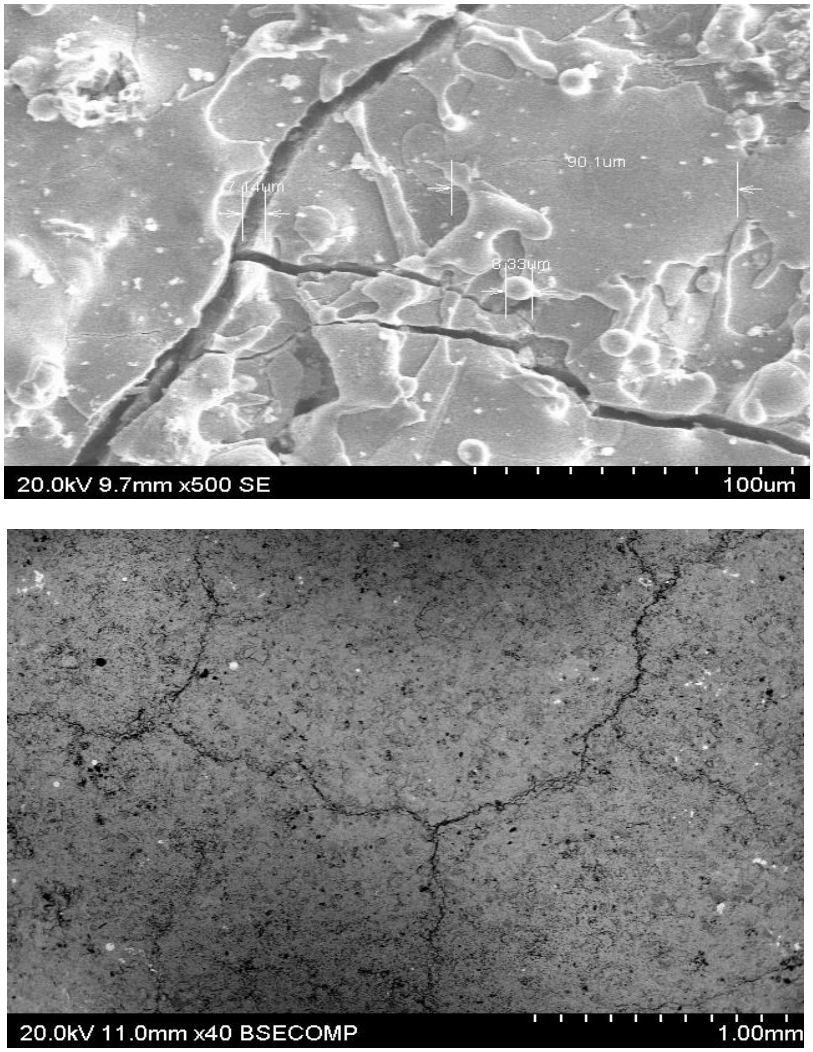

Figure 57: Surface Cracks due to thermal mismatching

The other term involved in thermal mismatching is the difference between the flame-deposited TMO temperature and room-temperature substrate. This will speed up the process of the cooling phase although it is rapid by the sudden exposure to the room temperature. In consequence, interval voids and cracks on the surface and within the bulk of the material are formed immediately. Voids and cracks will act as capacitors that store charge and cause the memory effect presented in the detectors. Therefore, heating up the substrate before depositing the material is strongly advisable. This fact is confirmed by Reichelt for Si-substrate thermal mismatching. Reichelt suggested heating up the substrate up to 900 ^{o}C for a superior Si micro-structural order (110).

For the reasons mentioned above, it is advisable to select a substrate with a close LTEC to that of the deposited TMOs. This will allow both the TMO and the substrate to shrink down in synchrony in the cooling down phase. So, no mechanical tension on the surface of the substrate or the bottom of the TMO material will be observed. Elimination of this mechanical tension will reduce the production of cracks and voids dramatically. Table 17 shows some LTEC values of some materials. NB: the lower the LTEC value, the less expansion occurs in the material per unit temperature [^{o}C].

Material	LTEC [x10^{-6}/^{o}C]	Reference
Spinel TMOs [ave. value]	9.0±0.4	(147)
Pure Si	2.63±0.04	(148)
silica	0.5	(112)
Al silicate	3.9	(149)
alumina	9	(150)

Table 17: LTEC of some materials

From Table 17, Bayer studied 24 spinel oxides, whereby 20 of them contain TMs. An average LTEC is calculated based on Bayer's results and the value of $9x10^{-6}/^{o}C$ is calculated. In order to prove this value [$9x10^{-6}/^{o}C$], a literature survey showed that Kumaravel and Lacheisserie quoted similar values for TMO spinels, such as $10x10^{-6}/^{o}C$ for $CoFe_2O_4$. For comparison purposes, Si has LTEC of $2.63x10^{-6}$. This indicates that TMOs increase by 70% more than Si per ^{o}C. This disadvantage [relative to Si] of TMOs has no influence on the performance of the TMOs once the manufacturing process is optimised in terms of TMO-substrate thermal matching (147,148,151,152).

Furthermore, the glazed-ceramic tile substrate and the ceramic tile substrate are both incompatible with the TMOs LTEC. This is because Table 17 shows that the TMOs expand by 94% per ^{o}C more than the glazed [silica]. Additionally, TMOs expand by 57% per ^{o}C more than the ceramic tile [Al silicate]. Thus, severe cracks are expected in the TMO layers. A trade off problem appears with using, either glazed-ceramic tile or

ceramic tile substrates. This is because the LTEC of the ceramic substrate is closer [57%] to the TMOs, however, the problem of porosity will have a significant effect as was explained in section 5.10 Cross-Sectional Analysis. Using the glazed-ceramic tile substrate will overcome the porosity but the high level of thermal mismatching in terms of LTEC would be the cause of cracks and voids.

Therefore, an alumina substrate is suggested. Alumina is rigid, insulator [10^{14} Ω.cm], does not absorb water and has high melting point 1890 ^{o}C. Due to these advantages, alumina is very common material in microelectronics and electronic boards. In terms of porosity, a company called Leatec Fine Ceramic Ltd., Taiwan has showed EM images of their alumina substrate products. These EM images show that the grain size of alumina substrate can be as small as 1 μm in diameter. Also, no gaps can be spotted in between the grains, which make alumina a promising non-porous substrate for Atmos TMOs. On top of that, Table 17 shows that alumina has a compatible [100%] LTEC, compared to TMOs. In accordance to the advantages of alumina substrate listed above, it is believed that cracks and voids will be significantly reduced together with the aid of annealing (153,154).

5.13 Failure of the Stacked Design

By reference back to Figure 7 in section 3.2 Detectors Manufacturing and Design, the second stacked design was studied using EM in order to assess the quality of the detector layers and contacts. The idea behind this design is to minimise the charge loss occurring due to long charge travelling distance in the first design. Also, an electrodes solution is attempted in this design, which considered flame-spraying pure Cu to act as electrodes for both, n-type and p-type TMOs (1).

In fact, all second design detectors showed no response to radiation at all. Thus, all EM tests were performed with the intention of finding out why there was no response. In the light of the EM results, it was possible to know exactly why there was no response to radiation owing to several limitations, which can be listed with relative importance from low to high as splash and contamination, poor quality of the Cu layer [porosity, oxidation and cut off], and layers diffusion. The latter forms the main issue of p-n hetrojunction elimination, which led to the failure of the second design. Hence, all listed limitations above will be analysed individually as follows.

- Contamination and Splash

The first expected limitation was mentioned in section 5.7 Contamination and Splash. Figure 37 and Figure 38 were obtained from a second design detector surface. The Cu electrode was interfering severely with the TMO [Cr_2O_3] nearby. This fact is also applied on the p-n hetrojunction surface. This is because splash is effective as the flame is on, which indicates that the splash was occurring in the inner core as well. This is confirmed in section 5.10 Cross-Sectional Analysis.

As it was mentioned in section 5.7 Contamination and Splash, Cu contamination will scatter incident radiation and, hence, reduce the sensitivity of the TMO detector. More importantly, any presence of metallic centres will act as charge scattering or absorbing [e-h recombination] media and result in an increase in the noise level due to deposition of free electrons by the metallic centres. So, R in Equation 4 will be minimised due to maximising the factor α.

In terms of first and second designs comparison, Cu electrode splash is not available in the first design due to the use of Cu tape. This will reduce the contamination by 17.04% [8.52% from each side] at the Cu-TMO interface [see Figure 38 explanation]. Moreover, p-n hetrojunction contamination is expected only in one side of the first design, where the p-n meet [see Figure 6]. This is unlike the second design, where the p-n meet along the whole TMO circle circumference [see Figure 7].

- Cu Layer Porosity and Oxidation

Another limitation can be seen in Figure 58, where the flame-sprayed Cu electrode is shown. The porosity of the flame-sprayed Cu is apparent and will affect the σ of Cu negatively. In other words, the charge collected by the electrode will suffer from loss before reaching charge collection wire. Also, this will give an indication about layers diffusion as the Cu electrode is sprayed and then the n-type TMO is sprayed on top of it. The n-type TMO will fill the holes presented in the Cu electrode surface, which will, again, affect the σ negatively as explained in section 5.3 Grain Size and Nature. NB: Appendix 9.1.7 shows additional flame-sprayed Cu electrode images.

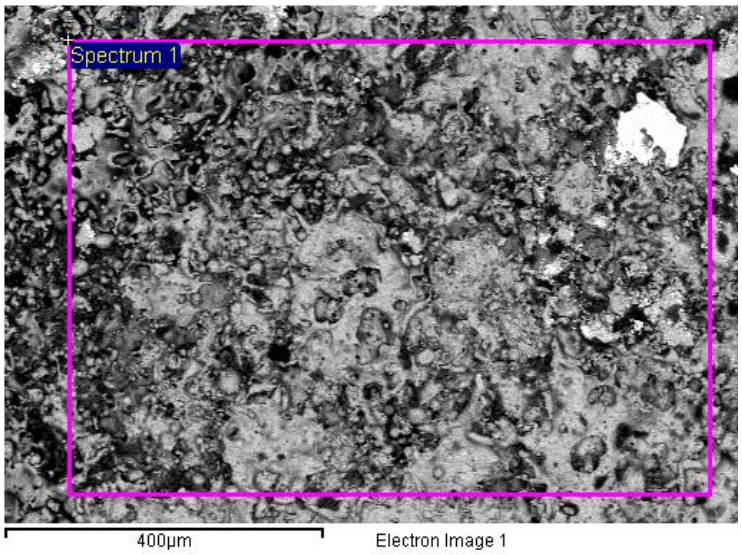

Figure 58: Porous flame-sprayed Cu electrode

Furthermore, Table 18 shows the average compositional analysis of two sites on the same sample. It is found that the flame-sprayed Cu electrode comprises only 45.21% Cu with 13.55% of O. This indicates that the flame-spraying mechanism leads the Cu to be oxidised. For reassuring purposes, the average pure Cu presented in Figure 36 together with Appendix 9.1.3 Contamination and Splash are analysed and found to be more than 70%. This means that electrodes are no longer efficient to deliver the collected charge as Cu is turned from pure metallic into p-type semiconducting material with a BG of 1.2 eV for CuO and 2.16 eV for Cu_2O (27,34,155). This is supported by Thomson et al. as he indicated that Cu can be easily oxidised at temperatures above few hundreds ^{o}C, which causes the Cu to become porous (93).

In addition, the presence of Cr [3.22%] indicates that Cu particles can find their way through the TMO layer underneath [layers diffusion]. Thus, Cr_2O_3 can be found on the surface of the Cu electrode as the Cu electrode depicted in Figure 58 is a p-type TMO [Cr_2O_3] Cu electrode. Moreover, severe [36.93%] C contamination is found to be caused by the nozzle.

Element	Weight %
Cu	45.21
C	36.93
O	13.55
Cr	3.22
Total	98.91

Table 18: Compositional analysis of the flame-sprayed Cu electrode

- Cu Layer Cut Off [cross-sectional analysis]

Thus far, the above analyses of the second design were on the surface of the sample. Cross-sectional analyses would prove useful at this stage to assess the internal structure of the second design sample. Therefore, some of the second design detectors are snapped to view the inner structure without preparing the sample to avoid any disturbance to the inner structure.

In Figure 59, the snapped sample with top electrode, TMOs [p-type then n-type], bottom electrode and finally, the substrate are shown. The electrodes have an average thickness of 15 μm each, meanwhile, the TMO layers have a thickness of 112 μm all together [p-type and n-type]. Note that, the black film layer on the top electrode is the soldering flux. This is because charge collection wire has to be soldered on the top electrode in this design.

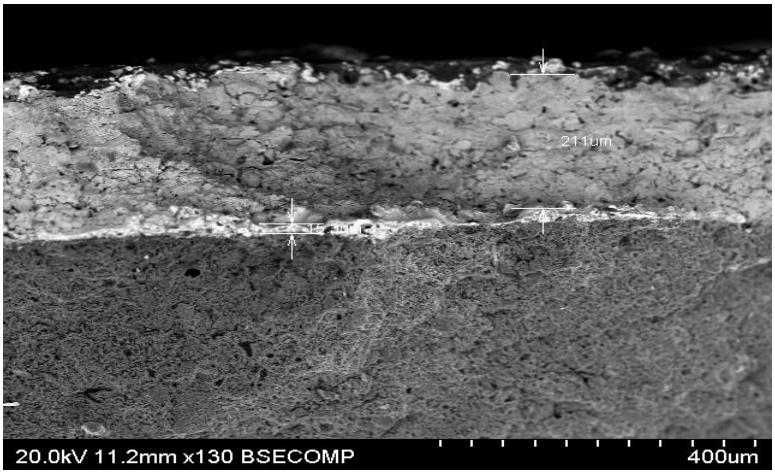

Figure 59: Cross-sectional view of a snapped second design TMO detector

Figure 60 shows a cross-sectional image focused on the lower electrode, which is sandwiched between the upper TMO layer and lower ceramic tile substrate. Clear discontinuation in the flame-sprayed Cu electrode would lead to cut off the flow of charge collected from the TMO. By this means, no response is expected from the stacked design detectors as the generated charge cannot reach the pico-ammeter to be read. A close up EM image would be useful to confirm the phenomena of electrode Cut off, which is apparent in Figure 60 where the circle shows where the cut off of the flame-sprayed Cu electrode is taking place.

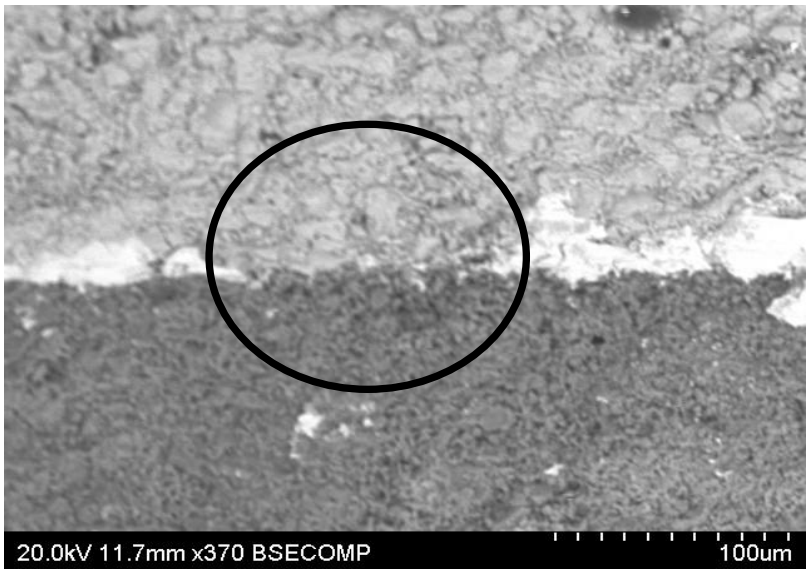

Figure 60: Flame-sprayed Cu electrode cut off

- Layers Diffusion [cross-sectional analysis]

Additionally, Figure 60 shows bright dots in the porous ceramic tile substrate. This confirms the idea of layers diffusion as firing Cu particles onto the porous substrate will force the substrate to act as sponge and absorb the molten Cu particles before they [Cu particles] cool down to solid state. This layer diffusion is also expected between electrodes and TMOs layers. If diffusion between layers is confirmed, the non-responding of the second design TMO detectors will not be surprising.

Figure 61 shows the confirmation of diffusion between layers in the second stacked TMO detector. The bulk of the TMO is interspersed by bright Cu areas. These bright areas are distributed all over the sample, confirming the migration of the flame-sprayed Cu electrode into the TMO layer underneath.

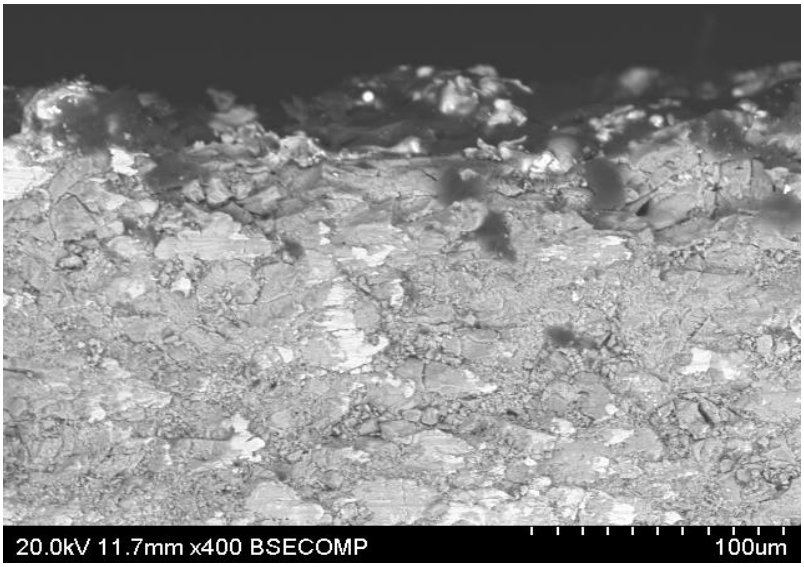

Figure 61: Top Cu electrode layer diffusion into the TMO layer underneath

In addition, Figure 62 shows the final confirmation of layers migration, where the flow of the molten Cu can be tracked in the bulk of the TMO layer. This shows that molten flame-sprayed Cu can drill through 100 µm thick TMO and reach the Cu electrode on the other side. Hence, the hetrojunction is completely omitted and the detector cannot be effective any longer. Also, Cu electrode diffusion in the substrate is clear [bright area].

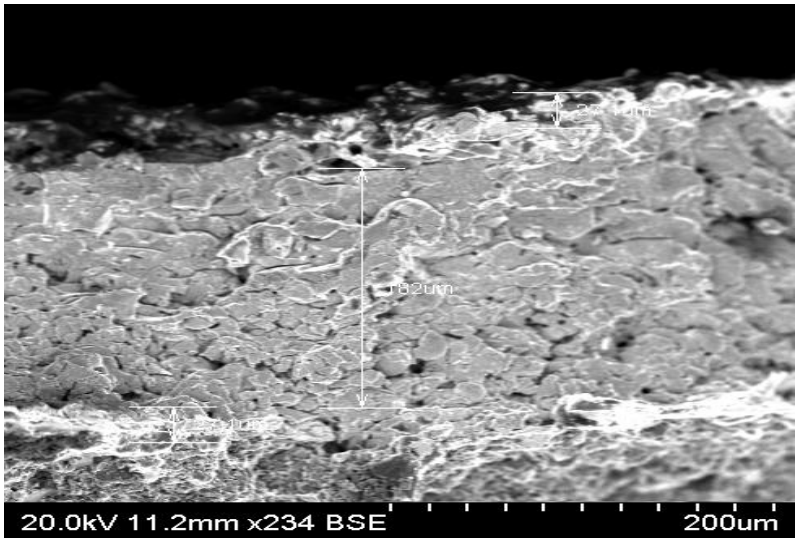

Figure 62: Different layers diffusion in the second design TMO detectors; flux, p-type electrode, p-type TMO, n-type TMO, n-type electrode and substrate in the descending order

So, in order to distinguish between the molten Cu and the TMO layers, the Outliers statistics are positioned on an ROI on Figure 62 [only UOF as the bright areas are only of interest]. An ROI is chosen to avoid measuring rulers interspersed within the

image. As was mentioned above, the molten Cu can fill the gaps between the TMO layers, until both electrodes [upper p-type and lower n-type electrodes] come in contact. On top of that, the lower n-type Cu electrode diffuses in the porous substrate underneath. This is represented by the lower part of the ROI in Figure 63. Note that, black areas represent the molten Cu between the TMO layers. It is found that in the ROI in Figure 63, the molten Cu forms 18% of the ROI corresponding materials.

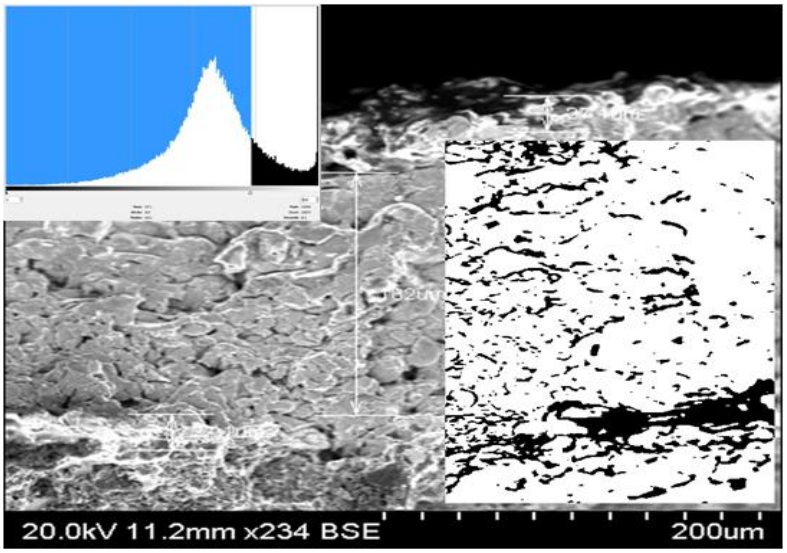

Figure 63: ROI on layers diffusion in Figure 62 with histogram inset; black areas are molten Cu electrodes

- Additional Limitations

Finally, in terms of assessing the design itself, the second design might suffer from insensitivity factors. It is noticeable from Figure 64 that the top of the detector, including Cu electrode, soldering blob and charge collection wire will scatter radiation before reaching the TMO layers.

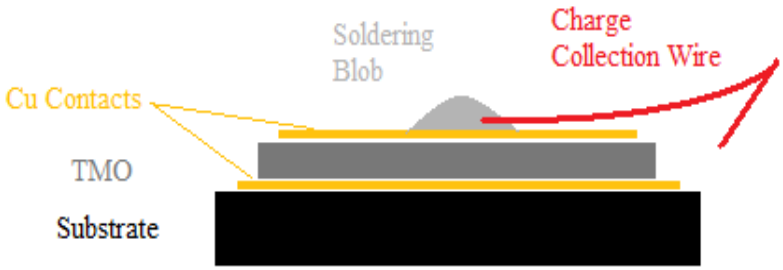

Figure 64: Second design insensitivity factors

After all the limitations listed above, it is not surprising that the second design did not respond to radiation. This is mainly due to layers migration, absence of hetrojunction, ceramic tile porosity and insensitivity factors. Thus, new electrode deposition and detector design will be given later.

5.14 Summary

EM images have given us a significant insight into the current shortcomings of these early prototypes and enabled us to refine the production process, as well as providing details of the elemental composition of the detectors on the micro-scale. Further work based on these results was carried out to improve Atmos manufacturing technique with the aim of producing sensitive, fully functioning, reliable consumer acceptable detector modules (1,2).

Table 19 gives a comprehensive summary of the findings of all tests performed together with recommendations in accordance to these findings. However, it is essential to emphasise that the variation differs from the amount presented in the sample. Variations may show relatively large percentage, meanwhile, the actual amount of the material is relatively small. Moreover, the acceptable maximum variation is set to 6.51%. Both aspects [amount and maximum acceptable variations] were explained in section 5.5 Surface Uniformity.

EM test	EM analyses	Recom-mendations	EM tests	EM analyses	Recom-mendations
Average grain size and nature	67% surface granularity	Gradual cooling and surface preparation	**Surface and bulk comparison**	94% of surface improvement by polishing and 30% of bulk defects	Surface preparation and annealing
Compositional analysis	Overall uniformity, non-hygroscopicity and flame-spray increases pre-oxidation by 2/3	--	**Cross-sectional analysis**	Interfaces elimination, layers diffusion and 30% of defects	Surface preparation and annealing
Surface uniformity	Surface uniformity [3.56%] and reproducible oxidation [3.49%]	Surface preparation	**Cu tape insufficiency**	33% of bare TMO and capacitance	PVD
Effect of continued X to radiation	No significant effect observed	--	**Substrate analysis**	Compact glaze silica, porous ceramic Al silicate and thermal mismatching	Alumina substrate and TMO-substrate thermal matching
Contamination and splash	Pure metallic contamination and splash at interfaces [8.52%]	Nozzle cleaning, flame masking and surface preparation	**Failure of stacked design**	Severe layers migration [18%] and porous Cu oxide electrodes	PVD and new design

Table 19: Summary of the EM analysis

Finally, EM analysis has clarified the failure of the second stacked design. The main reason for non-responding was layers diffusion. This is because when the molten top Cu electrode was deposited onto the pre-deposited porous TMO layers, Cu was diffusing through the TMO layers to reach the bottom electrodes [see Figure 63]. This would indicate the elimination of the p-n hetrojunction. Other reasons contributed to the failure of the stacked design, such as flame-sprayed Cu electrode oxidation and cut off. These reasons made the second stacked design not suitable for radiation test, although it is the preferred design for radiation monitors as explained in 1.2 Desirable Detector Specifications.

Chapter 6

6 Developments of TMO Detectors

6.1 Introduction

Following on from the results presented in the previous section, the application of some of the suggested developments to optimise the prototype TMO detectors are presented. Cu tape electrodes are the first source of detector limitation and hence, it will be analysed first. Improvements in the electrodes should improve the reproducibility, sensitivity and stability of the detectors drastically.

Moreover, surface preparation would contribute to offer the defined p-n hetrojunction. It is believed that this would improve the net signal magnitude owing to p-n hetrojunction contamination and elimination.

6.2 Electrodes Physical Vapour Deposition

In order to build a practical radiation detector, means must be provided to collect charge generated by incident radiation. By referencing back to section 3.2 Detectors Manufacturing and Design, the conventional design of the TMO detectors involves the implementation of Cu tape as electrodes. This electrode structure needs to be improved as was explained in section 5.11 Cu Tape Insufficiency (13).

Therefore, the PVD process is considered as a form of further development of the electrode structure for the TMO detectors, as many authors suggested the use of PVD of electrodes in different radiation fields. Kronawitter et al. used the PVD process to deposit Iron oxide electrodes for solar water splitting cells. Also, Rider et al. relied on PVD ITO electrodes on polymer solar cells. In terms of CMOS, Schaeffer et al. and Edge et al. used the PVD process in depositing metal and metal oxide gates electrodes, respectively. In addition, Schieber et al. used the PVD to deposit the semiconductor [HgI_2] and its electrodes [ITO and Au] on a glass substrate. All the authors listed above have proved the validity of the PVD electrodes, by testing the PVD electrodes under the EM, where EM

images showed acceptable level of compactness for CT and stability. This is together with testing the PVD ohmic electrodes with x-ray, which showed linear relation with x-ray tube current, using HgI_2 semiconductor detector. The steps followed to deposit the electrodes, using the PVD process can be found in section 3.6 Physical Vapour Deposition (16,156-159).

As it was mentioned in section 3.6 Physical Vapour Deposition, the conventional electrodes need to be improved in terms of deposition and material selection. Although Cu has the highest σ [$5.88x10^7$ $\Omega^{-1}m^{-1}$] after Ag, it is still not the best to be used on both TMO types. This will be accounted for after inspecting Table 20. NB: the material selection will be focused on the combination of n-type and p-type used in the radiation measurements. This combination involves $NiMn_2O_4$ as n-type TMO and Cr_2O_3 as p-type TMO only.

	Cr_2O_3 [p-type TMO]	**References**	**$NiMn_2O_4$ [n-type TMO]**	**References**
EA [eV]	1.3	(160,161)	4.2	(162)
BG [eV]	3.7	(60)	Not needed at this stage	--

Table 20: TMOs BG and EA

From Table 20, Cr_2O_3 EA [1.3 eV] is an average value of Chromium oxides EA's from references (160) and (161). This indicates that the φ of Cr_2O_3 should be in the order of 5 eV [sum of EA and BG]. Wilde et al. quoted a φ for Cr_2O_3 as 4.8±0.2 eV, which makes our approximation [5 eV] valid as it falls within the SD [±0.2 eV] (163). The value 4.2 eV for $NiMn_2O_4$ is the average value of typical spinel TM manganites [Mn oxides], where, 4.2 eV is a typical value for AMn_2O_4, where A = first-row TM. It is worth saying that many approximations, using results in literature are applied to find out the suitable electrode materials. This is because it is not possible to find the exact physical properties of TMOs in literature identical to Atmos TMOs (162).

By reference back to section 3.6 Physical Vapour Deposition, it is possible to say that in order to obtain ohmic electrodes with the p-type Cr_2O_3, the metal in contact φ

should have the value of 5 eV. On the other hand, a metal with 4.2 eV of φ can form ohmic contacts with the n-type $NiMn_2O_4$.

In consequence, an Al electrode is selected for the n-type $NiMn_2O_4$ and an Ag electrode for the p-type Cr_2O_3. These materials [Al and Ag] are selected due to their availability onsite and low cost. This is because a priority for this project is to maintain low cost throughout the production process. On top of that, they [Al and Ag] show compatible physical properties as n-type and p-type TMOs electrodes, respectively as depicted in Table 21.

	Al [n-type electrode]	**Ag [p-type electrode]**
φ [eV]	4.06	4.74
σ [$\Omega^{-1}.m^{-1}$]	$3.7x10^7$	$6.2x10^7$

Table 21: Electrode materials, φ and σ **(2,7,164)**

Although the φ's showed in Table 21 have a slight discrepancy from the required φ's based on Table 20, this discrepancy falls within the acceptable level. According to Yang et al., as long as the contact potential has the value of 0.51 eV or less, the corresponding electrode can be considered as ohmic or very low contact potential. From Table 20 and Table 21, the values of the contact potentials $|\varphi_{metal} - \varphi_{TMO}|$ can be calculated as 0.26 eV and 0.14 eV for p-type and n-type TMOs, respectively (113). Therefore, if funding was not problematic, Au would form compatible p-type electrode with φ of 5.1 eV (165) and ITO would act as n-type electrode with φ equals to 4.3 eV (166). These would produce a contact potential as low as 0.10 eV in both n-type and p-type TMOs.

By this method, PVD ohmic electrodes are believed to correct the irreproducibility showed in section 4.4 Reproducibility. So, no Cu tape capacitance [see section 5.11 Cu Tape Insufficiency] or rectification is expected. On top of that, a higher signal magnitude is anticipated as improved CCE is expected. NB: CCE will be addressed later in section 7.4 Efficiency. Also, improved sensitivity and less fluctuation [smaller SD] are also

expected. Finally, the same Cr_2O_3-$NiMn_2O_4$ detector [TMOD1] was tested in chapter 4 Initial Status of TMO Detectors will be fully assessed and compared in chapter 7 Current Status of TMO Detectors, where the expected improvements, listed above, are fulfilled.

6.3 Surface Preparation

6.3.1 Mechanical Polishing

As a form of surface preparation improvement, mechanical polishing is recommended at this stage, as this process is simple, cheap and effective [see section 5.8 Surface and Bulk Comparison]. As it was explained in section 3.5.4 Sample Preparation, the key factor in mechanical polishing is material Mohs hardness. SiC [9.2 (102)] and Al_2O_3 [9 (103)] have higher Mohs hardness compared to the TMOs Mohs values, which range from 5.5 for Fe_3O_4 (167) and $FeCr_2O_4$ (168) to 7 for Cr_2O_3 (31). Moreover, since polishing covered the substrates as well, the Mohs hardness can be quoted for SiO_2 and Al silicate as 7.5 and 5.5, respectively (11). These Mohs values indicate that SiC and Al_2O_3 are able to polish the TMO and substrate efficiently.

In terms of literature, Mott suggested polishing the surface of the TMOs in order to obtain better interfaces between different layers (12). Mechanical polishing, using SiC abrasive paper was also strongly recommended by Wagner et al. for sample surface preparations (116). More recent work performed by Grim suggested mechanical polishing for the SiC material itself. However, the SiC material this time will be treated as semiconductor, as SiC can be applied as a wide BG [2.7 eV] (169) LED (102). SiC polishing can be achieved by using Diamond polisher due to its high Mohs hardness [9.2] (102). In this work, Grim evaluated the mechanical polishing process and found it to cause subsurface damage to the SiC samples in the order of 50 nm of surface dislocation depth (170). At this stage, this relatively small level of surface damage is accepted as the TMO samples suffer from high level of voids and cracks [30%], which can be in depth identical to a single TMO layer [100±5 μm] [see section 5.10 Cross-Sectional Analysis].

From section 5.8 Surface and Bulk Comparison, mechanical polishing is found to reduce surface granularity by 94%. This is seen in the analysis as the average surface granularity after polishing is reduced to be 4%. In addition, a cross-sectional EM image would be very useful at this stage to enable the relatively low level of granularity [4%] to

be inspected clearly. This can be seen in Figure 65. NB: this cross-sectional image is of the same n-type $FeCrAlO_4$ sample shown in Figure 39.

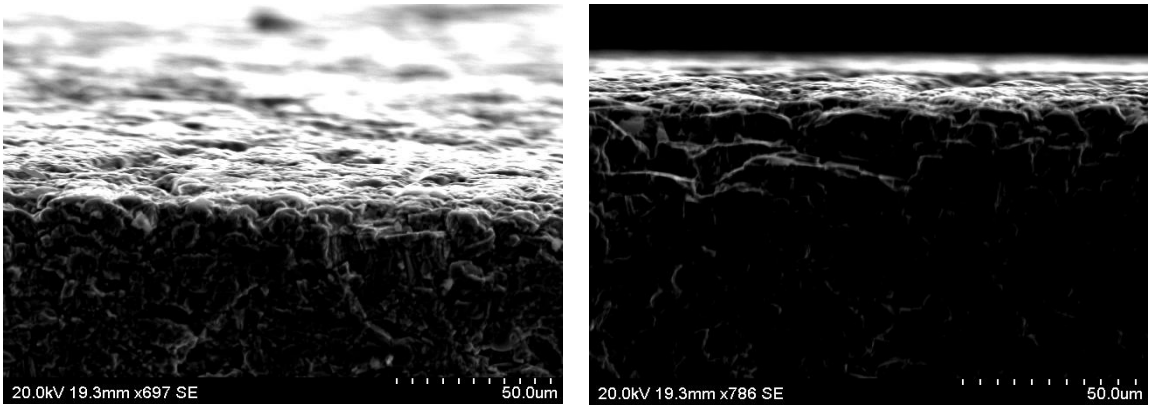

Figure 65: Cross-sectional image of the polished surface in Figure 39 **(2)**

From Figure 65, no surface grains can be spotted. However, valleys are still available as they form the defects, explained in section 5.8 Surface and Bulk Comparison. These defects have an average proportion of 30%. So, from the expectation mentioned in chapter 4 Initial Status of TMO Detectors, preparing the surface of the TMO after each deposition would have the effect of increasing the relatively low signal [pA]. This is together with correcting the near-linearity of the TMO response with photon fluence rate and kV. This is due to the defined hetrojunction formed at p-n contact.

It is also important to confirm that mechanical polishing is not capable of omitting voids, cracks and bulk contamination. This was fully addressed in sections 5.7 Contamination and Splash, 5.8 Surface and Bulk Comparison and 5.12 Substrate Analysis. Thus, annealing, nozzle cleaning and masking are still strongly recommended.

A linearity radiation test was performed on a TMO detector, manufactured by Atmos for solar cell applications. In this detector, mechanical polishing took place after each TMO deposition, and the substrate was compact glass. Hence, neither layers diffusion nor un-defined p-n hetrojunction was expected in this particular detector, although cracks and voids could still be present in the detector due to LTEC mismatching. Thus, Table 22 shows the response of the polished TMO detector at 50 kV, and for two photon fluence rates and at two time intervals [0 h and 2 h] in the setup explained in 3.4.2 System Setup and Measurements Protocols.

Photon fluence rate [p/m^2/sec]	Net signal at 0 h (nA)	Net signal after 2 h (nA)
7.965 x 10^{12}	6±2	6±2
1.625 x 10^{13}	33±5	33±5

Table 22: Net signal magnitude of polished TMO detector at 50 kV

From Table 22, the detector saturates at photon fluence rates above 1.625x10^{13} m^{-2}.sec^{-1} as it was made for solar cell applications mainly, thus, it was omitted from Table 22. Therefore, measurements were performed at two photon fluence rates [7.965 x10^{12} m^{-2}.sec^{-1} and 1.625x10^{13} m^{-2}.sec^{-1}].

More importantly, the magnitude of the signal is in the order of nA's, compared to the signal in chapter 4 Initial Status of TMO Detectors, which was in the order of pA's. This jump in signal magnitude can be referred to the defined p-n hetrojunction mainly. This is because no contamination at the hetrojunction would lead to e-h recombination. Furthermore, polishing is capable of omitting C contamination efficiently from the surfaces and hetrojunctions. Hence, this jump in signal is comparable to signal magnitude obtained by the IC, which was also in the order of nA. By this method, full agreement with the comparisons made by Martin, can be confirmed, who demonstrated comparable IC responses to Si photodiodes as was mentioned in section 4.5 Signal Stability (136).

It is essential to mention that the electrodes used in this detector were PVD Cu electrodes and part of the net signal magnitude increment can be referred to the PVD. However, this contribution is relatively small compared to the total net signal increment due to polishing. Also, the high level of reproducibility [1.3% as an average for 0 h and 2 h response and not quoted in Table 22] is principally due to the PVD electrodes. These features [relatively high net signal and high level of reproducibility] will be clarified later when the PVD electrodes are fully assessed in section 7.2 Radiation Tests for PVD. Finally, polishing the surface cleans the surface from contamination, so no surface scattering or e-h recombination is presented. Hence, superior sensitivity is expected.

6.3.2 Argon Ions Sputtering

Ar ion sputtering is suggested as another form of surface preparation mechanism. Sputtering is one of the most common techniques used for surface preparation. This is because sputtering will remove only hundreds of A^0's without causing any damage to the surface. The importance of surface preparation in XPS is to avoid the shadowing effect, which will lead to missing peaks in the spectra (171). In semiconductors, sputtering is important to remove surface contamination and loosely bound species [e.g. water molecules] (26). On top of that, similar advantages to mechanical polishing are expected with sputtering, including obtaining defined p-n hetrojunction for relatively low signal increment (85). Therefore, Ar ion sputtering is recommended for surface preparation by many authors in literature (26,85,116,124,142). Sputtering is evaluated by XPS, where both [XPS and sputtering] processes can be found in 3.7.1 X-ray Photoemission Spectroscopy above.

Thus, Figure 66 below shows two XPS spectra of the same p-type $FeCr_2O_4$ sample surface. The curve with cross points is an XPS spectrum of the unprepared surface. On the other hand, the curve with circle points represents the XPS spectrum of the prepared surface. The preparation performed by 15 min of sputtering. Additionally, every peak is labelled by its corresponding compositional element according to the BE, based on references (116,121).

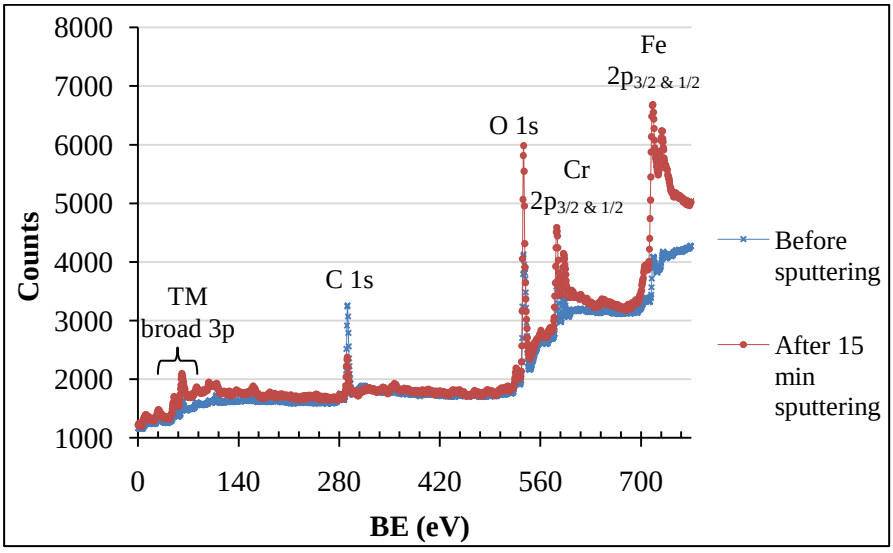

Figure 66: $FeCr_2O_4$ XPS spectra before sputtering [cross points] and after 15 min of sputtering [circle points]

In order to analyse the spectra in Figure 66, each peak was extracted and analysed independently from the rest of the spectra (116). After that, linear background subtraction (116,117,171) and Gaussian fitting (26,120,123-125,171) were applied. Note that, all analysed XPS peaks can be found in Appendix 9.2 X-ray Photoemission Spectroscopy for both, sputtered and un-sputtered surfaces.

In addition, Table 23 shows a summary and comparison of the unprepared [before sputtering] and prepared [after sputtering] XPS spectra. For simplicity, 'position' indicates the average of the sputtered and un-sputtered spectra as the position should be constant. 'Orb' indicates orbital, 'refe' indicates references, 'net int.' indicates peak intensity without background and 'Int. Com.' indicates intensity comparison.

Element	Position ± 3 [eV]	Orb	Refe	Net int. [un-sputtered]	χ^2 [un-sputtered]	Net int. [sputtered]	χ^2 [sputtered]	Int. Com. [%]
C	**291**	**1s**	(116, 121)	**1448**	**0.96**	**590**	**0.99**	**60**
O	**537**	**1s**	(26,116,118,119,121,122,143,171)	**2190**	**0.95**	**3461**	**0.94**	**37**
Cr	**583**	**$2p_{3/2}$**	(26,116,118,121)	**808**	**0.99**	**1421**	**0.99**	**43**
	593	**$2p_{1/2}$**	(26,116,118,121)	**399**	**0.98**	**682**	**0.98**	**41**
Fe	**716**	**$2p_{3/2}$**	(26,116,118,121)	**548**	**0.95**	**2032**	**0.97**	**73**
	729	**$2p_{1/2}$**	(26,116,118,121)	**195**	**0.98**	**687**	**0.99**	**72**

Table 23: Summary, and comparison of un-sputtered and 15 min sputtered XPS spectra from Figure 66

Looking at the values for C in Table 23, as was discussed in section 5.8 Surface and Bulk Comparison, the surface suffer from severe C contamination compared to the bulk of the material. The XPS technique showed a reduction in C of 60% in the bulk of the material, compared to the surface of the material. This value [60%] can be linked

directly to the EM value in Table 13, which showed the variation of 71.02% between bulk and surface C contents. Despite the discrepancy between the EM value [71.02%] and the XPS value [60%], both values are relatively high, compared to the baseline sat in section 5.5 Surface Uniformity, which is in the order of 6.51%. Also, a discrepancy in C contents is expected as C contamination is not uniform across all samples as it was pointed out in Table 11.

Furthermore, by referencing back to section 5.8 Surface and Bulk Comparison, C surface contamination was suspected to be in one of the forms CO, CO_2 or CO_3 according to Schulz. Using the XPS spectra, it was possible to confirm the contamination was due to CO_2 as expected, due to the waste product of the flame-spray mechanism [see section 3.1 Atmos Technologies Ltd.]. This is because NIST database confirms that C 1s 291±3 eV belongs to the compound CO_2. This is an important fact as it will be used in section 7.3 Attenuation Coefficient for μ corrections (121,139).

Interestingly, Table 23 shows an increment in bulk O by 37% compared to the surface O. This confirms the non-oxidisation of the surface. On the contrary, this value [37%] contradicts with the relatively low O variation between surface and bulk found by the EM, which was as low as 0.55% in Table 13. The reason for this fact is surface O loss. This is because the samples were examined by the EM within a few weeks of manufacturing, whereas, the XPS tests took place two years after the EM tests. So, according to Henrich, TMOs are likely to lose surface O as a function of time at room temperature (172). This is expanded on by Kung as he indicated the presence of incomplete TM-O bonds in the surface. This will lead surface TMs with incomplete TM-O bonds to migrate to the bulk of the material and hence, O is lost from the surface with time. This process can be halted by annealing, as annealing causes the re-oxidation of the surface and hence, no O loss would be expected owing to incomplete TM-O bonds (173).

Additionally, it is possible to calculate the global average difference between the bulk and the surface according to the XPS results. The global difference refers to the average percentage, including the contamination. Consequently, the average global difference can be assigned for surface and bulk comparison, using the XPS as 54% from Table 23, which can be compared directly to the result obtained by the EM in Table 13. However, it is important to include the contamination at this stage, in contrast to Table 13, where the contamination was excluded in order to assess the ideal flame-spray process. Hence, 31.5% of global average variation can be calculated from Table 13.

However, this discrepancy between XPS [54%] and EM [31.5%] is expected. This is owing to the O loss occurred in the XPS sample, which has a difference of 60% compared to the EM difference [0.55%]. Also, C contamination is not uniform as it was previously mentioned. Therefore, correcting for the O loss and the C contamination non-uniformity, the variation between surface and bulk EM analysis will be increased to 57%, which is in good agreement with the XPS at 54%.

From Table 23, Cr and Fe have relatively high variations between surface and bulk. The reason for this is missing Fe peaks and low Cr peaks intensities in Figure 66. Negri et al. accounted for these missing peaks as a shadowing result of the unprepared surface. This will clarify the behaviour of charge carriers at the hetrojunction. The shadowing effect means some electrons suffer more interactions than others. As a result, the rate of charge carriers crossing the p-n hetrojunction will not be constant, which will lead to e-h recombination at the hetrojunction. Hence, relatively low signal was seen (171).

Furthermore, Table 23 shows the χ^2 fitting, which represents the quality of the fitting. χ^2 values in Table 23 are in good agreement with Yamashita fittings, which are in the order of 0.96 on Iron oxide samples (26). Also, the E resolution [FWHM] of the Gaussian fit in Appendix 9.2 X-ray Photoemission Spectroscopy is in the average of 4 eV. This E resolution varies slightly from Grosvenor et al, who have the resolution of 3.2 eV on Ni oxides samples (142). This variation is mainly due to sample preparation as Atmos samples were not manufactured for XPS analysis primarily.

Finally, the group of small peaks at the low BE region represents the TMs [Fe and Cr] 3p orbitals. 3p orbital peaks are not common to be used as they are broad. Also, they are used as a single peak due to the inability to distinguish between the spin doublets, unlike 2p orbitals. Thus, 3p orbitals are avoided, especially in first-row TMOs as they are mainly used for material identification, which is not the case here (26,118,120,171).

From all the XPS analysis mentioned above, 15 min of sputtering has a comparable effect to the mechanical polishing. This is in terms of defined p-n hetrojunctions, relatively higher signal and surface contamination elimination. So, sputtering the surface would result in the same relatively high signal, as shown in Table 22.

To conclude that 15 min of sputtering at 500 kV is sufficient, an additional sputtering was performed on the same sputtered surface shown in Figure 66 for another 15 min, giving 30 min of sputtering in total. Identical XPS curves were obtained, with an average variation of only 2%. This can prove inner layers uniformity as depicted in Figure 67.

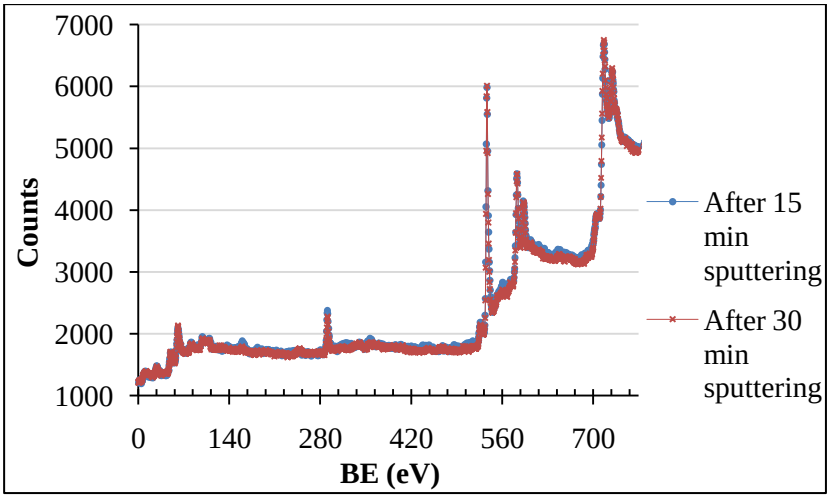

Figure 67: 15 min sputtering XPS [circle points] and 30 min sputtering XPS [cross points]

In terms of mechanical polishing and sputtering comparison, mechanical polishing is cheaper and faster method. However, sputtering is a much cleaner process as it does not involve lubricants, such as water and solutions. Ideally, both techniques ought to be used as the mechanical polishing will provide a faster and cheaper process. A few min of sputtering should be conducted which would clean the surface from any loosely bound species and water molecules (174).

6.4 Summary

The PVD process was used to deposit electrodes on both sides [n-type and p-type] of the TMO detectors. Certain electrode materials of Al and Ag were applied as they form ohmic electrodes to the $NiMn_2O_4$-Cr_2O_3 TMO detectors. Reproducibility, sensitivity and CCE are expected to be improved as it will be seen later in chapter 7 Current Status of TMO Detectors.

Both surface preparation techniques [polishing and sputtering] showed reliable degree of detector performance improvement. Net signal increased dramatically from pA's to nA's after mechanical polishing of every single flame-sprayed deposited layer. This degree of improvement is expected from sputtering as well.

Moreover, O loss as a function of time was observed together with C contamination. Both limitations can be omitted by polishing or sputtering. Additionally, inner layers uniformity was deduced by XPS spectra and found to vary by 2% as an average. Thus, both techniques are ought to be used as suggested by Zangwill (174). However, in the current time frame and cost, mechanical polishing is recommended as it is efficient to eliminate surface C contamination and produce improved signal magnitude due to defined boundaries between different layers.

Finally, annealing is strongly advisable for TMOs preservation. This would increase the feasibility of the TMO detectors in the long-term basis as stated by Kung (173).

Chapter 7

7 Current Status of TMO Detectors

7.1 Introduction

This chapter will evaluate the PVD electrodes then compare them with Cu tape performance and IC. By this method, it is possible to draw the conclusion of the validity of the PVD electrodes. Moreover, Elettra UV radiation tests have enriched the evaluation of the TMO with PVD electrodes in the UV E range. Accordingly, it is possible to raise the feasibility of the TMO detectors in the UV and diagnostic x-ray range. By this method, UV can be included in the final aim of this project, as UV has applications in medicine e.g. sterilisation and skin disease treatment [Psoriasis].

As the EM was able to give a detailed compositional analysis within acceptable error [±0.50%], the XMuDat can be used to generate μ/ρ [mass attenuation coefficient] from which μ could be calculated. By this mean, it is possible to calculate the ε_{abs} in order to be compared with a well known semiconductor radiation detectors, such as Si and CZT later on.

Additionally, ε_i is a key factor in evaluating radiation detectors. This will be performed for TMO theoretically and experimentally. Therefore, it is possible to compare it with radiation detectors currently on the market, such as CZT and Si. Finally, noise behaviour assessment for memory effect evaluation will be obtained and compared to Si photodiode. So, photovoltaic mode can be confirmed for TMO detectors.

7.2 Radiation Tests for PVD

7.2.1 Tube X-ray analysis

The same radiation measurements as applied in chapter 4 Initial Status of TMO Detectors on the TMOD1 with Cu tape will be applied on the same TMOD1 after implementing the PVD electrodes. In this way, it is possible to observe and quantify the degree of

improvement inherited by using the PVD electrodes. Thus, this section will provide a direct comparison between the IC, Cu tape with TMOD1 and PVD with TMOD1 to avoid any repetition to what was presented in section 4 Initial Status of TMO Detectors. Also, system setup and measurements protocols were listed in 3.4.2 System Setup and Measurements Protocols.

7.2.1.1 Linearity

Figure 68 shows the linearity of the TMOD1 with PVD electrodes, compared to the TMOD1 with Cu tape electrodes. The dashed line represents the PVD, meanwhile, the continuous line represents the Cu tape.

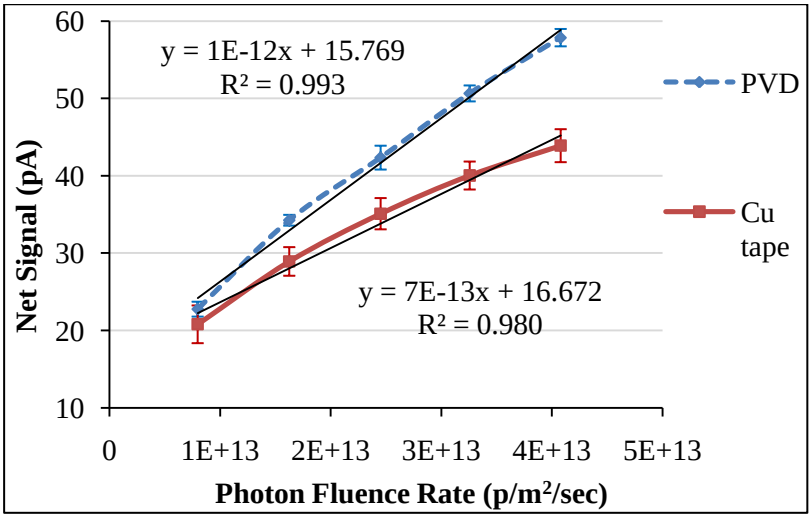

Figure 68: Linearity of TMOD1 at 50 kV with PVD [top dashed] and Cu tape [bottom continuous] electrodes

A near-linear relation from both, PVD and Cu tape is observed. However, the near-linearity is improved from $R^2 = 0.980$ in Cu tape to $R^2 = 0.993$ in PVD, which makes TMO detectors more suitable for radiation monitoring as explained in 1.2 Desirable Detector Specifications. This near-linearity persists due to the presence of defects as it was mentioned by Cox (27).

Moreover, PVD shows a higher signal by an average of 17%. This increment is expected as pasting the Cu tape on the granular surface of the detector will attach only to the peaks of the grains, leaving the valleys bare without any electrodes in contacts, which was estimated to be in the order of 33% of contactless area. This is together with the insulating adhesion of the Cu tape as it was explained in section 5.11 Cu Tape Insufficiency. In addition, PVD sensitivity, which is represented by the slope of the curve,

is increased by 30%, when compared to Cu tape sensitivity. This is because the PVD electrodes cover the whole area underneath it as well as no rectification is expected. This highlights an improvement in the CCE, which will be calculated in section 7.4 Efficiency.

Furthermore, PVD net signal shows a superior stability [less fluctuation], compared to the Cu tape net signal by 47%, represented by the SD. This is because no consecutive charging and discharging is expected at the TMO-PVD electrode interface owing to the elimination of the Cu tape capacitance.

This leads us to compare the improvement recorded for the PVD with our reference point. This reference point is the IC tested in chapter 4 Initial Status of TMO Detectors. Therefore, Figure 69 shows the linearity of the TMOD1 with PVD electrodes, compared to the IC. The dashed line represents the PVD, meanwhile, the continuous line represents the IC.

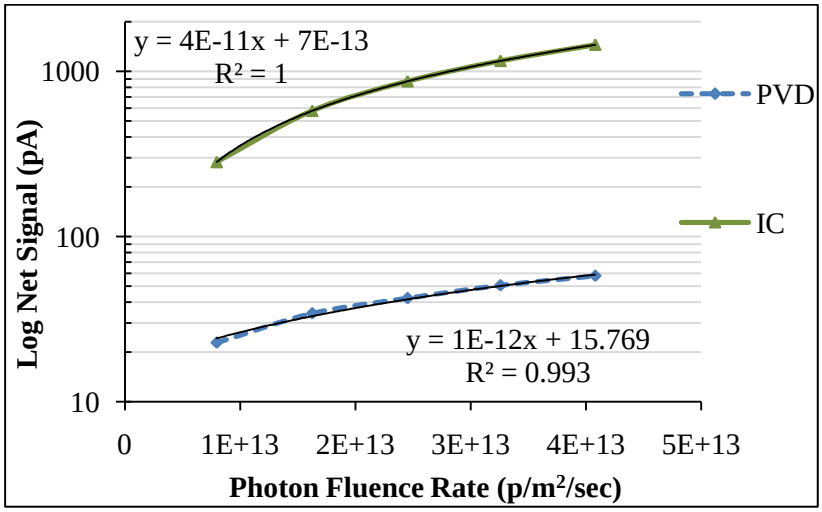

Figure 69: Linearity of TMOD1 at 50 kV with PVD TMOD1 [bottom dashed] and IC [top continuous]

Similarly, R^2 for IC [1] and PVD TMOD1 [0.993] are in better agreement than Cu TMOD1 [0.980]. The PVD net signal forms 5.4% of the IC net signal. Certainly, this is due to the undefined p-n hetrojunction as it was explained in section 6.3.1 Mechanical Polishing. The sensitivity of the PVD is 2.5% of the IC. So, surface preparation before the PVD process is required to avoid any gaps filling at the PVD-TMO interface. Finally, the PVD shows more fluctuation, compared to the IC by 45%. This is due to the presence of defects in the bulk of the material. Although no charge storage [capacitance] is expected at the TMO-PVD electrode interface, defects in the bulk of the material will continue to

store the charge carriers. This is by the successive trapping and de-trapping process explained in section 5.10 Cross-Sectional Analysis.

7.2.1.2 Photon Energy Dependence

Figure 70 shows the photon E dependence of the TMOD1 with PVD electrodes, compared to the TMOD1 with Cu tape electrodes. The dashed line represents the PVD, meanwhile, the continuous line represents the Cu tape.

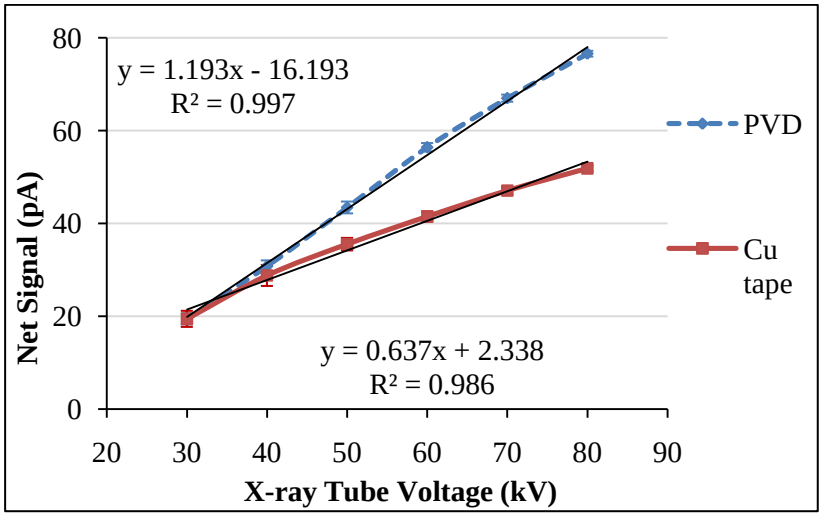

Figure 70: Photon E dependence of TMOD1 at 6 mA with PVD [top dashed] and Cu tape [bottom continuous] electrodes

Analogously, a near-linear relation from both, PVD and Cu tape is observed. However, the near-linearity is improved from $R^2 = 0.986$ with Cu tape to $R^2 = 0.997$ with PVD, which makes TMO detectors more suitable for radiation monitoring as discussed in 1.2 Desirable Detector Specifications. PVD shows higher signal by an average of 19%. PVD sensitivity is increased by 47%, compared to Cu tape sensitivity. PVD net signal shows less fluctuation, compared to the Cu tape net signal by 25%. NB: the same justifications mentioned in section 7.2.1.1 Linearity is applied in here.

On the same basis, a comparison between the IC and the PVD TMOD1 is performed. This is depicted in Figure 71. The dashed line represents the PVD, meanwhile, the continuous line represents the IC. The PVD net signal forms 5.2% of the IC net signal. The sensitivity of the PVD is 3.8% of the IC. Finally, PVD shows more fluctuation, compared to the IC by 49%, yet, close linearity of 0.999 for IC and 0.997 for PVD TMOD1 is observed.

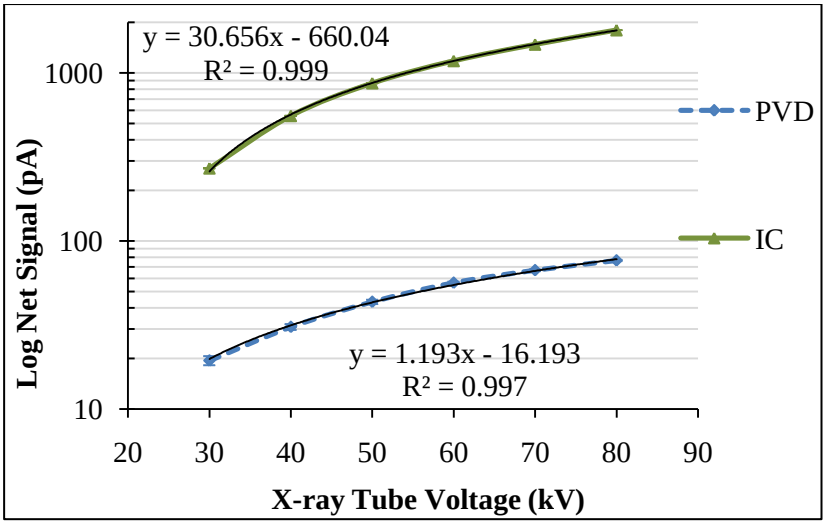

Figure 71: Photon E dependence of TMOD1 at 6 mA with PVD TMOD1 [bottom dashed] and IC [top continuous]

7.2.1.3 Reproducibility

Figure 72 illustrates the reproducibility in terms of linearity of the PVD and Cu tape electrodes alike. Measurements were taken at 0 h, 1 h and 24 h without moving the setup during the time intervals. Regarding the Cu tape, as it was deduced in chapter 4 Initial Status of TMO Detectors, linearity reproducibility is in the average of 17% from 0 h to 24 h. However, PVD linearity reproducibility is in the order of 4% as an average.

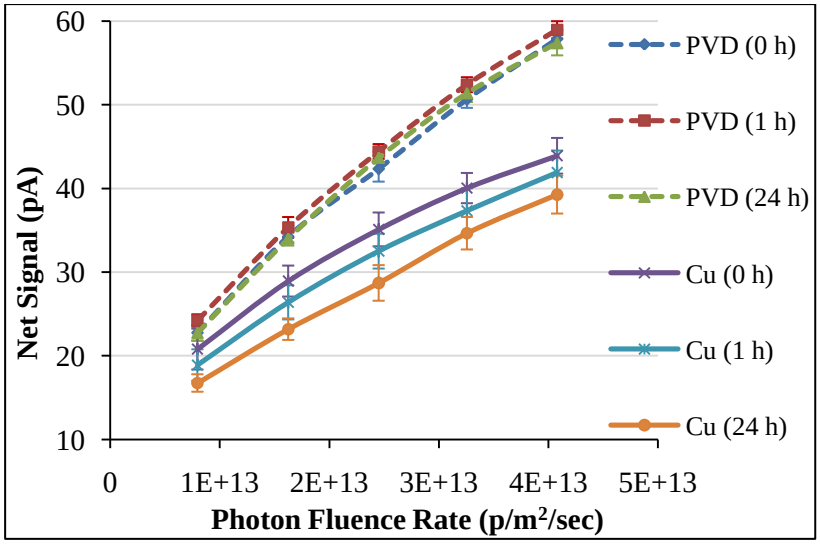

Figure 72: Linearity reproducibility of PVD [top dashed] and Cu tape [bottom continuous] at 50 kV

A comparison between PVD TMOD1 and IC in terms of linearity is, also, plotted in Figure 73. This indicates 4% of linearity reproducibility for PVD TMOD1, compared to 0.3% of linearity reproducibility for IC.

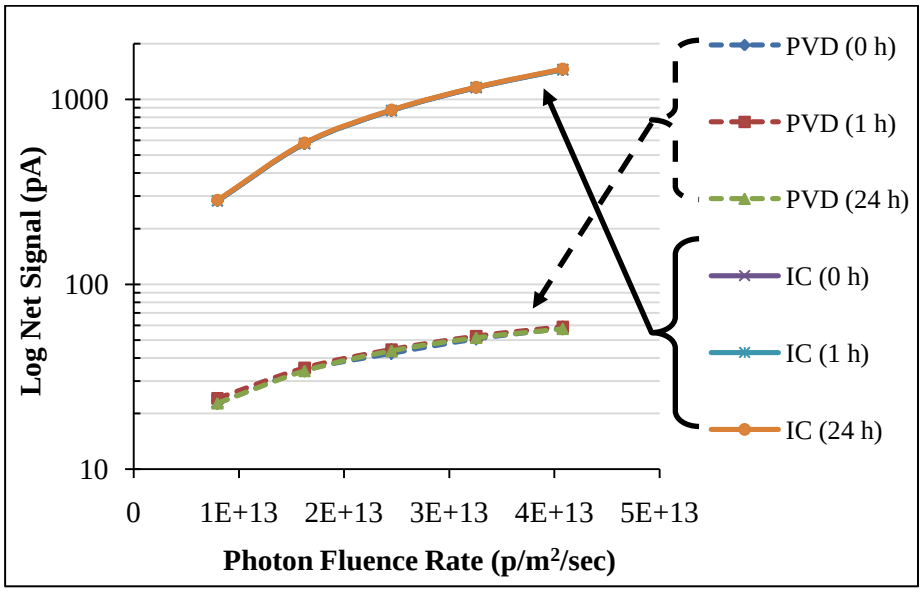

Figure 73: Linearity reproducibility of PVD [bottom dashed] and IC [top continuous] at 50 kV

Likewise, Figure 74 shows the typical photon E dependence reproducibility of the Cu tape, which is in the order of 17% from 0 h to 24 h. Meanwhile, PVD shows a relatively high degree of reproducibility in the order of 3% as an average.

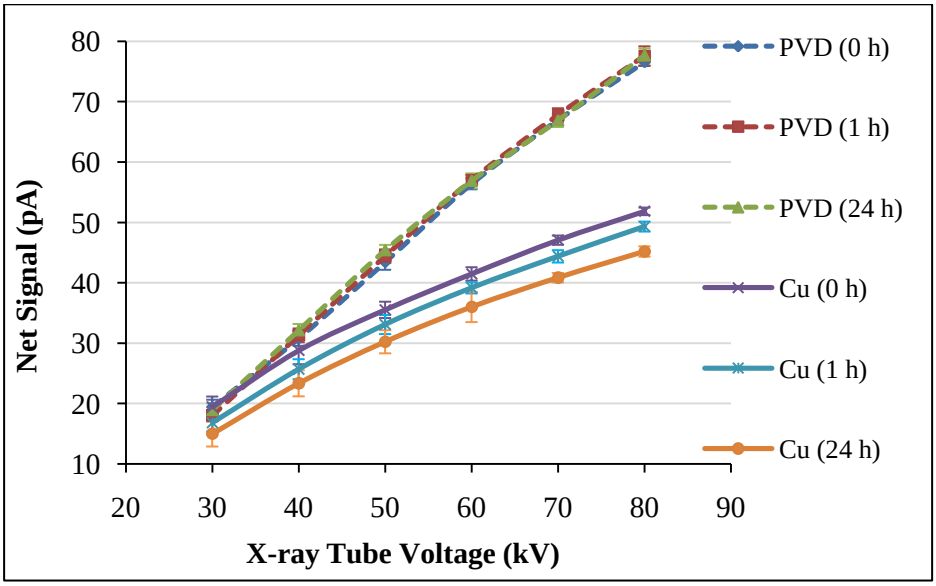

Figure 74: Photon E dependence reproducibility of PVD [top dashed] and Cu tape [bottom continuous] at 6 mA

For comparison, PVD TMOD1 photon E dependence reproducibility is plotted together with the IC photon E dependence reproducibility. PVD TMOD1 photon E dependence showed 3% of reproducibility. This is to be compared with the IC photon E dependence reproducibility, which is in the order of 0.3%.

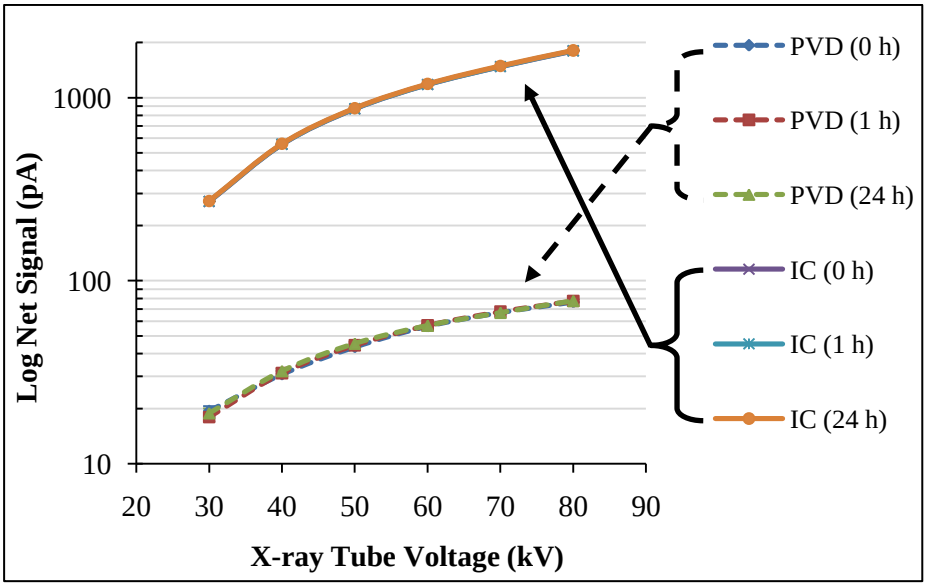

Figure 75: Photon E dependence reproducibility of PVD [bottom dashed] and IC [top continuous] at 6 mA

The detector TMOD2 was tested as well as the TMOD1, in order to confirm the high level of linearity reproducibility [4%] and photon E dependence reproducibility [3%], using PVD electrodes. Similar behaviour was identified and the figures can be found in Appendix 9.3.1. NB: TMOD2 has smaller size, when compared to the TMOD1. Thus, lower net signal magnitude is expected [see Table 3].

It is worth mentioning that Figure 72 and Figure 74 show identical responses for Cu tape, and PVD at 0 h with the lowest photon fluence rate [7.965×10^{12} p/m^2/sec] and kV [30 kV], respectively. However, at 1 h and 24 h Cu tape net signal decreases by 8.5% each, whereas, PVD net signal remains stable within 4% and 3%, respectively. This makes PVD reproducibility fall on the border line for the permissible reproducibility of radiation monitor as explained in 1.2 Desirable Detector Specifications.

7.2.1.4 Signal Stability

In order to complete assessing the PVD and prove its superiority over the Cu tape, signal stability measurements were performed on the detector TMOD1. These were performed for the time intervals of 1 min, 15 min, 30 min, 45 min, 60 min and 1440 min [24 h], and

details are given in Table 24. NB: each time interval in Table 24 is the sum of the previous time intervals as previously explained in section 4.5 Signal Stability.

From Table 24, Cu tape net signal continues to decrease with time until, at 1440 min [24 h], it reaches 14% of the magnitude at 1 min. In contrast, PVD showed a stable behaviour, where signal discrepancy did not exceed 2.5% at any time interval as a maximum in which all values fall within the SD. In addition, similar behaviour is spotted at PVD TMOD2 and can be found in Appendix 9.3.2 Signal Stability.

This relatively high level of stability [2.5%] is due to the elimination of the capacitance provided by the Cu tape, so, no charge was stored between the electrode material and the TMO layer. Also, no rectification was expected at the n-type TMO-electrode interface due to high φ material.

Table 24 shows net signal stability comparison between PVD TMOD1 and the IC. Both detectors experience a fall in their net signals within their SD's. In essence, the IC shows a variation of 0.3%, compared to the PVD TMOD1, which is in the order of 2.5%. This is to be compared with the Cu tape [14%].

Time (min)	IC net signal (pA)	PVD TMOD1 net signal (pA)	Cu tape TMOD1 net signal (pA)
1	870.0±0.5	43±1	35±2
15	870.0±0.5	43±1	34±1
45	--	43±1	33±1
90	--	43±1	32±2
150	870.5±0.5	44±1	31±2
1590	871.0±0.5	44±1	30±2

Table 24: Signal stability comparison of IC, PVD and Cu tape TMOD1 at 50 kV and 6 mA

7.2.1.5 Long Term Stability

It is noticeable that most stability measurements were taken up to 24 h. Thus, Table 25 and Table 26 show signal stability in the form of long-term stability. The detector PVD

TMOD3 was used and measurements were taken at the steps of 1 h, 24 h, 48 h and 96 h without changing the setup.

Time (h)	PVD TMOD3 net signal at 2 mA (pA)	PVD TMOD3 net signal at 6 mA (pA)
1	6.8±0.5	12.8±0.4
24	7.3±0.6	13.3±0.5
73	6.4±0.4	12.7±0.6
169	7.2±0.8	13.9±0.5

Table 25: Long-term signal stability of PVD TMOD3 at constant 50 kV with 2 mA and 6 mA

Table 25 shows the long-term stability in terms of linearity at constant x-ray tube voltage [50 kV] and at two different x-ray tube currents [mA], which are 2 mA and 6 mA. The average discrepancy between the points at different intervals is 4%.

In addition, Table 26 shows the same patterns as presented in Table 25 but presented in terms of photon E dependence. The x-ray tube current was fixed at 6 mA, where the signals were measured at 30 kV and 50 kV. The average difference between the points at different intervals is found to be 3%.

Time (h)	PVD TMOD3 net signal at 30 kV (pA)	PVD TMOD3 net signal at 50 kV (pA)
1	5.6±0.5	13.2±0.6
24	5.6±0.9	13.7±0.5
73	5.3±0.5	13.2±0.5
169	5.9±0.7	13.9±0.5

Table 26: Long-term signal stability of PVD TMOD3 at constant 6 mA with 30 kV and 50 kV

In comparing the short-term stability [signal stability] to the long-term stability, the short-term stability is superior by 29% as an average, compared to the long-term stability. This is because in the long-term stability, the TMO detector had enough time to recover and flush out all charges stored in its defects. This test contributes to the assessing the reliability of the TMO detectors for clinical applications as radiation monitoring devices.

7.2.1.6 Detailed Line Profile

Detailed line profile test was acquired to evaluate the uniformity of detection on the surface. This is because the active area [p-n hetrojunction] should, ideally, have constant response at constant kV and mA. Also, the electrodes should not contribute to the signal produced from the TMOs although the wide beam geometry was in use. Finally, this test could be useful in estimating the depletion layer magnitude at the p-n hetrojunction.

In this experiment, a collimated [2.5 mm] pencil x-ray beam scanned the TMOD4. Measurements were taken at four different locations with 3.0±0.5 mm step sizes as illustrated in Figure 76. The x-ray kV and mA were set to 50 kV and 4 mA, respectively, and the detector was positioned 5 cm away from the x-ray source.

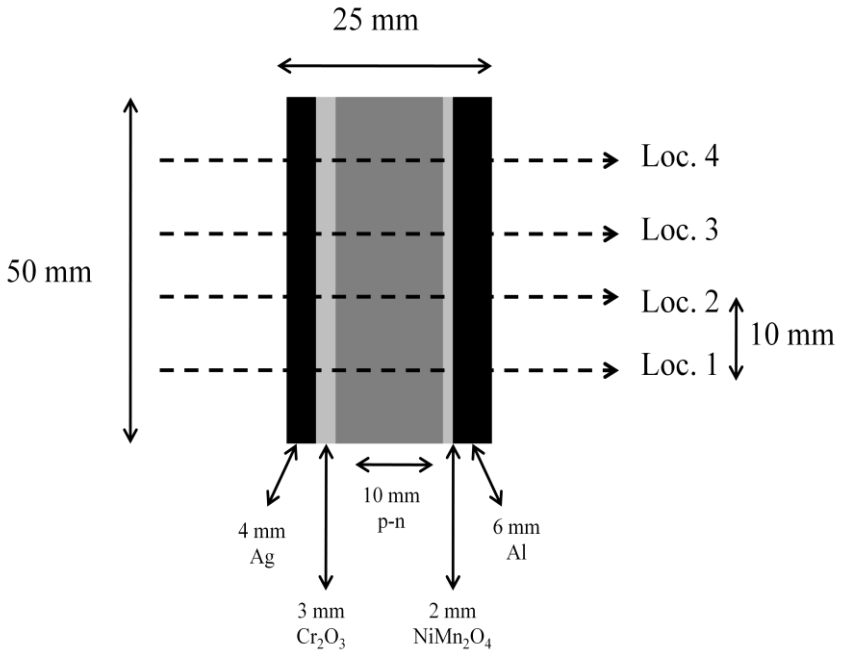

Figure 76: Schematic diagram of the TMOD4 detailed line profiles [plan view]

Figure 77 shows the detailed line profiles taken from the locations drawn in Figure 76. Figure 77 is sectioned in 5 portions, where each portion has a corresponding portion in Figure 76. p indicates Cr_2O_3, while, n indicates $NiMn_2O_4$.

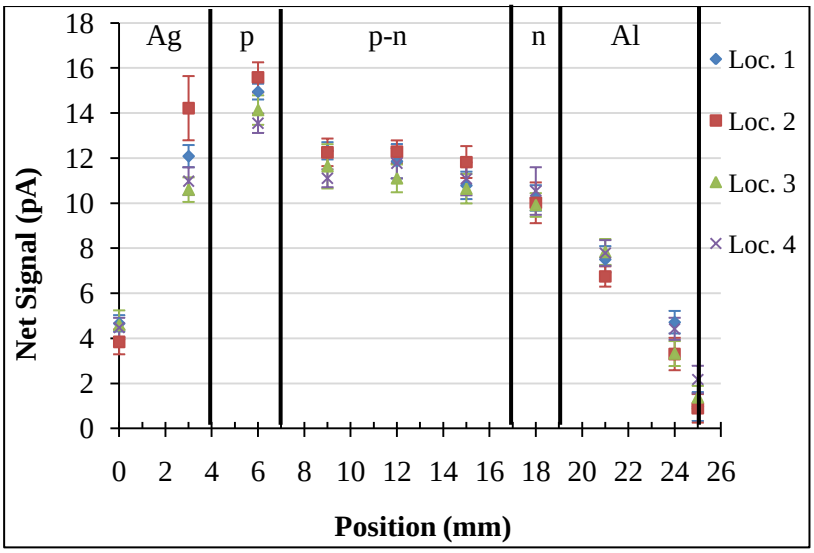

Figure 77: Detailed line profile on TMOD4 at 4 mA and 50 kV, following the steps in Figure 76

Interestingly, a characterised fixed pattern of surface response is observed for each portion. Although the wide beam geometry setup was used, no significant contribution from the electrodes was observed. This means that the Atmos TMO detectors can be used without any collimation to the effective area [p-n hetrojunction], which is a desired feature in radiation detectors as indicated in 1.2 Desirable Detector Specifications.

The Cr_2O_3 section shows the highest response [average of 14.6 pA], whereas, the $NiMn_2O_4$ section shows a lower response [average of 10.2 pA]. This difference in response between the two sections is due to the BG of each material. From Table 20, Cr_2O_3 has a BG value of 3.7 eV, and Pisarev stated that manganites have a typical BG value of 4.5 eV (60,175).

The p-n hetrojunction shows an average value of 11.6 pA for the four locations. Hence, it is possible to estimate the depletion layer at the p-n hetrojunction from Figure 77. This is achieved by increasing the BG of the Cr_2O_3 by the same reduction value as observed in the p-n hetrojunction net signal, when compared to the Cr_2O_3 net signal [14.6 pA]. On this basis, the reduction was found to be within 20.6%, as an average. Consequently, the p-n hetrojunction estimation can be in the order of 4.21 eV as an average. This average includes applying the same calculation on the $NiMn_2O_4$ net signal [10.2], which has the increment of 12%.

Furthermore, the profiles of the four locations were found to differ by an average of 8% across the whole detector from 0 mm to 25 mm in Figure 77. The reason for this difference can be linked to many factors; surface non-uniformity [3.56%] found in section 5.5 Surface Uniformity, defects, C random surface contamination, pure metal contamination and TMO thickness variation can be all considered as main factors for this discrepancy [8%].

7.2.1.7 Continuous Signal Stability

This experiment evaluates the non-stopping signal stability of the TMOD4. This is accomplished by placing the detector in the x-ray beam [115.0±0.5 mm away], then irradiating the detector with constant mA [4 mA] and kV [40 kV]. The x-ray tube was left on for 80 min in which a reading was taken every 10 min. This is can be seen in Figure 78.

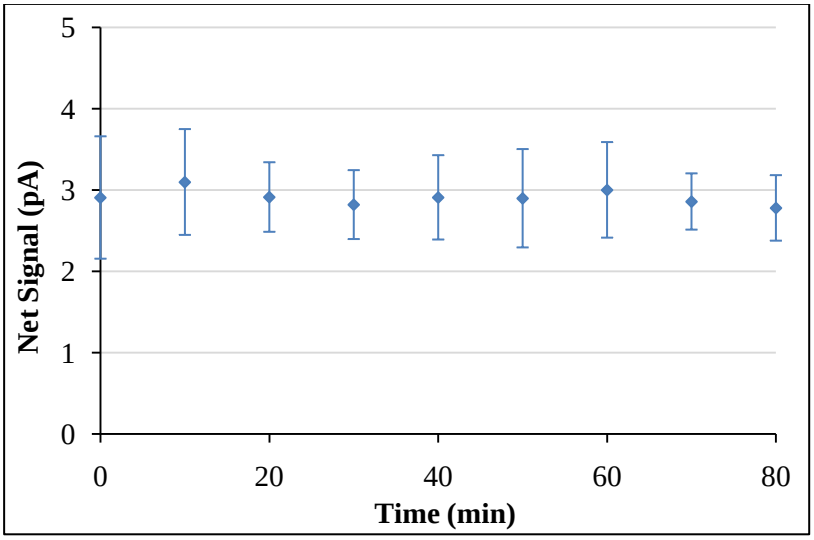

Figure 78: Continuous stability of TMOD4 at 4 mA and 40 kV

From Figure 78, the net signal is found to be varying by an average of 2%. This value falls within the signal stability value [2.5%] for TMOD1 analysed in section 7.2.1.4 Signal Stability. The reason that this continuous stability showed a superior stability [2%], compared to the signal stability [2.5%] was the measurement method. Signal stability required switching off and turning on the x-ray tube between time intervals, which led to more movement next to the pico-ammeter. This is in conjunction with warming up the tube after each pause. However, these had little impact on the continuous stability and thus, superior stability was observed.

Hence, it might be possible to conclude that the Atmos TMO detectors are stable and reliable for real time monitoring, validating the Atmos detectors for the ultimate goal of this project; building real time radiation detectors.

7.2.1.8 Conclusions and Summary

To conclude, it is essential to confirm that PVD showed a significant improvement in the detector response in all aspects. Mainly, the PVD omitted the capacitance presented in the Cu tape. This had the result of improving the reproducibility dramatically. Also, superior sensitivity, less fluctuation and signal stability are significantly improved. So, it is possible to conclude that PVD is effective and strongly recommended. The only possible improvement to the current PVD electrode structure, which may be suggested, is preparing the surface before applying the PVD electrode for better TMO-PVD electrode interface.

Also, by referencing back to section 6.3.1 Mechanical Polishing, the reproducibility confirms that the high level of reproducibility [1.3%] in Table 22 was because of the PVD electrodes. This value [1.3%] is smaller than the average value produced for linearity reproducibility [4%] because in Table 22, linearity was limited by low photon fluence rate to avoid saturation. Hence, there were not sufficient measurements points to be compared. Also, the magnitude of the signal increment [nA’s] was not mainly due to PVD electrodes, instead, it was mainly due to mechanical polishing.

It is of utmost importance to give a table of the summary in which summary all the comparison values obtained in this section are given. This is shown together with data from Table 6 for ease of comparison. This data is given in Table 27.

Radiation test	Field of comparison	Cu tape TMOD1 – IC [%]	PVD TMOD1 – Cu tape TMOD1 [%]	PVD TMOD1 – IC [%]
Linearity				
	Net signal magnitude	4.6	17	5.4
	Sensitivity	2	30	2.5
	SD	76	47	45
Photon E dependence				
	Net signal magnitude	4.3	19	5.2
	Sensitivity	2	47	3.8
	SD	62	25	49
Reproducibility				
	Average of linearity and photon E dependence	17 [Cu tape] and 0.3 [IC]	3.5 [PVD] and 17 [Cu tape]	3.5 [PVD] and 0.3 [IC]
Signal stability				
	Short-term signal stability	14 [Cu tape] and 0.3 [IC]	2.5 [PVD] and 14 [Cu tape]	2.5 [PVD] and 0.3 [IC]

Table 27: Table of summary for IC, Cu tape TMOD1 and PVD TMOD1 comparisons

TMOD3 showed a long-term stability of 3.5% as an average for linearity and photon E dependence. This is expected, when compared to the short-terms stability [2.5%] due to complete charge flush out in long-term stability. Note that, all stabilities fall within the acceptable range as shown in 1.2 Desirable Detector Specifications.

Finally, detailed line profiles have enlightened the path to estimate the depletion layer at the p-n hetrojunction. The estimated amount was found to be 4.21 eV, which is expected as TMOs are wide BG semiconductors. This is together with the continuous stability of the signal, which validated [variation of 2%] the Atmos TMOs to be used as real time monitoring devices.

7.2.2 Synchrotron UV Analysis

7.2.2.1 Introduction

Thus far, all radiation tests were performed with laboratory based tube x-ray sources. In this section, the TMO detectors are examined with UV. As UV has a lower E range [9 eV to 40 eV used in this project], when compared to x-ray [20 keV to 40 keV used in this project], the UV beam is less penetrating in comparison to x-rays. Hence, ε_{abs} is expected to increase as it will be seen in this section. By this method, it is possible to set a range of E's in which the TMO detectors can perform successfully. This section will present UV tests in terms of linearity, photon E dependence, reproducibility and detection uniformity. A Si photodiode [AXUV-100] will be compared to the TMO detectors response in each aspect. Additionally, it is important to state that TMO detectors and the Si photodiode signals are normalised to the electron beam current in the storage ring of 200 mA, as the current in the storage ring decays with time exponentially (125). Also, system setup and measurements protocols were listed in 3.4.2 System Setup and Measurements Protocols.

7.2.2.2 Linearity

Figure 79 shows two linearity curves at 40 eV. The curve with higher net signal belongs to Si, meanwhile, lower net signal curve is TMOD3. The TMOD3 shows a linear response [R^2=0.999], compared to Si photodiode [1]. Although the sensitivity of the TMOD3 forms only 0.6% of the Si sensitivity, the signal of the TMOD3 shows a much higher net signal magnitude, compared to the net signals obtained by tube x-ray in section 7.2.1 Tube X-ray analysis.

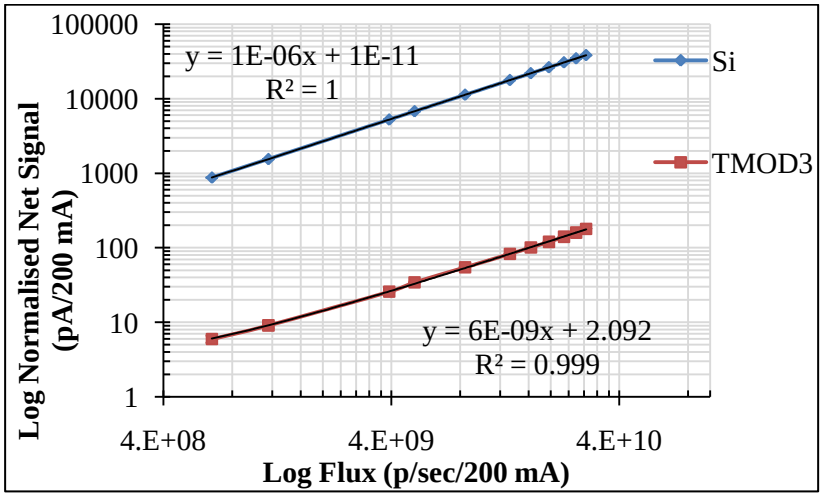

Figure 79: Linearity of TMOD3 at 40 eV

Interestingly, the net signals magnitude of the TMOD3 goes up to hundreds of the pA. It is believed that the reason for obtaining a higher signal in the TMO detectors with UV in comparison to when x-rays are used, is the low photon E's [UV]. This will drastically increase the bulk sensitivity of the TMO, as the mean free path of the electrons is expected to decrease with E's in the UV range (125). This will be proven shortly, when the full TMO/Si comparison is accomplished.

As the TMOD3 signal is stable, a linear [0.999] relation is obtained, which is due to the system setup in particular. As it was described in section 3.7.2 BaD ElPh Beamline, the TMOD3 was inserted in a leaded vacuum chamber and the pico-ammeter was placed in a metallic book shelves-like case. This kept the pico-ammeter shielded from any static noise added due to movement nearby. This setup would prevent from adding any static noise induced by movement. This will be fully addressed in section 7.5 Noise.

Additionally, Figure 80 shows the correlation between the TMOD3 and the Si photodiode at 40 eV, 9 eV and 5 eV, where an excellent correlation was observed. This can be deduced from the R^2 of the curves, which have the value 0.999, meaning that the same signal magnitude ratio induced in Si photodiode was induced in TMOD3. NB: a similar linear response was obtained from TMOD4 as it can be seen in Appendix 9.4 UV Analysis for PVD (7).

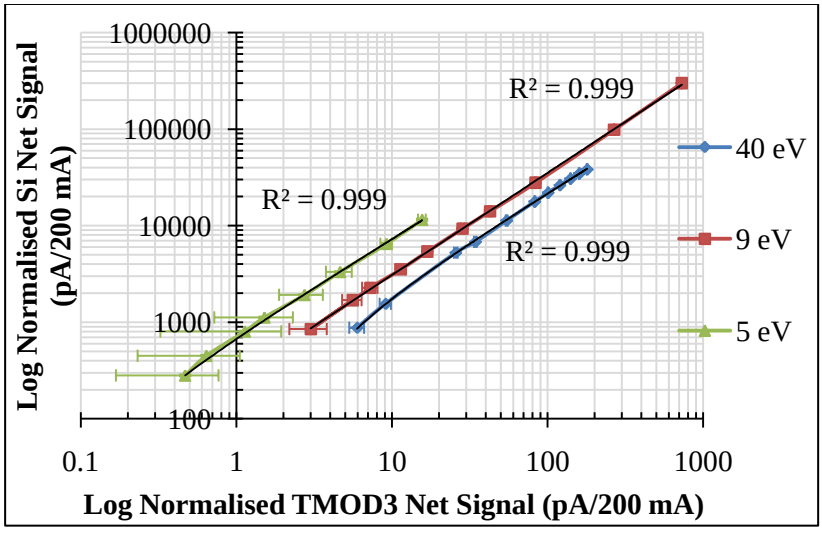

Figure 80: TMOD3-Si photodiode correlations at 40 eV, 9 eV and 5 eV

Note that, the SD does not increase at low photon flux in 5 eV for TMOD3. It is the Log x-axis, which has different scale before 1 pA/200 mA. Instead, the signal remains

detectable and stable as we reached the lowest photon E [5 eV] and photon flux [1.539x10^8 p/sec/200 mA] possible by the BaD ElPh beamline.

7.2.2.3 Photon Energy Dependence

So far, the TMO detectors have been compared with the Si photodiode in terms of flux only. Therefore, it is essential to be compared in terms of E. A linear E response was not expected with Synchrotron radiation as was achieved with the laboratory tube x-ray experiments. This is because synchrotron beamlines use monochromators, which have different efficiencies at different E's, as well as, pre-focusing mirrors [see section 3.7.2 BaD ElPh Beamline]. Hence, the Si photodiode was used to characterise the BaD ElPh beamline to plot the behaviour of the monochromators with different E's from 5 eV to 40 eV. Figure 81 shows the trend of the Si photodiode [top curve], which is confirmed by references (115,125).

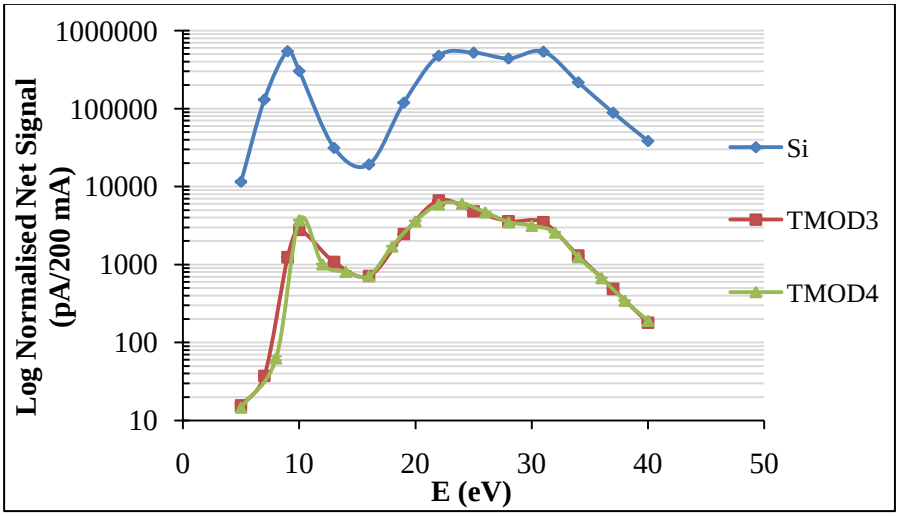

Figure 81: BaD ElPh beamline characterisation by Si [top], TMOD3 and TMOD4 [bottom]

The TMOD3 and TMOD4 were used to characterise the beamline as well. In Figure 81, the bottom two curves belong to TMOD3 and TMOD4. Although TMOD3 and TMOD4 are two different samples, a good agreement on the behaviour of the Cr_2O_3-$NiMn_2O_4$ with BaD ElPh beamline was observed. The difference between the two curves was found to be, on average, of 8%. This relatively low difference is assumed to be purely due to the manufacturing process, and reflects the reproduction ability of Atmos flame-spray system.

In order to compare the Si with the TMO detector, only the TMOD3 detector was compared with Si, to avoid any repetition as the TMOD4 should follow the same comparison deduced from the TMOD3. The Si photodiode and the TMOD3 agree on the drop of net signals at 5 eV, 14 eV and 40 eV. Additionally, three peaks are observed in Si and TMOD3 at 9 eV, 22 eV and 31 eV. However, Si shows the highest response at 9 eV [545.3 nA/200 mA]. On the other hand, TMOD3 shows the highest response at 22 eV [6.624 nA/200 mA], however, this does not contradict with Si as Si shows a comparable high peak at 22 eV [521.7 nA/200 mA] with 9 eV [545.3 nA/200 mA].

At this stage, it is important to emphasis the effect of mechanical polishing on the net signal of the TMO detectors, as the mechanical polishing is capable of magnifying the net signal of the TMO from few nA's to hundreds of nA's [see section 6.3.1 Mechanical Polishing]. Hence, this will make the TMOs detectors competitors to Si photodiodes.

7.2.2.4 Signal Stability

The signal stability test is performed on the Si and TMOD4 detector alike. These measurements were obtained using constant E of 40 eV and flux of 2.993×10^{10} p/sec/200 mA and the time intervals 0 h, 1 h and 2 h as seen in Table 28.

Time (h)	TMOD4 normalised net signal (pA/200 mA)	Si normalised net signal (pA/200 mA)
0	191±1	39962±38
1	187±1	40198±31
3	192±1	40270±28

Table 28: Signal Stability for Si and TMOD4 at constant 40 eV and 2.993×10^{10} p/sec/200 mA

From Table 28, it can be seen that the TMOD4 signal shows a stability of 2.4% as opposed to Si, which has stability of 0.8%. Moreover, the TMOD4 stability [2.4%] in the UV range is comparable with the stability found with the TMOD1 [2.5%] in the x-ray range in section 7.2.1.4 Signal Stability.

7.2.2.5 Detection Uniformity

The TMO detector was moved inside the vacuum chamber in x and y directions with an accuracy of fractions of mm's. Also, the beam spot size was approximately 300x300 µm. Combining these two conditions, it was possible to scan the detector to investigate the detection uniformity from the centre to the edge of the active areas [p-n hetrojunction]. TMOD4 was used for this purpose, where Figure 82 shows the mapping positions [white dots].

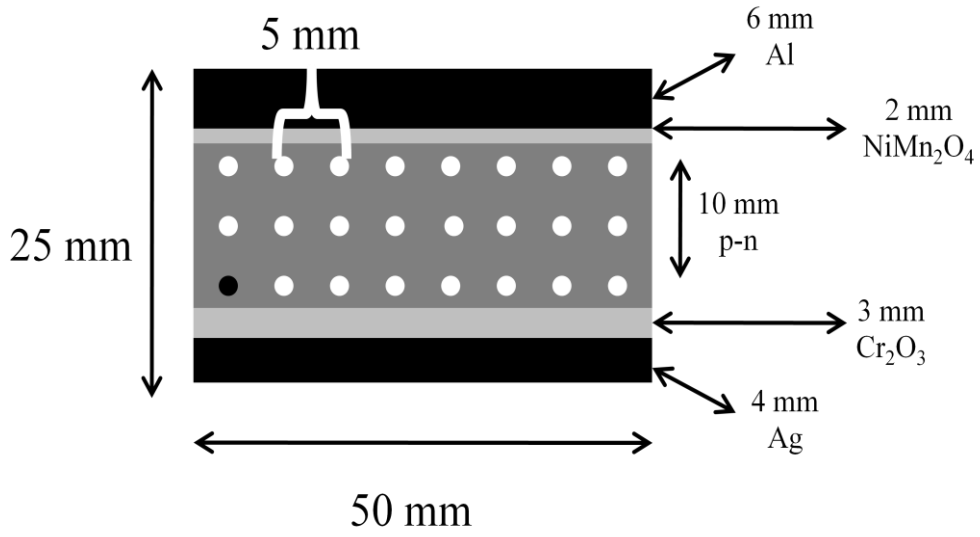

Figure 82: Schematic diagram of TMOD4 mapping positions for detection uniformity; black position indicates the location [1,1]

On this basis, it was possible to evaluate the response of the detector as a function of position on the active area [p-n hetrojunction]. NB: the detector shown in Figure 82 is the same detector as shown in Figure 76 [TMOD4]. Figure 83 shows the response of the TMOD4 at each point shown in Figure 82. Figure 83 [top] indicates the surface plot, while, Figure 83 [bottom] indicates the plan view of this surface plot. The E of the beam was fixed at 30 eV.

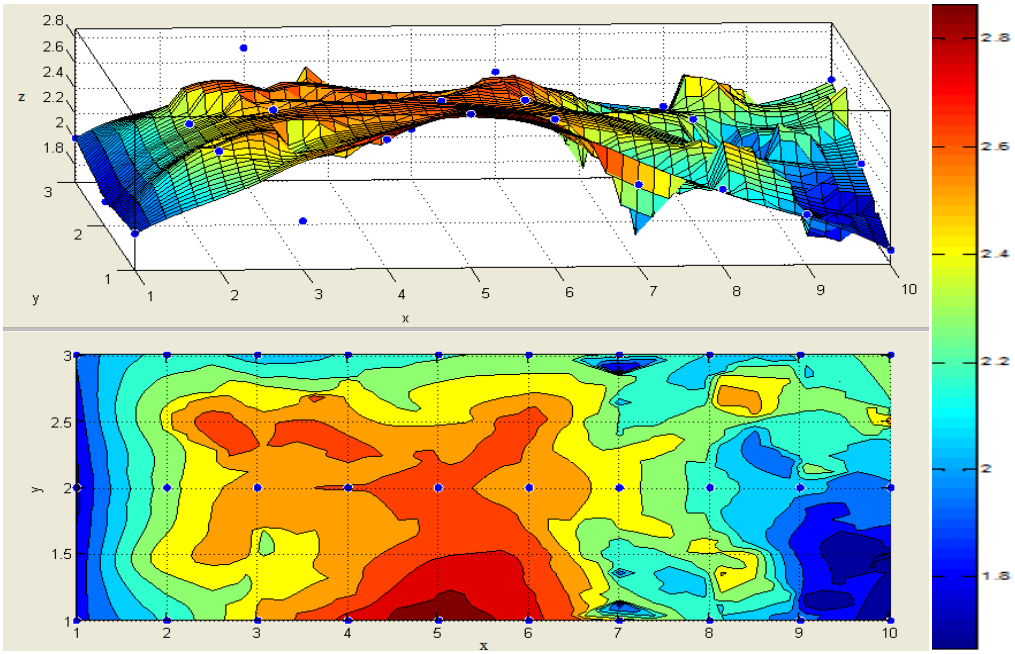

Figure 83: Mapping of the active area detection uniformity mapping. NB: the unit on the colour scale is nA/200 mA

From Figure 83, the corner [1,1] represents the black position in Figure 82. Red areas show hot spots, where the highest response was recorded, and blue areas show the lowest recorded response. Interestingly, the centre of the active area demonstrates a high and uniform response, when compared to the edges.

Notably, the top and bottom of the TMOD4 are relatively insensitive to radiation. This might be due to the substrate structure. The substrate is slightly curved at the top and bottom edges, which will lead to variations in the thickness of the TMOs deposited onto it. Particularly, 5 mm from the top i.e. from [2,1] to [2,3] and 10 mm from the bottom i.e. from [8,1] to [8,3]. This also indicates that due to the splashing discussed in 5.7 Contamination and Splash, the nozzle loses uniformity at the edges, which makes the thickness of the grown layer vary significantly with deposition. This is because TMO particles escape the flame from the sides and are deposited away from the ROI of deposition, which is perpendicular to the centre of the flame. Thus, a solution could be masking the flame or the deposition is performed on larger substrate then the large substrate is cut at the middle, where the uniform deposition is concentrated. Furthermore, the n-type side shows a cooler area, compared to the p-type side. This behaviour is expected and explained by Knoll. This is because when the beam is focused on the point, say, [5,1], the generated electrons will travel quickly to the p-type electrodes. On the other hand, holes will take a greater amount of time to reach the n-type electrode due to

the distance between the electrode and the point of generation. The opposite is true for point [5,3]. This is in addition to the high mobility of electrons, compared to holes, which is a feature of all p-n junction based semiconductor detectors, such as Si, Ge and GaAs (13).

Consequently, due to the mobility difference between electrons and holes, electrons are more likely to survive the trapping due to manufacturing limitations than holes. Therefore, the n-type side [hole collection] shows cooler areas, when compared to the p-type side [electron collection].

Finally, this behaviour was not seen in Figure 77 due to the difference in E's [30 eV to 30 keV]. So, we can conclude that holes are able to overcome the traps at 30 keV more efficiently than 30 eV. The detailed line profiles started at [3,1] from the top and ended at [8,1] from the bottom, and so, the cold areas are missed and not included in the plot. Instead, a good variation agreement in the p-n hetrojunction area is calculated, where, as shown in Figure 77, the variation between the four locations in the area from 7 mm to 17 mm was within an average of 6%. Similarly, the variation in the area from [3,1] to [8,1] in Figure 83 is found to be within an average of 7%.

7.2.2.6 Summary

The TMO detectors showed a high level of sensitivity to UV, as seen from the good agreement between TMO detectors when compared to Si across the UV experiments. A linear [R^2=0.999] response and good correlation with Si were spotted in TMO detectors. The TMO detectors showed relatively high net signal magnitude with UV [nA's], when compared to x-ray [pA's].

Two different TMO detectors characterised the BaD ElPh beamline with an average variation of 8% between them. This characterisation showed a similar trend to Si but with different intensities. Moreover, good agreement was seen between the x-ray signal stability [2.5%] and the UV signal stability [2.4%].

Finally, the detection uniformity across the p-n hetrojunction was evaluated. The expected behaviour presented in Si and Ge was also seen in the TMO detector. Comparison of the UV net signal response variation at the hetrojunction [7%] depicted good agreement with the x-ray net signal variation at the hetrojunction [6%]. Hence, a conclusion can be drawn to say that TMO detectors are feasible for operation in the E range of UV and x-ray.

7.3 Attenuation Coefficient

7.3.1 Introduction

In order to maximise the generated EM results, the compositional analysis tables were used to calculate the μ/ρ and then the μ as explained in section 3.8 Attenuation Coefficient and Efficiency. By this method, it is possible to evaluate the Atmos TMOs, including every level of contamination, such as C and core contaminations. However, trace elements of less than the SD [< 0.50%] were omitted and the remaining elements normalised to 1 by weight.

7.3.2 Mass Attenuation Coefficient

The fraction by weight together with the element were be input into the XMuDat software to produce a μ/ρ curve as a function of E. Table 29 shows a summary of the Atmos TMOs and their compositional analyses tables in the EM section. NB: XMuDat in Table 29 means the value as given by the software, based on reference (130).

TMO	Compositional analysis tables above	Z_{effe}	ρ [g/cm^3]	References for ρ
$FeCrAlO_4$	Table 9	22	--	--
Mixture of $CoFeVO_4$ and $CoFe_2O_4$	Table 10 and Table 14	24	5.3 [$CoFe_2O_4$ only]	(152)
Mixture of FeO and Fe_3O_4	Table 11	23	5.2 [Fe_3O_4 only]	(152)
Cr_2O_3	Table 11	21	5.2	(176)
$NiMn_2O_4$	Table 12	23	5.5	(177)
CO_2	XMuDat	8	$1.84x10^{-3}$	XMuDat
Si	XMuDat	14	2.3	(114)

Table 29: Summary of Atmos TMOs compositional analysis tables in the EM section and physical properties

After inputting details of the five TMOs given in Table 29, pure Si is added for comparison. This is shown in Figure 84. The E range 1 to 50000 keV was used to fully assess Atmos TMOs in comparison to Si.

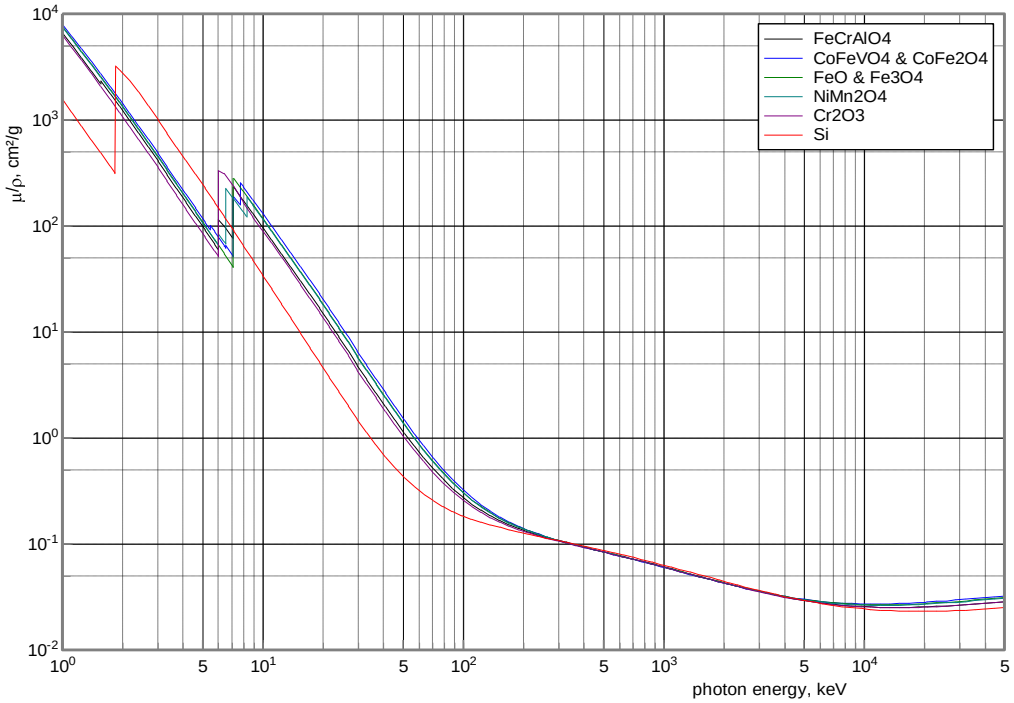

Figure 84: μ/ρ of Atmos TMOs and Si for comparison

From Figure 84, the Atmos TMOs show typical trends of μ/ρ curves and close K_α's [6 – 8 keV]. This fact is expected as first-row TMs [from V to Ni] have similar physical properties in terms of Z [23 – 28], ρ [6 – 9 g/cm^3] and k_α [5 – 7 keV]. Accordingly, the Atmos TMOs should have similar physical properties as well. Table 29 also shows the Z_{effe} values, calculated using the software, of the Atmos TMOs. The Atmos TMOs are expected to have similar densities, where a literature survey showed the range of 5.2 – 5.5 g/cm^3 for Atmos spinel TMOs densities [see Table 29] (114).

In terms of TMOs and Si comparison, μ/ρ TMOs are superior to Si in the range of 1 – 1.74 keV and 6 – 200 keV. In the portion of 1.74 – 6 keV Si shows higher μ/ρ values due to Si K_α, which is located at 1.74 keV. Then from 200 – 50000 keV TMO and Si show similar trends although the TMOs show slight increment at higher E's [4000 – 50000 keV] (114). Such a trend is expected as the TMOs have higher Z_{effe} values compared to Si [from Table 29], which is a desired feature as expressed in 1.2 Desirable Detector Specifications. This is because at low E's, the predominant interaction is the photoelectric effect, whereas at high E's the predominant interaction is pair production.

Both probabilities of interactions are dependent on Z^4 and Z^2, respectively. In comparison, Compton scattering at the medium E's shown does not show any dependency on Z, hence, an overlapping occurs between TMOs and Si in medium E's (13,17).

In terms of K_α comparison, TMOs show late soft x-ray K_α's [6 – 8 keV] when compared to Si [1.74 keV]. In terms of future applications, this feature makes TMOs suitable for soft x-ray imaging in the range of 6 – 8 keV. This is because the advantage of the dramatic increment in μ/ρ due to photoelectric effect can be used to enhance image contrast in the region of 6 – 8 keV (17,178).

7.3.3 Linear Attenuation Coefficient

Thus far, the calculation is made for μ/ρ, however, μ calculation would make more sense as the ε_{abs} and mean free path can be estimated. Recalling that the TMO detectors used in this project for radiation measurements are the combination of $NiMn_2O_4$ [n-type] and Cr_2O_3 [p-type]. Moreover, the E range used at the UCL laboratory is from 20 to 40 keV [section 3.4 Tube X-ray]. On this basis, it is essential to focus the study in to the effect on μ on this E range [20 – 40 keV] and for $NiMn_2O_4$-Cr_2O_3 materials only.

It is now important to apply some corrections to be able to obtain the most approximate calculated μ/ρ of the Atmos TMOs. As explained in section 3.8 Attenuation Coefficient and Efficiency, μ is obtained by multiplying the μ/ρ by the ρ. In this sense, the ρ values presented in Table 29 are for pure TMOs [stoichiometric]. However, the Atmos TMOs are non-stoichiometric due to the presence of contamination [core and C]. Thus, using the following equation is tested to calculate the ρ vlaues for the stoichiometric TMOs as their ρ vlaues are known. After that, the difference between the calculated and tabulated ρ will be used to correct for the calculated ρ for the non-stoichiometric TMOs.

$$\rho = \sum_{i=1}^{n} w_i \rho_i \qquad \text{Equation 19}$$

Where, w_i is the fraction of the i^{th} element by weight. The percentage by weight of the elements within the stoichiometric TMOs can be calculated, using the atomic weight together with the number of atoms. Therefore, Table 30 shows the stoichiometric calculation for $NiMn_2O_4$ and Cr_2O_3.

Element	Atomic weight	Number of atoms	Normalised weight [%]	Element	Atomic weight	Number of atoms	Normalised weight [%]
Ni	58.69	1	25.24	**Cr**	51.99	2	68.43
Mn	54.93	2	47.25	**O**	15.99	3	31.57
O	15.99	4	27.51	**--**	--	--	--
Total			100.00				100.00

Table 30: Stoichiometric calculation of $NiMn_2O_4$ and Cr_2O_3 **(114)**

Based on Equation 19 and Table 30, Table 31 shows a comparison between the calculated and tabulated ρ of $NiMn_2O_4$ and Cr_2O_3. The difference between the calculated and tabulated ρ of $NiMn_2O_4$ and Cr_2O_3 in particular can be applied as a correction factor when calculating the ρ, using Equation 19. This is to estimate the ρ for the Atmos TMOs [$NiMn_2O_4$ and Cr_2O_3], including the contamination and non- stoichiometry.

TMO	Calculated ρ [g/cm^3]	Tabulated ρ [g/cm^3]	Correction factor [%]	Estimation [cal. – tab.]
$NiMn_2O_4$	5.7	5.5	3.5	Over estimation
Cr_2O_4	4.9	5.2	5.7	Under estimation

Table 31: Calculated and tabulated ρ **(176,177)**

By this method, it is possible to estimate the ρ of Atmos $NiMn_2O_4$ and Cr_2O_3. This ρ would take in account the presence of any contamination together with trace elements provided that the fraction is above the SD [> 0.50%]. This calculation [after applying the correction factors in Table 31] showed the ρ of $NiMn_2O_4$ as 5.2 g/cm^3 and the ρ of Cr_2O_3 as 4.7 g/cm^3. Reduction in ρ is expected due to the presence of C, which would lower the total ρ due to its [C] relatively low ρ [2.27 g/cm^3] compared to TMs.

With these calculated ρ values, it is possible to apply the mixture rule to calculate the total μ/ρ and then the total μ. However, another correction factor is required at this stage, which is to account for defects in the TMO layers deposited by the flame-spray process. Recalling sections 5.8 Surface and Bulk Comparison and 5.10 Cross-Sectional

Analysis, it was found that 30% of defects are contained within each sample, and also, in section 3.1 Atmos Technologies Ltd., it was shown that the waste product of the flame-spray process is CO_2 only, it is important to correct for the defects, voids and cracks which are considered to be filled with CO_2. So, the modelling of the Atmos TMOs can be considered as shown in Figure 85 in order to be able to calculate the total μ.

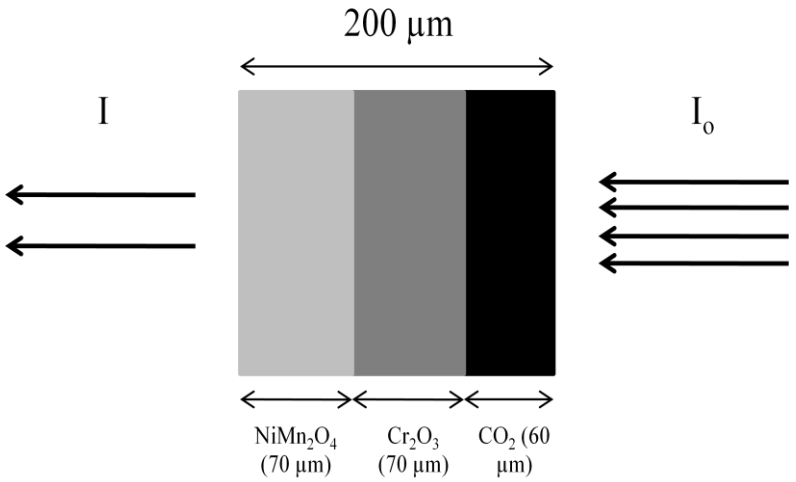

Figure 85: TMOs modelling for total μ calculation; I and I_o indicate transmitted and primary photons, respectively

After applying the defect and ρ corrections, it is possible to apply the mixture rule to calculate the total μ for Cr_2O_3, $NiMn_2O_4$ and CO_2. The calculated total μ can be seen in Figure 86, for the E range of 20 to 40 keV only. Si is also shown for comparison purposes.

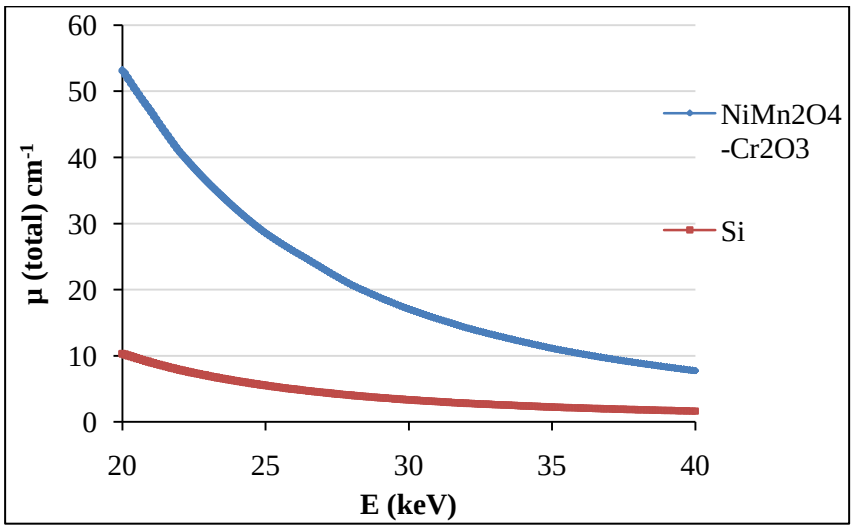

Figure 86: Total calculated μ compared to Si

The effect of the corrections is to cause the total μ to be reduced by 35%. This is due to the insertion of the CO_2 layer, which has much lower ρ and Z_{effe}, compared to the TMOs. This will reduce the overall Z_{effe} of the materials [$NiMn_2O_4$-Cr_2O_3-CO_2] to the order of 19 [see Table 29]. In addition, the expected lower ρ of TMOs due to contamination and non-stoichiometric also contribute to this reduction [35%].

In terms of TMOs and Si comparison, it is apparent from Figure 86 that TMOs are superior across the whole range of E [20 – 40 keV]. The superiority varies with E according to the dependency of photoelectric effect on [$Z^4/E^{3.5}$] and Compton scattering on E only. NB: no pair production is expected in this range of E as pair production has a threshold of occurrence, which is 1022 keV (13,17).

Single E will be chosen for further analysis. This E is 33 keV and is chosen in particular as an experimental comparison will be conducted later on around this E [33 keV], in section 7.4 Efficiency. From Figure 86, the mean free path can be calculated at 33 keV and given in Table 32, which shows the total μ and mean free path for both, TMO and Si.

Material	μ cm^{-1}	Mean free path [cm]
$NiMn_2O_4$-Cr_2O_3-CO_2	13.1	0.08
Si	2.6	0.38

Table 32: μ and mean free path at 33 keV

By referencing back to Mott in section 2.4 Type of Charge Carriers, in every 800 μm [0.08 cm] of the lattice, polarons are ready to hop to a near-neighbour empty site. However, this process is interrupted as polarons cannot delocalise to hop, instead, polarons remain localised owing to the presence of voids and cracks in the average of 30% (63). This can be observed by going back to section 5.10 Cross-Sectional Analysis. μ is also confirmed by Takahashi et al. for Si at this E [33 keV] (179).

Finally, the stacked rule can be applied at E = 33 keV and d = 0.02 cm. In consequence, it is possible to calculate the ε_{abs} as follows.

$$\varepsilon_{abs} = 100 - (\frac{I}{I_o} x100) = e^{-[\left(\frac{\mu}{\rho}\rho d\right)_{NiMn_2O_4} + \left(\frac{\mu}{\rho}\rho d\right)_{Cr_2O_3} + \left(\frac{\mu}{\rho}\rho d\right)_{CO_2}]}$$

$$\varepsilon_{abs} = 100 - \{100xe^{-[(4.29x5.2x70E-4)_{NiMn_2O_4} + (3.19x4.7x70E-4)_{Cr_2O_3} + (0.302x1.84E-3x60E-4)_{CO_2}]}\}$$

$$\varepsilon_{abs} = 23\% \qquad \text{Equation 20}$$

From the calculation performed above, the model shown in Figure 85 is expected to attenuate 23% of the primary beam. However, one last correction is necessary. Jonge et al. compared Hubbell et al. μ/ρ with an improved technique for measuring the μ/ρ, based on synchrotron radiation. Jonge et al. claimed a range of discrepancies with a range of E's. However, in the E range of 20 to 40 keV, the discrepancy is within 4% less than Hubbell's values, which in practice, will bring the ε_{abs} value down to 22% (180).

The same calculation is performed for Si and the ε_{abs} is found to be 5%. This means that any thickness of the Atmos TMOs [even including the effect of defects and contamination] is 77% more efficient at attenuating photons with E = 33 keV than Si.

7.3.4 Summary

Several corrections were applied on the calculation of the μ, based on the EM results. These corrections decreased the true μ value by 35% due defects and contamination. Moreover, the theoretical ε_{abs} at 33 keV was found to be 22%, which is superior to Si [ε_{abs}=5%] by 77%.

7.4 Efficiency

7.4.1 Absorption Efficiency

The ε_{abs} is the ratio of I to the I_0 through a certain thickness of the detector material and photon E (17). Following the steps explained in section 3.8 Attenuation Coefficient and Efficiency, the ε_{abs} can be measured experimentally. This is achieved by obtaining the net ε_{abs} [TMOD1 - substrate] of the Cr_2O_3-$NiMn_2O_4$. Note that, the measurements were based on three different locations on the TMOD1. These locations were focused on the active area of the detector [p-n hetrojunction], principally, the hot spots shown in Figure 83. It was found that the ε_{abs} of the Cr_2O_3-$NiMn_2O_4$ hetrojunction is in the order of 19%. This value was corrected for the ε_i of the CZT as it will be explained shortly.

This will take us back to section 7.3 Attenuation Coefficient. The theoretical calculation showed an ε_{abs} of 22%., where the remaining 3% [22%-19%] is considered as an uncertainty in the experiment. This is due mainly to the sample and substrate thickness variations. Thus, it is possible to generate a correction factor to bring the theoretical ε_{abs} to the experimental ε_{abs}. This factor equals 0.136.

As a result, it is possible now to calculate the ε_{abs} for a 0.5 cm thick Cr_2O_3-$NiMn_2O_4$ hetrojunction. This is because the TMOD1 sample used possesses an average thickness of 200±5 μm. For consistency, this should be modified to 0.5 cm as a comparison will be attained with a 0.5 cm thick CZT detector later on.

By referring back to Equation 15, the ε_{abs} of 0.5 cm thick Cr_2O_3-$NiMn_2O_4$ can be calculated by applying the correction factor [0.136] to calculate the value 86%. Note that, the μ of TMOD1 is obtained from Table 32 at 33 keV. This is because the source used in the efficiency experiment was Cs-137, which has a photopeak around 33 keV (133).

7.4.2 Charge Collection Efficiency

While the CCE is defined as the ratio of the total charge observed to the actual charge, it is possible to use the PVD curves in Figure 72 for this purpose. The photon fluence rate is corrected to consider only the photons which fall on the CZT equivalent detector area [5 x 5 mm^2]. Then the signal of a single photon with an E of 50 kV [around 30 keV according to xcomp5r] is calculated. By this method, it is possible to estimate the charge generated by this photon. Consequently, the number of generated electrons can be calculated as an electron has the value of $1.6x10^{-19}$ C. This number of generated electrons was compared to the expected number of electrons, based on the BG and photons E [30 keV]. The BG was estimated to be 4.12 eV as shown in section 7.2.1.6 Detailed Line Profile (17).

However, by referring back to section 2.4 Type of Charge Carriers, the charge carrier type in the TMOs is polarons. Stoneham demonstrated that due to the localisation of the polarons, the E needed to generate an e-h pair in a defective material would be the BG plus the extra E of the localisation. The extra E can be even more than the BG in the worst scenario, which makes the expected number of electrons rely on a two BG's-order. Numerically, this will move the E needed to generate an e-h pair to 8.24 eV in the Cr_2O_3-$NiMn_2O_4$ hetrojunction (56). In an earlier work, this fact was confirmed by Sangaletti et al. as he quoted that the CT E of the FeO to be 7 eV, whereas, the BG is 2.5 eV (53,181).

In fact, at this early stage of detector optimisation, a single photon with E = 30 keV is found to produce a fraction of the electron charge in the p-n hetrojunction. Accordingly, the CCE is calculated to be in the order of 0.023% as an average.

It is of utmost importance to clarify the actual meaning of CCE. CCE is a global term which includes the electrodes, material purity and geometry. Therefore, in order to optimise the CCE, the material deposition method and design of the detector should be improved, due to the charge carrier trapping/scattering, e-h recombination and charge loss due to long charge travelling distance to reach the electrodes (21).

7.4.3 Intrinsic Efficiency

So far, ε_{abs} and the CCE have been calculated. According to Ahmed and Giakos, the ε_i is the product of ε_{abs} and CCE. Mathematically, (17,21).

$$\varepsilon_i = \varepsilon_{abs}\ x\ CCE \qquad \text{Equation 21}$$

The ε_i represents the number of detected photons as a proportion of the number of photons which fall on the detector surface. This is optimised by the solid angle, which can be represented as the detector area divided by the square of the source-to-detector distance (13). As a result, the ε_i is calculated as follows.

$$\varepsilon_i = 0.86\ x\ 2.30E-4 = 0.02\% \qquad \text{Equation 22}$$

The ε_i of the CZT is measured and found to be 0.47%, meaning that the CZT ε_i is superior to the TMO ε_i by 96%. However, this relatively low level of ε_i value for TMO is not the worst. As semiconductors are expected to have higher ε_i than scintillation detectors due to direct conversion, Lee addressed an ε_i value for CsI[Na] of 10^{-2}% at a range of E's below 80 keV (182). This confirms that even with the early stage of the TMO detector manufacturing, superior ε_i is recorded, compared to CsI[Na].

In addition, the above ε_i would support the mechanical polishing of the detectors after each deposition to be able to obtain a signal in the order of nA's, instead of pA's as shown in section 6.3.1 Mechanical Polishing. By this method, the CCE will increase dramatically, which will lead to a rapid improvement in the ε_i. This improvement can potentially be comparable to the CZT ε_i [0.47%].

7.4.4 Summary

Experimentally, ε_{abs} was obtained and found it to be in the order of 19%. This value is comparable to the theoretical value, which was in the order of 22%. Both values [19% and 22%] were for 200 µm TMOs thick and at 33 keV.

Poor CCE was obtained due to contamination, defects and detector design. This led to the ε_i calculation of TMO which was found to be 0.02% at 33 keV. This was compared with the measured ε_i of CZT, which was found to be in the order of 0.47%. Finally, mechanical polishing is expected to increase the CCE dramatically and hence, make the ε_i, of TMOs comparable to that of CZT.

7.5 Noise

7.5.1 Introduction

At this early stage of detector optimisation, two principle sources of noise contribute to the signal; static noise and manufacturing noise. The static noise is mainly represented by the SD and is affected by movement next to the pico-ammeter or TMO detector. As movement within 1-2 m will add a few pA's to the measured signal, this will affect the SD increasingly since the pico-ammeter calculates the SD according to (183,184).

$$SD = \sqrt{\frac{\sum_{i=1}^{n}(Ave - x_i)^2}{n-1}} \qquad \text{Equation 23}$$

Where,

x_i: stored reading in the pico-ammeter buffer

n: number of stored readings

Ave: mean of the buffer readings

Fundamentally, electrostatic interface will occur as the moving object will inject charge to the circuit, which will not dissipate rapidly, and will cause instability in the measurements. However, according to tube x-ray experiment setup [section 3.4.2 System Setup and Measurements Protocols], movement would affect the pico-ammeter only as the detector is isolated in a separate room. A few pA's can be added due to sudden motion, so, care was taken prior to each reading to keep movement to minimum as well as time was allowed for the detector to stabilise if sudden movement occurred nearby (183).

Manufacturing noise is linked firmly to the manufacturing process, principally the presence of voids and cracks as these act as sinks for the flowing charge and will store them. This causes local potential differences, which cause random fluctuations due to consistent leakage current. Anderson indicated that defects lead to localisation due to static intrinsic disorder as it was explained in section 2.5 Charge Transport Mechanism (71). In consequence, the memory effect takes place, which requires time to flush out all charge, and return voids and cracks to neutral. On top of that, pure metal contamination in the vicinity of the TMOs would inject more electrons to the medium and cause a noisy environment.

7.5.2 TMO Noise Behaviour and Recovery Time

Figure 87 shows the noise behaviours of TMOD1, TMOD2 and Si photodiode at time intervals of 1 min, 15 min, 30 min, 45 min, 60 min, 1440 min [24 h] and 2880 min [48 h]. Si shows a steady level of noise as all of the points fall within the SD. Also, Si produces noise in pA's, where its signals are in nA's. This is unlike the TMOD1 and TMOD2, which have noise and signals in the pA's range. In terms of the TMOD1 and TMOD2, the predicted memory effect in chapter 5 Identification of Materials and Limitations, is observed.

For TMOD1, it is noticeable that the noise keeps increasing until it reaches 24 h. After a 48 h pause, however, the detector fully recovers and returns to the 1 min status. In other words, the detector stored charge of 31 pA in its defects, which needs 48 h to self-flush out this stored charge. Due to difference in sizes between TMOD1 and TMOD2 [see Table 3], TMOD2 takes only 24 h to fully recover. As the detector size increases, more charge will be stored in its defects, which therefore needs more time to be self-flushed out.

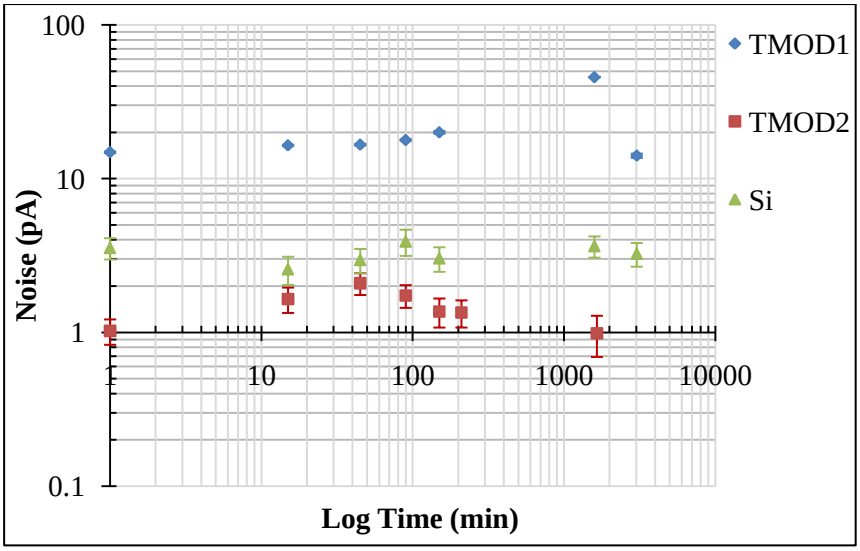

Figure 87: TMOD1, TMOD2 and Si photodiode noise pattern in 1 min, 15 min, 30 min, 45 min, 60 min, 1440 min [24 h] and 2880 min [48 h]

The noise level is expected to be suppressed as the manufacturing process is improved. This is because 30% of defects are relatively high degree of defects and elimination of the 30% would lower the noise dramatically. Additionally, the net signal will be increased as charge carriers will suffer less trapping/scattering effect. Hence, it will be possible to reach the 4 orders of signal magnitude, compared to the noise as recommended in 1.2 Desirable Detector Specifications.

7.5.3 Summary

The memory issue plays a big role in the behaviour of the detector. This leads to the finding that the detector needs time to self-flush out all the stored charge. It was found that TMOD1 took 48 h to go back to 0 h behaviour, while, TMOD2 took only 24 h to return to 0 h behaviour. This difference is due mainly to the deference in detectors size. Recall that this project is aiming to operate the TMO detectors in the photovoltaic mode i.e. no reverse bias is applied.

Increasing the signal together with improving the manufacturing process are believed to increase the stability of the detector. This might lead to an insensitivity to static charge [pA's] as the net signal is increased greatly [hundreds of nA's], when compared to the introduced static pA's.

Chapter 8

8 Conclusions and Future work

To conclude, it is important to clarify the significant contribution of this thesis to the scientific field. Addressing the theory of the Atmos TMOs in particular made it possible to tune current TMOs to a specific application, such as p-n hetrojunction based x-ray and UV radiation detectors. Moreover, evaluating Atmos prototype TMO detectors against the IC proved useful in estimating how far these prototypes are from current detectors. It is found that the Atmos prototype TMO detector's signal magnitude is 4.5% [average value of linearity and photon E dependence] of the IC signal magnitude. Also, reproducibility is found to be decreased by 17% at 24 h in the prototype TMO detectors, compared to the IC, which has 0.3% variation in 24 h. All these factors make the initial design far from its true potential, compared to the desired features.

EM enabled solutions of the physical limitations of the prototypes, such as electrode structure and surface granularity. This led to the application of the new methods of PVD and surface preparation [polishing and sputtering]. PVD improved the prototype signal magnitude and sensitivity by 18% and 39%, respectively. On top of that, the PVD played a big role in reproducibility as it was improved from 17% at 24 h in the prototype to the 3.5% at 24 h in the PVD. On the other hand, surface preparation improved the magnitude of the signal to increase from pA to nA, making the TMO detectors' signal magnitude comparable to those of the IC and Si photodiode for both x-ray and UV detection. This is because a good agreement between the correlation of Si photodiode and PVD TMO detectors were obtained with linear response [R^2=0.999].

Calculations of ε_i proved that the factor which prevents the current TMO detectors from their true potential is the CCE. Relatively low ε_i values were calculated for TMO [0.02%], when compared to CZT values for ε_i [0.47%] at 33 keV. This is believed to be mainly due to defects inherited from the manufacturing process.

According to the work detailed in this thesis, TMO detectors show high potential to be used as radiation detectors. It was demonstrated that TMO detectors are feasible as room temperature photovoltaic radiation detectors. This is together with the fact that TMO detectors are able to detect radiation in the E range of 5 eV up to 40 keV. This range of E opens the field in front of the TMO detectors to be applied widely in many fields.

Therefore, it is the time to directly compare the current TMO detectors performance with the desirable detector features detailed in 1.2 Desirable Detector Specifications. The same sequence of features will be listed for ease of use as follows.

- Cost and Robustness

TMOs are found to be much cheaper than survey meters and Si solar panels. For example, Si solar panel would cost £700 per m^2 (9), compared to the TMO, which will cost less than £100 per m^2. This price includes the manufacturing process as well. Also, in comparison with market survey meters, TMOs can provide sensitivity to the same range of energy [> 7 keV of γ–ray] with much lower price.

In terms of robustness, TMOs is not fragile, compared to IC and can be more robust than Si e.g. Si Mohs hardness is 6.5, while, Cr_2O_3 Mohs hardness is 7 (11). On top of that TMOs do not require the presence of the passivation film on top of the active area surface, which makes life easier for the manufacturer and user. Annealing is the only required process to compensate for surface O loss presented in 6.3.2 Argon Ions Sputtering.

- Design

As it was expressed in 1.2 Desirable Detector Specifications, bare and large active area detectors are preferable for solar cell applications. This is because few μm of electrode on top of the active area will scatter radiation in the UV range, meanwhile, it will not contribute to the signal in the diagnostic x-ray range [see 7.2.1.6 Detailed Line Profile] (3).

This means that the first design [see Figure 6] is more convenient for Solar cell applications, whereas, the second design [see Figure 7] is more convenient for radiation monitoring. On top of that, the suggested co-planar buried electrode design would provide convenient design for both solar cells and radiation monitors (12), which will reduce running cost.

- Range

As it was mentioned in 1.2 Desirable Detector Specifications, typical diagnostic x-ray IC covers the range from 25 kV to 150 kV (8,10), where TMO detectors was tested for the range of 30 kV to 80 kV and showed comparable behaviour to IC.

In terms of solar cells, TMOs were tested for the range of 5 eV to 40 eV. Although UV range starts from 3 eV (3), TMOs cannot be sensitive to less than 4 eV as TMOs are wide BG semiconductors [see 7.2.2.5 Detection Uniformity].

- Linearity

TMO detectors showed near-linear relationship with photon fluence rate, which can be quantified by the R^2=0.993, compared to IC [R^2=1]. Although this linearity is acceptable by the American Association of Physicist in Medicine, a correction factor should be applied to modify this near-linearity. Therefore, it is advisable to work out a correction factor for linearity after the manufacturing process is optimised, otherwise, the linearity will vary significantly due to the presence of defects and contamination.

- Photon Energy Dependence

As it was explained in 1.2 Desirable Detector Specifications, radiation detectors are not expected to show linear response with radiation energy. Interestingly, TMOs showed linear response with diagnostic x-ray range as it is in the IC [see Figure 71]. Also, typical pattern of the BaD ElPh beamline with Si photodiode was followed by TMO detects [see Figure 81]. This makes TMO detectors competitors to Si and IC. However, the manufacturing process is still holding these TMO detectors to meet their true potential and hence, it should be optimised according to the suggestion in 5 Identification of Materials and Limitations.

- Reproducibility and Signal Stability

TMO showed boarder line [3%] of reproducibility and stability as was sat by the American Association of Physicist in Medicine (18). This is to be compared with IC [0.3%] and Si [0.8%] reproducibility. It is believed that optimising the deposition process together with the electrode structure would improve the reproducibility to fall beyond the border line.

- Atomic Number [Z]

From Table 29 it is found that TMOs have their Z_{effe} vary from 21-24, which makes TMOs more suitable for high energies, compared to Si. Also, from Table 32, TMOs showed μ values of 13.1/cm, compared to Si, which was 2.9/cm at 33 keV. Note that, this is for 30%-defected TMOs, hence, once the manufacturing process is optimised, μ is expected to be increased by 35%.

- Efficiency

In order to compare TMOs efficiency [2%] to CZT [47%] at 33 keV, the main factor affecting TMO detectors is the CCE. Mechanical polishing was found effective to elevate the net signal by 3-4 orders of magnitude, compared to the unprepared samples. Thus, it is strongly advisable to prepare the sample after each deposition, either by mechanical polishing or sputtering. This will make TMO detectors even compatible to amorphous photovoltaic Si in the UV range, which has the maximum efficiency of 8% (3).

- Noise Level

TMOs still away from reaching 4 orders of magnitude of the noise in the diagnostic x-ray range. However, synchrotron UV could make the TMO to meet this condition [see Figure 79 Figure 87]. Moreover, polishing the surface after each deposition and controlling the deposition process defects by annealing will increase the signal dramatically to meet this condition even with diagnostic x-ray as shown in Table 22.

These novel TMO radiation detectors are at an early prototype stage, with many iterations of detector optimisation still to be carried out. However, optimised prototype TMO detectors showed comparable behaviour to IC and Si photodiode. PVD electrodes and surface preparation ought to be applied as their usefulness has been shown here. Recommendations for material depositions, such as gradual cooling process, thermal matching substrate together with nozzle masking and cleaning would increase the efficiency of the TMO detectors toward their theoretical best.

Once the optimisation of the TMO detectors is accomplished, TMO detectors can deliver a low cost, large area and robust alternative radiation monitor. By this process, it will be possible to achieve the aim of this project, which is the active wall tile.

In terms of future work, solutions presented throughout the thesis for each limitation spotted on the TMO detectors should be implemented. It was possible to fulfil some of them [PVD and surface preparation], yet, many developments are still to be applied to improve the operation of the current TMO detectors.

Detector design would have a significant effect in improving the performance of the detector and the magnitude of the output signal. Thus, the Co-planar buried electrodes design is highly recommended at this stage (12). In this design, no charge loss is expected due to the large charge carriers travelling distance. Also, as the mobility of the charge carriers in the bulk of the material is twice the mobility on the surface, CCE is expected to be improved with the buried electrodes (137). This will improve the ε_i in return.

Also, the process of annealing has been mentioned in many sites in the thesis. This is because annealing is believed to eliminate many of the defects presented in the material, and will enable the TMO layers to re-orientate their particles for relaxed packing density. Also, the effect of O loss will be eliminated due to re-oxidation of the surface, so long-term reliability is expected. Hence, vacuum annealing is highly recommended (12,140,142-144,172). Finally, the use of an alumina substrate is advisable as an alternative to the standard ceramic tile substrate. This is because alumina showed compatible thermal properties with TMO materials, and so, no cracks due to surface tension would be expected. Also, alumina offers a compact surface, which will reduce the layers migration effect provided due to ceramic substrate porosity (153,154).

References List

1. Subahi AM, Royle GJ, Griffiths JA, Speller RD, Moir-Riches P, Boardman J. Assessment of novel Transition Metal Oxide radiation detectors [Internet]. In: Nuclear Science Symposium Conference Record, 2008. NSS '08. IEEE. 2008 [cited 2010 Jun 27]. p. 2418-2423.Available from: 10.1109/NSSMIC.2008.4774843

2. Subahi AM, Griffiths JA, Mannan S, Boardman J, Moir-Riches P, Royle GJ. Assessment and development of novel transition metal oxide materials as a photovoltaic sensor [Internet]. In: Berghmans F, Mignani AG, van Hoof CA, editors. Optical Sensing and Detection. Brussels, Belgium: SPIE; 2010 [cited 2010 Jun 27]. p. 77262E-9.Available from: http://link.aip.org/link/?PSI/7726/77262E/1

3. Solanki. Solar Photovoltaics: Fundamentals Technologies And Applications. PHI Learning Pvt. Ltd. 2009.

4. Luque A, Hegedus S. Handbook of photovoltaic science and engineering. John Wiley and Sons; 2003.

5. Lawrence WG, Thacker S, Palamakumbura S, Riley KJ, Nagarkar VV. Quantum dot — Organic polymer composite materials for X-ray detection and imaging. In: 2010 IEEE Nuclear Science Symposium Conference Record (NSS/MIC). IEEE; 2010. p. 246-252.

6. Maged AF, Amin GAM, Semary M, Borham E. Metal induced effects on some physical properties of Se0.8Te0.2 amorphous system. Thin Solid Films. 2010 Mar 1;518(10):2628-2631.

7. Subahi A, Griffiths J, Petaccia L, Moir-Riches P, Boardman J, Royle G. UV Response of a Transition Metal Oxide Diode. In: NSS. USA: 2010. p. 1502-1504.

8. Fluke Biomedical [Internet]. 2011 [cited 2011 Mar 21];Available from: http://www.flukebiomedical.com/biomedical/usen/home/

9. Free Solar Panels UK [Internet]. 2011 [cited 2001 Jul 29];Available from: http://www.freesolarpanelsuk.co.uk/solar-panel-cost.php

10. 96035B Ion Chmaber [Internet]. USA: Fluke Biomedical; 2006 [cited 2011 Mar 21]. Available from: http://www.flukebiomedical.com/biomedical/usen/diagnostic-imaging-qa/x-ray-qa-instruments/10100at.htm?PID=54355

11. Zhou ZZ, Li Z, Deng QF, Wang JC, Yuan JL. Sapphire-SiO_2 Solid-Phase Reaction of Polishing Proving Research. AMR. 2011 Feb;189-193:4053-4058.

12. Mott NF, Davis EA. Electronic Processes in Non-Crystalline Materials. 1st ed. Oxford: Clarendon Press; 1971.

13. Knoll GF. Radiation Detection and Measurement. 3rd ed. USA: John Wiley & Sons; 2000.

14. Jacobson AF. Determination of peak x-ray tube potential from measurements of peak radiation intensity. Radiology. 1982 Jun;143(3):779-781.

15. Webb S. The Physics of medical imaging. Hilger; 1988.

16. Schieber M, Hermon H, Zuck A, Vilensky A, Melekhov L, Shatunovsky R, et al. Thick films of X-ray polycrystalline mercuric iodide detectors. Journal of Crystal Growth. 2001 May;225(2-4):118-123.

17. Ahmed SN. Physics and Engineering of Radiation Detection. Canada: Academic Press Elsevier; 2007.

18. Wagner L. RECOMMENDATIONSON PERFORMANCE CHARACTERISTICSOF DIAGNOSTIC EXPOSURE METERS. USA: American Association of Physicists in Medicine; 1992.

19. Theocharous E. Absolute linearity measurements on a PbSe detector in the infrared. Infrared Physics & Technology. 2007 Mar;50(1):63-69.

20. Veale M. Charge Transport and Low Temperature Phenomena in Single Crystal CdZnTe. 2009;

21. Giakos GC, Guntupalli R, De Abreu-Garcia JA, Shah N, Vedantham S, Suryanarayanan S, et al. Intrinsic sensitivity of Cd1-xZnxTe semiconductors for digital radiographic imaging. Instrumentation and Measurement, IEEE Transactions on. 2003;52(5):1559-1565.

22. Kong X, Liu C, Dong W, Zhang X, Tao C, Shen L, et al. Metal-semiconductor-metal TiO[sub 2] ultraviolet detectors with Ni electrodes. Appl. Phys. Lett. 2009;94(12):123502.

23. Glatzel T, Marron DF, Schedel-Niedrig T, Sadewasser S, Lux-Steiner MC. CuGaSe2 solar cell cross section studied by Kelvin probe force microscopy in ultrahigh vacuum. Applied Physics Letters. 2002 Sep;81(11):2017-2019.

24. Gerloch M, Constable EC. Transition Metal Chemistry: Valence Shell in d-Block Chemistry. Wiley VCH; 1994.

25. Bismuto A, Lettieri S, Maddalena P, Baratto C, Comini E, Faglia G, et al. Room-temperature gas sensing based on visible photoluminescence properties of metal oxide nanobelts. J. Opt. A: Pure Appl. Opt. 2006 Jul;8(7):S585-S588.

26. Yamashita T, Hayes P. Analysis of XPS spectra of Fe2+ and Fe3+ ions in oxide materials. Applied Surface Science. 2008 Feb 15;254(8):2441-2449.

27. Cox PA. Transition Metal Oxides. Oxford, UK: Clarendon Press; 1992.

28. Gaule G, LaPlante P, Levy S, Schneider S. Metal-oxide devices for rapid high current switching. In: Electron Devices Meeting, 1976 International. 1976. p. 279-282.

29. Mitsuoka M, Otofuji A, Arakawa T. Sensing properties of LnMO3/SnO2 (Ln = rare earth, M = Cr, Co, Mn, Fe) having a heterojunction. Sensors and Actuators B: Chemical. 1992 Oct;9(3):205-207.

30. Traversa E, Bearzotti A, Miyayama M, Yanagida H. Influence of the electrode materials on the electrical response of Zno-based contact sensors. Journal of the European Ceramic Society. 1998;18(6):621-631.

31. Chekhomova LF. Abrasive Properties of Modified Chromia. Inorganic Materials. 37(3):274-280.

32. Kröger M, Hamwi S, Meyer J, Riedl T, Kowalsky W, Kahn A. P-type doping of organic wide band gap materials by transition metal oxides: A case-study on Molybdenum trioxide. Organic Electronics. 2009 Aug;10(5):932-938.

33. Michel C, Baerends EJ. What Singles out the FeO2+ Moiety? A Density-Functional Theory Study of the Methane-to-Methanol Reaction Catalyzed by the First Row Transition-Metal Oxide Dications MO(H2O)p2+, M = V−Cu. Inorganic Chemistry. 2009 Apr 20;48(8):3628-3638.

34. Duffy JA. Bonding, Energy Levels and Bands in Inorganic Solids. Aberdeen, UK: Longman Group Limited; 1990.

35. Mehrabian M, Azimirad R, Mirabbaszadeh K, Afarideh H, Davoudian M. UV detecting properties of hydrothermal synthesized ZnO nanorods. Physica E: Low-dimensional Systems and Nanostructures. 2011 Apr;43(6):1141-1145.

36. Liang S, Sheng H, Liu Y, Huo Z, Lu Y, Shen H. ZnO Schottky ultraviolet photodetectors. Journal of Crystal Growth. 2001 May;225(2-4):110-113.

37. Young SJ, Ji LW, Fang TH, Chang SJ, Su YK, Du XL. ZnO ultraviolet photodiodes with Pd contact electrodes. Acta Materialia. 2007 Jan;55(1):329-333.

38. Ohta H, Kamiya M, Kamiya T, Hirano M, Hosono H. UV-detector based on pn-heterojunction diode composed of transparent oxide semiconductors, p-NiO/n-ZnO. Thin Solid Films. 2003 Dec 15;445(2):317-321.

39. Sun JR, Xiong CM, Shen BG, Wang PY, Weng YX. Manganite-based heterojunction and its photovoltaic effects. Appl. Phys. Lett. 2004;84(14):2611.

40. Seong H, Cho K, Kim S. A pn heterojunction diode constructed with a n-type ZnO nanowire and a p-type HgTe nanoparticle thin film. Appl. Phys. Lett. 2009;94(4):043102.

41. Du X, Mei Z, Liu Z, Guo Y, Zhang T, Hou Y, et al. Controlled Growth of High-Quality ZnO-Based Films and Fabrication of Visible-Blind and Solar-Blind Ultra-Violet Detectors. Advanced Materials. 2009 Dec 4;21(45):4625-4630.

42. Zhu H, Shan CX, Wang LK, Zheng J, Zhang JY, Yao B, et al. Metal−Oxide−Semiconductor-Structured MgZnO Ultraviolet Photodetector with High Internal Gain. The Journal of Physical Chemistry C. 2010 Apr 22;114(15):7169-7172.

43. Kuznetsov IA, Greenfield MJ, Mehta YU, Merchan-Merchan W, Salkar G, Saveliev AV. Increasing the solar cell power output by coating with transition metal-oxide nanorods. Applied Energy [Internet]. [cited 2011 May 26];In Press, Corrected Proof. Available from: http://www.sciencedirect.com/science/article/pii/S0306261911002558

44. Arshak K, Corcoran J, Korostynska O. Gamma radiation sensing properties of TiO2, ZnO, CuO and CdO thick film pn-junctions. Sensors and Actuators A: Physical. 2005 Sep 23;123-124:194-198.

45. Arshak K, Korostynska O, Henry J. MnO/TeO2 thin film gamma radiation sensors. In: Microelectronics, 2004. 24th International Conference on. 2004. p. 177-180 vol.1.

46. Arshak K, Korostynska O. Preliminary studies of properties of oxide thin/thick films for gamma radiation dosimetry. Materials Science and Engineering B. 2004 Mar 15;107(2):224-232.

47. Arshak K, Korostynska O. Influence of gamma radiation on the electrical properties of MnO and MnO/TeO2 thin films. Annalen der Physik. 2004 Jan 29;13(1-2):87-89.

48. Arshak K, Arshak A, Zleetni S, Korostynska O. Thin and thick films of metal oxides and metal phthalocyanines as gamma radiation dosimeters. Nuclear Science, IEEE Transactions on. 2004;51(5):2250-2255.

49. Korostynska O, Arshak K, Mahon M. Gamma radiation sensing properties of NiO thick film pn-junctions. In: Sensors, 2003. Proceedings of IEEE. 2003. p. 79-83 Vol.1.

50. Rao CN, Raveau B. Transition Metal Oxides. Canada: John Wiley & Sons; 1998.

51. Okutan M, Bakan HI, Korkmaz K, Yakuphanoglu F. Variable range hopping conduction and microstructure properties of semiconducting Co-doped TiO2. Physica B: Condensed Matter. 2005 Jan 31;355(1-4):176-181.

52. Iordanova N, Dupuis M, Rosso KM. Charge transport in metal oxides: a theoretical study of hematite alpha-Fe2O3. J Chem Phys. 2005 Apr 8;122(14):144305.

53. Cornell RM, Schwertmann U. The Iron Oxides. Germany: VCH; 1996.

54. Reinert F, Hüfner S. Photoemission spectroscopy—from early days to recent applications. New J. Phys. 2005 Apr;7:97-97.

55. Tokura Y. Correlated-Electron Physics in Transition-Metal Oxides. Phys. Today. 2003;56(7):50.

56. Stoneham AM. Electronic and defect processes in oxides. The polaron in action. Dielectrics and Electrical Insulation, IEEE Transactions on. 1997;4(5):604-613.

57. Mott NF. Conduction in glasses containing transition metal ions. Journal of Non-Crystalline Solids. 1968 Dec;1(1):1-17.

58. Tanner B. Introduction to the Physics of Electrons in Solids. Durham, UK: Cambridge University Press; 1995.

59. Brennan KF. The Physics of Semiconductors. UK: Cambridge University Press; 1999.

60. Qin P, Fang G, Sun N, Fan X, Zheng Q, Chen F, et al. Organic solar cells with p-type amorphous chromium oxide thin film as hole-transporting layer. Thin Solid Films. 2011 Apr 29;519(13):4334-4341.

61. Jonsson A. Charge Transport in Transition Metal Oxide Thin Films and Electrochromic Devices. 2001;

62. Boufayed F, Leroy S, Teyssedre G, Laurent C, Segur P, Dissado LA, et al. Simulation of bipolar charge transport in polyethylene featuring trapping and hopping conduction through an exponential distribution of traps. In: International Symposium on Electrical Insulating Materials. Los Alamitos, CA, USA: IEEE Computer Society; 2005. p. 340-343 Vol. 2.

63. Mott NF. Metal - Insulator Transitions. 2nd ed. Cambridge, UK: Taylor & Francis; 1990.

64. Hopfield JJ. Electron Transfer Between Biological Molecules by Thermally Activated Tunneling. Proceedings of the National Academy of Sciences of the United States of America. 1974;71(9):3640-3644.

65. Hornung M, Löhneysen H. Crossover from Mott to Efros-Shklovskii variable range-hopping in Si:P. Czechoslovak Journal of Physics. 1996 May 1;46(0):2437-2438.

66. Efros AL, Shklovskii BI. Coulomb Gap and Low Temperature Conductivity of Disordered Systems. J. Phys. C: Solid State Phys. 1975;8(4).

67. Chaparadza A, Rananavare S. Towards p-type Conductivity in SnO2 Nanocrystals through Li Doping. IOP. 2010;21(3).

68. Wu J, Huang Z, Hou Y, Gao Y, Chu J. Variation in hopping conduction across the magnetic transition in spinel Mn[sub 1.56]Co[sub 0.96]Ni[sub 0.48]O[sub 4] films. Appl. Phys. Lett. 2010;96(8):082103.

69. Lamba S, Kumar D. Variable-range hopping: Role of Coulomb interactions. Phys. Rev. B. 1999 Feb 15;59(7):4752.

70. Boutiche S. Variable Range Hopping Conductivity: Case of the non-constant density of states. HAL [Internet]. 2005;Available from: http://hal.archives-ouvertes.fr/docs/00/03/00/41/PDF/Variable_range_hopping_conductivity.pdf

71. Anderson PW. Absence of Diffusion in Certain Random Lattices. Phys. Rev. 1958 Mar 1;109(5):1492.

72. Miller A, Abrahams E. Impurity Conduction at Low Concentrations. Phys. Rev. 1960 Nov 1;120(3):745.

73. Shante VKS. Hopping conduction in quasi-one-dimensional disordered compounds. Phys. Rev. B. 1977;16(6):2597.

74. Triberis GP. A conductivity study on V2O5 layers deposited from gels. Journal of Non-Crystalline Solids. 1988 Aug;104(1):135-138.

75. Jung W-H. Variable range hopping conduction in Gd1/3Sr2/3FeO3. Physica B: Condensed Matter. 2001 Sep;304(1-4):75-78.

76. Yu D, Wang C, Wehrenberg BL, Guyot-Sionnest P. Variable Range Hopping Conduction in Semiconductor Nanocrystal Solids. Phys. Rev. Lett. 2004 May 25;92(21):216802.

77. Mott NF. Introductory talk; Conduction in non-crystalline materials. Journal of Non-Crystalline Solids. 1972 Jun;8-10:1-18.

78. Prior J, Somoza AM, Ortuño M. Quantum effects in Mott's variable-range hopping. physica status solidi (c). 2004;1(1):136-139.

79. Huang Y-L, Chiu S-P, Zhu Z-X, Li Z-Q, Lin J-J. Variable-range-hopping conduction processes in oxygen deficient polycrystalline ZnO films. J. Appl. Phys. 2010;107(6):063715.

80. Redfield D. Observation of log sigma ~T-12 in Three-Dimensional Energy-Band Tails. Phys. Rev. Lett. 1973 Jun 25;30(26):1319.

81. Innovations Technology Access Centre - Atmos Technologies Ltd [Internet]. 2011 [cited 2011 Mar 4];Available from: http://www.itac.stfc.ac.uk/Tenants/20603.aspx

82. 2D Heat Ltd. [Internet]. 2011 [cited 2011 Mar 4];Available from: http://www.2dheat.com/

83. Thermal Spraying Process [Internet]. TWI. 2011 [cited 2011 Jun 25];Available from: http://www.twi.co.uk/content/bptsps02.html#ref2

84. Thermal Spray [Internet]. Hazmat Alternatives. 2009 [cited 2011 Jun 25];Available from: http://www.hazmat-alternatives.com/

85. Wasa K, Hayakawa S. Handbook of sputter deposition technology: principles, technology, and applications. William Andrew; 1992.

86. COMET. Metal-Ceramic X-ray Tube Assembly [Internet]. Switzerland: Available from: http://www.comet.ch/en

87. AGO. A.G.O. HS X-ray System. UK:

88. Meyer P, Buffard E, Mertz L, Kennel C, Constantinesco A, Siffert P. Evaluation of the use of six diagnostic X-ray spectra computer codes. Br J Radiol. 2004 Mar 1;77(915):224-230.

89. Attix FH. Introduction to Radiological Physics and Radiation Dosimetry. 1st ed. Wiley-VCH; 1986.

90. National Institute of Standars and Technology [Internet]. 2011 [cited 2011 Feb 1];Available from: http://www.nist.gov/index.html

91. Goldstein J, Newbury DE, Joy DC, Lyman CE, Echlin P, Lifshin E, et al. Scanning Electron Microscopy and X-ray Microanalysis. 3rd ed. Springer; 2003.

92. Gautreau R, Savin W. Modern Physics. New Jersey, USA: McGraw-Hill; 1999.

93. Thomson J, Callick EB. Electron Physics and Technology. London, UK: The English Universities Press LTD; 1959.

94. EDS Analysis using The S-3400 SEM [Internet]. Electron Microscope Unit. 2007 Aug 13 [cited 2008 Aug 3];Available from: http://srv.emunit.unsw.edu.au/pdfs/S3400%20EDS%20%20BSE%20user%20notes.pdf

95. Hitachi S-3400N [Internet]. Hitachi High-Technologies. 2008 [cited 2008 Aug 3];Available from: http://www.hht-eu.com/pls/hht/wt_show.text_page?p_text_id=5405&p_htr_url_id=349&p_htr_search=vp&p_htr_fuzzy=0&p_flag=(hht-eu)

96. Hitachi S-3400 SEM User Guide [Internet]. Electron Microscope Unit. 2007 Jun 28 [cited 2008 Aug 3];Available from: http://srv.emunit.unsw.edu.au/pdfs/S3400%20USER%20NOTES_high%20vac110407.pdf

97. INCA Microanalysis System [Internet]. Oxford Instruments. 2005 [cited 2008 Aug 3];Available from: http://www.x-raymicroanalysis.com/pages/main/inca.htm

98. Subahi A. An Investigation into the Performance of an Autoradiographic Film Digitisation System. 2007;

99. Taylor JR. An Introduction to Error Analysis: The Study of Uncertainties in Physical Measurements. 2nd ed. University Science Books; 1996.

100. OriginPro 8 [Internet]. OriginLab. 2008 [cited 2008 Aug 6];Available from: http://www.originlab.com/

101. Schumann W. Minerals of the World. Sterling Publishing Company, Inc. 2008.

102. Schubert EF. Light-emitting diodes. Cambridge University Press; 2006.

103. Noferesti H, Rao KS. Role of Crystal Interlocking on the Strength of Brittle Rocks. Rock Mech Rock Eng. 2010 Apr;44(2):221-230.

104. ImageJ [Internet]. 2004 Nov 17 [cited 2011 Mar 31];Available from: http://imagej.nih.gov/ij/

105. GIMP [Internet]. 2011 [cited 2011 Apr 26];Available from: http://www.gimp.org/

106. Bohndiek SE, Royle GJ, Speller RD. An active pixel sensor x-ray diffraction (APXRD) system for breast cancer diagnosis. Phys. Med. Biol. 2009 Jun;54(11):3513-3527.

107. Pappachen James A, Dimitrijev S. Inter-image outliers and their application to image classification. Pattern Recognition. 2010 Dec;43(12):4101-4112.

108. Upton G, Cook I. Understanding statistics. Oxford University Press; 1996.

109. What are outliers in the data? [Internet]. NIST. 2010 [cited 2011 Apr 27];Available from: http://www.itl.nist.gov/div898/handbook/prc/section1/prc16.htm

110. Reichelt K, Jiang X. The preparation of thin films by physical vapour deposition methods. Thin Solid Films. 1990 Oct 1;191(1):91-126.

111. Zeghbroeck BV. Principles of Semiconductor Devices [Internet]. USA: University of Colorado; 2007 [cited 2010 Sep 28]. Available from: http://ecee.colorado.edu/~bart/book/book/chapter3/ch3_5.htm#3_5_2

112. Sze SM, Ng KK. Physics of semiconductor devices. John Wiley and Sons; 2007.

113. Yang W-Y, Rhee S-W. Effect of electrode material on the resistance switching of Cu[sub 2]O film. Appl. Phys. Lett. 2007;91(23):232907.

114. Lawrence Berkeley National Laboratory. X-ray Data Booklet [Internet]. USA: Center for X-ray Optics and Advanced Light Source; 2001. Available from: http://xdb.lbl.gov/

115. Elettra Synchrotron [Internet]. 2011 [cited 2011 Mar 15];Available from: http://www.elettra.trieste.it/

116. Wagner CD, Riggs WM, Davis LE, Moulder JF. Handbook of X-ray Photoelectron Spectroscopy. 1st ed. USA: Perkin-Elmer; 1979.

117. Briggs D. Practical surface analysis : by auger and x-ray photoelectron spectroscopy. Chichester ;;New York: Wiley; 1983.

118. Oku M, Suzuki S, Ohtsu N, Shishido T, Wagatsuma K. Comparison of intrinsic zero-energy loss and Shirley-type background corrected profiles of XPS spectra for quantitative surface analysis: Study of Cr, Mn and Fe oxides. Applied Surface Science. 2008 Jun 15;254(16):5141-5148.

119. Biesinger MC, Lau LWM, Gerson AR, Smart RSC. Resolving surface chemical states in XPS analysis of first row transition metals, oxides and hydroxides: Sc, Ti, V, Cu and Zn. Applied Surface Science. 2010 Nov 15;257(3):887-898.

120. Cerrato JM, Hochella MF, Knocke WR, Dietrich AM, Cromer TF. Use of XPS to Identify the Oxidation State of Mn in Solid Surfaces of Filtration Media Oxide Samples from Drinking Water Treatment Plants. Environmental Science & Technology. 2010;44(15):5881-5886.

121. NIST X-ray Photoelectron Spectroscopy Database [Internet]. 2007 Aug 27 [cited 2011 May 8];Available from: http://srdata.nist.gov/xps/Default.aspx

122. Biesinger MC, Payne BP, Lau LWM, Gerson A, Smart RSC. X-ray photoelectron spectroscopic chemical state quantification of mixed nickel metal, oxide and hydroxide systems. Surf. Interface Anal. 2009 Apr;41(4):324-332.

123. Grant JT. Methods for quantitative analysis in XPS and AES. Surf. Interface Anal. 1989 Jun;14(6-7):271-283.

124. Biesinger MC, Payne BP, Hart BR, Grosvenor AP, McIntryre NS, Lau LW, et al. Quantitative chemical state XPS analysis of first row transition metals, oxides and hydroxides. J. Phys.: Conf. Ser. 2008 Mar;100(1):012025.

125. Petaccia L, Vilmercati P, Gorovikov S, Barnaba M, Bianco A, Cocco D, et al. BaD ElPh: A 4 m normal-incidence monochromator beamline at Elettra. Nuclear Instruments and Methods in Physics Research Section A: Accelerators, Spectrometers, Detectors and Associated Equipment. 2009 Jul 21;606(3):780-784.

126. TX400 X-ray Source [Internet]. PSP Vacuum Technology. 2011 [cited 2011 Mar 1];Available from: http://home.btconnect.com/pspvacuum99/x-ray_source.html

127. Electron Analyser and CCD Detector [Internet]. SPECS. 2011 [cited 2011 Mar 15];Available from: http://www.specs.de/cms/front_content.php?idcat=209

128. AXUV-100 Photodiode [Internet]. International Radiation Detector Inc. 2010 [cited 2011 Mar 15];Available from: http://www.ird-inc.com/

129. XMuDat [Internet]. IAEA. 1998 [cited 2011 May 23];Available from: http://www-nds.iaea.org/reports/nds-195.htm

130. Hubbell JH, Seltzer SM. Tables of X-Ray Mass Attenuation Coefficientsand Mass Energy-Absorption Coefficientsfrom 1 keV to 20 MeV for Elements Z = 1 to 92and 48 Additional Substances of Dosimetric Interest [Internet]. NIST: X-Ray Mass Attenuation Coefficients. 1995 [cited 2011 May 23];Available from: http://www.nist.gov/pml/data/xraycoef/index.cfm

131. Dedek N, Speller RD, Spendley P, Horrocks JA. Performance Evaluation of 98 CZT Sensors for Their Use in Gamma-Ray Imaging. Nuclear Science, IEEE Transactions on. 2008;55(5):2689-2697.

132. CZT SPEAR Detector [Internet]. Endicott Interconnect Technologies Inc. 2011 [cited 2011 Mar 20];Available from: http://www.evmicroelectronics.com/spear.html

133. Ignatov SM, Potapov VN. Parameters of the new scintillation detectors. Instrum Exp Tech. 2011 Apr;54(2):169-175.

134. Cember H. Introduction to Health Physics. 3rd ed. McGraw-Hill Medical; 1996.

135. Alkhazov GD, Komar AP, Vorob'ev AA. Ionization fluctuations and resolution of ionization chambers and semiconductor detectors. Nuclear Instruments and Methods. 1967 Feb 2;48(1):1-12.

136. Martin CJ. An evaluation of semiconductor and ionization chamber detectors for diagnostic x-ray dosimetry measurements. Phys. Med. Biol. 2007 Aug;52(15):4465-4480.

137. Busch KW, Busch MA. Multielement Detection Systems for Spectrochemical Analysis. Wiley-Interscience; 1990.

138. Tan M, Liu Q, Zhang N, Hu H, Li B, Kang X. Characterization of the surface film on Zr-based bulk metallic glass using X-ray photoelectron spectroscopy (XPS) and scanning electron microscopy (SEM). Journal of Alloys and Compounds. 2011 May 12;509(19):5926-5930.

139. Schulz C, Kuhr S, Geffers H, Schmidt T, Flege JI, Aschenbrenner T, et al. Cleaning of GaN(2110) surfaces. J. Vac. Sci. Technol. A. 2011;29(1):011013.

140. van Diepen AM, Lotgering FK. Preparation and Mössbauer spectra of CoV2O4 spinel doped with Fe2+ on tetrahedral sites. Solid State Communications. 1978 Dec;28(11):951-955.

141. Prineas JP. PIN versus PN homojunctions in GaInAsSb 2.0-2.5 micron mesa photodiodes [Internet]. In: Proceedings of SPIE. San Jose, CA, USA: 2006 [cited 2011 May 25]. p. 611903-611903-8.Available from: http://spie.org/x648.html?product_id=647109

142. Grosvenor AP, Biesinger MC, Smart RSC, McIntyre NS. New interpretations of XPS spectra of nickel metal and oxides. Surface Science. 2006 May 1;600(9):1771-1779.

143. Grosvenor AP, Kobe BA, McIntyre NS. Examination of the oxidation of iron by oxygen using X-ray photoelectron spectroscopy and QUASESTM. Surface Science. 2004 Sep 10;565(2-3):151-162.

144. Gong Y, Zhou M, Andrews L. Spectroscopic and theoretical studies of transition metal oxides and dioxygen complexes. Chem. Rev. 2009 Dec;109(12):6765-6808.

145. Taylor J, Institute of Ceramics (Great Britain). Ceramics glaze technology. 1st ed. Oxford [Oxfordshire] ;;New York: Published on behalf of the Institute of Ceramics by Pergamon Press; 1986.

146. Ahrens TJ. A Handbook of Physical Constants. Washington: American Geophysical Union; 1995.

147. Bayer G. Thermal expansion of oxide compounds with spinel structure. Thermochimica Acta. 1972 Apr;3(6):421-426.

148. Watanabe H, Yamada N, Okaji M. Linear Thermal Expansion Coefficient of Silicon from 293 to 1000 K. International Journal of Thermophysics. 2004 Jan;25(1):221-236.

149. Schneider H, Eberhard E. Thermal Expansion of Mullite. Journal of the American Ceramic Society. 1990 Jul 1;73(7):2073-2076.

150. Min W, Miyahara D, Yokoi K, Yamaguchi T, Daimon K, Hikichi Y, et al. Thermal and mechanical properties of sintered LaPO4-Al2O3 composites. Materials Research Bulletin. March;36(5-6):939-945.

151. Kumaravel A, Ganesan N, Sethuraman R. Steady-state analysis of a three-layered electro-magneto-elastic strip in a thermal environment. Smart Mater. Struct. 2007 Apr;16(2):282-295.

152. Lacheisserie EDT de, Gignoux D, Schlenker M. Magnetism: Fundamentals. Springer; 2005.

153. Alumina Substrate [Internet]. Leatec Fine Ceramics Co. 2007 [cited 2011 Apr 10];Available from: http://www.leatec.com.tw/index/index2/lang/en.html

154. KLUG FJ, PROCHAZKA S, DOREMUS RH. Alumina-Silica Phase Diagram in the Mollite Region. Journal of the American Ceramic Society. 1987 Oct 1;70(10):750-759.

155. Jeong YK, Choi GM. Nonstoichiometry and electrical conduction of CuO. Journal of Physics and Chemistry of Solids. 1996 Jan;57(1):81-84.

156. Kronawitter CX, Mao SS, Antoun BR. Doped, porous iron oxide films and their optical functions and anodic photocurrents for solar water splitting. Appl. Phys. Lett. 2011;98(9):092108.

157. Rider DA, Tucker RT, Worfolk BJ, Krause KM, Lalany A, Brett MJ, et al. Indium tin oxide nanopillar electrodes in polymer/fullerene solar cells. Nanotechnology. 2011 Feb;22(8):085706.

158. Schaeffer JK, Samavedam SB, Gilmer DC, Dhandapani V, Tobin PJ, Mogab J, et al. Physical and electrical properties of metal gate electrodes on HfO2 gate dielectrics. 2003;

159. Edge LF, Vo T, Paruchuri VK, Iijima R, Bruley J, Jordan-Sweet J, et al. Materials and electrical characterization of physical vapor deposited La[sub x]Lu[sub 1−x]O[sub 3] thin films on 300 mm silicon. Appl. Phys. Lett. 2011;98(12):122905.

160. Wenthold PG, Gunion RF, Lineberger WC. Ultraviolet negative-ion photoelectron spectroscopy of the chromium oxide negative ion. Chemical Physics Letters. 1996 Aug 9;258(1-2):101-106.

161. Chromium Oxide [Internet]. NIST Chemistry WebBook. 2011 [cited 2011 May 3];Available from: http://webbook.nist.gov/cgi/cbook.cgi?ID=C196695622&Mask=20#ref-1

162. Bessekhouad Y, Trari M. Photocatalytic hydrogen production from suspension of spinel powders AMn2O4(A=Cu and Zn). International Journal of Hydrogen Energy. 2002 Apr;27(4):357-362.

163. Wilde M, Beauport I, Stuhl F, Al-Shamery K, Freund H-J. Adsorption of potassium on Cr2O3(0001) at ionic and metallic coverages and uv-laser-induced desorption. Phys. Rev. B. 1999 May;59(20):13401-13412.

164. Lide D. Handbook of Chemistry and Physics. 89th ed. CRC Press; 2008.

165. Chikamatsu M, Nagamatsu S, Taima T, Yoshida Y, Sakai N, Yokokawa H, et al. C60 thin-film transistors with low work-function metal electrodes. 2004;

166. Centurioni E, Iencinella D. Role of front contact work function on amorphous silicon/crystalline silicon heterojunction solar cell performance. Electron Device Letters, IEEE. 2003;24(3):177-179.

167. Ilyina TN, Sevostyanov VS, Uralskii VI, Sevostyanov MV, Shkarpetkin EA. Research, design, calculations, and operating experience. Processes and equipment for chemical and oil-gas production. Chem Petrol Eng. 2010 Jul;46(3-4):193-200.

168. Chen M, Shu J, Mao H-kwang. Xieite, a new mineral of high-pressure FeCr2O4 polymorph. Chin. Sci. Bull. 2008 Sep;53(21):3341-3345.

169. Qamar A, Mahmood A, Sarwar T, Ahmed N. Synthesis and characterization of porous crystalline SiC thin films prepared by radio frequency reactive magnetron sputtering technique. Applied Surface Science. 2011 May 15;257(15):6923-6927.

170. Grim JR, Benamara M, Skowronski M, Everson WJ, Heydemann VD. Transmission electron microscopy analysis of mechanical polishing-related damage in silicon carbide wafers. Semicond. Sci. Technol. 2006 Dec;21(12):1709-1713.

171. Negri RE, Taylor JW, Beall CE, Rosseel TM. Quantitative oxidation-state determination of titanium and manganese in binary oxide mixtures by photoelectron spectroscopy. Analytical Chemistry. 1986 Nov 1;58(13):2637-2640.

172. Henrich VE, Cox PA. The surface science of metal oxides. Cambridge University Press; 1996.

173. Kung HH. Transition metal oxides: surface chemistry and catalysis. Elsevier; 1989.

174. Zangwill A. Physics at surfaces. Cambridge University Press; 1988.

175. Pisarev RV, Moskvin AS, Kalashnikova AM, Rasing T. Charge transfer transitions in multiferroic BiFeO_{3} and related ferrite insulators. Phys. Rev. B. 2009 Jun 23;79(23):235128.

176. Ilavsky J. Microstructure - Wear and Corrosion Relationships for Thermally Sprayed Metallic Deposits. In: Surface Engineering via Applied Research. Canada: EMPA (Swiss Federal Laboratories for Materials Testing and Research); 2000. p. 449-454.

177. Salvi SV, Parab MR. Synthesis and Characteristics of Nickel Manganite by Lithiation. Turkish Journal of Physics. 2000 Nov 1;24:701-708.

178. Bushberg JT. The essential physics of medical imaging. Lippincott Williams & Wilkins; 2002.

179. Takahashi T, Watanabe S. Recent progress in CdTe and CdZnTe detectors. Nuclear Science, IEEE Transactions on. 2001;48(4):950-959.

180. de Jonge MD, Tran CQ, Chantler CT, Barnea Z. Improved techniques for measuring x-ray mass attenuation coefficients. Opt. Eng. 2006;45(4):046501.

181. Sangaletti L, Depero LE, Bagus PS, Parmigiani F. A proper Anderson Hamiltonian treatment of the 3s photoelectron spectra of MnO, FeO, CoO and NiO. Chemical Physics Letters. 1995 Nov 3;245(4-5):463-468.

182. Lee W, Lee T. A compact Compton camera using scintillators for the investigation of nuclear materials. Nuclear Instruments and Methods in Physics Research Section A: Accelerators, Spectrometers, Detectors and Associated Equipment. 2010 Dec 1;624(1):118-124.

183. Keithley Instruments. Model 6487 Picoammeter/Voltage Source Reference Manual [Internet]. 2002;Available from: www.keithley.com

184. Esten MJ. Treatment of Experimental Data. UK: UCL; 2004.

9 Appendices

9.1 Electron Microscopy

9.1.1 Electron Microscopy Spatial Resolution

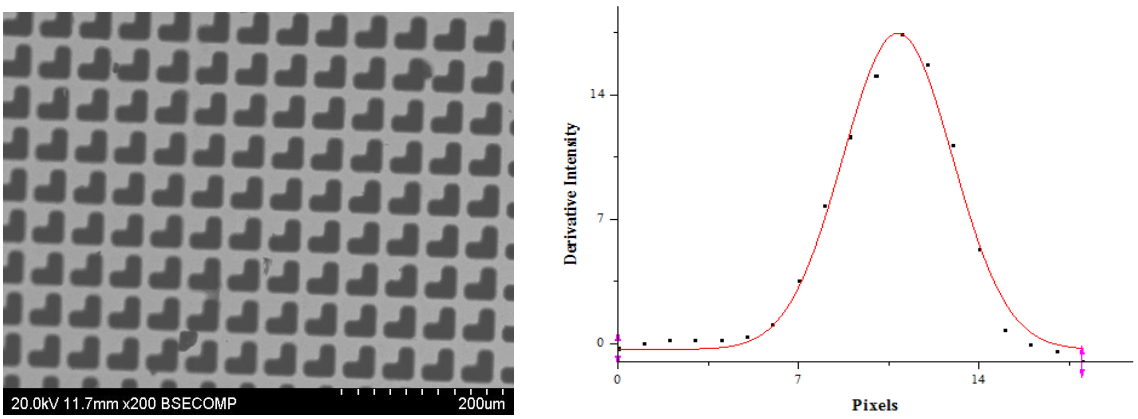

Figure 88: x200 magnification of SSR patches [left] and differentiated data points with fitted Gaussian model [right]

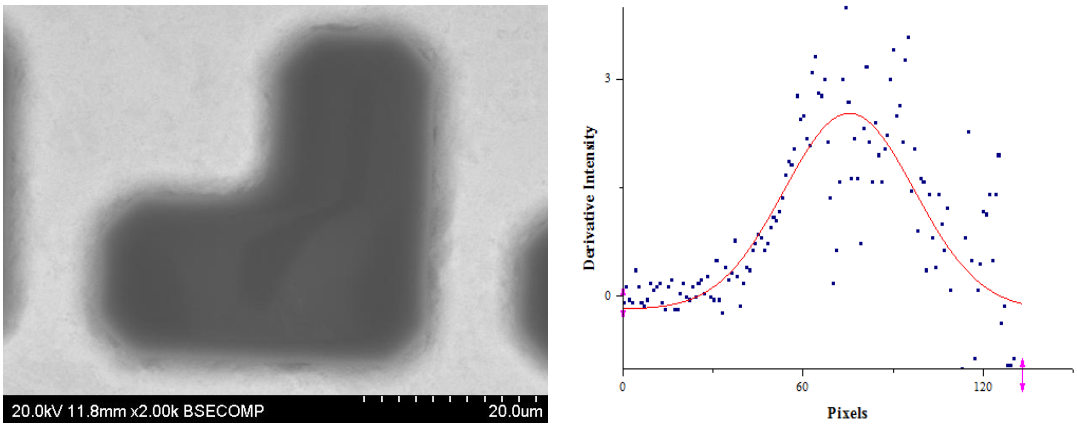

Figure 89: x2k magnification of SSR patches [left] and differentiated data points with fitted Gaussian model [right]

9.1.2 Grain Size and Nature

9.1.2.1 Pre-oxidised Powders

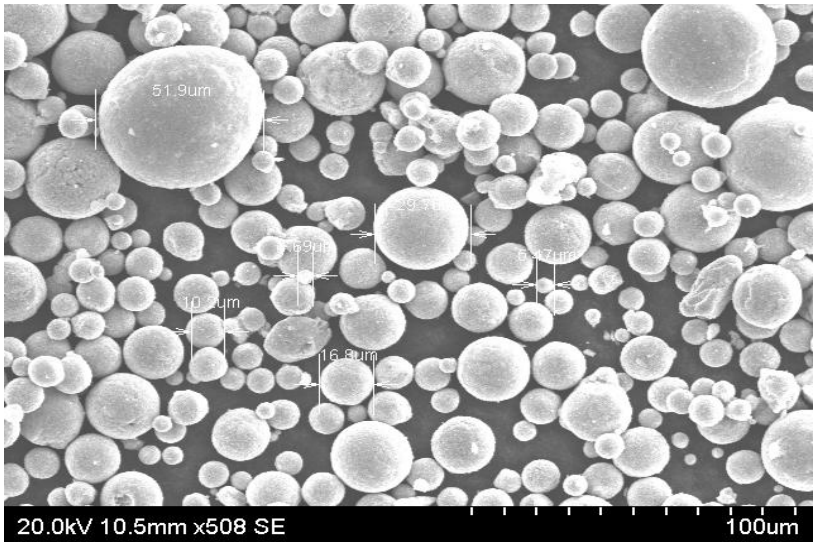

Figure 90: n-type MnNi pre-oxidised powder grain before flame-spray [max 50±5 µm]

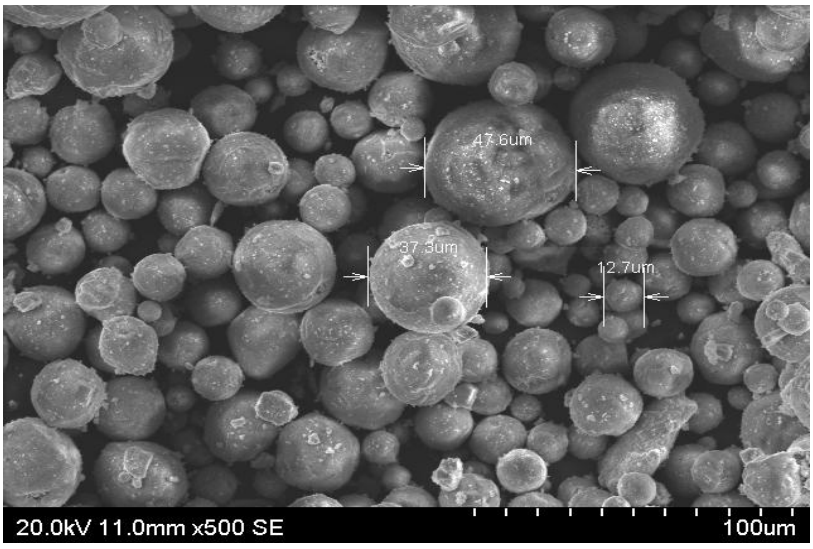

Figure 91: n-type NiAl pre-oxidised powder grain before flame-spray [max 50±5 µm]

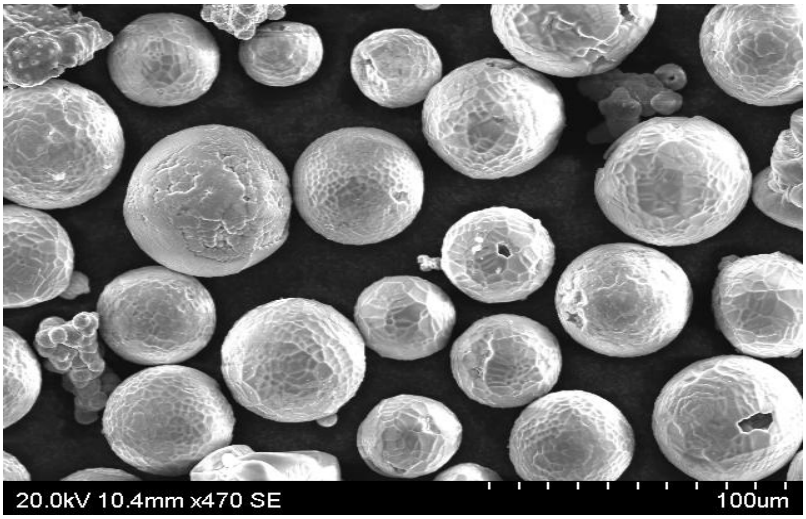

Figure 92: p-type Ni pre-oxidised powder grain before flame-spray [max 60±5 µm]

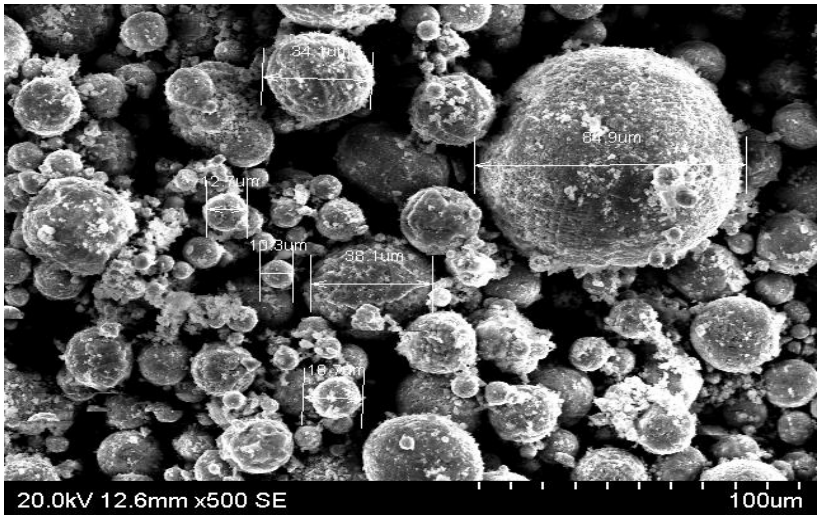

Figure 93: p-type FeCr pre-oxidised powder grain before flame-spray [max 85±5 µm]

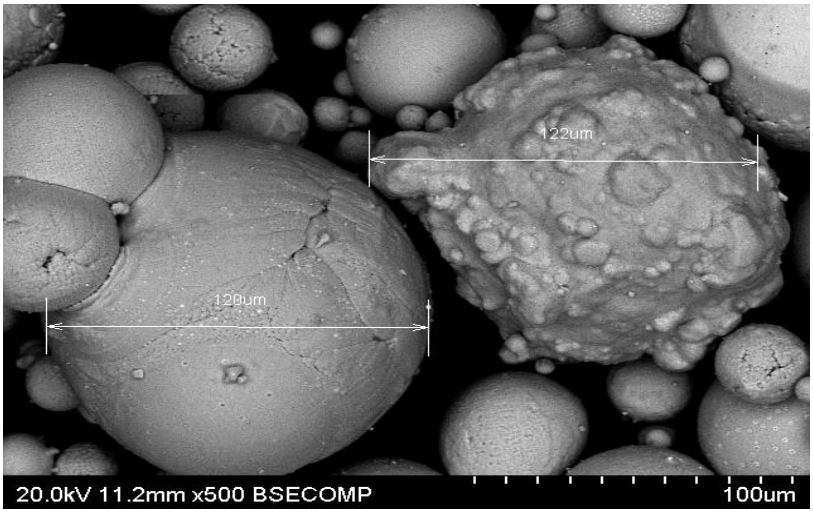

Figure 94: p-type FeNiCo pre-oxidised powder grain before flame-spray [max 128±5 µm]

9.1.2.2 Flame-sprayed Surface

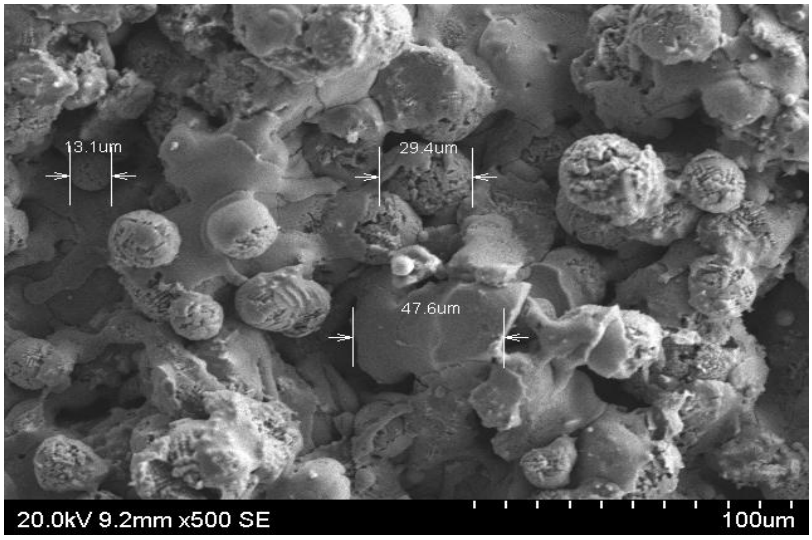

Figure 95: Another position on the n-type $FeCrAlO_4$ unprepared surface

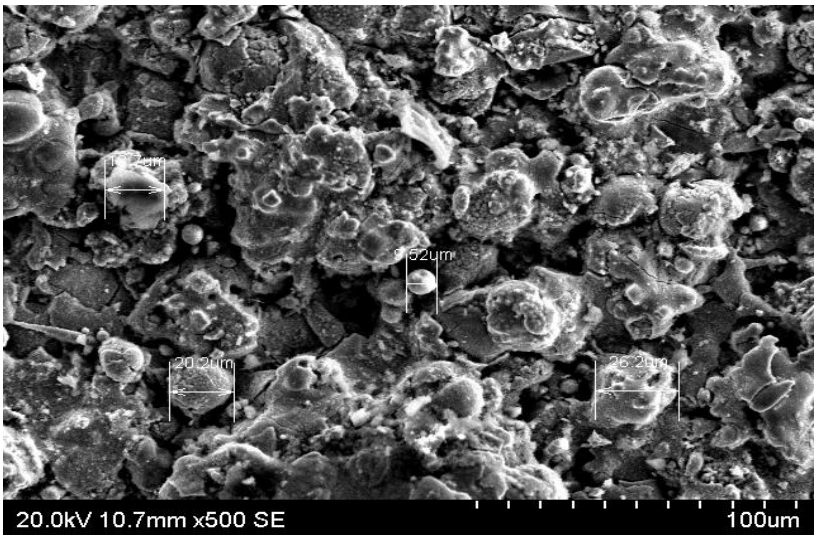

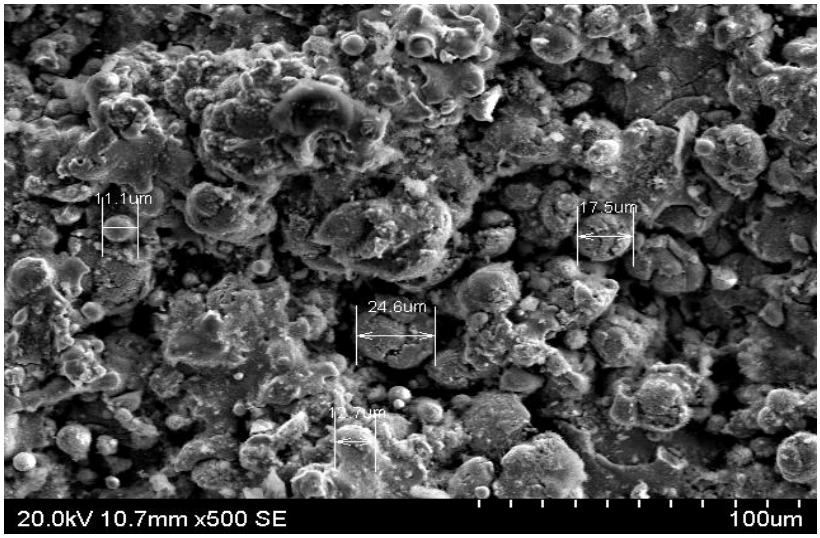

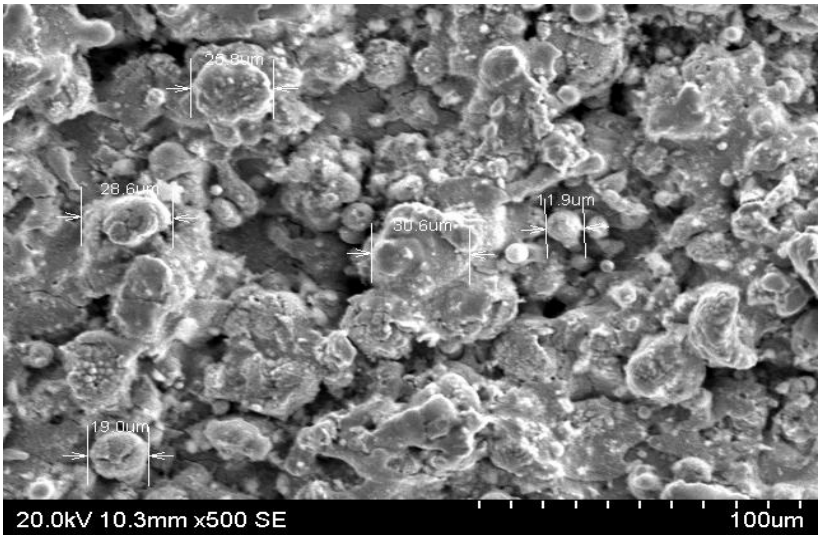

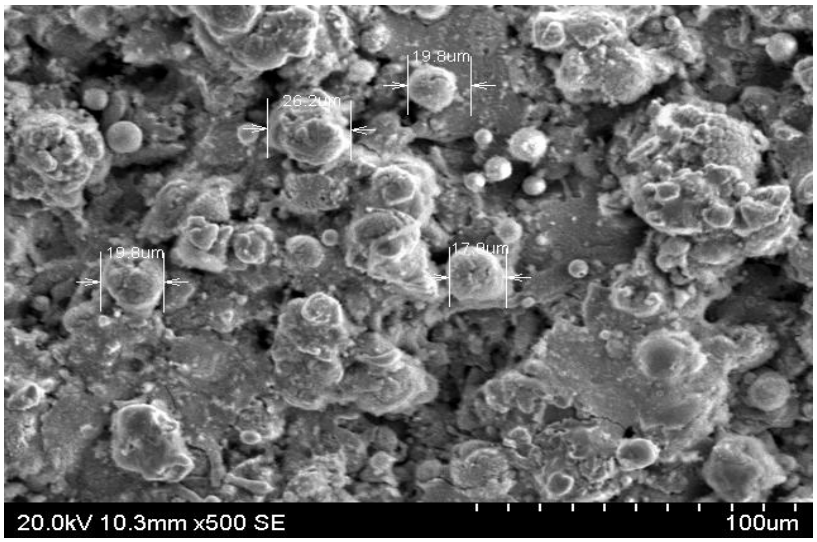

Figure 96: Flame-sprayed surface of n-type $NiMn_2O_4$

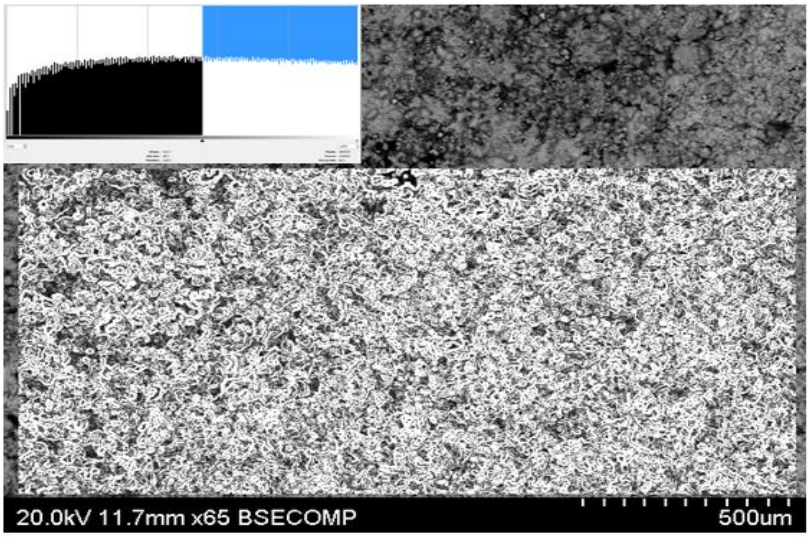

Figure 97: ROI of granular surface at x65 with histogram inset

9.1.3 Contamination and Splash

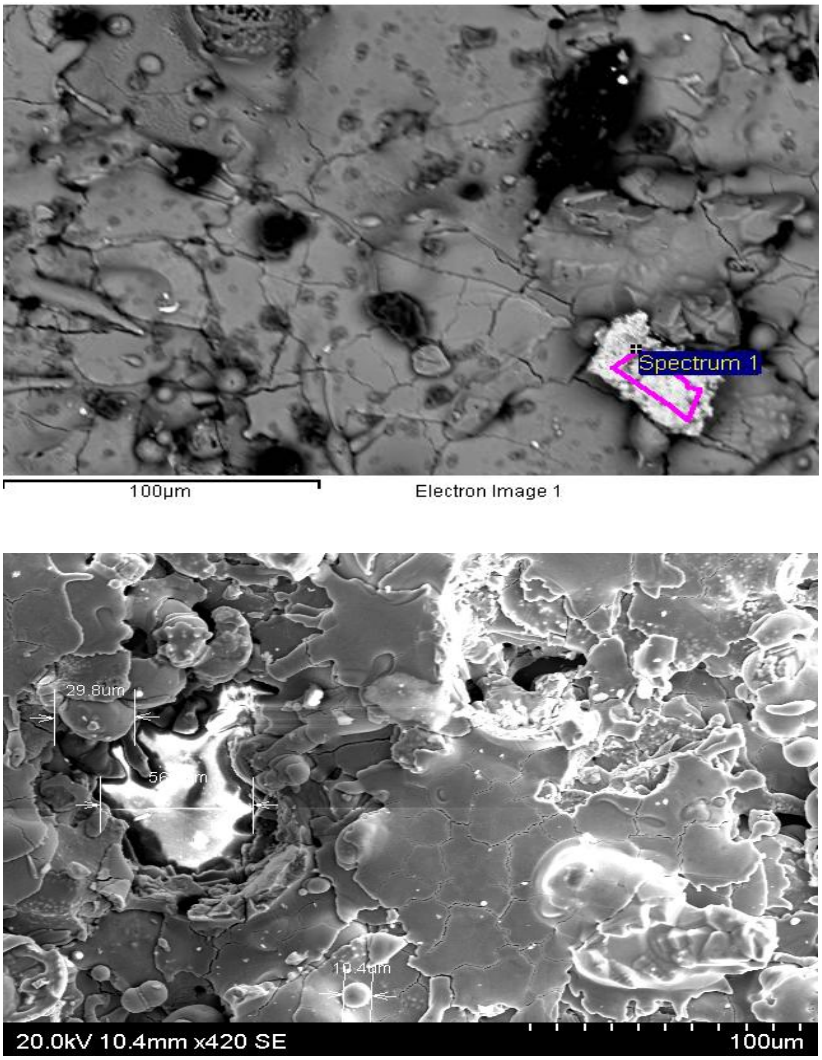

Figure 98: Cu surface contamination of p-type TMO [mixture of FeO and Fe_2O_3]

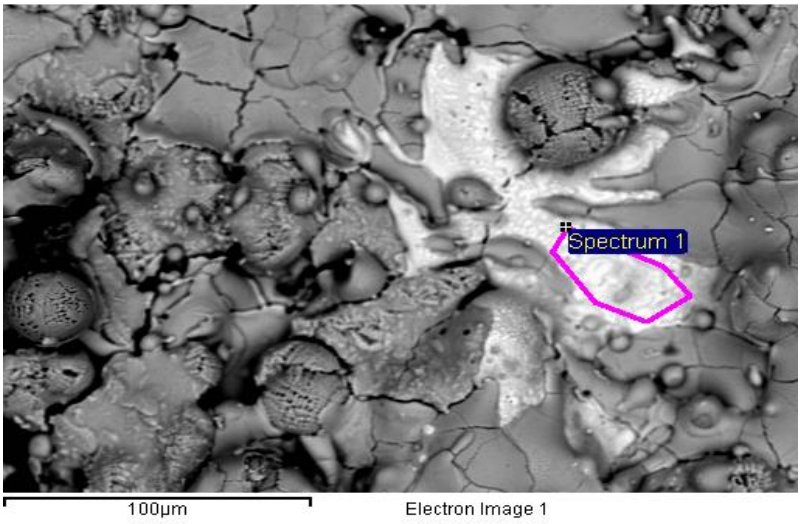

Figure 99: Cu surface contamination of p-type TMO [mixture of $CoFe_2O_4$ and $NiFe_2O_4$]

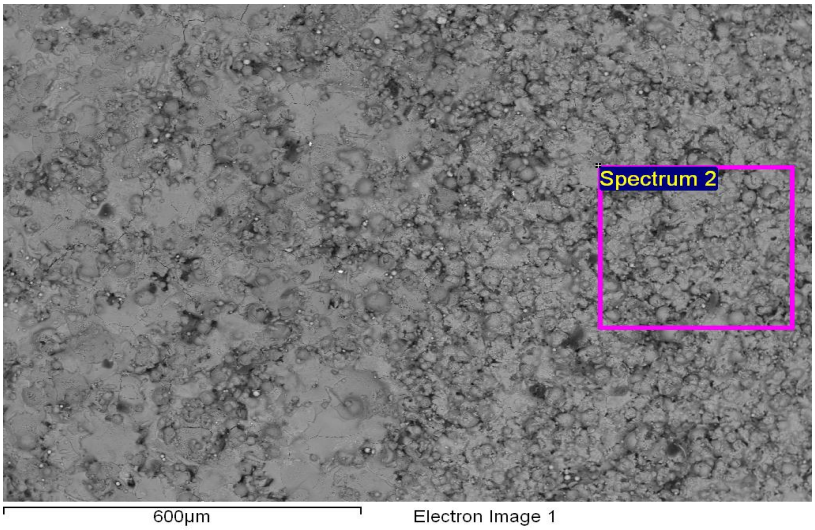

Figure 100: p-n hetrojunction [top view] of the p-type Cr_2O_3 [left] and n-type $NiMn_2O_4$ [right]

9.1.4 Surface and Bulk Comparison

9.1.4.1 Polishing Granularity Estimation

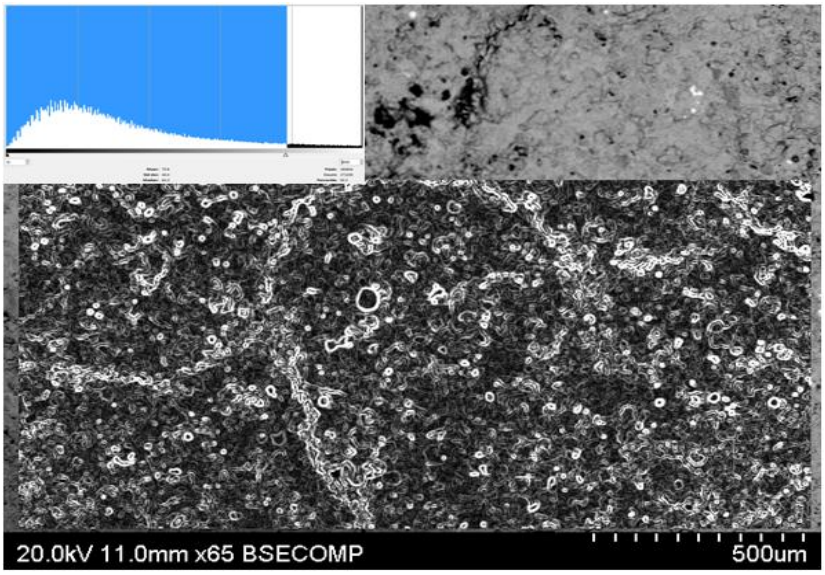

Figure 101: ROI of mechanically polished surface at x65 with histogram inset

9.1.4.2 Bulk Defects Estimation

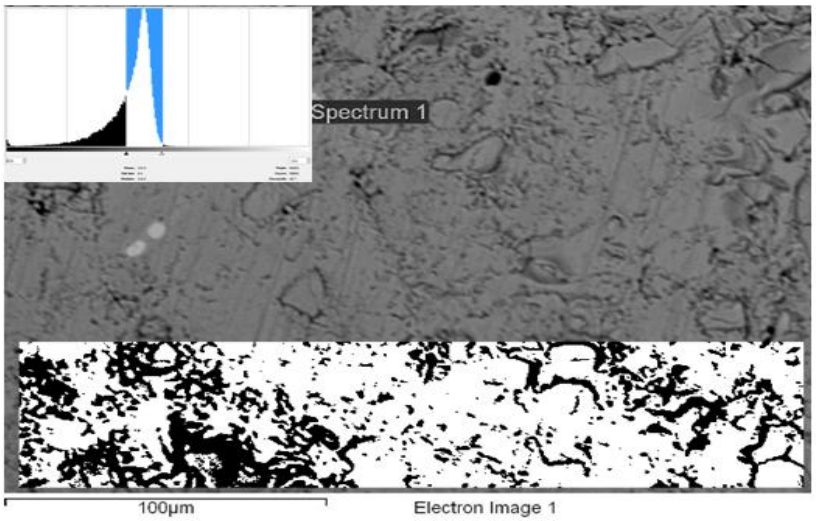

Figure 102: Defects estimation of the ROI with histogram inset; black areas indicate defects

9.1.5 Cross-sectional Analysis

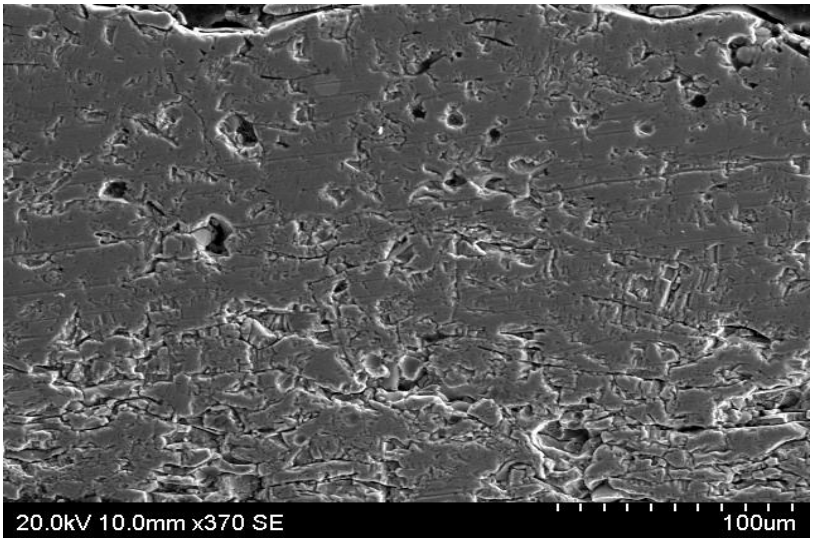

Figure 103: SEM cross-sectional image for defects identification

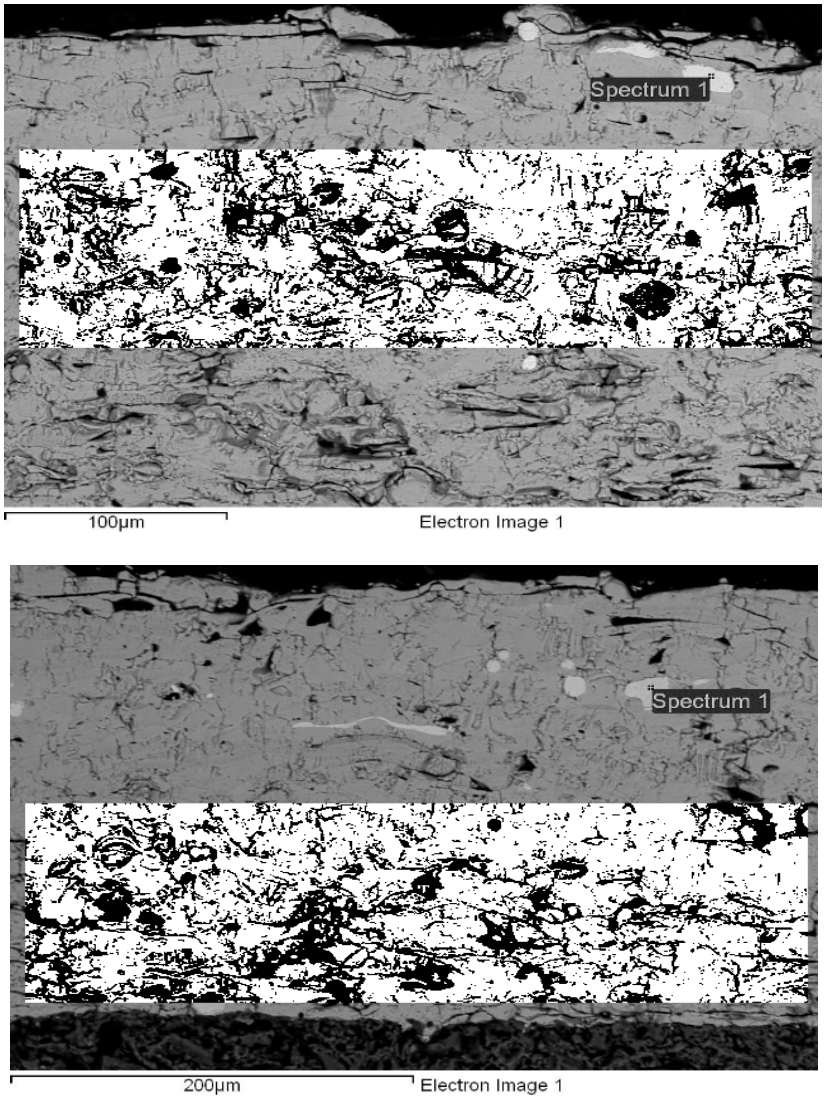

Figure 104: BSE thresholded cross-sectional images for defects and contamination identification; black areas indicate defects

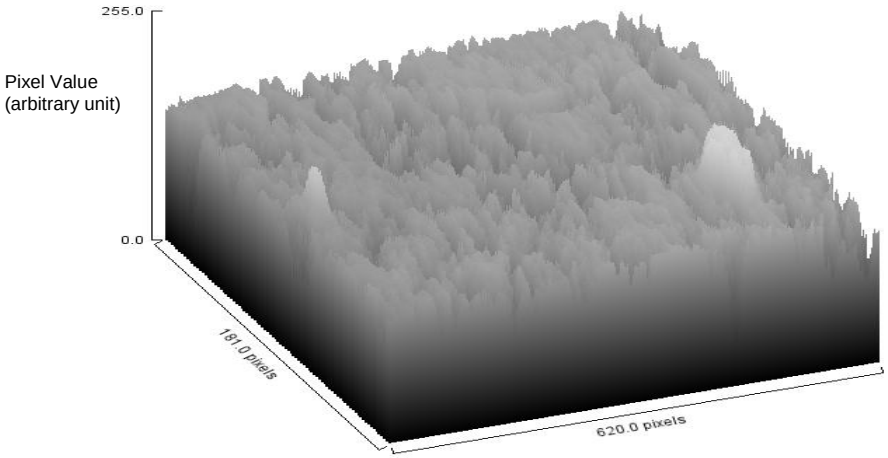

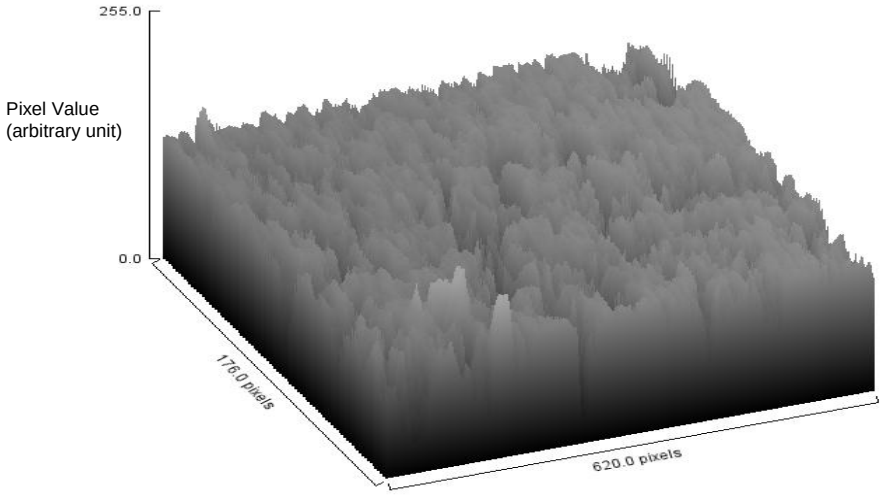

Figure 105: Surface plot of the ROI shown in Figure 104, respectively

9.1.6 Substrate Analysis

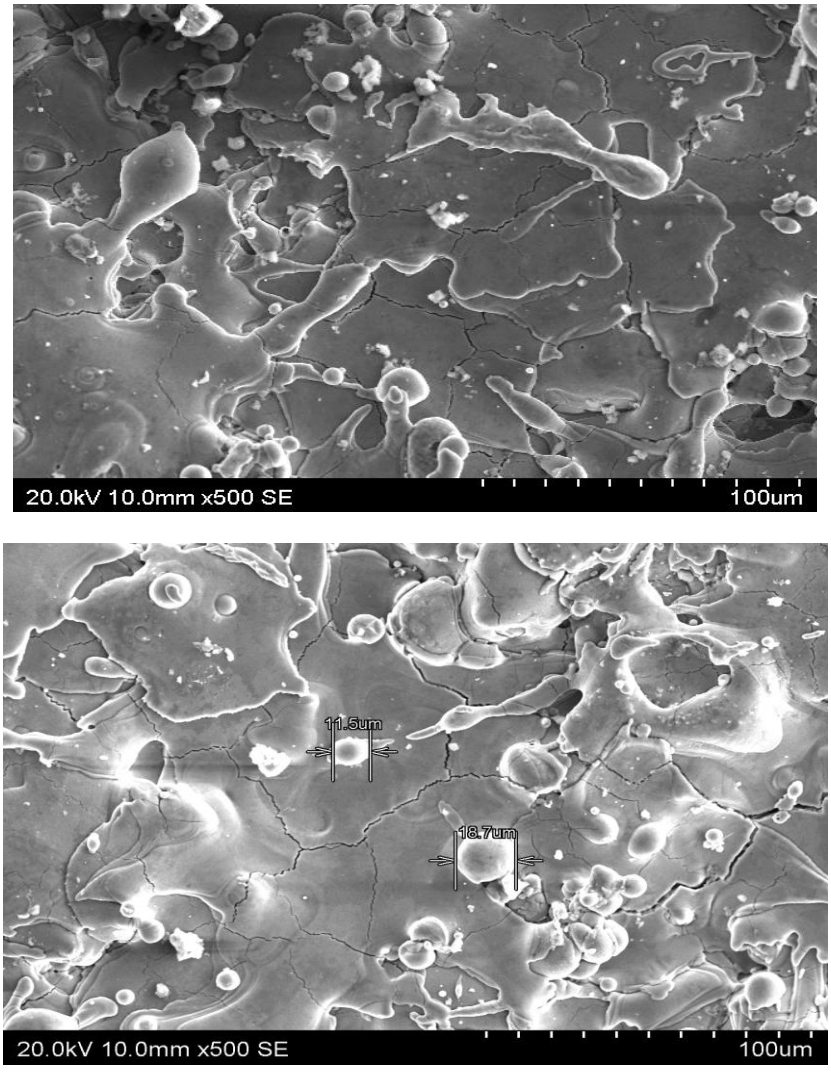

Figure 106: Surface cracks of unprepared sample

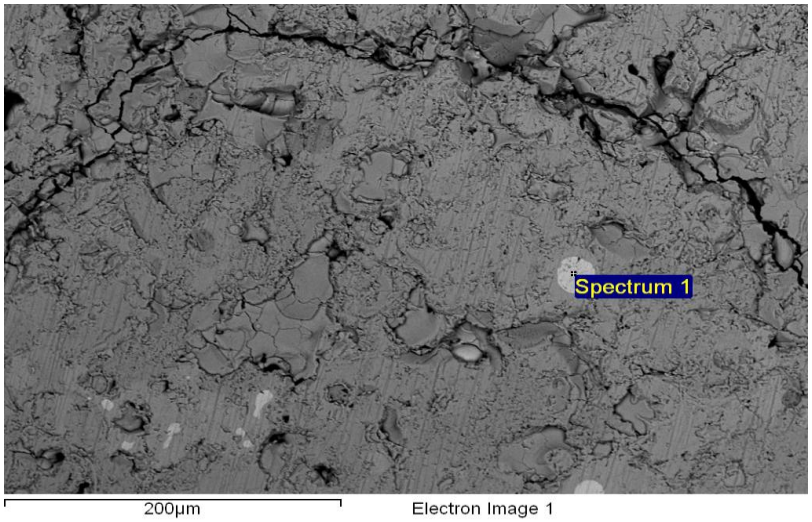

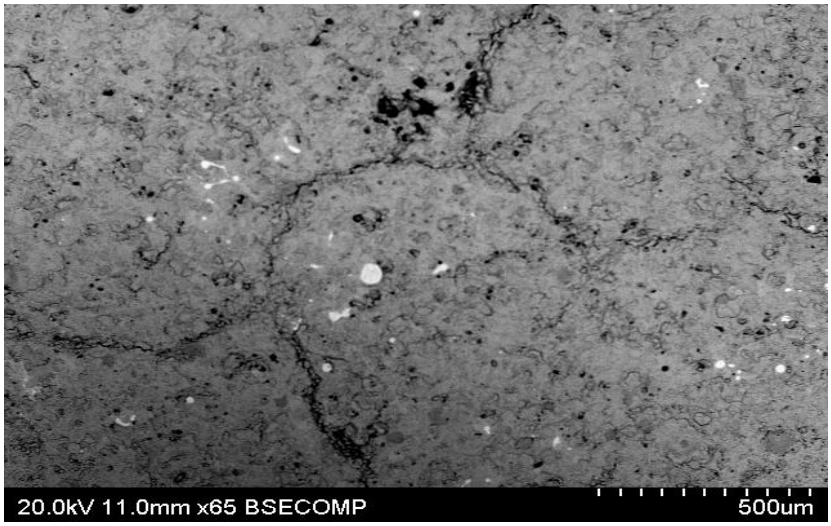

Figure 107: Core cracks of polished samples

9.1.7 Failure of Stacked Design

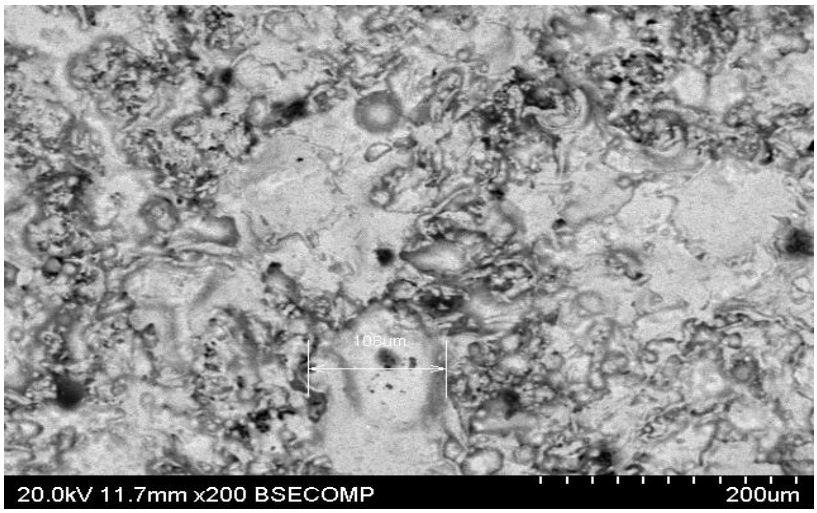

Figure 108: Flame-sprayed Cu electrode

9.2 X-ray Photoemission Spectroscopy

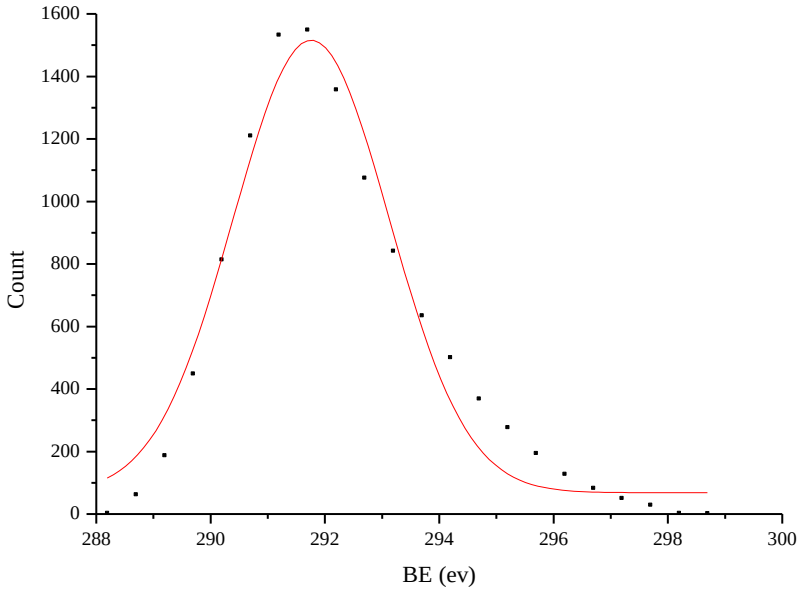

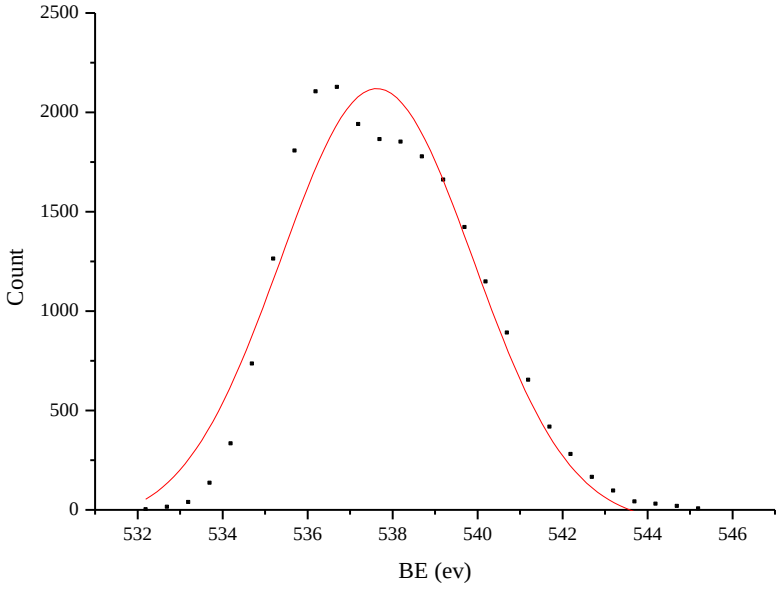

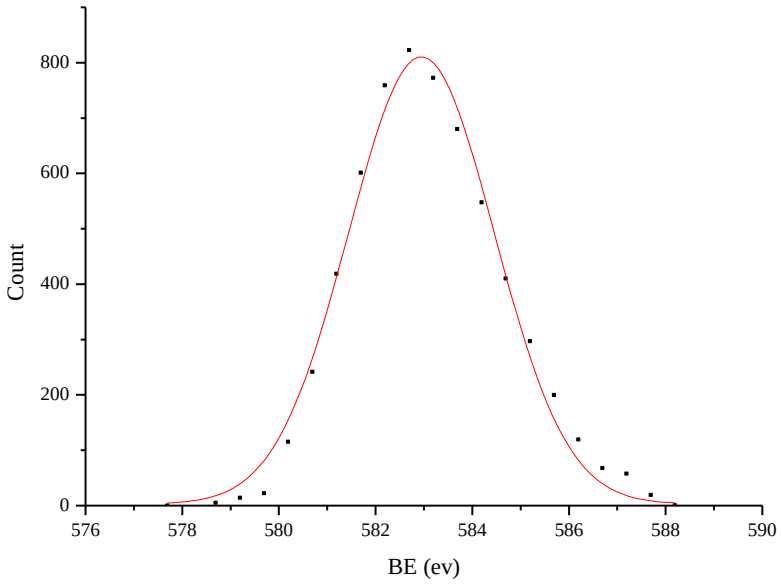
Count
800
600
400
200
0
576
578
580
582
584
586
588
590
BE (ev)

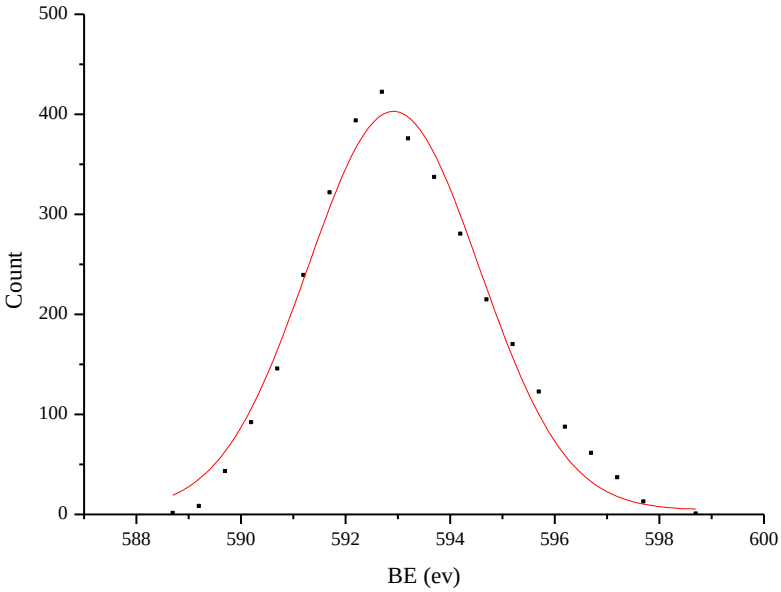
Count
500
400
300
200
100
0
588
590
592
594
596
598
600
BE (ev)

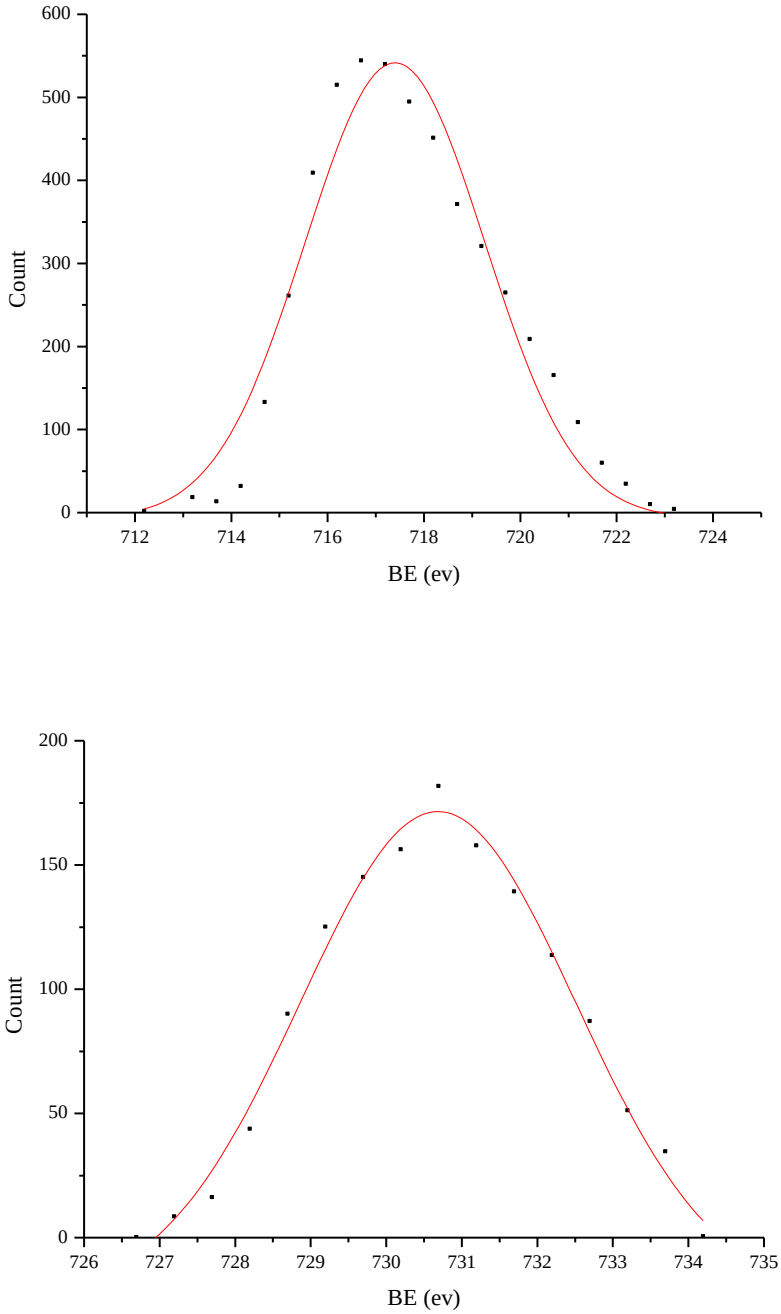

Figure 109: $FeCr_2O_4$ XPS spectra extracted peaks [data points] and their Gaussian fittings [continues lines] of the unprepared surface [before sputtering] shown in Figure 66; in order from top to bottom, C 1s, O 1s, Cr $2p_{3/2}$, Cr $2p_{1/2}$, Fe $2p_{3/2}$ and Fe $2p_{1/2}$

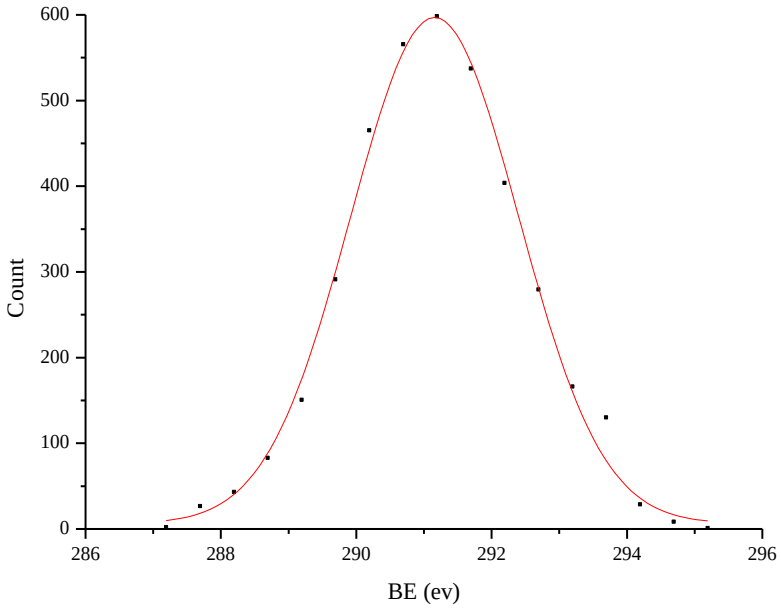
600
500
400
300
200
100
0
Count
286
288
290
292
294
296
BE (ev)

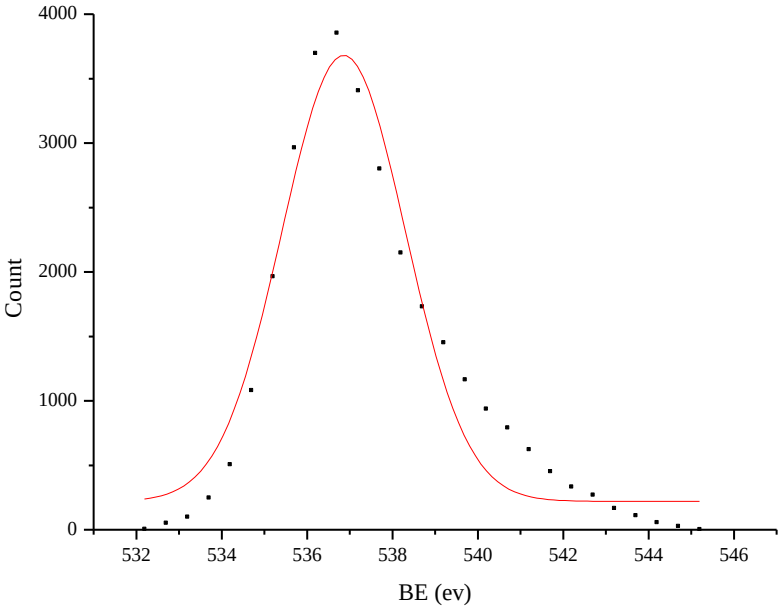
4000
3000
2000
1000
0
Count
532
534
536
538
540
542
544
546
BE (ev)

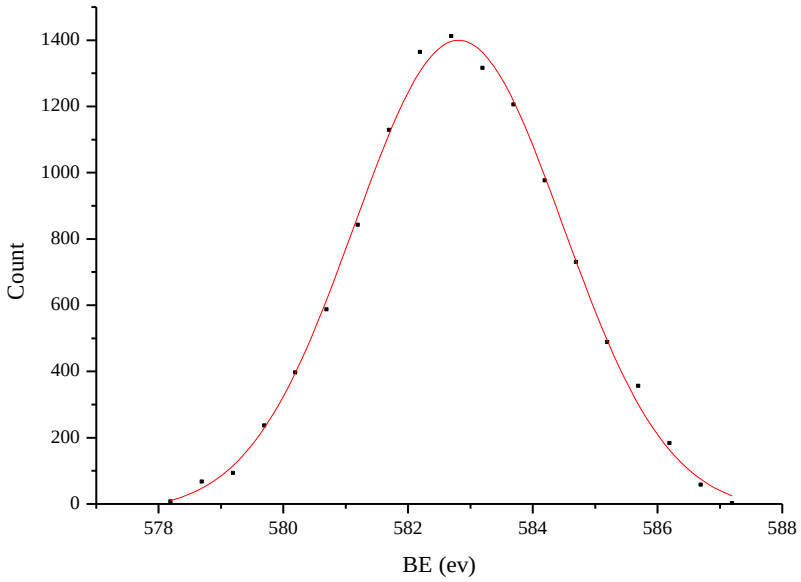
Count
1400
1200
1000
800
600
400
200
0
578
580
582
584
586
588
BE (ev)

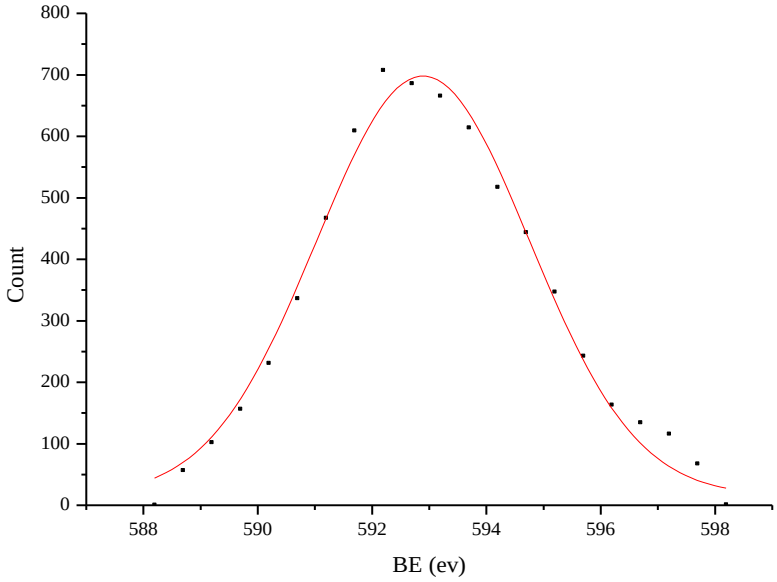
Count
800
700
600
500
400
300
200
100
0
588
590
592
594
596
598
BE (ev)

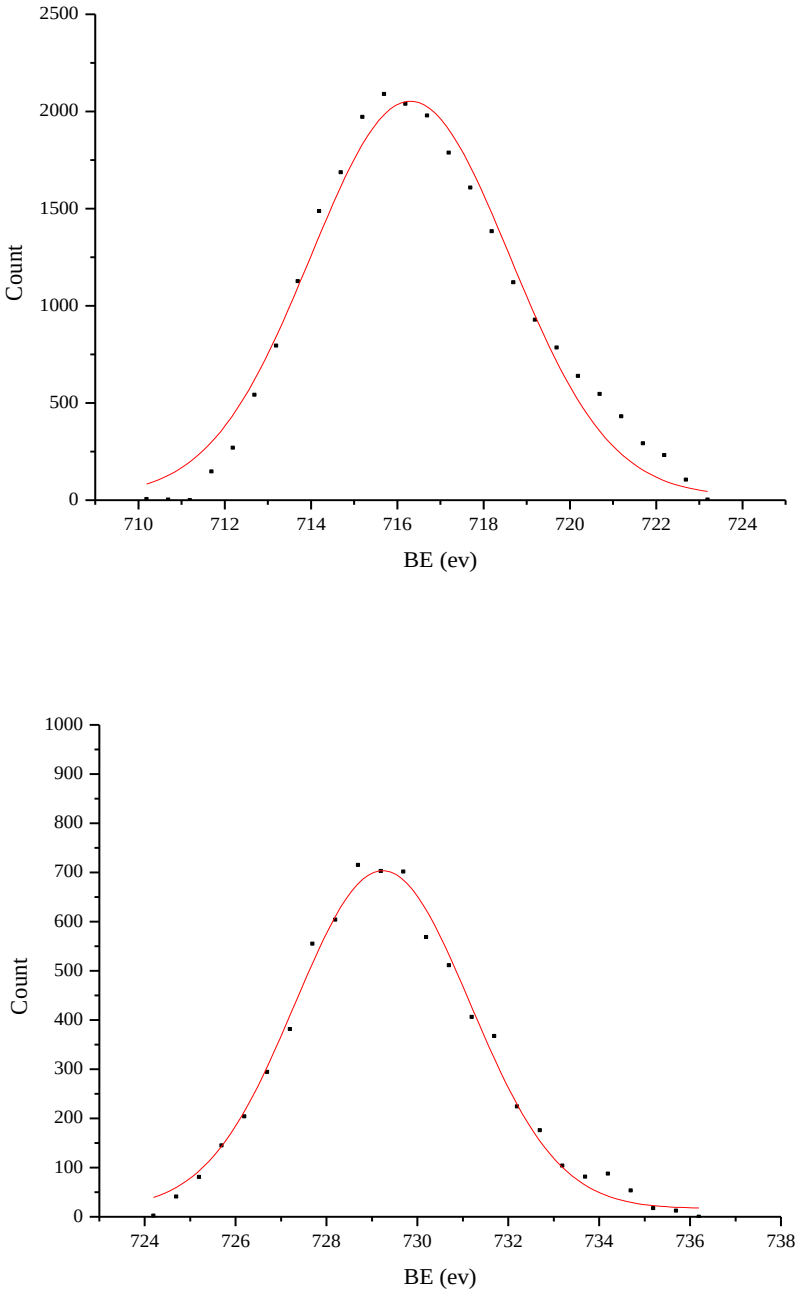

Figure 110: $FeCr_2O_4$ XPS spectra extracted peaks [data points] and their Gaussian fittings [continues lines] of the prepared surface [after sputtering] shown in Figure 66; in order from top to bottom, C 1s, O 1s, Cr $2p_{3/2}$, Cr $2p_{1/2}$, Fe $2p_{3/2}$ and Fe $2p_{1/2}$

9.3 Tube X-ray Analysis for PVD

9.3.1 Reproducibility

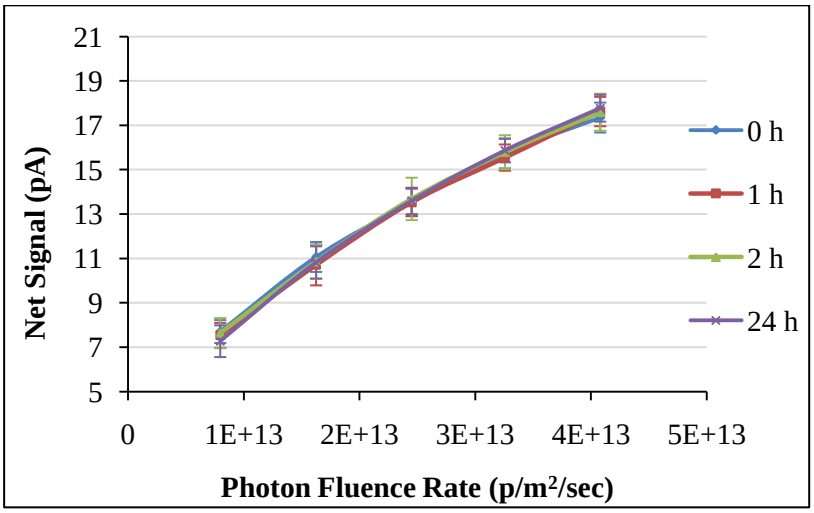

Figure 111: Linearity reproducibility of PVD TMOD2 at 50 kV

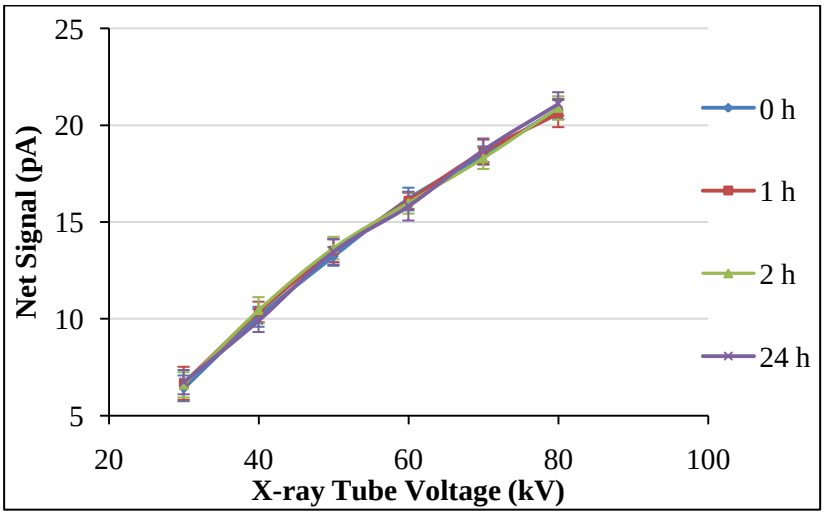

Figure 112: Photon E dependence reproducibility of PVD TMOD2 at 6 mA

9.3.2 Signal Stability

Time (min)	PVD TMOD2 net signal (pA)
1	13.5±0.6
15	13.6±0.7
45	13.7±0.8
90	13.5±0.8
150	13.5±0.6
1590	13.7±0.6

Table 33: Signal stability comparison of PVD TMOD2 at 50 kV and 6 mA

9.4 UV Analysis for PVD

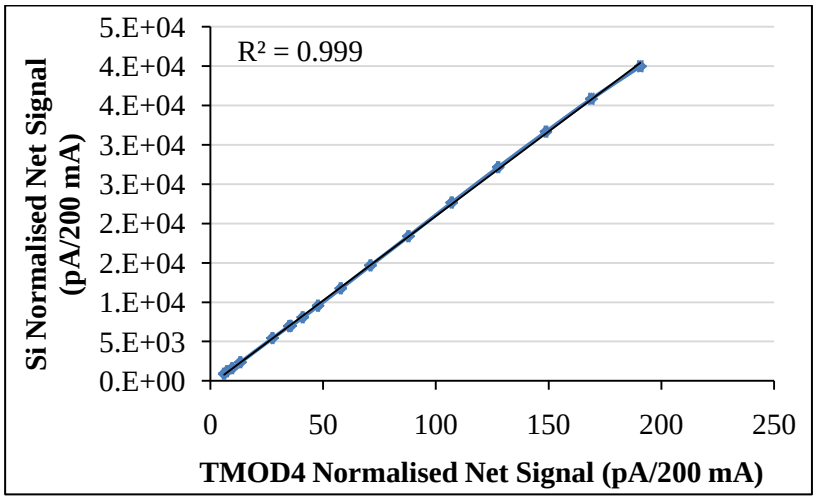

Figure 113: TMOD4-Si photodiode correlation at 40 eV